Title
Nitrogen Cycling in Permeable Sediments: Process-based Models for Streams and the Coastal Ocean

Permalink
https://escholarship.org/uc/item/0r4720nz

Author
Azizian, Morvarid

Publication Date
2017

Peer reviewed|Thesis/dissertation

UNIVERSITY OF CALIFORNIA,
IRVINE

Nitrogen Cycling in Permeable Sediments: Process-based Models for Streams and the Coastal Ocean

DISSERTATION

submitted in partial satisfaction of the requirements
for the degree of

DOCTOR OF PHILOSOPHY

in Chemical and Biochemical Engineering

by

Morvarid Azizian

Dissertation Committee:
Professor Stanley Grant, Chair
Professor Vasan Venugopalan
Professor Said Elghobashi

2017

DEDICATED TO

MY PARENTS

AND

MY HUSBAND

TABLE OF CONTENTS

LIST OF FIGURES

LIST OF TABLES

ACKNOWLEDGMENTS

I would like to express the deepest appreciation to my committee chair, Professor Stanley Grant, who has the attitude and the substance of a genius: he continually and convincingly conveyed a spirit of adventure in regard to research and scholarship, and an excitement in regard to teaching. Without his guidance and persistent help this dissertation would not have been possible.

I would like to thank my committee members, Professor Vasan Venugopalan and Professor Said Elghobashi, for sharing with me their insights and enthusiasm for research and gaining knowledge. I am also grateful for the opportunity to work closely with Dr. Megan Rippy and benefit from her comments on my research to improve my dissertation.

In addition, a thank you to Doctors Fulvio Boano of the Politecnico di Torino, Perran Cook of the Monash University, Russel Detwiler of the University of California-Irvine, Michael Stewardson of the University of Melbourne, Keith Stolzenbach of the University of California-Los Angeles, Adam Kessler of the Monash University, Alexander McCluskey of the University of Melbourne, and Laura Bardini of the Politecnico di Torino for their insights on this research and their contributions in my journal publications.

I gratefully acknowledge financial support from the U.S. National Science Foundation Partnerships for International Research and Education (OISE-1243543), an Australian Research Council Discovery Project (DPI30103619), and UC office of the President Multi-campus Research Program Initiative award (MRPI-17-455083).

I would like to thank my loved ones, who have supported me throughout the entire process, both by keeping me harmonious and helping me putting pieces together. This dissertation would not have been possible without the support and encouragement from my dear parents, Roohangiz Badami and MohammadReza Azizian; my parents in law, Foroughosadat Mirzadeh and Hamidreza Esmaili; my dear brothers Alireza and Amirreza. And a special thank to my beloved husband Omid Esmaili, who was always my support in the moments when there was no one to help me and/or answer my queries.

All people mentioned here deserve special thanks for the completion of this dissertation. Without their encouragement, support, and sacrifice, I would not have made it to UCI, and could not have finished this dissertation. I would like to take this opportunity to express my deepest gratitude for what they have done for me. This is the extent to which my appreciation can be expressed through words and I believe it comes tremendously short of what is due. This work is dedicated to them.

CURRICULUM VITAE

Morvarid Azizian

2004—2008	Bachelor of Science (B.Sc.) in Chemical Engineering, Azad University, Tehran
2009—2011	Master of Science (M.Sc.) in Chemical Engineering, Tehran University, Tehran
2011—2017	Doctor of Philosophy (Ph.D.) in Chemical Engineering, University of California, Irvine

09/2011—09/2017	Research Assistant, University of California, Irvine (UCI)
3/2015—6/2015	Teaching Assistant – CEE162: Introduction to Environmental Chemistry, UCI
1/2012—3/2012	Teaching Assistant - ChEMS 140A: Unit Operation Systems, UCI
3/2011—6/2011	Chemical Engineer Intern, RHI AG Technology Center, Leoben, Austria
12/2010—3/2011	Chemical Engineer Intern, PARS Refractories Co., Yazd, Iran
9/2008—12/2010	Chemical Engineer, MIRCOH Inc., Tehran, Iran
1/2010—3/2010	Teaching Assistant – Process Control, Azad University, Tehran, Iran
5/2008—9/2008	Chemical Engineer Intern, Ekbatan Cement Co., Tehran, Iran
6/2006—5/2008	Chemical Engineer Intern, Mircoh Inc., Tehran, Iran

FIELD OF STUDY

Fate and Transport of nutrients in streams and coastal ocean

PUBLICATIONS

Azizian, M.; F. Boano; P.L.M. Cook; R. Detwiler; M.A. Rippy; S. B. Grant (**2017**) “Ambient Groundwater Flow Diminishes Nitrate Processing in Hyporheic Zone of Streams” Water Resources Research, doi:10.1002/2016WR020048.

Azizian, M.; A. Kessler; P.L.M. Cook; S.B. Grant; M.A. Rippy; M. Stewardson (**2015**) “Bedforms as Biocatalitic Filters: A Pumping and Streamline Segregation (PASS) Model for Nitrogen Removal in Prermeable Sediments” Environmental Science & Technoogy, 49 (18), 10993–11002, doi: 10.1021/acs.est.5b01941.

Grant, S. B.; K. Stolzenbach,; **M. Azizian**; M. J. Stewardson; F. Boano; L. Bardini (**2014**) “First-Order Contaminant Removal in the Hyporheic Zone of Streams: Physical Insights from a Simple Analytical Model” Environmental Science & Technoogy, 48, 11369-11378, doi: 10.1021/es501694k.

ABSTRACT OF THE DISSERTATION

Nitrogen Cycling in Permeable Sediments:
Process-based Models for Streams and the Coastal Ocean

By

Morvarid Azizian

Doctor of Philosophy in Chemical and Biochemical Engineering

University of California, Irvine, 2017

Professor Stanley B. Grant, Chair

Bioavailable forms of nitrogen, such as nitrate, are necessary for aquatic ecosystem productivity. Excess nitrate in aquatic systems, however, can adversely affect ecosystems and degrade both surface water and groundwater. Some of this excess nitrate can be removed in the sediments that line the bottom of rivers and coastal waters, through the exchange of water between surface water and groundwater (known as hyporheic exchange).

Several process-based models have been proposed for estimating nitrate removal in aquatic systems but these (1) do not consider the multiscale nature of hyporheic exchange flows; (2) rely on simplified conceptualizations of mixing within streambed sediments (e.g., a well-mixed box); (3) neglect important steps in the N-cycle (e.g., nitrification and ammonification); and/or (4) adopt pseudo-first-order kinetic descriptions of denitrification. On the other hand, a number of empirical correlations have been published based on in-stream measurements of nitrate uptake using reach-scale stable isotope tracer experiments. While these correlations are noteworthy in many respects, they do not account for physical processes known to play an

important role in nutrient processing, such as the exchange of water between a stream, sediments, and groundwater.

In this thesis, I develop and test a simple and scalable process-based model for estimating the nitrate uptake velocity that addresses the limitations identified above. In particular, my model accounts for: (1) hyporheic exchange at multiple scales together with ambient groundwater flow; (2) the broad residence time distributions characteristic of hyporheic exchange; (3) key biogeochemical reactions associated with N-cycling, including respiration, ammonification, nitrification, and denitrification; and (4) the nonlinear nature of the pertinent biogeochemical reaction rates, including Monod kinetics for aerobic respiration and denitrification, and second-order kinetics for nitrification. Using this modeling framework I systematically evaluate primary controls on stream N-cycling and evaluate how multi-scale and regional factors are likely to affect this process. I also demonstrate how my model predictions compare with previously published reach-scale measurements of nitrate removal, develop scaling relationships by which my process-based model can be applicable to larger scales (i.e., watershed and regional scales), and provide some mechanistic explanations for previous observations.

Chapter 1

Introduction

1.1. Problem Statement

Bioavailable forms of nitrogen (N), such as nitrate (NO_3), are necessary for aquatic ecosystem productivity. Excess nitrate in aquatic systems, however, can adversely affect ecosystems and degrade both surface water and groundwater [Aber, 1992; Smith et al., 1999; Canfield et al., 2010]. Human activities more than doubled the bioavailable nitrogen added to terrestrial landscapes during the last century and recent projections suggest that human contributions to the terrestrial nitrogen budget will grow still more in the future [Seitzinger et al., 2006; Galloway et al., 2004]. Much of this nitrogen finds its way to rivers and streams though myriad point and non-point sources and negatively impacts water quality and stream and coastal water ecosystems [Yates, 1985; Jongbloed and Lenis, 1998; Marti et al., 2004; David et al., 2006; Carey and Migliaccio, 2009]. Thousands of stream, river, lake, groundwater, and coastal sites in the U.S. are classified as impaired for nitrogen by the U.S. Environmental Protection Agency [Schot and van der Wal, 1992, Hancock, 2002; U.S. E.P.A, 2017]. The U.S. National Academy of Engineering has identified restoring balance to the nitrogen cycle as one of the 14 Grand Challenges facing engineers in the 21st Century [U.S. N.A.E., 2017].

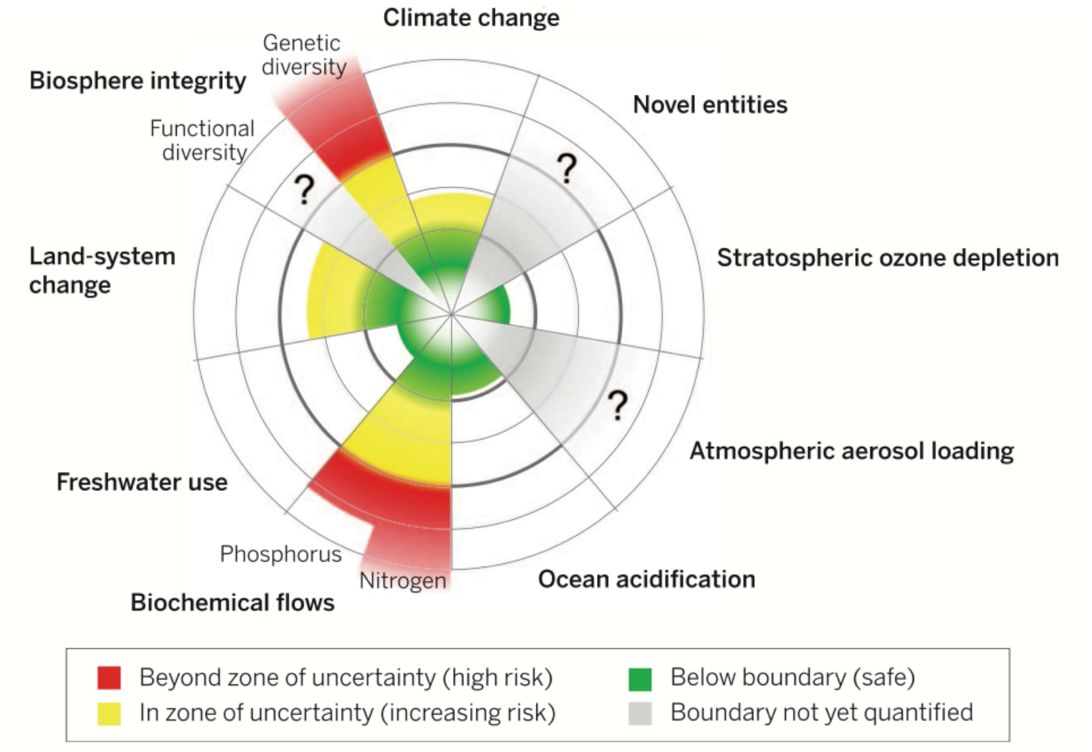

Figure 1.1. The current status of the control variables for seven of the planetary boundaries (from Steffen et al. [2015]).

In a recent assessment of planetary boundaries (limits beyond which the earth system could change to a new state that is potentially inhospitable to humans) the nitrate inputs to freshwater and marine ecosystems, derived primarily from agricultural runoff, was identified as one of three planetary boundaries that humans have already been "transgressed" (**Figure 1.1**) [Steffen et al., 2015]. Consequently, there is an urgent need to understand the factors that control the fate and transport of reactive nitrogen in streams and the influence of changing hydrologic and biogeochemical conditions.

1.2. Research Objectives and Contributions

The cycling of nitrate in aquatic systems is complex and couples multiple scales of time (i.e. from seconds to years) and space (e.g. from single bedforms to the earth system as a whole). In this thesis I focus on one important process that determines the impact that nitrate sources (e.g., from the over application of fertilizers) have on downstream ecosystems: the processing of nitrate (through microbial respiration, ammonification, nitrification, and denitrification) in sediments that line the bottom of rivers and coastal waters. Specifically, I focus on the so-called uptake velocity of nitrate, which represents the flux of nitrate across the sediment-water interface, normalized by the nitrate concentration in the water column (the uptake velocity has units of m s^{-1}).

Several process-based models have been proposed for estimating the uptake velocity of nitrate v_f in aquatic systems [see Stream Solute Workshop, 1990; Runkel, 2007; Botter et al., 2010; Argerich et al., 2011] but these rely on highly simplified conceptualizations of mixing within sediments (e.g., a well-mixed box, Cheong et al. [2007]), do not take into account the influence of subsurface flow fields operating at multiple scales (e.g., the influence of regional groundwater flow, Trauth et al. [2013]), and adopt pseudo-first-order kinetic descriptions of denitrification that neglect important steps in the nitrogen cycle (e.g., nitrification and ammonification). On the other hand, a number of empirical correlations for v_f have been published based on in-stream measurements of nitrate uptake using reach-scale stable isotope tracer experiments [Wolheim et al., 2006; Mulholland et al., 2008]. While these correlations are noteworthy in many respects, they do not account for physical processes known to play an important role in nutrient processing, such as the exchange of water between a stream, sediments, and groundwater.

In this thesis I present a process-based model for nitrogen cycling in permeable surficial sediments that line the bottom of streams and the coastal ocean. Specifically, I demonstrate how nitrate processing in streams and the coastal ocean—a globally important ecosystem service—is affected by the coupling between the physics of water flow through surficial sediments (driven by both dynamic and static pressure variations over the sediment-water interface [Boano et al., 2014; Trauth et al., 2013; Bardini et al., 2012] and biogeochemical reactions carried out by biofilm-associated microbial communities that grow in the sediment's interstitial void space [see National Environmental Research Institute, 2004].

This coupling of flow through, and reaction within, surficial permeable sediments falls under the general heading of "hyporheic exchange" in the stream literature (the hyporheic zone is an ecotone characterized by unique organisms and strong redox, temperature, and nutrient gradients from the subsurface mixing of stream water and groundwater [Boano et al., 2014]). In this thesis I also adopt the term "hyporheic exchange", while acknowledging that the models I am developing could equally well be used to examine nitrate transformations in sediments that line the coastal ocean (the coastal ocean literature would refer to this process as "pore water flushing" instead of "hyporheic exchange" [Huettel et al., 2014]—it is a case where different fields have different terminology for the same basic phenomenon).

The present state-of-the-art for modeling hyporheic exchange involves three steps: (1) calculate the pressure distribution at the sediment-water interface (SWI) by numerically

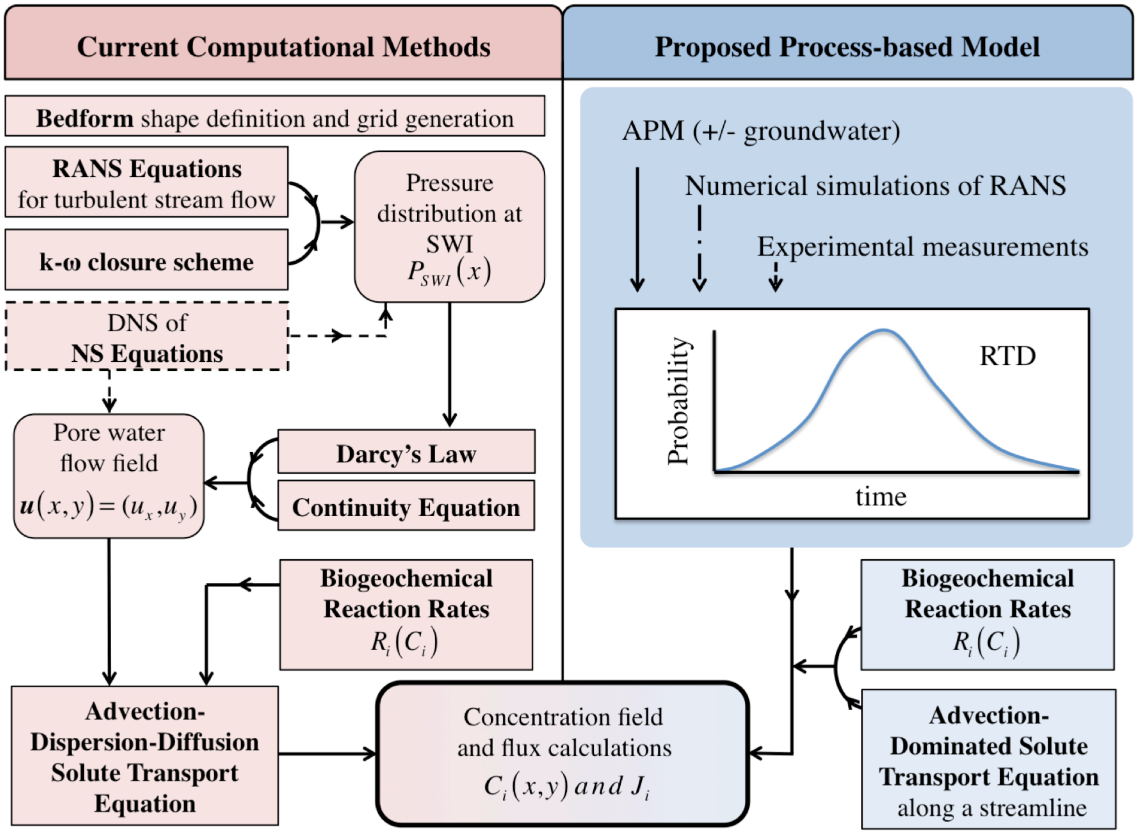

Figure 1.2. Schematic presentation of the state-of-the-art computational modeling processes for predicting solute concentrations in permeable sediments (red area) versus my proposed process-based model (blue area).

integrating the Navier-Stokes (NS) equations for turbulent stream flow over the streambed topography of interest; (2) calculate the flow of water through the hyporheic zone from Darcy's Law and the continuity equation using pressure distributions along the sediment-water interface (from step (1)) and along the stream-aquifer boundary together with an assumed sediment permeability field; and (3) calculate solute concentrations in the interstitial fluids of the sediment from a mass conservation equation that accounts for physical transport processes (advection, mechanical dispersion, and molecular diffusion) and the chemical and biogeochemical transformations of interest (red side of **Figure 1.2**)

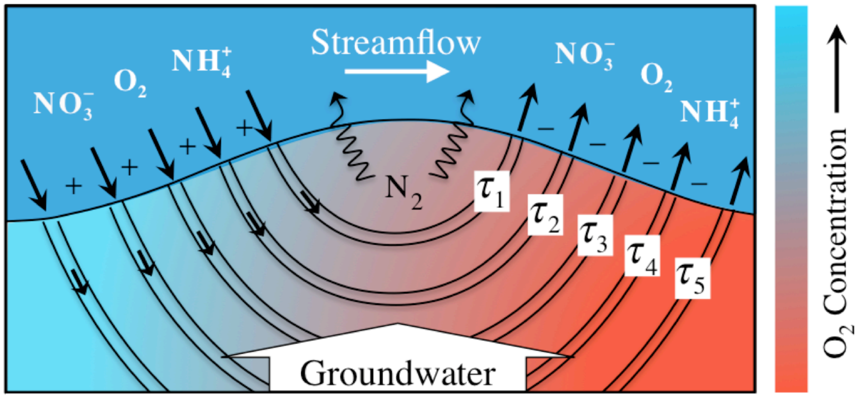

Figure 1.3. Schematic of hyporheic zone tubes (HZT) and their interaction with stream flow and groundwater flow. Aerobic respiration carried out by biofilm communities living in the sediments consume oxygen, leading to a bulk decline in oxygen as stream water travels from the downwelling zone (left side of figure) to the upwelling zone (right side of figure).

[Cardenas and Wilson, 2007a, 2007b; Kessler et al., 2013a, 2013b]. Note that this "state-of-the-art" model does not take into account potential feedbacks, for example precipitation reactions which change the permeability of the sediments, which change the flow field, which change the reaction field, and so on.

To complement the relatively computationally- and data-intensive numerical approach described above (and inspired by similar problems in chemical engineering reactor design [Levenspiel, 1972; Hill, 1977]), my work relies on a simpler process-based model founded on the following assumptions (**Figure 1.3**): (1) the hyporheic zone can be conceptualized as a bundle of isolated tubes that collectively represent the various flow paths stream water takes as it passes through the sediment (I refer to these tubes as "hyporheic zone tubes" or HZT); (2) water parcels moving through one HZT do not mix with water parcels in adjacent HZT (i.e., the streamlines are segregated); and (3) the fate and transport of reactive solutes in any individual HZT occurs by convection and reaction alone (i.e., molecular diffusion and mechanical dispersion are neglected).

By adopting these simplifying assumptions, the final concentration of nitrate exiting any particular HZT will depend on the time water spends in the tube (the tube's residence time, τ) and the subsurface reactions that collectively alter the chemical make-up of the water as it passes through the tube (i.e., the sediment's "chemistry"): $C_{\text{HZT-NO}_3^-}(\tau,\text{"chemistry"})$. As used here, "chemistry" is shorthand for the set of reactions (and associated kinetic rate expressions) affecting nitrate processing in the hyporheic zone. With these simplifying assumptions, the nitrate uptake velocity v_f can be calculated from the following integral expression:

$$\bar{C}_{\text{HZT-NO}_3^-} = \frac{1}{C_{\text{S-NO}_3^-}} \int_0^\infty C_{\text{HZT-NO}_3^-}(\tau,\text{"chemistry"}) \times E(\tau)\,d\tau \tag{1a}$$

$$v_\text{f} = q_\text{H}\left[\bar{C}_{\text{HZT-NO}_3^-} - 1\right] \tag{1b}$$

The quantity $\bar{C}_{\text{HZT-NO}_3^-}$ can be interpreted as the normalized flow-weighted concentration of nitrate exiting the hyporheic zone, the variable $C_{\text{S-NO}_3^-}$ represents the nitrate concentration in a stream reach, and the pore-water flushing rate q_H represents the flux of stream water across the sediment-water interface due to hyporheic exchange; i.e., volume of stream water moving through the sediment per unit streambed area per unit time (units of m s^{-1}). The residence time distribution (RTD) of the hyporheic zone is represented by a probability density function E (units s^{-1}), where the quantity $E(\tau)d\tau$ represents the fraction of stream water moving through the hyporheic zone with residence times within $d\tau$ of τ.

The last two equations are at the heart of my thesis, and represent the organizing principle around which all the following chapters of this thesis revolve. Specifically, my research thesis will focus on the evaluation of equations (1a) and (1b) for different forms of the RTD (obtained from an analytical model, numerical integration of the Navier-Stokes equations, and experimental measurements) and different choices of chemical reactions (first-order reactive solute and a previously published biogeochemical model for nitrogen cycling in the coastal ocean.

1.3. Organization of the Dissertation

In this dissertation, within the framework mentioned in previous section, I develop a process-based model for nitrate removal in the hyporheic zone of the streams and coastal oceans. Here below I describe the organization of the different chapters and appendices of this dissertation.

In **Chapter 2** [Grant et al., 2014], I adopt the RTD associated with a highly idealized model of the hyporheic exchange flow field in duned or rippled streambeds, which is called the Advective Pumping Model (APM) and was originally proposed by Elliott and Brooks [1997a, 1997b]. Using this idealized model of hyporheic exchange, I solve the concentration flow field in the hyporheic zone and the mass flux across the sediment-water interface for a reactive solute following first-order decay. I compare the predictions of my analytical solution to previously published numerical simulations and experimental measurements of hyporheic exchange, and perform COMSOL Multiphysics numerical simulations to determine if mechanical dispersion and molecular diffusion can be neglected (a key assumption of my process-based model). Finally, in order to test whether or not mass transfer coefficient can be used to model hyporheic exchange, I compare several empirical approaches for estimating the mass transfer coefficient for 42 previously published hyporheic exchange experiments. The supplementary information of this chapter is provided in **Appendix A**.

In **Chapter 3** [Azizian et al., 2015], I combine the APM flow field described above with some key biogeochemical reactions involved in nitrogen cycle in streams (respiration, ammonification, nitrification, and denitrification). I compare my results with previously published experimental measurements of oxygen reaction and transport through sand ripples (carried out by our colleagues in Australia in laboratory flumes) and numerical flume predictions obtained from computational fluid dynamic (CFD) simulations of turbulent flow over periodic bedforms [Kessler et al., 2013a, 2013b]. The goal of this analysis is to see whether my simple model can be used in place of the more labor- and data-intensive numerical flume approach to estimate nitrogen budgets and benthic fluxes in permeable bedforms. Then I apply my model to six representative aquatic environments, including three riverine environments and three coastal waters to understand if the combination of biogeochemical cycling of nitrate within permeable sediments through direct denitrification or coupled nitrification-denitrification is environment-specific. At the end I compare my model's results with a previously published power-law relationship between nitrate uptake velocity and stream nitrate concentration —a result that was published in the journal *Nature* several years ago [Mulholland et al., 2008]. The supplementary information of this chapter is provided in **Appendix B**.

In **Chapter 4** [Azizian et al., 2017], I set out to investigate the effect of several regional and multi-scale factors such as groundwater flow (neutral, gaining, and losing conditions), stream discharge (high versus low discharge), bedform scales (ripples versus riffle-pool sequences), and biogeochemical settings of the environment on nitrogen cycling in permeable sediments. This analysis is done through the Principal Component Analysis (PCA) of oxygen, nitrate, ammonium, and ecosystem respiration of 70 stream sites across the United States (including pristine or reference streams, urban runoff-impacted streams, and agricultural runoff-impacted streams), with which I select three sites with three different biogeochemical settings. The change in nitrogen cycling potential of streambed sediments due to changes in physical factors (i.e., groundwater flow, stream discharge, and bedform scale) is also investigated through using the PASS modeling framework and applying it to a broad range of physical scenarios that were mentioned above. At the end, I translate my model-predicted nitrate uptake velocity into the fraction of nitrate load removed or added by hyporheic exchange over a stream reach and provide some estimates on how groundwater flow would affect stream nitrate load across different biogeochemical and hydrological settings. The supplementary information of this chapter is provided in **Appendix C**.

Finally, in **Chapter 5**, I aim to determine the relative importance of stream physics, chemistry, and biology as controls on in-stream nitrate removal. This issue has important management implications because the best tools for managing watersheds and even global nitrogen budgets are apt to change based on whether nitrogen uptake in the hyporheic zone is modulated by stream physics or biogeochemistry. If the system is physics-controlled, adding flow obstructions (such as logs) or constructing riffle-pool sequences may increase hyporheic exchange and accelerate the natural attenuation of nitrate pollution. On the other hand, if the system is biogeochemistry-controlled, nitrate processing will be modulated primarily by chemistry or resident microbial, plant, and animal communities in the system, perhaps requiring stream re-vegetation, restoration, and other more ecologically-driven approaches. Many seminal studies on nitrogen spiraling in headwater streams have concluded that the nitrate removal is primarily controlled by stream chemistry (i.e., nitrate and ammonium concentrations) and metabolism (i.e., gross primary production or ecosystem respiration) and only weakly by physics (a measure of residence time in the hyporheic zone). Therefore, in this study, I set out to reanalyze a set of previously published nitrogen tracer data measured across 72 U.S. headwater streams and assess the relative importance of physics and biogeochemistry in the context of nitrogen removal in natural streams. The supplementary information of this chapter is provided in **Appendix D**.

References

Aber, J. D. (1992), Nitrogen Cycling and Nitrogen Saturation in Temperate Forest Ecosystems. Tren. Ecol. Evol. 7 (7), 220-223.

Argerich, A., R. Haggerty, E. Marti, F. Sabater, and J. Zarnetske (2011), Quantification of metabolically active transient storage (MATS) in two reaches with constraining transient storage and ecosystem respiration. Geophys. Res., 116, G03034, doi:10.1029/2010JG001379.

Azizian, M.; Grant, S.B.; Kessler, A.J.; Cook, P.L.M.; Rippy, A.; Stewardson, M. (2015), Bedforms as Biocatalytic Filters: A Pumping and Streamline Segregation (PASS) Model for Nitrate Removal in Permeable Sediments. Environ. Sci. Technol. 49(18), 10993-1002, doi: 10.1021/acs.est.5b01941.

Azizian, M.; F. Boano; P.L.M. Cook; R. Detwiler; M.A. Rippy; S. B. Grant (2017), Ambient Groundwater Flow Diminishes Nitrate Processing in Hyporheic Zone of Streams, Water Resources Research, 53(5),3941-3967, doi:10.1002/2016WR020048.

Bardini, L., F. Boano, M.B. Cardenas, R. Revelli, L. Ridolfi (2012), Nutrient cycling in bedform induces hyporheic zones. Geochimica et Cosmochimica Acta, 84, 47–61.

Boano, F., J.W. Harvey, A. Marion, A. I. Packman, R. Revelli, L. Ridolfi, A. Worman (2014), Hyporheic Flow and Transport Processes: Mechanisms, Models, and Biogeochemical Implications. Rev. Geophys., 25, doi:10.1002/2012RG000417.

Botter, G., N.N. Basu, S. Zanardo, P.S. C. Rao, a. Rinaldo (2010) Stochastic modeling of nutrient losses in streams: interactions of climatic, hydrologic, and biogeochemical controls. Water Resour. Res. 46, W08509.

Canfield, D. E., A. N. Glazer, P. G. Falkowski (2010), The Evolution and Future of Earth's Nitrogen Cycle. Science, 330, 192-196.

Cardenas, M. B., and J. L. Wilson (2007a), Exchange across a sediment-water interface with ambient groundwater discharge, J. Hydrol., 346(3–4), 69–80, doi:10.1016/j.jhydrol.2007.08.019, 69-80.

Cardenas, M. B., and J. L Wilson (2007b), Hydrodynamics of coupled flow above and below a sediment-water interface with triangular bed forms: Underflow case, Adv. Water. Res., 30(3), 301–313, doi:10.1016/j.advwaters.2006.06.009.

Carey, R. O. and K. W. Migliaccio (2009), Contribution of Wastewater Treatment Plant Effluents to Nutrient Dynamics in aquatic Systems: A Review. Environ. Manage., 44, 205-217.

Cheong, T. S., B. A. Younis, I. W. Seo (2007), Estimation of key parameters in model for solute transport in rivers and streams. Water Recour Manage, 21, 1165-1186.

David, M., L. Wall, T. Royer, and J. Tank (2006), Denitrification and the Nitrogen Budget of a Reservoir in an Agricultural Landscape. Ecol. Appl., 16, 2177–2190.

Elliott, A. H., N. H. Brooks (1997a), Transfer of nonsorbing solutes to a streambed with bed forms: Theory. Water Resour. Res., 33, 123– 136.

Elliott, A. H., N. H. Brooks (1997b), Transfer of nonsorbing solutes to a streambed with bed forms: Laboratory experiments. Water Resour. Res., 33, 137–151.

Galloway, J.N. et al. (2004), Nitrogen Cycles: Past, Present, and Future. Biogeochemistry, 70, 153–226.

Grant, S. B., K. Stolzenbach, M. Azizian, M. J. Stewardson, F. Boano, L. Bardini (2014), First-Order Contaminant Removal in the Hyporheic Zone of Streams: Physical Insights from a Simple Analytical Model. Environ. Sci. Technol., 48, 11369-11378.

Hancock, P. J. Human impacts on the stream-groundwater exchange zone. Environ. Manage. 2002, 29, 763–781.

Hill, C.G. (1977), An Introduction to Chemical Engineering Kinetics and Reactor Design, Chapter 11, John Wiley and Sons: New York, U.S..

Huettel, M.; Berg, P.; Kostka, J. E. (2014), Benthic Exchange and Biogeochemical Cycling in Permeable Sediments. Ann. Rev. Mar. Sci., 6, 23–51.

Jongbloed, A. W., N. P. Lenis (1998), Environmental concerns about animal manure. J. Anim. Sci. 76 (10), 2641-8.

Kessler, A.J., R.N. Glud, M.B. Cardenas, P.L.M. Cook (2013a), Transport Zonation Limits Coupled Nitrification-Denitrification in Permeable Sediments. Environ. Sci. Technol., 47, 13404-13411.

Kessler, A.J., R.N. Glud, , M.B. Cardenas, M. Larsen, M.F. Bourke, P.L.M. Cook (2013b), Quantifying Denitrification in Rippled Permeable Sands through Combined Flume Experiments and Modeling. Limnol. Oceanogr., 57, 1217-1232.

Levenspiel, O. (1972), Chemical Reaction Engineering, Wiley: New York, U.S..

Marti, E., J. Aumatell, L. Code, M. Poch, and F. Sabater (2004), Nutrient Retention Efficiency in Streams Receiving Inputs from Wastewater Treatment Plants. J. Environ. Qual., 33, 285-293.

Mulholland, P.J. et al. (2008), Stream denitrification across biomes and its response to anthropogenic nitrate loading. Nature, 452, 202-205.

National Academy of Engineering (2017), NAE Grand Challenges for Engineering. [online] Available at: http://www.engineeringchallenges.org/challenges.aspx [Accessed 30 May, 2017].

National Environmental Research Institute (2004), A model set-up for an oxygen and nutrient flux model for Aarhus Bay (Denmark), NERI Tech. Rep. 483, Denmark.

Runkel, R.L. (2007) Toward the transport-based analysis of nutrient spiraling and uptake in streams. Limnol. Oceanogr.: Methods, 5, 50-62.

Schot, P. P. and J. van der Wal (1992), Human impact on regional groundwater composition through intervention in natural flow patterns and changes in land use, Elsevier, 134, 297-313, doi: 10.1016/0022-1694(92)90040-3.

Seitzinger, S., J. A. Harrison, J. K. Bohlke, A.F. Bouwman, and R. Lowrance, B. Peterson, C. Tobias, and G. Van Drecht (2006), Denitrification across Landscapes and Waterscapes: A Synthesis. Ecol. Appl., 16, 2064-2090.

Smith, V. H., G. D. Tilman, J. C. Nekola (1999), Eutrophication: Impacts of Excess Nutrient Inputs on Freshwater, Marine, and Terrestrial Ecosystems. Environ. Poll., 100, 179-196.

Steffen, W. et al. (2015), Planetary boundaries: guiding human development on a changing planet. Science, 347, 1259855. doi: 10.1126/science.1259855.

Stream Solute Workshop (1990), Concepts and Methods for Assessing Solute Dynamics in Stream Ecosystem. J. N. Am. Benthol. Soc., 9, 95-119.

Trauth, N., C. Schmidth, U. Maier, M. Wieweg, and J. H. Fleckenstein (2013), Coupled 3-D stream flow and hyporheic flow model under varying stream and ambient groundwater flow conditions in a pool-riffle system. Water Resour. Res. 49, 5834-5850, doi: 10.1002/wrcr.20442.

United States Environmental Protection Agency (2017), U. S. Environmental Protection Agency. [online] Available at: http://www.citethisforme.com/guides/harvard/how-to-cite-a-website [Accessed 30 May, 2017].

Wollheim, W.M., C.J.Vorosmarty, B.J. Peterson, S.P. Setizinger, and C.S. Hopkinson (2006), Relationship Between River Sixe and Nutrient Removal. Geophys. Res. Let., 33, L06410, doi:10.1029/2006GL025845

Yates, M. V. (1985), Septic Tank Density and Ground-Water Contamination. Ground Water, 23, 586-591.

First-Order Contaminant Removal in the Hyporheic Zone of Streams: Physical Insights from a Simple Analytical Model[1]

Abstract

A simple analytical model is presented for the removal of stream-borne contaminants by hyporheic exchange across duned or rippled streambeds. The model assumes a steady-state balance between contaminant supply from the stream and first-order reaction in the sediment. Hyporheic exchange occurs by bed form pumping, in which water and contaminants flow into bed forms in high-pressure regions (downwelling zones) and out of bed forms in low-pressure regions (upwelling zones). Model-predicted contaminant concentrations are higher in downwelling zones than upwelling zones, reflecting the strong coupling that exists between transport and reaction in these systems. When flow-averaged, the concentration difference across upwelling and downwelling zones drives a net contaminant flux into the sediment bed proportional to the average downwelling velocity. The downwelling velocity is functionally equivalent to a mass transfer coefficient, and can be estimated from stream state variables including stream velocity, bed form geometry, and the hydraulic conductivity and porosity of the sediment. Increasing the mass transfer coefficient increases the fraction of stream water cycling through the hyporheic zone (per unit length of stream) but also decreases the time contaminants undergo first-order reaction in the sediment. As a consequence, small

---

[1] A version of this chapter was published as [Grant, S. B., K. Stolzenbach, M. Azizian, M. J. Stewardson, F. Boano, L. Bardini (2014), First-Order Contaminant Removal in the Hyporheic Zone of Streams: Physical Insights from a Simple Analytical Model. Environ. Sci. Technol., 48, 11369-11378].

changes in stream state variables can significantly alter the performance of hyporheic zone treatment systems.

2.1. Introduction

The hyporheic zone is the region beneath and adjacent to a stream where surface water and groundwater mix. Its physical and chemical environment supports a community of organisms that collectively remove contaminants and cycle carbon, energy, and nutrients [The Hyporheic Handbook, 2009; Krause et al., 2011]. The hyporheic zone also regulates stream temperature and sediment budgets, serves as a spawning ground/refuge for fish species, and provides a rooting zone for aquatic plants. These ecosystem services require vigorous exchange of water, nutrients and energy across the sediment-water interface, a process referred to as hyporheic exchange. Stream restoration can include features--such as pools, riffles, steps, debris dams, bars, meander bends, and side channels—that enhance hyporheic exchange [Hester and Gooseff, 2010]. Hyporheic exchange can also be incorporated into the design of engineered streams to facilitate the removal of carbon, phosphorous, nitrogen and other contaminants from polluted waters. In arid urban settings, for example, dry streambeds can be converted to hyporheic zone treatment systems for polishing effluent from wastewater treatment plants [Lawrence et al., 2013]. Potential benefits include improved receiving water quality, groundwater protection, new stream habitat, low energy consumption, and a small carbon footprint. On the other hand, a poorly managed hyporheic zone can degrade surface water quality, for example by polluting the overlying water column with fecal bacteria growing in the sediment bed [Grant et al., 2011] or releasing heavy metals and nutrients [Hancock, 2002]. Whether the goal is restoring natural streams, engineering low-energy treatment systems, or managing existing water quality impairments, quantitative tools are needed to predict the effects of hyporheic exchange on the transport and transformation of contaminants in streams.

Here we focus on a particular type of hyporheic exchange that occurs when a turbulent stream flows over bed forms (such as ripples and dunes) on a permeable sediment bed. The central role of turbulence in this problem poses special (multi-physics) challenges that set it apart from other low-energy treatment systems where the bulk flow is often laminar or transitionally turbulent, such as surface [Wu et al., 2014] and subsurface [Monhanty et al., 2013] wetlands. The present state-of-the-art involves three steps [e.g., Bardini et al., 2012; Huettel et al., 2014; and Janssen et al., 2012]: (1) calculating the pressure distribution at the sediment-water interface by numerically solving the Navier-Stokes equations for turbulent stream flow over the bed forms of interest; (2) calculating water flow through the hyporheic zone from Darcy's Law and the continuity equation using pressure distributions along the sediment-water interface (from step (1)) and stream-aquifer boundary together with an assumed sediment permeability field; and (3) calculating solute concentrations in the interstitial fluids of the sediment from a mass conservation equation that accounts for physical transport processes (advection, mechanical dispersion, molecular diffusion) and the chemical and biogeochemical transformations of interest. To complement this relatively computationally- and data-intensive numerical approach, in this chapter we derive and solve a simple analytical model of hyporheic exchange and in-sediment reaction. Our simple model builds on an idealized flow field for hyporheic exchange first proposed by Elliott and Brooks (hereafter referred to as EB) [Elliott and Brooks, [1997a,b] and generalizes a solution for hyporheic exchange and reaction presented by Rutherford et al. that focused on benthic oxygen uptake of sediments in a polluted stream [Rutherford et al., 1995].

2.2. The Elliott and Brooks Model for Pumping Across Bed Forms

The EB flow model is premised on the idea that turbulent flow over periodic bed forms causes the dynamic pressure at the sediment-water interface to oscillate with distance downstream. Pressure variation is caused by acceleration of flow and detachment of the velocity boundary layer over the crest of the bed form [Cardenas and Wilson, 2007; Thibodeaux and Boyle, 1987]. The resulting stream-parallel pressure oscillation drives flow across the sediment-water interface, into the sediment in high-pressure regions (downwelling) and out of the sediment in low-pressure regions (upwelling). In the EB flow model, this periodic pressure variation at the sediment-water interface is idealized as a sinusoidal function, where the variable h_{SWI} (units of length, L) refers to pressure head (i.e., pressure normalized by the specific weight of water) (**Figure 2.1A**):

$$h_{SWI} = h_m \sin(\bar{x}) \tag{1}$$

Variables in equation (1) include the reduced horizontal coordinate $\bar{x} = 2\pi x/\lambda$ [-], the horizontal coordinate parallel to the sediment-water interface x [L], and the wavelength λ [L] and amplitude h_m [L] of the pressure head variation. The wavelength λ of the pressure wave corresponds to the wavelength of the bed form, and the trough and peak of the pressure wave correspond to where the velocity boundary layer detaches (at the bed form crest) and reattaches (on the lee side of the bed form), respectively.

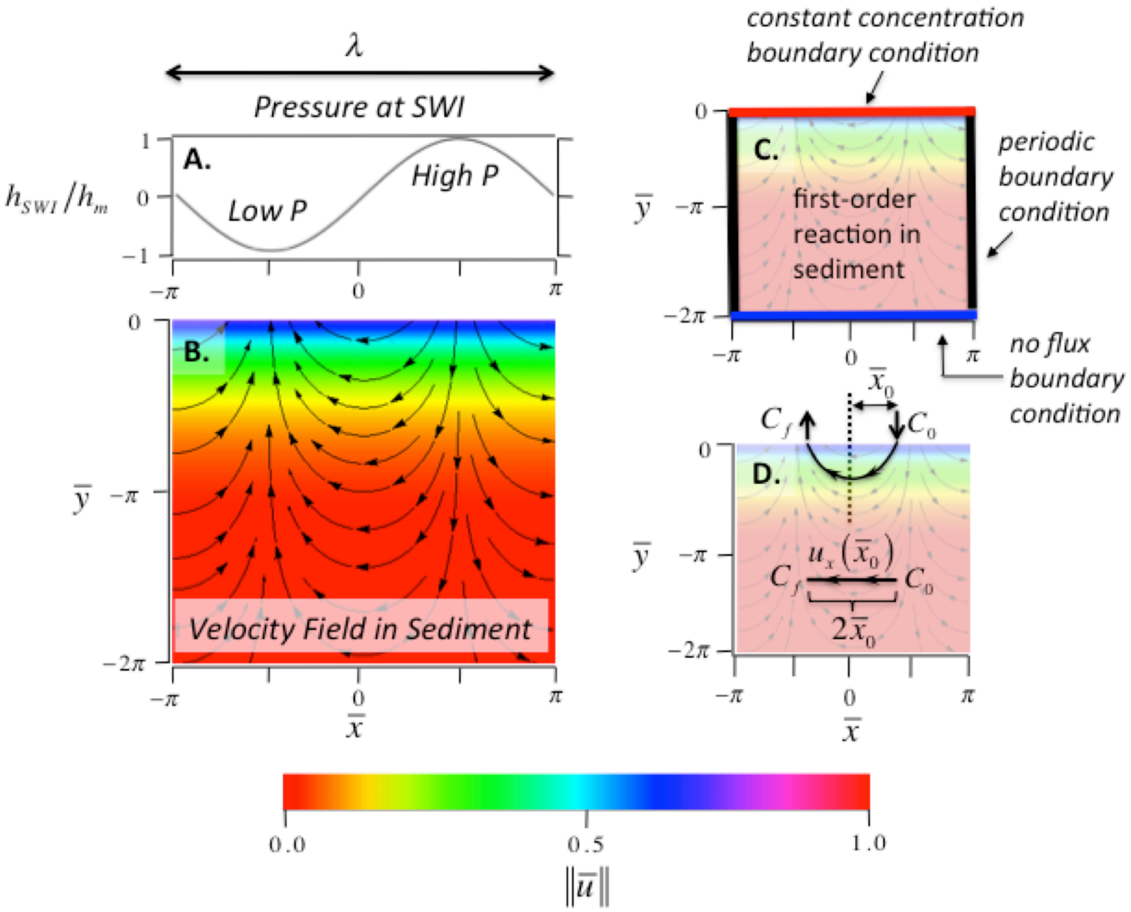

Figure 2.1. The Elliott and Brooks (EB) model for flow through the hyporheic zone of a stream with bed forms, including the assumed pressure head distribution at the sediment-water interface (SWI, panel A) and the derived velocity field in the hyporheic zone (panel B). Flow from the stream into the sediment (downwelling) occurs in high-pressure regions; flow from the sediment into the stream (upwelling) occurs in low-pressure regions. The color denotes the modulus of the Darcy flux vector (see equation (2d)). Horizontal and vertical distances are reduced by the wavelength λ of a bed form: $\bar{x} = 2\pi x/\lambda$ and $\bar{y} = 2\pi y/\lambda$. Contaminant transport and first-order reaction in the hyporheic zone can be modeled numerically (assuming that mass transfer in the sediment occurs by advection, mechanical dispersion, and molecular diffusion) (panel C) or with an analytical solution (assuming that mass transfer in the sediment occurs only by advection) (panel D).

Assuming a sinusoidal pressure distribution h_{SWI} at the sediment-water interface and constant hydraulic conductivity K_h [units of length per time, L T^{-1}] throughout the sediment bed, application of Darcy's Law and the continuity equation yields the following solution for the pressure head and velocity field in the interstitial pores of the hyporheic zone [Elliott and Brooks, 1997a]:

$$\bar{h}(\bar{x},\bar{y}) = h/h_m = \sin\bar{x}e^{\bar{y}} \tag{2a}$$

$$\bar{u}_x = u_x/u_m = -\cos\bar{x}e^{\bar{y}} \tag{2b}$$

$$\bar{u}_y = u_y/u_m = -\sin\bar{x}e^{\bar{y}} \tag{2c}$$

$$\|\bar{u}\| = \sqrt{\bar{u}_x^2 + \bar{u}_y^2} = e^{\bar{y}} \tag{2d}$$

$$\bar{x} = 2\pi x/\lambda \tag{2e}$$

$$\bar{y} = 2\pi y/\lambda \tag{2f}$$

$$u_m = 2\pi K_h h_m/\lambda \tag{2g}$$

The vertical distance above the sediment-water interface is denoted by the coordinate y [L]. The variables u_x [L T^{-1}], u_y [L T^{-1}], and $\|\bar{u}\|$ [L T^{-1}] represent, respectively, the x-component, y-component, and a reduced form of the modulus of the Darcy flux (flow volume per unit area) through the sediment. Application of the EB flow model requires an estimate for either the maximum Darcy velocity u_m [L T^{-1}] or pressure head amplitude h_m. These parameters can be estimated from stream state variables using one of several empirical relationships, detailed later.

There are two striking features of the velocity field predicted by the EB flow model (**Figure 2.1B**). First, circulation of water across the sediment-water interface occurs in a series of identical (or mirror-image) unit cells; a single unit cell extends from $\bar{x} = -\pi/2$ to $\bar{x} = \pi/2$ in **Figure 2.1B**. Second, the modulus of the Darcy velocity vector decays exponentially with depth (equation 2d; see color in **Figure 2.1B**; note that the vertical coordinate y is negative into the streambed). These two features of the EB flow field—its unit cell structure and exponential decline with depth—are qualitatively similar to numerical predictions of in-sediment circulation patterns generated by turbulent flow over asymmetrical dunes (e.g., see Figure 1 in [Cardenas and Wilson, 2007]) and experimental observations of streaklines through sediment during hyporheic exchange [Elliott and Brooks, 1997a; Thibodeaux and Boyle, 1987]. The depth to which the velocity field extends into the sediment bed ($1/e$-folding depth approximately equal to λ) also agrees well with experimental measurements and numerical simulations of hyporheic exchange under dunes, $d_{HZ} \approx a\lambda$, where d_{HZ} [L] is the depth of the hyporheic zone and the constant a varies between 0.4 and 0.7 depending on dune geometry [Janssen et al. 2012; Cardenas and Wilson, 2007].

A potential limitation of the EB model is its assumption that the sediment-water interface is flat. To explore this potential limitation, we compared the modulus of the Darcy flux predicted by the EB model (equation (2d)) with the Darcy flux simulated using the approach outlined earlier; namely, solving the Navier-Stokes equation for turbulent flow over a bed form, and then solving flow through the hyporheic zone by application of Darcy's equation and the continuity equation (see **Text A.1** in **Appendix A**). Below the base of the bed form the modulus of the Darcy flux predicted by the numerical solution exhibits the same functional behavior as EB's flatbed solution (i.e., both solutions decay exponentially with depth). As might be expected, the functional form of the two solutions differs for elevations between the base and crest of the bed form (**Appendix A**, **Figure A.2**). The surface-averaged Darcy flux across the sediment-water interface is also similar (within about 11%, see **Appendix A**). In summary, given its simplicity and relative consistency with both experimental observations and numerical simulations, the EB velocity field is an excellent starting point for the modeling described next.

2.3. Numerical Simulation of Contaminant Removal in the Hyporheic Zone

To illustrate how the EB velocity field affects mass transport and reaction in the hyporheic zone, we carried out a series of numerical simulations. For these simulations the following boundary conditions were adopted [Bardini et al., 2012]: (1) constant concentration at the top boundary ($C = C_0$ at $\bar{y} = 0$, red line in **Figure 2.1C**), (2) a no-flux condition at the bottom boundary ($\partial C/\partial \bar{y} = 0$ at $\bar{y} = -2\pi$, blue line in **Figure 2.1C**); and (3) periodic boundaries at the edges (matching concentrations and fluxes at $\bar{x} = \pm\pi$, black lines in **Figure 2.1C**). At every point in the numerical domain we assumed a steady-state balance between first-order reaction in the sediment and contaminant supply from the stream [Bardini et al., 2012]:

$$\nabla \cdot \left(\frac{\mathbf{u}}{\theta} C - D \cdot \nabla C \right) = -k_r C \qquad (3)$$

Equation (3) accounts for transport and mixing through the hyporheic zone by advection, mechanical dispersion, and molecular diffusion (two terms on left-hand side) and removal within the sediment by first-order reaction (term on right hand side). The variables C (mass per volume [M L^{-3}]), θ [-], $\mathbf{u}$ [L T^{-1}], $\mathbf{D}$ [L^2 T^{-1}], and k_r [T^{-1}]

represent contaminant concentration in the sediment's interstitial pores, sediment porosity, Darcy flux vector, dispersion/diffusion tensor, and first-order rate constant for contaminant removal, respectively. According to the EB velocity field (equations (2b) and (2c)) the Darcy velocity vector and the dispersion/diffusion tensor (see Bardini et al. [2012]) can be written as follows:

$$\mathbf{u} = -u_m \cos\bar{x} e^{\bar{y}} \hat{i} - u_m \sin\bar{x} e^{\bar{y}} \hat{j} \tag{4a}$$

$$\mathbf{D} = \begin{bmatrix} \frac{u_m e^{\bar{y}}}{\theta}\left(\alpha_L \cos^2\bar{x} + \alpha_T \sin^2\bar{x}\right) + D_m' & \frac{u_m e^{\bar{y}}}{\theta}\left(\alpha_L - \alpha_T\right)\frac{\sin 2\bar{x}}{2} \\ \frac{u_m e^{\bar{y}}}{\theta}\left(\alpha_L - \alpha_T\right)\frac{\sin 2\bar{x}}{2} & \frac{u_m e^{\bar{y}}}{\theta}\left(\alpha_L \sin^2\bar{x} + \alpha_T \cos^2\bar{x}\right) + D_m' \end{bmatrix} \tag{4b}$$

Variables appearing here include the dispersivities parallel α_L [L] and transverse α_T [L] to the streamlines, and the molecular diffusion coefficient of solute in water D_m [L^2 T^{-1}] modified by a tortuosity parameter β [-] that takes into account the twists and turns associated with diffusion through connected pore spaces in the sediment: $D_m' = \beta D_m$ where $\beta = \left(1 + 3(1+\theta)\right)^{-1}$ [Iversen and Jorgensen, 1993]. As is common for these types of analyses (e.g., Bardini et al. [2012] and Janssen et al. [2012]), our model does not consider variations in the permeability field, and exchange between so-called mobile and immobile zones in the sediment. However, a recent numerical study found that, under the steady-state conditions employed here, small-scale heterogeneities in the permeability field have relatively little effect on the overall reaction rates observed within the streambed [Bardini et al., 2013].

Equations (4a) and (4b) were substituted into equation (3) and the resulting partial differential equation was solved using a generic multi-physics finite element solver with adaptive meshing and error control (COMSOL, version 4.4). The parameter values utilized for this numerical simulation (**Appendix A**, **Table A.1**) were taken from a previously published modeling study of hyporheic exchange [Bardini et al., 2012]; they are representative of a medium-sized stream flowing over periodic dunes on a permeable bed of well-sorted sand. The first-order rate constant corresponds to a contaminant half-life of 1.6 days, which is typical for the respiration of dissolved organic carbon in a stream [Bardini et al., 2012] or the mineralization of a low persistence anthropogenic contaminant, such as the pharmaceutical compound paracetamol, in a sediment/water matrix under environmentally relevant conditions [Loffler et al., 2005].

Contaminant concentrations predicted by the numerical simulation vary dramatically across the upwelling and downwelling zones of the bed form (**Figure 2.2A**). In the downwelling (high pressure) zone, contaminant-rich water penetrates approximately half a dune wavelength into the sediment ($\bar{y} \approx -\pi$). In the upwelling (low pressure) zone contaminant-depleted waters extend nearly all the way to the surface ($\bar{y} \approx 0$). For the steady-state form of the mass balance equation adopted here (equation (3)), the mass of contaminant crossing the sediment-water interface exactly balances the mass removed in the hyporheic zone by first-order reaction. Under such conditions, the average flux across the sediment-water interface can be calculated as follows: $J = \theta C_{\mathrm{ave}} k_r d_{\mathrm{CD}}$ [M L^{-2} T^{-1}] where C_{ave} is the average contaminant concentration in the computational domain, k_r is the first-order reaction rate, θ is streambed porosity, and d_{CD} is the depth of the computational domain. Here and throughout the remainder of the chapter, J is defined as the mass transported per unit streambed area (including both sediment matrix and pore

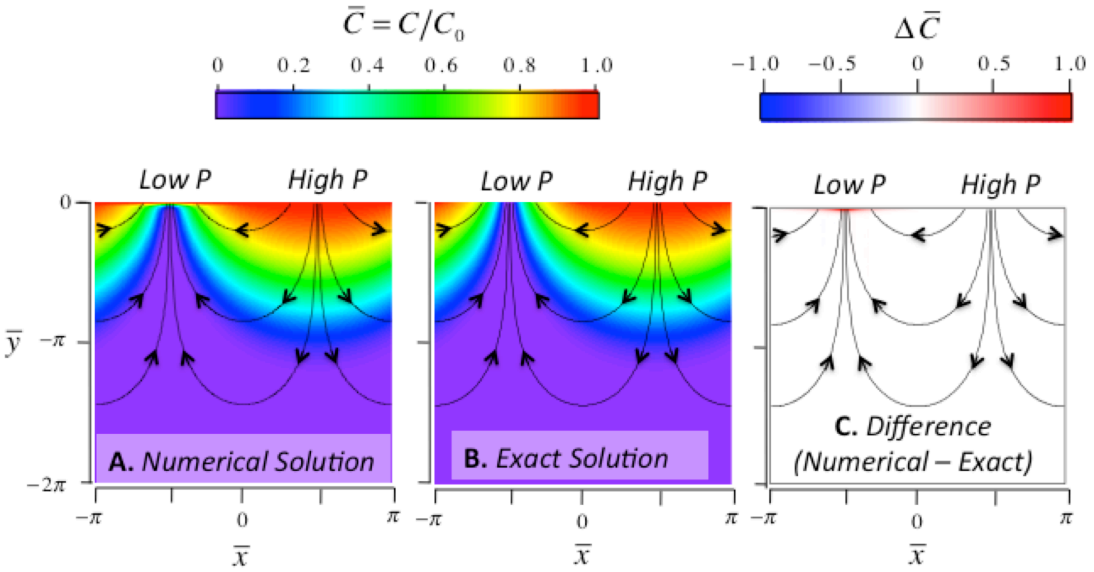

Figure 2.2. Concentration fields predicted by the numerical (panel A) and analytical (panel B) solutions of hyporheic exchange and first-order reaction, assuming flow through the hyporheic zone follows the EB velocity model (see **Figure 2.1**). The colors in panel A and B denote the concentration of contaminant in the pore fluid C normalized by the concentration of contaminant in the stream (C_0): $\bar{C} = C/C_0$. The difference between numerical and exact solutions ($\Delta\bar{C} = \bar{C}_{numerical} - \bar{C}_{exact}$) is shown in Panel C.

spaces) per time; the negative sign denotes mass transport into the sediment bed (i.e. in the direction opposite of the y–axis which is oriented upwards, see **Figure 2.1B**). In our numerical simulation the first-order reaction rate is $k_r = 5 \times 10^{-6} s^{-1}$, the depth of the computational domain is $d_{CD} = \lambda = 1m$, $\theta = 0.4$, and $C_{ave} = 0.206C_0$ where C_0 is the fixed concentration of contaminant in the stream. Therefore, the flux of contaminant across the sediment-water interface for this particular numerical simulation is: $J = -(4 \times 10^{-7} \text{ms}^{-1})C_0$.

2.4. Relative Importance of Advection, Mechanical Dispersion, And Molecular Diffusion

The numerical simulation used to generate **Figure 2.2A** includes all three transport mechanisms potentially operative in the hyporheic zone; namely, advection, mechanical dispersion, and molecular diffusion. An order-of-magnitude analysis suggests that, for the set of parameters listed in **Appendix A**, **Table A.1**, mass transport in the hyporheic zone is dominated by advection (see **Text A.2** and **A.3** in **Appendix A**). To test this idea, we carried out a series of numerical simulations in which different combinations of transport mechanisms were turned on or off. Three scenarios were tested: (1) all three transport mechanisms turned-on (i.e., the simulation used to generate **Figure 2.2A**); (2) advection and mechanical dispersion turned-on and molecular diffusion turned-off; and (3) advection and molecular diffusion turned-on and mechanical dispersion turned-off. The obvious fourth scenario (both mechanical dispersion and molecular diffusion turned-off) could not be run because of an artifact associated with the surface boundary condition; this artifact will be discussed in the next section. For the three scenarios, the concentration fields are indistinguishable (**Figure A.3** in **Appendix A**) and the flux (J) across the sediment-water interface is the same to within three significant digits. Because the concentration field is unchanged when mechanical dispersion is substituted for molecular diffusion (and vice versa), we conclude that the order-of-magnitude analysis is correct: mass transport within the hyporheic zone is dominated by advection in this case. More generally, when a contaminant is removed by first-order reaction in the sediment bed, advection will dominate over mechanical dispersion when $\alpha_L k_r \theta / u_m << 1$; advection will dominate over molecular diffusion when $\theta^2 \beta D_m k_r / u_m^2 << 1$ (see **Appendix A** for derivations).

2.5. Artifacts Associated with the Surface Boundary Condition

In numerical simulations of hyporheic exchange and reaction it is common to apply a constant concentration (i.e., a Dirichlet or first-type) boundary condition $C = C_0$ at the sediment-water interface [e.g., Bardini et al. [2012], [2013], and Hester et al. [2013], as was the case for the numerical simulation described in the last section. As is evident from **Figure 2.1B**, flow fields in the downwelling and upwelling zones are symmetrical. For a constant concentration boundary condition at the surface, the advective mass flow into the sediment must equal the advective mass flow out of the sediment. If advection dominates over dispersion and diffusion, then mass loss by reaction will cause concentration to decrease along a streamline, from the initial value of C_0 in the downwelling zone to the upwelling zone where the concentration rapidly rebounds to C_0 at the sediment-water interface. Total mass conservation is achieved by dispersive and/or diffusive mass transport into the sediment due to the steep concentration gradient at the sediment-water interface (see **Text A.4** in **Appendix A**). This explains why the fourth scenario described in the last section (both mechanical dispersion and molecular diffusion turned-off) could not be simulated—in numerical simulations of hyporheic exchange in which a constant concentration boundary condition is applied at the sediment-water interface, overall mass balance cannot be satisfied without including some form of Fickian diffusion/dispersion.

2.6. Analytical Model of Hyporheic Exchange: Mass-Transfer-Limit Solution

In this section we derive an exact solution for mass flux across the sediment-water interface under mass-transfer limited conditions. We focus on a single streamline; namely, the one that intersects the sediment-water interface at $x = x_0$ (top highlighted streamline, **Figure 2.1D**). Along this particular streamline and assuming mass transport occurs by advection alone (i.e., mechanical dispersion and molecular diffusion are neglected, see last section), mass flows into the hyporheic zone at a rate of $dm_{\text{in}}(x_0) = \left|C_0 W u_y (x = x_0, y = 0) dx_0\right|$ and out of the hyporheic zone at a rate of $dm_{\text{out}}(x_0) = \left|C_f(x_0) W u_y (x = -x_0, y = 0) dx_0\right|$ where $C_f(x_0)$ represents the final contaminant concentration at the point where a water parcel exits the hyporheic zone (and enters the stream) and W represents the width of the stream. The average contaminant flux across the sediment-water interface can be found by substituting the EB flow model for u_y (equation (2c)), adding up the net mass transferred ($m_{\text{out}}(x_0) - m_{\text{in}}(x_0)$) over all streamlines in the unit cell, and dividing by the interfacial area over which the mass is transferred:

$$J = \frac{u_{\text{m}}}{\pi} \int_0^{\pi/2} \left(-C_0 + C_f(\bar{x}_0)\right) \sin \bar{x}_0 d\bar{x}_0 \qquad (5)$$

Where $\bar{x}_0 = 2\pi \bar{x}_0 / \lambda$

To solve this integral the final concentration $C_f(\bar{x}_0)$ must be specified. When all mass entering the hyporheic zone is lost by reaction (referred to here as the mass transfer-limit) the final concentration will be zero ($C_f(\bar{x}_0) = 0$) and equation (5) simplifies:

$$J_{\mathrm{MTL}} = -\frac{C_0 u_{\mathrm{m}}}{\pi} \tag{6}$$

The mass-transfer limited flux J_{MTL} represents the maximum mass flux that can be achieved by the EB model of hyporheic exchange; the negative sign in equation (6) indicates that the net mass flux is directed into the sediments.

2.7. Analytical Model of Hyporheic Exchange: Full Solution

In general, not all solute will react as a water parcel moves through the hyporheic zone. In such cases the final concentration will be greater than zero ($C_f\left(\overline{x}_0\right) > 0$) and the magnitude of mass flux across the sediment-water interface will be less than the mass-transfer limited case (i.e., $J/J_{MTL} < 1$). To solve this more general problem requires specification of the function $C_f\left(\overline{x}_0\right)$. If the solute in question is removed by first-order reaction then the final concentration will depend only on the time $\tau_f\left(\overline{x}_0\right)$ [T] it takes a water parcel to traverse the streamline that began at $\overline{x} = \overline{x}_0$:

$$C_f\left(\overline{x}_0\right) = C_0 e^{-k_r \tau_f\left(\overline{x}_0\right)} \tag{7}$$

Where $k_r\left[T^{-1}\right]$ is a first-order reaction rate constant.

To obtain an expression for the transit time function $\tau_f\left(\overline{x}_0\right)$ we exploit a surprising feature of the EB flow model: the x-component of the velocity is everywhere constant along the $\overline{x}_0$ streamline (equation (8), see proof in **Text A.5** of **Appendix A**).

$$u_x\left(\overline{x}_0\right) = -u_m \cos \overline{x}_0 \tag{8}$$

The constancy of the x-velocity along a streamline can be understood by noting that near the sediment-water interface the modulus of the velocity vector is large but its x-component is small, whereas deeper into the sediment column the modulus of the velocity vector is small but its x-component is large (see **Figure 2.1B**). The constancy of $u_x(\bar{x}_0)$ implies that each streamline in the hyporheic zone can be analyzed as if it were a horizontal streamline beginning and ending at $\bar{x}_0$ and $-\bar{x}_0$, respectively, and through which mass is transported at a constant velocity $u_x(\bar{x}_0)/\theta$ (bottom highlighted streamline, **Figure 2.1D**). The residence time of a water parcel on the $\bar{x}_0$ streamline is therefore the ratio of the x-distance a fluid particle travels ($2x_0$) and its constant velocity in the x-direction:

$$\tau_f(\bar{x}_0) = \frac{2x_0}{-u_x(x_0)/\theta} = \frac{\lambda \bar{x}_0 \theta}{\pi u_m \cos \bar{x}_0} \tag{9}$$

Combining equations (5), (7), and (9) we obtain a final expression for mass flux across the sediment-water interface:

$$J(\mathrm{Da}) = J_{MTL}\left[1 - \frac{C_{exit}(\mathrm{Da})}{C_0}\right] \tag{10a}$$

$$C_{exit}(\mathrm{Da}) = C_0 \int_0^{\pi/2} \exp\left[-\frac{\mathrm{Da}\,\bar{x}_0}{\pi^2 \cos \bar{x}_0}\right] \sin \bar{x}_0 \, d\bar{x}_0 \tag{10b}$$

$$\mathrm{Da} = \frac{k_r \lambda \theta \pi}{u_m} \tag{10c}$$

The function C_{exit} is the flow-averaged concentration of contaminant exiting the hyporheic zone (and entering the stream) in an upwelling zone (proof in **Text A.6** of **Appendix A**). The dimensionless Damköhler number Da is the ratio of reaction rate to mass transport rate. According to our model, contaminant removal by hyporheic exchange and first-order reaction is fully determined by the value of Da (**Figure 2.3**). When the reaction rate is much slower than the mass transport rate ($\mathrm{Da} < 0.01$)

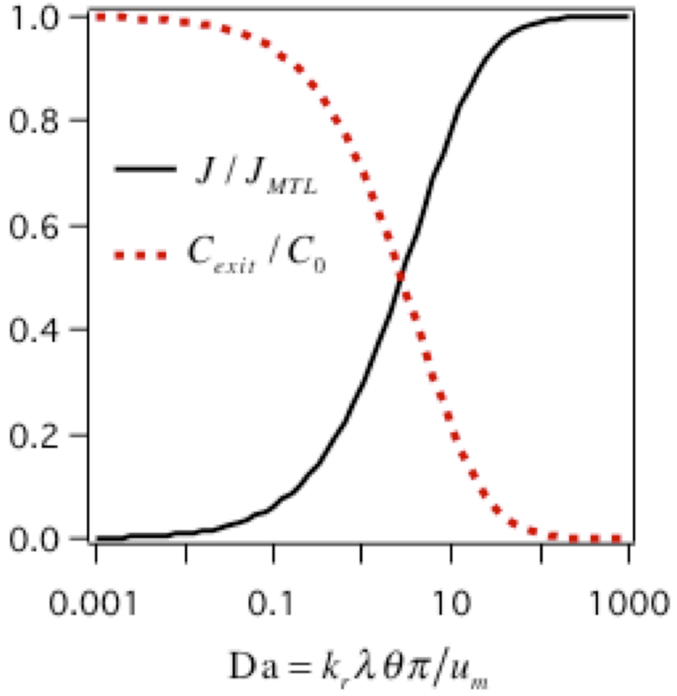

Figure 2.3. Model predictions of mass flux across the sediment-water interface (J) and flow-weighted concentration of contaminant exiting the hyporheic zone in an upwelling zone (C_{exit}) as a function of a nondimensional Damköhler number, Da (see equations (10a) – (10c)). The variables J_{MTL} and C_0 represent the mass-transfer-limited flux (equation (6)) and fixed concentration of contaminant in the stream, respectively.

contaminants pass too quickly through the sediment to undergo reaction ($C_{exit}/C_0=1$) and the net mass flux across the sediment-water interface is zero ($J=0$). When the reaction rate is much faster than the mass transport rate ($\mathrm{Da}>100$) contaminants undergo complete reaction ($C_{exit}/C_0=0$) and flux across the sediment-water interface is mass transfer limited ($J=J_{MTL}$). Between these two limits, mass flux across the sediment-water interface depends sensitively on the value of the Damköhler number.

2.8. Comparison of Mass Flux Estimated by Numerical and Analytical Solutions

For the parameter values listed in **Table A.1** of **Appendix A**, the average flux predicted from equation (10a), $J = -(4\times10^{-7}\,\mathrm{ms}^{-1})C_0$, matches the average flux calculated from the numerical simulations presented earlier. Thus, the numerical and analytical solutions are in concordance.

2.9. Analytical Model of Hyporheic Exchange: Concentration Field

An exact solution for the concentration field in the sediment can also be derived for steady-state first-order reaction and advective transport through the hyporheic zone (see **Text A.7** in **Appendix A**):

$$\bar{C}(\bar{x},\bar{y},\mathrm{Da}) = \frac{C(\bar{x},\bar{y},\mathrm{Da})}{C_0} = \exp\left[-\frac{\mathrm{Da}\left(\cos^{-1}\left[e^{\bar{y}}\cos\bar{x}\right]-\bar{x}\right)}{2\pi^2 e^{\bar{y}}\cos\bar{x}}\right], \quad -\pi/2<\bar{x}<\pi/2, \quad \bar{y}<0 \quad (11)$$

This solution applies only within the single unit cell of the EB velocity field ($-\pi/2<\bar{x}<\pi/2$). However, because all other unit cells are identical or mirror image, concentration in all other unit cells can be obtained from equation (11) by translation or reflection. Similar to the flux results presented earlier, contaminant concentration in the sediment pore fluids depends only on the value of the Damköhler number. For the set of parameters listed in **Appendix A**, **Table A.1**, the Damköhler number is $\mathrm{Da}=2.2$ and the concentration field calculated from equation (11) is nearly identical to the concentration field generated from the numerical simulation (**Figure 2.2B**). The exception is in the upwelling zone near the sediment-water interface where the numerical simulation predicts a steep concentration gradient (see difference plot in **Figure 2.2C**). As noted earlier, this concentration gradient is an artifact of the constant concentration boundary condition imposed at the top of the numerical domain.

2.10. A Mass Transfer Coefficient for Hyporheic Exchange

There is controversy in the literature regarding whether or not mass transfer coefficients can be used to model hyporheic exchange [Grant and Marusic, 2011; Thibodeaux et al., 2012]. Our solution sheds light on this issue. The solution for mass flux across the sediment-water interface (equation (10a)) can be rearranged as follows:

$$J = -k_m\left(C_0 - C_{exit}\right) \tag{12a}$$

$$k_{\mathrm{m}} = \frac{u_{\mathrm{m}}}{\pi} \tag{12b}$$

The form of equation (12a) is mathematically identical to a film model of interfacial mass transfer [Cussler, 2009]. The driving force for mass transfer across the sediment-water interface is the difference in the flow-averaged concentration in downwelling (C_0) and upwelling (C_{exit}) zones. The quantity $k_{\mathrm{m}} = u_{\mathrm{m}}/\pi$ [L T^{-1}] represents the average volume of water per unit area (i.e., the Darcy flux) flowing into the sediment over a bedform [Elliott and Brooks, 1997a]. The Damköhler number introduced earlier can be written explicitly in terms of the mass transfer coefficient:

$$\mathrm{Da} = k_{\mathrm{r}}\lambda\theta/k_{\mathrm{m}} \tag{13}$$

Several empirical approaches for estimating the mass transfer coefficient are described next.

2.11. Estimating the Mass Transfer Coefficient for Hyporheic Exchange

In this section we present several empirical approaches for estimating the mass transfer coefficient for hyporheic exchange. Because k_m is proportional to u_m (see equation (12b)), any empirical formula that relates u_m to stream state variables can also be used to estimate k_m. We evaluate two such expressions:

$$k_{\mathrm{m}}^{\mathrm{EB}} = 0.28\frac{K_{\mathrm{h}}U^2}{g\lambda}\left(\frac{\Delta/H}{0.34}\right)^{\gamma}, \gamma = \begin{cases} 3/8 \text{ for } \Delta/H < 0.34 \\ 3/2 \text{ for } \Delta/H \geq 0.34 \end{cases} \tag{14a}$$

$$k_{\mathrm{m}}^{\mathrm{CW}} = K_h\left(a_1 + a_2\,\mathrm{Re}_{\lambda}^{b_1}\right), \mathrm{Re}_{\lambda} = \frac{U\lambda}{\nu}, a_1 = 1.1\times10^{-5}, a_2 = 1.45\times10^{-15}, b_1 = 2.18 \tag{14b}$$

Equation (14a) follows from a formula reported by EB [Elliott and Brooks, 1997a] based on experiments conducted by Fehlman [1985], which involved pressure measurements over artificial dunes submerged in a turbulent flow. Equation (14b) follows from a formula proposed by Cardenas and Wilson [2007] (hereafter referred to as CW) based on numerical studies of turbulent flow over permeable dunes. Variables in these equations include the hydraulic conductivity K_h [L T^{-1}] of the sediment, stream velocity U [L T^{-1}] and depth H [L], bed form wavelength λ [L] and height Δ [L], gravitational acceleration g [L T^{-2}], and kinematic viscosity υ [L^2 T^{-1}].

To evaluate the empirical expressions above, mass transfer coefficients were calculated from 42 previously published hyporheic exchange experiments (reviewed in [Grant et al. 2012] and [O'Connor and Harvey, 2008]). Collectively, these experiments capture a variety of flow rates (0.09 to 0.5 m s^{-1}), bed form morphologies (ripples, dunes), sediment grain sizes (median values of 0.13 to 6 mm), and flume lengths (2.5 to 18.4 m) [Elliott and Brooks, 1997b, Ren and Packman, 2004; Marion et al., 2002; Packman et al., 2004; Packman et al., 2000; Packman and MacKay, 2003; Rehg and Packman, 2005]. These experiments all had the same basic design. A recirculating flume is configured to mimic turbulent flow of water over a permeable sediment bed with periodic bed forms. A conservative (nonreactive and nonadsorbing) tracer is then added to the water column of the flume, and its concentration monitored over time. From mass balance, the instantaneous flux of tracer across the sediment-water interface can be calculated from the decline of tracer concentration (C_w) in the water column: $J = \left(V_w/A_s\right)\left(dC_w/dt\right)$ where the variables represent elapsed time t [T], the total volume (V_w [L^3]) of water overlying the sediment bed (including water in the recirculating pipes but excluding interstitial fluids in the sediment), and the surface area (A_s [L^2]) of the sediment-water interface. Mass-transfer-limited conditions are approximated at the very beginning of an experiment when $C_{exit} \approx 0$ (see equation (10a)), and therefore a mass transfer coefficient can be calculated from initial measurements of the instantaneous flux J_0:

$$k_m^{\exp} = -\frac{J_0}{C_0} \tag{15}$$

Equation (15) is obtained by combining equations (6) and (12b) and setting $J_{MTL} = J_0$.

Experimental mass transfer coefficients calculated from equation (15) range over three orders of magnitude from 5.2 x10^{-7} to 5.8x10^{-4} m s^{-1}. The EB formula (equation (14a)) correctly predicts the magnitude and overall trend of these data, although some values are over- or under-predicted by up to a factor of 10 (**Figure 2.4A**, normalized root-mean-square deviance (NRMSD) of 16%, see **Text A.8** of **Appendix A** for details of the

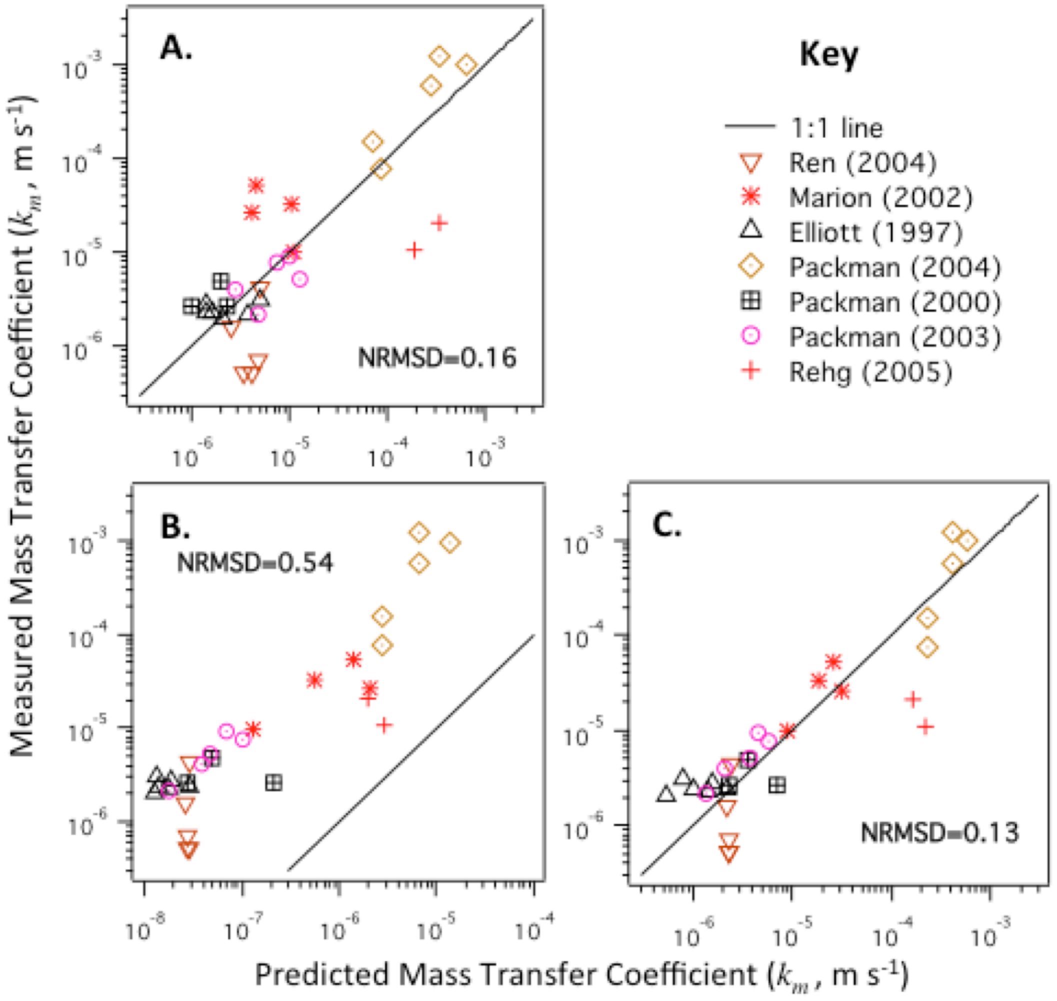

Figure 2.4. Measured versus model-predicted mass transfer coefficients for hyporheic exchange. Model-predicted mass transfer coefficients were calculated from: (A) equation (14a) proposed by Elliott and Brooks; (B) equation (14b) proposed by Cardenas and Wilson; and (C) a modified form of the model proposed by Cardenas and Wilson (equation (14b) with $a_1 = 0$, $a_2 = 2.51 \times 10^{-7}$, $b_1 = 0.85$).

NRMSD calculation). The CW formula (equation (14b)) correctly reproduces the trend of the measured data, but consistently under-predicts their magnitude by approximately 10 fold (**Figure 2.4B**, NRMSD = 54%). The CW model can be made to fit the data by setting the constant $a_1 = 0$, and then performing a linear regression on the log-transformed k_m^{CW} and $k_m^{\exp}$ values ($a_1 = 0,\ a_2 = 2.51\times10^{-7},\ b_1 = 0.85$) (**Figure 2.4C**, NRMSD = 13%). Of the three correlations evaluated here (EB, CW, and modified-CW), the EB best matches both the numerical simulations of hyporheic exchange through a triangular dune (see **Appendix A**) and the trend and magnitude of measured mass transfer coefficients (**Figure 2.4A**). Therefore, the EB correlation (equation (14a)) was adopted for estimating u_m from stream state variables in **Appendix A**, **Table A.1**, and in the application of our model to contaminant removal in streams described later.

2.12. Model Limitations

Our analytical model's simplicity is both its strength and weakness. Stripping the problem to its essential elements (a canonical velocity field and first-order reaction in the sediment) allows for explicit solutions for the flux and concentration fields, and provides a theoretical foundation for the application of mass transfer coefficients to the modeling and study of hyporheic exchange. However, in so doing we neglect many hydrological, biophysical, and chemical processes that can influence contaminant fate and transport in streams. First, the EB velocity field is an idealization of bed form pumping that simplifies many details of that process [Janssen et al. 2012; Cardenas and Wilson, 2007; Thibodeaux and Boyle, 1987]. Second, bed form pumping is only one of many transport mechanisms that can induce hyporheic exchange. Turbulent eddies in the water column of a stream, for example, can cause flow across the sediment-water interface in the presence or absence of bed forms [Manes et al., 2009]. Third, plants and animals colonizing the hyporheic zone can exert profound impacts on stream-sediment exchange, by forming mounds across which pumping occurs, inducing pore water flow within sediments, and structuring the permeability field with burrows and roots (reviewed in Meysman et al. [2007]). Fourth, at a larger scale geomorphic features of a stream such as riffle-pool sequences, debris dams, meander bends, and regional groundwater flow all influence hyporheic exchange [The Hyporheic Handbook, 2009; Krause et al., 2011; Hester et al., 2008; Gomez et al., 2012]. Finally, many contaminants of practical interest are removed in the sediment by reactions and processes that do not conform to first-order kinetics [Kessler et al., 2013]. Keeping these limitations in mind, below we utilize our simple model to evaluate the distances over which stream contaminants might be removed by hyporheic exchange through reactive sediments.

2.13. Evaluating the Distance over Which Contaminants Are Removed

The distance over which streamborne contaminants are removed can be estimated by combining our solution for flux across the sediment-water interface (equation (10a)) with a steady-state model of streamflow where x is distance along the stream and $C_{stream,0}$ is the contaminant concentration in the stream at $x=0$:

$$C_{stream} = C_{stream,0}e^{-x/\ell} \tag{16a}$$

$$\ell = \frac{\lambda}{f_Q f_R} \tag{16b}$$

$$f_Q = \frac{u_m \lambda}{UH\pi} = \frac{k_m \theta \lambda}{UH} \tag{16c}$$

$$f_R = \frac{J(\mathrm{Da})}{J_{MTL}} \tag{16d}$$

In this model we assume: (1) steady state conditions; (2) down stream mass transport occurs by advection alone (i.e., longitudinal dispersion is neglected); (3) decline of contaminant concentration in the stream occurs over distances much larger than the wavelength of a single dune (i.e., contaminant concentration in the stream is constant over any single dune); and (4) any other in-stream processes (e.g., transient storage zones, decay in the water column) contribute negligibly to contaminant fate and transport. The parameter ℓ represents the downstream distance over which contaminant concentration is significantly reduced (i.e., by the fraction $1/e$) due to hyporheic exchange and first-order reaction in the sediment bed. In the stream ecosystem literature, ℓ is referred to as a "processing length" [Fisher et al., 1998]. The fraction f_Q is the portion of stream discharge ($Q = UHW$) that flows through a single bed form ($u_m \lambda W/\pi$); the quantity f_Q/λ is therefore the fraction of stream discharge processed by the hyporheic zone per unit length of stream. The variable f_R represents the fraction of contaminant removed by first-order reaction as water flows through the hyporheic zone; its value can be calculated for any choice of the Damköhler number (compare equations (16d) and (10a)).

Minimizing the processing length ℓ by manipulating stream state variables could provide the basis for design of constructed runoff or wastewater treatment systems [Lawrence et al., 2013]. Similarly, river restoration plans could be designed to minimize ℓ when contaminant removal within the hyporheic zone is a key objective [Kaushal et al., 2008; Veraart et al., 2014; Hughes et al., 2014], although this may need to be balanced with other objectives of hyporheic restoration [Boulton, 2007; Hester and Gooseff, 2011]. From equation (16b) we deduce that decreasing ℓ requires maximizing both f_Q/λ and f_R. Interestingly, these two fractions exhibit opposite dependencies on the mass transfer coefficient k_m. Increasing the mass transfer coefficient increases the fraction of streamwater processed by the hyporheic zone per unit length of stream ($f_Q/\lambda \propto k_m$) but reduces the time available for contaminants to undergo reaction in the hyporheic zone ($\mathrm{Da} \propto 1/k_m$). The trade-off between reaction and transport implies that small changes in stream state variables can cause substantial changes in the processing length ℓ. This can be demonstrated by writing f_Q/λ and Da explicitly in terms of state variables:

$$\frac{f_Q}{\lambda} = \frac{\delta K_h}{gH}\left(\frac{U}{\lambda}\right) \tag{17a}$$

$$\mathrm{Da} = \frac{g k_r \theta}{\delta K_h}\left(\frac{\lambda}{U}\right)^2 \tag{17b}$$

where $\delta = 0.18$. Equations (17a) and (17b) are obtained by substituting the EB correlation for k_m (equation (14a)) into the definitions of f_Q/λ and Da, and assuming the dune height is 1/10 the water depth, as is typically the case in natural streams [Marion et al., 2002].

For the set of stream state values used to generate **Figure 2.2** (and listed in **Appendix A Table A.1**), the processing length calculated from equations (17a), (17b), and (16b) is very large ($\ell = 275 km$). Can this processing length be reduced by manipulation of stream characteristics? Because f_Q/λ depends inversely on H , decreasing water depth will decrease the processing length by a proportional amount. For example, a five-fold decrease in water depth (from $H = 0.5$ to 0.1 m) will cause a five-fold reduction in the processing length (from 275 to 55 km). For the set of values listed in **Appendix A**, **Table A.1**, $f_R = 0.45$. Thus, an increase in k_r and/or θ will yield, at most, a 2-fold reduction in the processing length (from 275 to 138 km). Reach-averaged values of hydraulic conductivity typically range from 10^{-5} to 10^{-3} m/s (e.g., ref Genereux et al. [2008]). The value for K_h in **Appendix A**, **Table A.1** ($9.81\text{x}10^{-4}$ ms^{-1}) is already near the upper end of that range, and therefore this state variable can only be decreased. Decreasing K_h by a factor of 10 increases the processing length by a factor of 5 from 275 to 1400 km. The variables U and λ have an opposite effect on f_Q/λ and Da. Decreasing the bed form wavelength (e.g., from $\lambda = 1\text{m}$ to 0.1 m) increases the value of f_Q/λ by a factor of 10, decreases the value of Da by a factor of 100, and increases the processing length by a factor of 2.3, from 275 to 630 km.

The example calculations above illustrate how small changes in state variables can significantly alter the performance of hyporheic zone treatment systems. The calculations also reveal that engineered or natural hyporheic zone treatment systems operating outside their optimal state confer little water quality improvement over short distances (i.e., < 1 km). However, different empirical correlations for the mass transfer coefficient appear to give different predictions for the processing length. For example, when the modified CW correlation (equation 14b with modified coefficients) is used in place of the EB correlation (equation 14a), the predicted processing length is consistently shorter, in some cases by up to an order of magnitude. The different correlations also exhibit different degrees of agreement with numerical simulations of hyporheic exchange across triangular bed forms (see **Appendix A**). Further research should focus on improving and field-testing empirical correlations for hyporheic exchange rates (k_m or equivalently u_m, see equation (12b)), and developing more sophisticated quantitative models that can guide the experimental investigation and design of these low-energy natural treatment systems.

Appendix A. Numerical simulations, derivations, and supplemental figures and tables

References

Bardini, L.; Boano, F.; Cardenas, M.B.; Revelli, R.; Ridolfi, L. (2012), Nutrient cycling in bed form induced hyporheic zones, Geochemica et Cosmochimica Acta, 84, 47-61.

Bardini, L.; Boano, F.; Cardenas, M.B.; Sawyer, A.H.; Revelli, R.; Ridolfi, L. (2013) Small-scale permeability heterogeneity has negligible effects on nutrient cycling in streambeds, Geophys. Res. Lett., 40, 1118-1122.

Boulton A.J. (2007), Hyporheic rehabilitation in rivers: restoring vertical connectivity. Freshwater Biology, 52, 632–650; doi:10.1111/j.1365-2427.2006.01710.x

Cardenas, M.B.; Wilson, J.L. (2007), Dunes, turbulent eddies, and interfacial exchange with permeable sediments Wat. Resour. Res., 43, doi:10.1029/2006WR005787.

Cussler, E.L. (2009), Diffusion: Mass Transfer in Fluid Systems (Third Edition), Cambridge Series in Chemical Engineering, Cambridge, UK.

Elliott, A.H.; Brooks, N.H. (1997a), Transfer of nonsorbing solutes to a streambed with bed forms: theory, Water Resources Research, 33, 123-136.

Elliott, A.H.; Brooks, N.H. (1997b), Transfer of nonsorbing solutes to a streambed with bed forms: laboratory experiments, Water Resources Research, 33, 137-151.

Fehlman, J.M. (1985), Resistance components and velocity distributions of open chanel flows over bedforms, M.S. Thesis, Colorado State University, Fort Collins.

Fisher, S.G.; Grimm, N.B.; Marti, E.; Holmes, R.M.; Jones, J.B. (1998), Material spiraling in stream corridors: A telescoping ecosystem model, Ecosystems, 1, 19-34.

Genereux, D. P.; Leahy, S.; Mitasova, H.; Kennedy, C. D; Corbett, D. R. (2008), Spatial and temporal variability of streambed hydraulic conductivity in West Bear Creek, North Carolina, USA. Journal of Hydrology, 358, 332-353.

Gomez, J.D.; Wilson, J.L.; Cardenas, M.B., (2012), Residence time distributions in sinuosity-driven hyporheic zones and their biogeochemical effects, Wat. Resour. Res., 48, doi:10.1029/2012WR012180.

Grant, S.B.; Litton-Mueller, R.M.; Ahn, J.H. (2011), Measuring and modeling the flux of fecal bacteria across the sediment-water interface in a turbulent stream, Water Resources Research, 47, W05517, doi:10.1029/2010WR009460.

Grant, S.B.; Marusic, I. (2011), Crossing turbulent boundaries: interfacial flux in environmental flows, Environ. Sci. Technol., 45, 7107-7113.

Grant, S.B.; Stewardson, M.J.; Marusic, I. (2012), Effective diffusivity and mass flux across the sediment-water interface in streams, Wat. Resour. Res., 48, W05548, doi:10.1029/2011WR011148.

Hancock, P.J. (2002), Human impacts on the stream-groundwater exchange zone, Environmental Management, 29, 763-781.

Hester, E.T.; Doyle, M.W. (2008), In-stream geomorphic structures as drivers of hyporheic exchange, Wat. Resour. Res., 33, doi:10.1029/2006WR0058.

Hester, E.T; Gooseff, M.N. (2010), Moving beyond the banks: hyporheic restoration is fundamental to restoring ecological services and functions of streams, Environ. Sci. Technol., 44, 1521-1525.

Hester, E.T.; Gooseff, M.N (2011), Hyporheic restoration in streams and rivers. In Stream Restoration in Dynamic Fluvial Systems: Scientific Approaches, Analyses, and tools. Geophysical Monograph Series 194, American Geophysical Union, DOI10.1029/2010GM000966.

Hester, E.T.; Young, K.I.; Widdowson, M.A. (2013), Mixing of surface and groundwater induced by riverbed dunes: implications for hyporheic zone definitions and pollutant reactions, Wat. Resour. Res., 49, 5221-5237.

Huettel, M.; Berg, P.; Kotska, J.E. (2014), Benthic exchange and biogeochemical cycling in permeable sediments, Annu. Rev. Mar. Sci., 6, 23-51.

Hughes, R.M.; Dunham, S.; Maas-Hebner, K. G.; Yeakley, J. A.; Schreck, C.; Harte, M.; Molina, N.; Shock, C. C.; Kaczynski, V.W.; Schaeffer, J. (2014), A Review of Urban Water Body Challenges and Approaches: (1) Rehabilitation and Remediation, Fisheries, 39, 18-29, DOI: 10.1080/03632415.2013.836500

Iversen, N.; Jorgensen, B.B. (1993), Diffusion coefficients of sulfate and methane in marine sediments: influence of porosity, Geochim. Cosmochim. Acta, 57, 571-578.

Janssen, F.; Cardenas, M.B.; Sawyer, A.H.; Dammrich, T.; Krietsch, J.; de Beer, D. (2012), A comparative experimental and multiphysics computational fluid dynamics study of coupled surface-subsurface flow in bed forms, Water Resources Research, 48, doi:10.1029/2012WR011982.

Kaushal, S. S., P. M. Groffman, P. M. Mayer, E. Striz, and A. J. Gold (2008), Effects of stream restoration on denitrification in an urbanizing watershed. Ecological Applications 18, 789–804.

Kessler, A.J.; Glud, R.N.; Cardenas, M.B.; Cook ,P.L.M. (2013), Transport zonation limits coupled nitrification-denitrification in permeable sediments, Environ. Sci. Technol., 47, 13404-13411.

Krause, S.; Hannah, D.M.; Fleckenstein, J.H.; Heppell, C.M.; Kaeser, D.; Pickup, R.; Pinay, G.; Robertson, A.L.; Wood, P.J. (2011), Inter-disciplinary perspectives on processes in the hyporheic zone, Ecohydrology, 4, 481-499.

Lawrence, J.E.; Skold, M.E.; Hussain, F.A.; Silverman, D.R.; Resh, V.H.; Sedlak, D.L.; Luthy, R.G.; McCray, J.E. (2013), Hyporheic zone in urban streams: A review and opportunities for enhancing water quality and improving aquatic habitat by active management, Environ. Eng. Sci., 30, 480-501.

Loffler, D.; Rombke, J.; Meller, M.; Ternes, T.A. (2005), Environmental fate of pharmaceuticals in water/sediment systems, Environ. Sci. Technol., 39, 5209-5218.

Manes, C.; Pokrajac, D.; McEwan, I.; Nikora, V. (2009), Turbulence structure of open channel flows over permeable and impermeable beds: a comparative study, Physics of Fluids, 21, 125109.

Marion, A.; Bellinello, M.; Guymer, I.; Packman, A. (2002), Effect of bed form geometry on the penetration of nonreactive solutes into a streambed, Wat. Resour. Res., 38, doi:10.1029/2001WR000264.

Meysman, F.J.R.; Galaktionov, O.S.; Cook, P.L.M.; Janssen, F.; Huettel, M.; Middelburg, J.J. (2007), Quantifying biologically and physically induced flow and tracer dynamics in permeable sediments, Biogeosciences, 4, 627-646.

Monhanty, S.K.; Torkelson, A.A.; Dodd, H.; Nelson, K.L.; Boehm, A.B. (2013), Engineering solutions to improve the removal of fecal indicator bacteria by bioinfiltration systems during intermittent flow of stormwater, Environ. Sci. Technol., 47, 10791-10798.

O'Connor, B.L.; Harvey, J.W. (2008), Scaling hyporheic exchange and its influence on biogeochemical reactions in aquatic ecosystems, Water Resources Research, 44, doi:10.1029/2008WR007160.

Ren, J.; Packman, A.I. (2004), Stream-subsurface exchange of zinc in the presence of silica and kaolinite colloids, Environ. Sci. Technol., 38, 6571-6581.

Packman, A.I.; Brooks, N.H.; Morgan, J.J. (2000), Kaolinite exchange between a stream and streambed: Laboratory experiments and validation of a colloid transport model, Wat. Resour. Res., 36, 2363-2372.

Packman, A.I.; MacKay, J.S. (2003), Interplay of stream-subsurface exchange, clay particle deposition, and streambed evolution, Wat. Resour. Res., 39, doi:10.1029/2002WR001432.

Packman, A.I.; Salehin, M.; Zaramella, M. (2004), Hyporheic exchange with gravel beds: basic hydrodynamic interactions and bedform-induced advective flows, ASCE J. Hydraulic Eng., 130, 647-656.

Rehg, K.J., Packman, A.I.; Ren, J. (2005), Effects of suspended sediment characteristics and bed sediment transport on streambed clogging, Hydrological Processes, 19, 413-427.

Rutherford, J.C.; Boyle, J.D.; Elliott, A.H.; Hatherell, T.V.J.; Chiu, T.W. (1995), Modeling benthic oxygen uptake by pumping, ASCE J. Environ. Eng., 121, 84-95.

The Hyporheic Handbook: A handbook on the groundwater-surface water interface and hyporheic zone for environmental managers (2009); Integrated catchment science programme science report: SC050070; UK Environment Agency: Almondsbury, Bristol.

Thibodeaux, L.J.; Boyle, J.D. (1987), Bedform-generated convective transport in bottom sediment Nature, 325, 341-343.

Thibodeaux, L.; Valsaraj, K.; Reible, D. (2012), Letter to the editor regarding, "Crossing turbulent boundaries: interfacial flux in environmental flows", Environ. Sci. Technol., 46, 1293-1294.

Veraart, A. J., Audet, J., Dimitrov, M. R., Hoffmann, C. C., Gillissen, F., and de Klein, J. J. (2014), Denitrification in restored and unrestored Danish streams. Ecological Engineering, 66, 129-140.

Wu, L.; Munoz-Carpena, R.; Gao, B.; Yang, W.; Pachepsky, Y. (2014), Colloid filtration in surface dense vegetation: experimental results and theoretical predictions, Environ. Sci. Technol., doi:10.1021/es404603g

Chapter 3

Bedforms as Biocatalytic Filters:

A Pumping and Streamline Segregation (PASS) Model for Nitrate Removal in Permeable Sediments[1]

Abstract

Bedforms are a focal point of carbon and nitrogen cycling in streams and coastal marine ecosystems. In this chapter we develop and test a mechanistic model—the "pumping and streamline segregation" or PASS model—for nitrate removal in bedforms. The PASS model dramatically reduces the computational overhead associated with modeling nitrogen transformations in bedforms and reproduces (within a factor of 2 or better) previously published measurements and models of biogeochemical reaction rates, benthic fluxes, and in-sediment nutrient and oxygen concentrations. Application of the PASS model to a diverse set of marine and freshwater environments indicates that (1) physical controls on nitrate removal in a bedform include the pore water flushing rate, residence time distribution, and relative rates of respiration and transport (as represented by the Damköhler number); (2) the biogeochemical pathway for nitrate removal is an environment-specific combination of direct denitrification of stream nitrate and coupled nitrification-denitrification of stream and/or sediment ammonium; and (3) permeable sediments are almost always a net source of dissolved inorganic nitrogen. The PASS

---

[1] A version of this chapter was published as [Azizian, M.; Grant, S.B.; Kessler, A.J.; Cook, P.L.M.; Rippy, A.; Stewardson, M. (2015), Bedforms as Biocatalytic Filters: A Pumping and Streamline Segregation (PASS) Model for Nitrate Removal in Permeable Sediments. Environ. Sci. Technol. 49(18), 10993-1002, doi: 10.1021/acs.est.5b01941].

model also provides a mechanistic explanation for previously published empirical correlations showing denitrification velocity (N_2 flux divided by nitrate concentration) declines as a power law of nitrate concentration in a stream [Mulholland et al., 2008].

3.1. Introduction

Permeable sediments line the bottom of rivers and marine coastlines worldwide. The movement of water, heat, and mass through permeable sediments is a key component of many globally important ecosystem services, including the provision of benthic habitats [Hall, 2002; Brunke and Gonser, 1997; Young et al., 2011], pollutant attenuation [Gandy et al., 2007; Lawrence et al., 2013], and biogeochemical cycling [Cook and Wenzhöfer, 2006; Pinay et al., 2009; Bardini et al., 2012]. In the highly productive inner shelf region of the world's oceans, permeable sands are responsible for 24 to 73% of benthic respiration and 15% of denitrification [Huettel et al., 2014]. On land, the fate of 75% of nitrogen added by agricultural activities is unaccounted for [Howarth et al., 2002; David et al., 2006] and much of the missing nitrogen is thought to be denitrified within permeable stream sediments [Galloway et al., 2004]. Permeable sediments can also serve as sources or sinks for phosphorous [Lawrence et al, 2013; Galloway et al., 2004; Haggard et al., 2005], heavy metals [Gandy et al., 2007; Lawrence et al., 2013], fecal indicator bacteria [Grant et al., 2011; Litton et al., 2010], and human pathogens [Sinigalliano et al., 2007; Searcy et al., 2006].

The profound influence permeable sediments exert on global biogeochemical cycling and regional water quality can be attributed to [Huettel et al., 2014; Boano et al., 2014;

Meysman et al., 2007; Santos et al., 2012; Hester and Gooseff, 2010]: (1) the transport of mass and heat across the sediment-water interface by physical and biological processes; and (2) the presence of microbial communities in the sediments that catalyze oxidation-reduction reactions. As noted in a recent review article, these two features transform permeable sediments into highly reactive biocatalytic filters [Huettel et al., 2014]. Here we present a simple mechanistic model for the biocatalytic transformation of nitrate by permeable sediments in marine and freshwater systems. The chaoter is organized as follows. We begin with a description of the modeling framework adopted in this study, and then evaluate the model in light of: (1) previously published experimental measurements; (2) previously published numerical simulations; and (3) relaxation of one of the model's key assumptions. The model is then used to identify physical and biocatalytic controls on nitrate removal in six environments (three coastal marine and three terrestrial streams) and to evaluate a previously published empirical correlation for the uptake velocity of nitrate in streams.

3.2. Advective Pumping Model (APM) for Flow-Topography Pore Water Exchange

As water flows over the top of a bedform, dynamic pressure variations along the sediment-water interface arise due to acceleration and deceleration of the flow and boundary layer separation [Meysman et al., 2007; Santos et al., 2012; Hester and Gooseff, 2010; Stonedahl et al., 2010, 2012; Grant and Marusic, 2011]. These dynamic pressure variations pump water, oxygen, and nutrients into the sediment in high-pressure regions (downwelling zones) and out of the sediment in low-pressure regions (upwelling zones). Here we adopt an idealized model of this pumping process (called the advective pumping model or APM) first proposed and experimentally validated by Elliott and Brooks [1997a,b]. In the APM, the variation in dynamic pressure is mimicked with an assumed sinusoidal pressure variation over a flat sediment-water interface (**Figure 3.1A**). Of course, real bedforms are not flat and the dynamic pressure variation over a bedform is not purely sinusoidal [Cardenas and Wilson, 2007]. Nevertheless, the flow field predicted by the APM is qualitatively similar to experimental and computational observations of pore fluid flow fields induced by stream-bedform interactions [Elliott and Brooks, 1997b; Cardenas and Wilson, 2007; Janssen et al., 2012] and reproduces to within 11% computational estimates of benthic water flux [Grant et al., 2014] (the APM stream function, from which the x- and y-components of the two-dimensional velocity field can be calculated, is presented in **Text B.1** of **Appendix B**). Given its simplicity and consistency with experimental observations and numerical simulations, the APM is an excellent starting point for the modeling described next.

3.3. APM Water Parcel Age and Residence Time Distribution (RTD)

If permeable bedforms are biocatalytic filters then it stands to reason that methods developed for the design and analysis of chemical reactors may prove useful. A critical feature of any chemical reactor is the time water parcels spend in the reactor [Levenspiel, 1972]. Here we define two such transport time scales: water parcel age and residence time distribution.

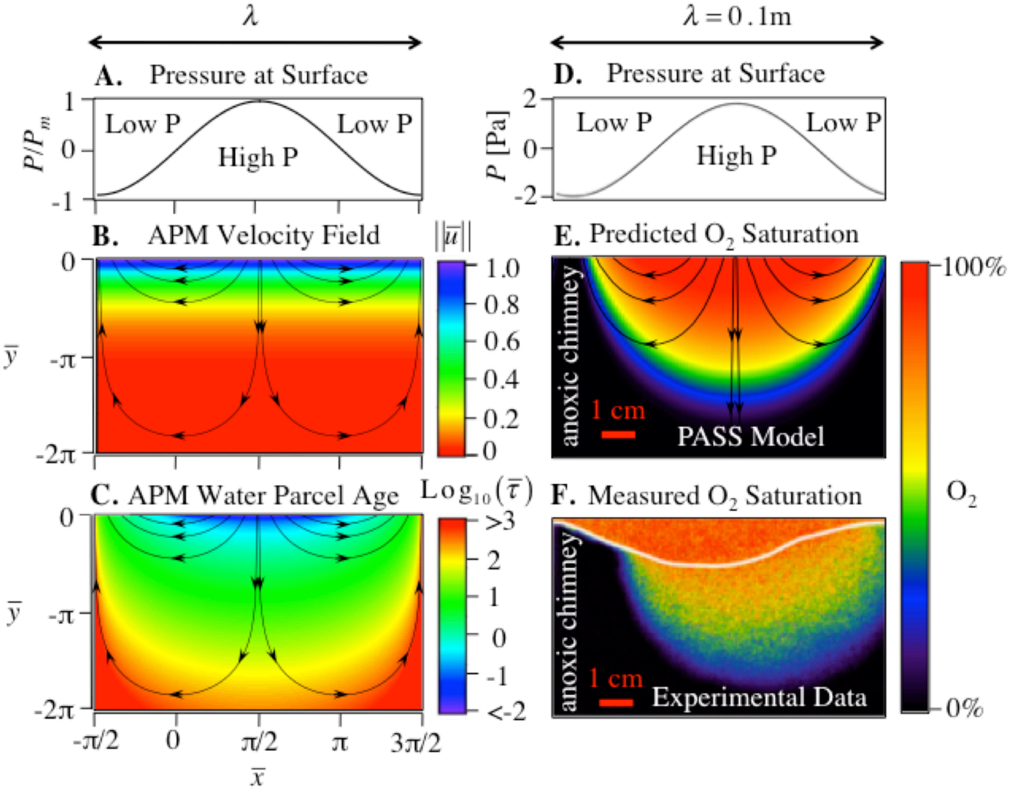

Figure 3.1. Features of the APM velocity field (**A**-**C**) and an experimental test of the PASS model (**D**-**F**). The APM assumes flow across the sediment-water interface is driven by a sinuosoidal pressure variation over a flat sediment bed (**A**). This pressure variation drives flow into the sediment in high pressure regions (downwelling zones) and out of the sediment in low pressure regions (upwelling zones) (**B**). Water parcels moving through the sediment experience a diverse range of streamline trajectories and ages (**C**). The PASS model was used to simulate the reactive transport of oxygen through a sandy ripple with a 10 cm wavelength (**D**). The pore fluid concentrations of oxygen predicted by the PASS model (**E**) are qualitatively similar to oxygen measurements with a two-dimensional planar optode (see main text) (**F**). Variables appearing in this figure include bedform wavelength (λ); pressure (P) and maximum pressure (P_m) at the sediment-water interface; reduced horizontal ($\bar{x}$) and vertical ($\bar{y}$) coordinates (depth into the sediment bed corresponds to $\bar{y} < 0$); absolute magnitude of the reduced pore fluid velocity ($\|\bar{\mathbf{u}}\| = \|\mathbf{u}\| / (\pi k_m)$, where k_m is the pore-water flushing rate); and $\bar{\tau} = \tau / \tau_T$ represents a reduced form of the water parcel age. The five streamlines shown in panels (**B**), (**C**), and (**E**) were chosen so that the volume of water (per unit width of stream) flowing between any two adjacent streamlines is the same and equal to 1.7 L per meter per day (see **Appendix B**).

3.3.1. Water Parcel Age

The water parcel age $\tau(\bar{x},\bar{y})$ is the time a water parcel spends traveling from where it first crosses into the sediment in a downwelling zone to any location $(\bar{x},\bar{y})$ in the sediment. Here, the variables $\bar{x}=2\pi x/\lambda$ and $\bar{y}=2\pi y/\lambda$ are reduced forms of the horizontal and vertical coordinates x and y, respectively, where λ represents the wavelength of the sinusoidal pressure variation (assumed equal to the wavelength of a bedform) (**Figure 3.1A**). Several points should be kept in mind. First, the APM flow field is steady-state, stream-wise periodic, and two-dimensional. Consequently, any location $(\bar{x},\bar{y})$ in the sediment is associated with a single streamline and a single value for the water parcel age. Second, all downwelling zones in the APM are identical or mirror image (e.g., compare the one located for $\bar{x}$ values between $0 \le \bar{x} \le \pi/2$ and its mirror image located for $\bar{x}$ values between $\pi/2 \le \bar{x} \le \pi$, **Figure 3.1B)**. Thus, without loss of generality we can calculate the age of water parcels that transit from one downwelling zone ($0 \le \bar{x} \le \pi/2$) to an adjacent upwelling zone ($-\pi/2 \le \bar{x} \le 0$) (**Figure 3.1B**). An explicit formula for the age of water parcels entering this particular downwelling zone (and by inference all downwelling zones) can be derived from the APM (see **Text B.2** in **Appendix B**):

$$\bar{\tau}(\bar{x},\bar{y})=\frac{\tau(\bar{x},\bar{y})}{\tau_T}=\frac{\cos^{-1}\left(e^{\bar{y}}\cos\bar{x}\right)-\bar{x}}{2e^{\bar{y}}\cos\bar{x}}, \quad \bar{y}\le 0, \quad -\pi/2\le\bar{x}\le\pi/2 \tag{1a}$$

$$\tau_T=\lambda\theta/\pi^2 k_m \tag{1b}$$

The parameter τ_T is a characteristic timescale for transport through a bedform. It can be interpreted as the time it would take a water parcel to travel the distance λ while moving at speed k_m/θ, where k_m is the volume of water flowing through the bedform per unit area of bed surface [m^3 s^{-1} m^{-2}] (also called the Darcy flux [Rutherford et al., 1995], pore-water flushing rate [Huettel et al., 2014], downwelling velocity [Grant et al., 2014], and mass transfer coefficient [Grant et al., 2014]) and θ [-] is sediment porosity (the π^2 appearing in the denominator of equation (1b) is included for mathematical convenience). For the duration of this chapter we refer to k_m as the pore-water flushing rate. The pore water flushing rate can be measured in the field [Berg et al., 2013], in laboratory flumes [Grant et al., 2014], or calculated from equation (2) based on bedform geometry (wavelength λ [m] and height Δ [m]), hydraulic conductivity of the sediment (K_h [m s^{-1}]), stream flow velocity (U [m s^{-1}]), and stream depth (H [m]) [Elliott and Brooks, 1997a,b].

$$k_m = 0.28\frac{K_h U^2}{g\lambda}\left(\frac{\Delta/H}{0.34}\right)^{\gamma},\ \gamma = \begin{cases} 3/8 \text{ for } \Delta/H < 0.34 \\ 3/2 \text{ for } \Delta/H \geq 0.34 \end{cases} \tag{2}$$

Water parcel ages predicted by equation (1a) vary more than 5 orders of magnitude (**Figure 3.1C**). Some water parcels move quickly along short streamlines located near the surface ($\bar{\tau} < 0.1$, dark blue to purple colors in **Figure 3.1C**), while others travel slowly along long streamlines that penetrate deep into the sediment ($\bar{\tau} > 100$, yellow to red colors).

3.3.2. Residence Time Distribution

The residence time distribution (RTD) function $F_{RTD}(\tau_f)$ is defined as the fraction of water volume cycling through a bedform with final age τ_f or younger upon exiting. The

RTD takes into account both the age of water parcels exiting the sediments and the partitioning of water flux across streamlines [Levenspiel, 1972]. The distinction between $\tau(\bar{x},\bar{y})$ and τ_f is the former represents the age of the water parcel at any location in the sediment (see equation (1a)) while the latter represents the final age of a water parcel leaving the sediment bed. The final age τ_f varies by where a streamline intersects the x-axis (at $y=0$) in a downwelling zone. We denote this intersection point as $x=x_0$, which in reduced form becomes $\bar{x}=\bar{x}_0$ where $\bar{x}_0=2\pi x_0/\lambda$. Given these definitions, an RTD can be derived for the same downwelling zone analyzed above (and by inference all downwelling zones, see **Text B.3** in **Appendix B**):

$$F_{RTD}\left(\bar{\tau}_f\right)=1-\cos\left[\bar{x}_0\left(\bar{\tau}_f\right)\right],\quad 0\le\bar{x}_0\le\pi/2 \tag{3a}$$

$$\bar{\tau}_f\equiv\frac{\tau_f}{\tau_T}=\frac{\bar{x}_0}{\cos\bar{x}_0},\quad 0\le\bar{x}_0\le\pi/2 \tag{3b}$$

Equation (3b) is an implicit form of the function $\bar{x}_0\left(\bar{\tau}_f\right)$; i.e., for any choice of the final age $\bar{\tau}_f$, the equation can be solved to find the corresponding value of $\bar{x}_0$, which can then be substituted into equation (3a) to yield a value for F_{RTD}. Consistent with the diversity of streamline trajectories shown in **Figure 3.1C**, the RTD exhibits a broad (logarithmic) range of final ages (**Figure B.1** in **Appendix B**). The RTD derived here (equations (3a) and (3b)) is mathematically equivalent to the residence time expression derived for the APM by Elliott and Brooks [1997a] (see **Text B.4** in **Appendix B**).

3.4. Pumping and Segregated Streamline (PASS) Model for Nitrate

In this chapter, we combine the APM flow field with biogeochemical reactions for aerobic respiration (AR), nitrification (NI), denitrification (DN), and ammonification (AM) [*A model set-up for an oxygen and nutrient flux model for Aarhus Bay (Denmark),* 2004].

AR: $CH_2O+O_2 \rightarrow CO_2+H_2O$ (4a)

DN: $CH_2O+0.8NO_3^-+0.8H^+ \rightarrow CO_2+0.4N_2+1.4H_2O$ (4b)

NI: $NH_4^++2O_2 \rightarrow NO_3^-+2H^++H_2O$ (4c)

AM: $\left\{NH_3\right\}_{OM}+H^+ \rightarrow NH_4^+$ (4d)

The notation $\left\{NH_3\right\}_{OM}$ in equation (4d) refers to the generation of ammonium by the microbial respiration of sediment organic matter.

The APM assumes that flow through a bedform is laminar. Under laminar flow, it can often be assumed that water parcels do not mix with adjacent water parcels as they travel through the reactor [Levenspiel, 1972; Hill, 1977], although this assumption may breakdown in heterogeneous bedform sediments (discussed later) [Briggs et al., 2015]. As applied to bedforms, this "segregated streamline hypothesis" implies that molecular diffusion and mechanical dispersion can be neglected, and therefore the steady-state concentrations of oxygen (C_{O_2}), ammonium ($C_{NH_4^+}$), and nitrate ($C_{NO_3^-}$) along any streamline through the sediment will evolve with water parcel age (τ) according to the following set of mass balance expressions [Rutherford et al., 1995; Hill, 1977; Marzadri et al., 2011]:

$$\frac{dC_{O_2}}{d\tau} = -R_{AR} - 2R_{NI} \tag{5a}$$

$$\frac{dC_{NO_3^-}}{d\tau} = R_{NI} - R_{DN} \tag{5b}$$

$$\frac{dC_{NH_4^+}}{d\tau} = R_{AM} - R_{NI} \tag{5c}$$

Consensus Monod rate expressions (based on a consensus evaluation of field and laboratory data [*A model set-up for an oxygen and nutrient flux model for Aarhus Bay (Denmark),* 2004]) were adopted for the rates of aerobic respiration (R_{AR}), ammonification (R_{AM}), nitrification (R_{NI}), and denitrification (R_{DN}):

$$R_{AR} = \frac{R_{\min} C_{O_2}}{C_{O_2} + K_{O_2}^{sat}} \tag{6a}$$

$$R_{AM} = \frac{1}{\gamma_{CN}} R_{\min} \tag{6b}$$

$$R_{NI} = k_{NI} C_{O_2} C_{NH_4^+} \tag{6c}$$

$$R_{DN} = \theta_{O_2}^{inh} \kappa \frac{R_{\min} C_{NO_3^-}}{C_{NO_3^-} + K_{NO_3^-}^{sat}} \; ; \; \theta_{O_2}^{inh} = \frac{K_{O_2}^{inh}}{C_{O_2} + K_{O_2}^{inh}} \tag{6d}$$

Parameters appearing here include the respiration rate of sediment organic matter ($R_{\min}$ [mol m^{-3} s^{-1}]), a constant for ammonification (γ_{CN} [-]), a bi-molecular nitrification rate constant (k_{NI} [m^3 mol^{-1} s^{-1}]), half-saturation constants for aerobic respiration ($K_{O_2}^{sat}$ [mol m^{-3}]), denitrification ($K_{NO_3^-}^{sat}$ [mol m^{-3}]), and oxygen inhibition ($K_{O_2}^{inh}$ [mol m^{-3}]), and an empirical factor $\kappa = 0.05$ [-].

Combining equations (5a) through (6d) we arrive at three ordinary differential equations (equations (B12a) through (B12c), **Text B.5** in **Appendix B**) that can be numerically integrated to yield the chemical evolution of a water parcel as it moves along a streamline through the sediment:

$$\bar{C}_i\left(\bar{\tau}_R;\mathbf{chemistry}\right)\equiv\frac{C_i\left(\bar{\tau}_R;\mathbf{chemistry}\right)}{C_{O_2}(0)} \tag{7a}$$

$$\bar{\tau}_R\equiv\frac{\tau\left(\bar{x},\bar{y}\right)}{\tau_R} \tag{7b}$$

$$\tau_R=\frac{K_{O_2}^{sat}}{R_{\min}} \tag{7c}$$

Here, C_i [mol m^{-3}] represents the pore fluid concentration of the i th chemical species (oxygen, nitrate, or ammonium), $\bar{\tau}_R$ is the reduced age of the water parcel, $C_{O_2}(0)$ [mol m^{-3}] is the in-stream concentration of oxygen, and τ_R [s] is a time scale for the respiration of sediment organic matter. Conceptually, reduced age is a nondimensional quantity that represents the time a water parcel travels through the sediment normalized by the characteristic time scale associated with aerobic respiration of organic matter in the sediment. The word "chemistry" in equation (7a) is shorthand for the seven reduced parameters that collectively define in-stream concentrations and reaction rates including: (1) the relative rates of nitrification and aerobic mineralization ($\delta=k_{NI}C_{O_2}(0)/\left(R_{\min}/K_{O_2}^{sat}\right)$); (2) normalized saturation constants for oxygen ($\bar{K}_{O_2}^{sat}\equiv K_{O_2}^{sat}/C_{O_2}(0)$), nitrate ($\bar{K}_{NO_3^-}^{sat}\equiv K_{NO_3^-}^{sat}/C_{O_2}(0)$), and oxygen inhibition of denitrification ($\bar{K}_{O_2}^{inh}\equiv K_{O_2}^{inh}/C_{O_2}(0)$); (3) normalized stream concentrations of ammonium ($\alpha\equiv C_{NH_4^+}(0)/C_{O_2}(0)$) and nitrate ($\beta\equiv C_{NO_3^-}(0)/C_{O_2}(0)$); and (4) net mineralization of carbon relative to production of ammonium (γ_{CN}) (top seven rows of **Table B.1**).

When equation (7a) is combined with the APM solution for water parcel age ($\bar{\tau}(\bar{x},\bar{y})$, equation (1a)) we arrive at a solution for the pore fluid concentrations of oxygen and nutrients from which all other parameters of interest (e.g., benthic flux, average reaction rates, and uptake velocities, see later) can be calculated:

$$\frac{C_i(\bar{x},\bar{y};\mathbf{chemistry})}{C_{O_2}(0)} = \bar{C}_i\left(\bar{\tau}_R = \mathbf{Da}\,\bar{\tau}(\bar{x},\bar{y});\mathbf{chemistry}\right) \tag{8a}$$

$$\mathbf{Da} = \frac{\tau_T}{\tau_R} \tag{8b}$$

The Damköhler number number (**Da**) is defined as the ratio of time scales for transport (τ_T, equation (1b)) and respiration of sediment organic matter (τ_R, equation (7b)); it can also be interpreted as the relative rate of respiration and transport within the bedform. Note that our definition of the Damköhler number differs from that presented in a similar study by Zarnetske et al. [2012]. Specifically, our definition of **Da** is fixed by the values of τ_T and τ_R (corresponding to specific choices of the RTD of water parcels and respiration rate in the sediment, respectively), while Zarnetske et al.'s definition varies continuously along any streamline through the sediment. As will be shown later, by adopting equation (8b) as the definition of **Da**, this nondimensional parameter becomes a controlling variable for the net flux of nitrate across the sediment-water interface over a wide spectrum of aquatic environments. Because our model relies on both the APM and the streamline segregation hypothesis (SSH), we refer to it as the pumping and streamline segregation (PASS) model.

3.5. Testing the PASS Model

The PASS model is derived from a number of assumptions that individually or collectively may render it unsatisfactory in practice. To address this concern, we compared the PASS model with (1) O_2 measurements in an experimental flume; (2) concentrations and fluxes predicted by an experimentally validated flow and reactive transport model; and (3) a numerical simulation in which the SSH was relaxed.

3.5.1. Comparison with O_2 Measurements

As a first test, the PASS model was compared to oxygen measurements reported in a study of nitrogen cycling in sandy marine sediments by Kessler et al. [2013]. The experimental setup involved a recirculating flume to which sediment (from Port Phillip Bay, Melbourne, Australia) was added and artificially sculpted into ripples of height ~ 1 cm and wavelength ~ 10 cm. Water collected from the same field site was circulated through the flume at a depth and average flow velocity of approximately of 13 cm and 16 cm s^{-1}, respectively. From the set of parameter values reported by Kessler (**Table B.2**, **Appendix B**) we estimate a pore water flushing rate (from equation (2)) of $k_m = 1.64 \times 10^{-6}$ m s^{-1}, a characteristic travel time through a single ripple (from equation (1b)) of $\tau_T = 36$ min, and a sinusoidal pressure amplitude at the sediment-water interface of approximately 2 Pa (using a rearranged form of equation (2g) in Grant et al., 2014, **Figure 3.1D**). Kessler also reported in-stream nutrient concentrations and rate constants needed to calculate values for the seven reduced parameters in **Table B.1** in **Appendix B** (first column). From these data, we estimate a respiration timescale of

$\tau_R = K_{O_2}^{sat} / R_{\min} = 23$ min. Thus, oxygen consumption in the bedform is likely to be both reaction and transport controlled (i.e., the relative rate of respiration and transport is approximately unity, $\mathbf{Da} = \tau_T / \tau_R = 1.6$). Indeed, pore fluid oxygen concentrations predicted by the PASS model (**Figure 3.1E**) indicate that the reaction field is strongly influenced by the flow field: oxygen saturated waters penetrate to a depth of ~4 cm in the downwelling zone, and an "anoxic chimney" extends to the surface in the upwelling zone. These PASS predictions are qualitatively similar to measured two-dimensional profiles of oxygen saturation beneath a single ripple in Kessler's flume experiments (obtained with a 2D planar optode, **Figure 3.1F**)[Kessler et al., 2013]. While the experimental and model results are similar, there are two noteworthy differences. First, the concentration gradient along the edge of the aerobic zone is steeper in the PASS model than in the experimental study. Second, the areal extent of the aerobic zone appears smaller in the experimental study (taking into account the undulating nature of the ripple surface, as denoted by the white curve in **Figure 3.1F**). The first difference is a consequence of neglecting molecular diffusion and mechanical dispersion, while the latter difference reflects the PASS model's oversimplification of mass transfer across the sediment-water interface (i.e., flat sediment-water interface and a simplified velocity field). These two limitations are explored in more detail below.

3.5.2. Comparison with Numerical Flume Studies

Kessler also presented "numerical flume" studies in which the pore fluid concentrations of oxygen, nitrate, and ammonium beneath a single ripple were calculated using an experimentally calibrated flow and reactive transport model [Kessler et al., 2012, 2013] (see **Text B.6** in **Appendix B**, **Figure B.3**, **Table B.2**). Pore fluid concentrations calculated from the PASS model are qualitatively similar to Kessler's numerical flume results except that (**Figure B.4**, **Appendix B**): (1) the PASS model predicts symmetrical concentration fields (consistent with the APM's symmetric velocity field), while the numerical flume predicts asymmetrical concentration fields (reflecting the more realistic pore fluid velocity field generated by turbulent streamflow over a ripple); and (2) the PASS model has a larger aerobic zone compared to the numerical flume prediction (consistent with the 2D planar optode measurements discussed above). The PASS model approximately reproduces Kessler's predictions for: (1) location of reaction zones in the sediment (aerobic respiration, nitrification, denitrification: **Figure B.5**, **Appendix B**); (2) where concentration fields in the sediment oxygen, nitrate, and ammonium are produced or consumed (**Figure B.6**, **Appendix B**); (3) benthic flux of nitrate and ammonium, although the benthic flux of oxygen is somewhat overestimated (relative differences of 18%, 24%, and 64%, **Table 3.1**); (4) average rates for the production or consumption of oxygen, nitrate, and ammonium in the sediment (relative differences of 30%, 34%, and 0%, **Table 3.1**); and (5) average rates for respiration, nitrification, and denitrification in the sediment (relative differences of 31%, 30%, and 8%, **Table 3.1**).

In summary, the PASS model reproduces (within 35% or better) Kessler et al.'s estimates of biogeochemical reactions rates and benthic fluxes, with the exception of the benthic flux of oxygen, which is overestimated by 64%. As will be shown in the following sections, the fact that the PASS model's overestimation of benthic oxygen flux probably

Table 3.1. Benthic fluxes, average rates of production (>0) or consumption (<0) of oxygen, nitrate, and ammonium in the sediment (P_{ave}), and average rates of aerobic respiration, nitrification, denitrification, and ammonification in the sediment (R_{ave}) calculated from the PASS model, Kessler numerical flume studies, and COMSOL simulations in which the Segregated Streamline Hypothesis (or SSH) is relaxed. [a]

	Flux [mol m^{-2} s^{-1}] x10^8			P_{ave} [mol m^{-3} s^{-1}] x10^7			R_{ave} [b] [mol m^{-3} s^{-1}] x10^7			
	O_2	NO_3^-	NH_4^+	O_2	NO_3^-	NH_4^+	AR	NI	DN	AM
PASS	-23	-0.32	5.2	-65	-0.93	15	63	1.3	2.3	16
Kessler et al.	-14	-0.39	4.2	-50	-1.4	15	48	1.0	2.5	16
COMSOL	-23	-0.06	4.9	-65	-0.18	14	62	1.8	2.0	16

[a] Positive (negative) flux values correspond to net transport out of (into) the sediment bed.
[b] AR=aerobic respiration; NI=nitrification; DN=denitrification; AM=ammonification.

stems from its assumption that the sediment-water interface is flat and the hyporheic exchange flow-field is symmetrical.

3.5.3. Evaluating the Segregated Streamline Hypothesis (SSH)

As a final test we conducted a numerical simulation (using COMSOL Multiphysics (version 4.4), see **Text B.7** in **Appendix B** for details) in which the SSH was relaxed (i.e., water parcels were allowed to mix across streamlines by molecular diffusion and mechanical dispersion), but all other aspects of the PASS model were retained (flat sediment-water interface, the APM velocity field, and reaction rate laws described above). Comparing benthic fluxes predicted by the PASS and COMSOL models (first three columns in **Table 3.1**) we find that relaxing the SSH causes: (1) no change in the benthic flux of oxygen (relative difference of 0%); (2) a large reduction in the flux of nitrate into the sediment (relative difference of 81%); and (3) a small reduction in the flux of ammonium out of the sediment (relative difference of 6%). These results can be explained by the role of molecular diffusion and mechanical dispersion in delivering oxygen to anoxic regions of the sediment. In particular, when the SSH is relaxed more oxygen is delivered to the anoxic chimney which, in turn, increases the average rate of nitrification, decreases the average rate of denitrification, and thereby reduces the net flux of nitrate across the sediment-water interface (see difference plots in **Figure B.7**, Appendix B, and average nitrification and denitrification rates for the PASS and COMSOL models in **Table 3.1**). By contrast, relaxing the SSH has no effect on the benthic flux of oxygen because mass transport across the sediment-water interface is dominated by advection. Remarkably, when benchmarked relative to Kessler's numerical flume experiment, relaxing the SSH increases the nitrate flux error from 18% (for the PASS model) to 64% (for the COMSOL model) (**Table 3.1**). This surprising result can be explained by a fortuitous canceling of errors: the PASS model overestimates the flux of oxygen across the sediment-water interface (by oversimplifying the velocity field and the geometry of the interface) and also underestimates the mixing of oxygen into the anoxic chimney (by neglecting molecular diffusion and mechanical dispersion). Because these two errors have opposing effects on the delivery of oxygen to the anoxic regions of the sediment (increasing it in the first instance and reducing it in the second instance), the net result is that the PASS and Kessler models yield similar estimates for the benthic flux of nitrate.

Collectively, these results suggest that the PASS model can be used in place of more numerically sophisticated models (such as Kessler's numerical flume model) for estimating nitrogen budgets and benthic fluxes in aquatic systems, while acknowledging that the fortuitous canceling of errors observed here may not apply in all cases. On the other hand, our COMSOL simulations (which are intermediate in sophistication and complexity between the PASS model and Kessler's numerical flume model) performed relatively poorly, and would not be suitable for estimating nitrate budgets in aquatic systems.

3.6. Application of the PASS Model to Six Representative Riverine and Coastal Marine Systems

Next we apply the PASS model to six aquatic environments where bedforms play an important role in nitrogen cycling. Three are rivers impacted by agriculture runoff, urban runoff, or sewage. The rest are marine systems with oligotrophic, low oxygen, or eutrophic bottom waters. Note that, for the marine settings, we assume that the ripples are formed by steady-state unidirectional currents (e.g., associated with persistent or tidal alongshore currents [Fischer et al., 1979]) and not by shoaling waves. The latter are excluded because porewater flow induced by shoaling waves differs from that induced by unidirectional currents in a number of significant ways [Cardenas et al., 2011].

We define the six environments by their "chemistry" (i.e., values of the seven nondimensional parameters in **Table B.1** in **Appendix B**, columns 2 through 7) but leave their physical features (e.g., pore water flushing rate) as free variables. For each environment we set out to answer the following questions: (1) How do physical features of a bedform influence nitrate removal? (2) What are the dominant biogeochemical pathways by which nitrate is generated and removed? (3) What is the relative contribution of direct denitrification and coupled nitrification-denitrification to overall nitrogen removal? (4) Are permeable sediments net sources or sinks of dissolved inorganic nitrogen?

To answer these questions, the PASS model was implemented in three steps. First, the "chemistry" of the six environments was established by selecting rate constants and in-stream oxygen and nutrient concentrations consistent with the literature [Kessler et al. 2012; Evrard et al., 2013; Howarth et al., 1996] (columns 2 through 7, **Table B.1**). Second, for each environment the rate equations (equations (B12a)-(B12c), **Appendix B**) were numerically integrated to yield the concentrations of oxygen, nitrate, and ammonium along any streamline through the sediment (**Figure B.2**). Finally, the benthic flux of the *i*th species U_i (where the species of interest varied depending on the question being answered) was calculated as follows (derivation in **Text B.8** of **Appendix B**):

$$U_i = -k_m \left[C_i(0) - C_{i,bed} \right] \tag{9a}$$

$$C_{i,bed} = \int_{-\infty}^{\infty} C_i\left(\overline{\tau}_R = \mathbf{Da}\,\overline{\tau}_f; \mathbf{chemistry}\right) \frac{dF_{RTD}}{d\log_{10}\overline{\tau}_f}\, d\log_{10}\overline{\tau}_f \tag{9b}$$

Equation (9a) is analogous to a film model for interfacial mass transfer in which the pore-water flushing rate k_m is equivalent to a mass transfer coefficient, $C_i(0)$ represents the in-stream concentration of the *i*th species entering the downwelling zone, and $C_{i,bed}$ represents the RTD-weighted concentration of the *i*th species leaving the upwelling zone [Grant et al., 2014]. In the results shown below we present benthic fluxes in terms of a so-called uptake velocity [*Stream Solute Workshop,* 1990]: $v_i = U_i / C_{NO_3^-}(0)$ where $C_{NO_3^-}(0)$ is the nitrate concentration in the stream. Given our coordinate system, the sign of the uptake velocity indicates if bedforms are a net source ($v_i > 0$) or sink ($v_i < 0$) of the *i*th chemical species.

3.6.1. How Do Physical Features of A Bedform Influence Nitrate Removal?

Across all environments, the nitrate uptake velocity ($v_{fNO_3^-} = U_{NO_3^-} / C_{NO_3^-}(0)$) depends on the pore water flushing rate, both directly and through the definition of the Damköhler number (which depends on k_m through the transport time scale τ_T (see equation (1b)) (**Figure 3.2A**). Stream nitrate passes through the bedform without change when the Damköhler number is small ($v_{fNO_3^-} / k_m \to 0$, $\mathbf{Da} < 10^{-2}$) and is completely removed when the Damköhler number is large ($v_{fNO_3^-} / k_m \to -1$, $\mathbf{Da} > 10^3$). The limit $v_{fNO_3^-} / k_m \to -1$ corresponds to the case where the removal of stream nitrate in the bedform is mass-transfer limited [Grant et al., 2014]. Between these two extremes, the magnitude and sign of the nitrate uptake velocity varies by environment.

In three environments (agriculture-impacted river, urban-impacted river, and low O_2 marine bottom water) the bedform is never a net source of nitrate ($v_{fNO_3^-} / k_m < 0$, brown, dark blue, and red curves, **Figure 3.2A**). In the rest, bedforms are a net source of nitrate over some restricted range of the Damköhler number ($v_{fNO_3^-} / k_m > 0$, green, light blue, and black curves, **Figure 3.2A**). In summary, the nitrate uptake velocity depends on sediment biogeochemistry ("**chemistry**"), the pore-water flushing rate (k_m), and the balance between respiration and transport rates in a bedform (as represented by the Damköhler number).

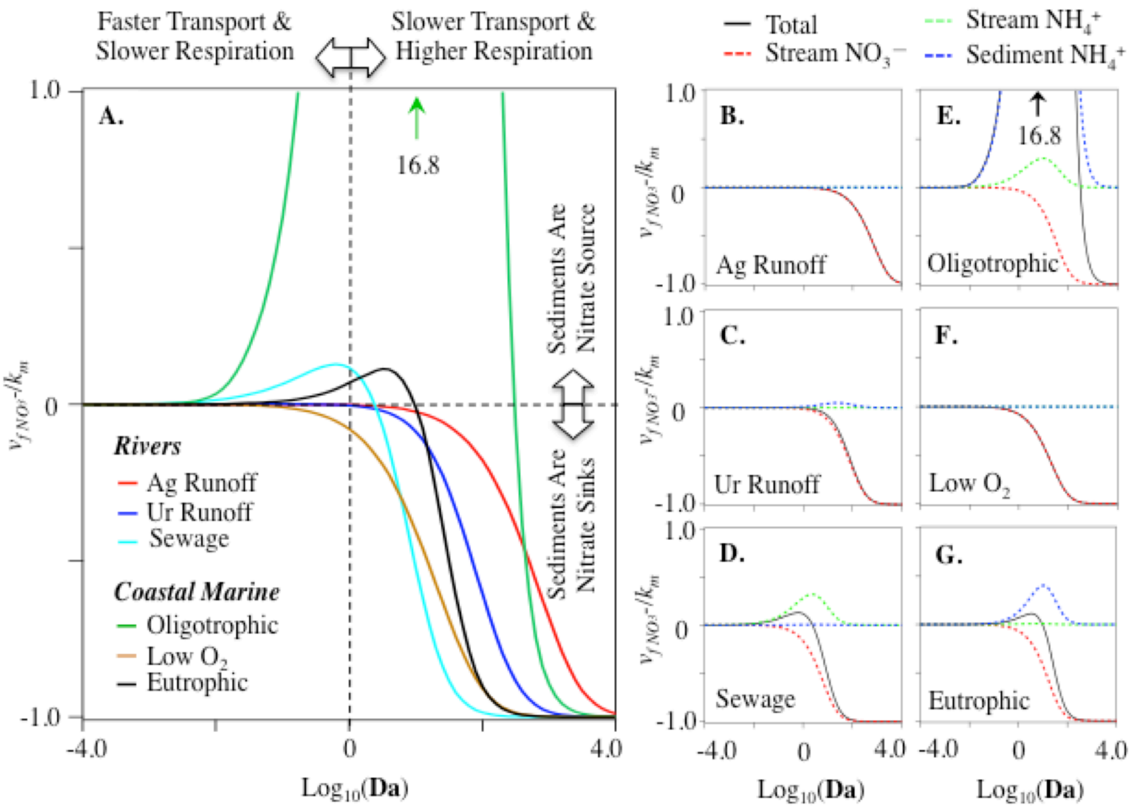

Figure 3.2. Application of the PASS model to six environments, including three rivers (impacted by agriculture runoff, urban runoff, or sewage) and three marine systems (with oligotrophic, low oxygen, or eutrophic bottom waters). The uptake velocity of nitrate ($v_{f\mathrm{NO}_3^-}$) depends on the pore-water flushing rate (k_m, both directly and through the definition of the Damköhler number) and environment-specific biogeochemical rate constants and in-stream concentrations of oxygen, nitrate, and ammonium (Table B.1, Appendix B). The sign of the total uptake velocity indicates whether the streambed is a net source ($v_{fNO_3^-} > 0$) or sink ($v_{fNO_3^-} < 0$) of nitrate (**A**). The small panels show the contribution of different sources of nitrogen (including nitrate from the stream ("stream NO_3^-"), ammonium from the stream ("stream NH_4^+"), and ammonium generated in situ from the respiration of sediment organic matter ("sediment NH_4^+")) to the uptake velocity of nitrate in three streams (agricultural runoff (**B**), urban runoff (**C**), and sewage (**D**)) and three marine systems (oligotrophic (**E**), low oxygen bottom water (**F**), and eutrophic (**G**)).

3.6.2. What Biogeochemical Pathways Dominate Nitrate Generation and Removal?

To answer this question we evaluated the contribution of each nitrogen source to the nitrate uptake velocity (by integrating equations (B17)-(B20), **Text B.9** in **Appendix B**). In the two environments with limited nitrification (agriculture-impacted river and low-O_2 marine waters), the nitrate uptake velocity is determined solely by denitrification of stream nitrate (i.e., the red dashed and black curves overlap, **Figures 3.2B**,**F**). In the sewage-impacted river, on the other hand, the nitrate uptake velocity is the sum of uptake velocities associated with the oxidation of stream ammonium to nitrate and the reduction of stream nitrate to dinitrogen gas (i.e., the black curve is the sum of the red and green dashed curves, **Figure 3.2D**). In urban impacted rivers and eutrophic marine waters the nitrate uptake velocity has contributions from both the oxidation of sediment ammonium (generated by the respiration of sediment organic matter) and the reduction of stream nitrate (i.e., the black curve is the sum of the blue and red dashed curves, **Figure 3.2** panels **C** and **G**). Finally, in oligotrophic marine waters the nitrate uptake velocity has contributions from the reduction of stream nitrate, nitrification of sediment ammonium, and to a lesser extent nitrification of stream ammonium (i.e., the black curve is the sum of the dashed red, blue, and green curves, **Figure 3.2E**). The latter's large peak value ($v_{fNO_3^-}/k_m = 16.8$) can be attributed to conditions favorable for nitrification (oxygen saturated bottom waters) together with low nitrate concentrations in the overlying water column (recall that $v_{fNO_3^-}$ is the ratio of nitrate benthic flux and in-stream nitrate concentration).

3.6.3. What Is the Relative Importance of Direct Denitrification Versus Coupled Nitrification-Denitrification?

Nitrogen removal in bedforms can occur through direct denitrification (denitrification of stream nitrate) and/or coupled nitrification-denitrification (nitrification of stream and/or sediment ammonium followed by denitrification of the produced nitrate). To determine their relative importance, a denitrification velocity was calculated as follows [*Stream Solute Workshop,* 1990]: $v_{fden} = 2U_{N_2} / C_{NO_3^-}(0)$, where the factor of 2 accounts for the fact that two molecules of nitrate are consumed for every one molecule of di-nitrogen gas produced by denitrification. Because sediments can only be a source of N_2 (from denitrification) the denitrification velocity will always be positive ($v_{fden} > 0$). As illustrated in **Figure 3.3A**, the denitrification velocity depends sensitively on the Consistent with the results presented by Zarnetske et al. [2012], the transition to net denitrification occurs around $\mathbf{Da} \approx 1$ (although the exact transition value for $\mathbf{Da}$ varies by environment, **Figure 3.3A**).

The relative importance of direct denitrification and coupled nitrification-denitrification can be ascertained from the limiting value of v_{fden}. When all stream nitrate entering a bedform is denitrified (and coupled nitrification-denitrification can be neglected), the flux of nitrate into the sediment bed is mass-transfer limited: $U_{NO_3^-} = -k_m C_{NO_3^-}(0)$. For every molecule of nitrate denitrified, one-half molecules of N_2 gas are formed. Thus, the corresponding mass transfer-limited flux of nitrogen gas out of the sediment bed is:

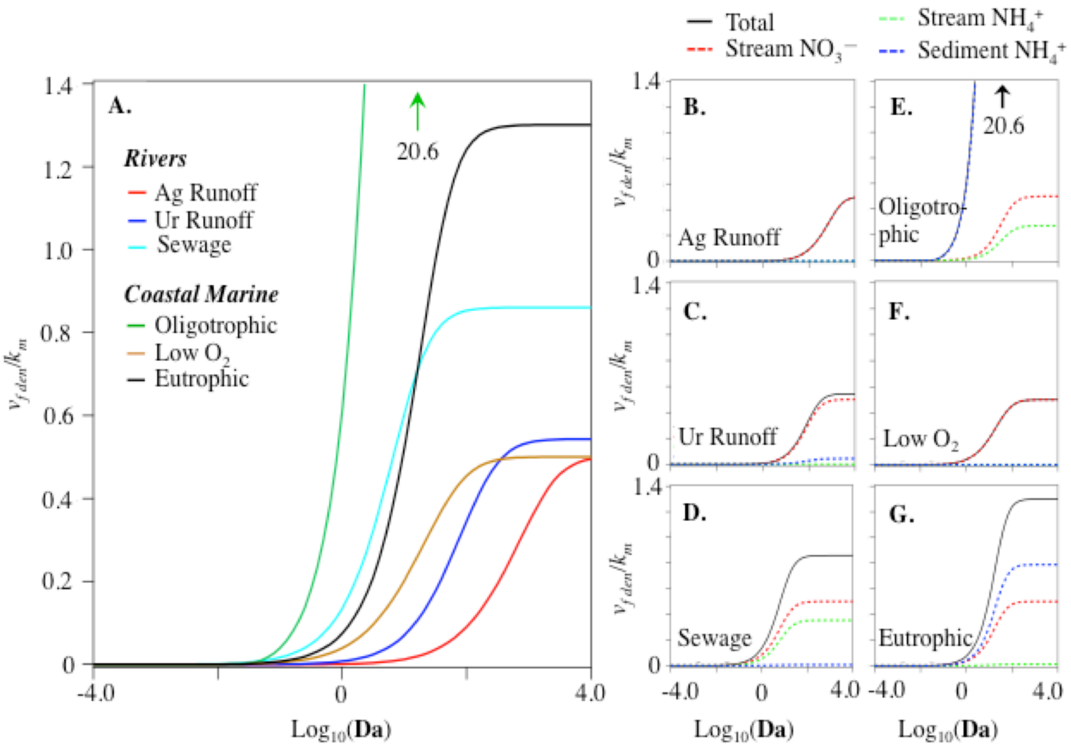

Figure 3.3. Same as Figure 3.2, except that the denitrification uptake velocity (v_{fden}) is plotted instead of total uptake velocity of nitrate ($v_{fNO_3^-}$).

$U_{N_2} = (k_m/2)C_{NO_3^-}(0)$. Substituting this last result into the definition of v_{fden} we arrive at the maximum denitrification velocity that can be achieved with direct-denitrification alone: $v_{fden}/k_m \rightarrow 1.0$. This is precisely the limiting value observed in the two environments where nitrification rates are low (agricultural runoff and low-O$_2$ marine waters, red and brown curves, **Figure 3.3A**). In the other four environments the limiting value of v_{fden}/k_m exceeds one, implying that at least some of the nitrogen loss can be attributed to coupled nitrification-denitrification (dark blue, light blue, black, and green curves, **Figure 3.3A**).

To obtain more detailed information on denitrification pathways, we evaluated the contribution of different nitrogen sources to the denitrification velocity. As expected, in the two environments with low nitrification rates (agricultural runoff and low-O_2 marine waters) all N_2 gas production can be attributed to direct denitrification of stream nitrate (i.e., the red dashed and black curves overlap, **Figure 3.3B**,**F**). In the remaining marine environments (oligotrophic and eutrophic), dinitrogen gas is formed from coupled nitrification-denitrification of sediment ammonium (produced from respiration of sediment organic material), direct denitrification of stream nitrate, and coupled nitrification-denitrification of stream ammonium (**Figure 3.3E**,**G**). Direct denitrification of stream nitrate dominates nitrogen removal in the urban runoff-impacted and sewage-impacted streams, with secondary contributions from coupled nitrification-denitrification of stream ammonium (sewage-impacted stream) or sediment ammonium (urban-impacted stream) (**Figure 3.3C**,**D**). In summary, under the right conditions, the PASS model suggests that coupled nitrification-denitrification can be an important pathway for nitrogen removal in bedforms, and even dominates in settings where stream nitrate concentrations are low (oliogotrophic and eutrophic marine waters). This conclusion – that coupled nitrification-denitrification dominates in the overlying water column—is consistent with field observation in lake, river, estuary, coastal, and continental shelf sediments [Seitzinger et al., 2006].

3.6.4. Are Bedforms Net Sources or Sinks of Dissolved Inorganic Nitrogen?

To determine if bedforms generate more nitrate (by ammonification) than they remove (by dentrification) we calculated for each environment the dissolved inorganic nitrogen

(DIN) uptake velocity: $v_{fDIN} = v_{fNO_3^-} + v_{fNH_4^+}$, where $v_{fNH_4^+} = U_{NH_4^+} / C_{NO_3^-}(0)$. In all cases, the DIN uptake velocity is greater than zero ($v_{fDIN} \geq 0$, **Figure B.8**) implying that bedforms are a net source of DIN. It should be noted that the PASS model presented here assumes ammonification occurs at a constant rate throughout the sediment column (this was done so that we could directly compare PASS model results to the numerical flume results reported by Kessler, see earlier discussion). The sediments might have produced less DIN (and perhaps even been a net sink of DIN for some values of the Damköhler number) in the more realistic case where ammonification declines with depth [Kessler et al., 2012; Evrard et al., 2013].

3.7. Dependence of Denitrification Velocity on In-Stream Nitrate Concentration

In a recent study of nitrogen cycling in 49 streams across the U.S., Mulholland et al. [2008] reported that the denitrification velocity declines as a power-law of in-stream nitrate concentration:

$$v_{fden} = 0.001 \times C_{NO_3^-}(0)^{-b} \text{ , } b = 0.5 \tag{10}$$

This finding is significant because it implies a stream's ability to process and remove nitrate (an important ecosystem service) is diminished as the nitrate concentration in a stream increases (e.g., due to increased loading of nitrate from agricultural runoff). Provided that nitrification and oxygen inhibition of denitrification are negligible, two exact solutions for v_{fden} can be derived from the PASS model in the limits where in-stream nitrate concentration is much larger or smaller than the half-saturation constant for denitrification (derivation in **Text B.10** of **Appendix B**):

$$v_{fden} = k_m G\left(\frac{\mathbf{Da}\,\kappa K_{O_2}^{sat}}{K_{NO_3^-}^{sat}}\right) \propto C_{NO_3^-}(0)^0, \quad C_{NO_3^-}(0) << K_{NO_3^-}^{sat} \tag{11a}$$

$$v_{fden} = \frac{57.6 k_m \mathbf{Da}\,\kappa K_{O_2}^{sat}}{C_{NO_3^-}(0)} \propto C_{NO_3^-}(0)^{-1}, \quad C_{NO_3^-}(0) \gg K_{NO_3^-}^{sat} \tag{11b}$$

The function $G(v)$ appearing in equation (11a) is an integral expression that can be evaluated numerically for any choice of the independent variable $v = \mathbf{Da}\kappa K_{O_2}^{sat} \big/ K_{NO_3^-}^{sat}$ (see the **Appendix B**). These two limits imply that denitrification velocity will decline with increasing in-stream nitrate concentration (consistent with Mulholland's empirical correlation). However, instead of a single-power-law exponent b (as in equation (10)), the PASS model predicts that the power-law exponent transitions from $b=0$ to $b=1$ in the limit of large in-stream nitrate concentration. These two exponent limits bracket error bounds for Muholland's single power-law exponent (95% and 5% confidence values of $b=0.2$ and 0.7, respectively) computed using nonparametric bootstrap techniques (see **Text B.11** in **Appendix B**). Thus, our PASS model predictions are consistent with Mulholland's empirical correlation, at least within the scatter of Muholland's data set and the assumptions employed to derive equations (11a) and (11b). Importantly, the PASS model provides a mechanism for Mulholland's observation that v_{fden} declines with $C_{NO_3^-}(0)$: the change in exponent value corresponds to a transition in the denitrification rate from first-order at low nitrate concentrations ($C_{NO_3^-}(0) << K_{NO_3^-}^{sat}$, $b=0$) to zero-order at high nitrate concentrations ($C_{NO_3^-}(0) >> K_{NO_3^-}^{sat}$, $b=1$) (see equation (6d)). Indeed, the in-stream nitrate concentrations reported by Mulholland (average 0.04 mol m^{-3}, range 0 to 1.51 mol m^{-3}) straddle values of $K_{NO_3^-}^{sat}$ adopted earlier for sewage-, agricultural-, and urban- impacted streams (0.002, 0.01, and 0.02 mol m^{-3}, see **Table B.1**). Thus, both first-order and zero-order denitrification kinetics were likely represented in the streams Mulholland selected for their study.

As noted by Mulholland et al. [2008], the fraction $f_{NO_3^-}$ of nitrate mass loading removed over a stream reach can be calculated from the nitrate uptake velocity v_f , the volumetric flow rate Q , and sediment bed surface area SA : $f_{NO_3^-} = 1 - e^{-vf\,SA/Q}$. The degree to which a stream network removes nitrate from the terrestrial landscape will therefore depend on the topology of the stream network (i.e., how the stream reaches are organized within the watershed) as well as hydraulic and chemical features of the stream that affect v_f (the focus of the present chapter). It remains an open question how these three factors—stream topology, hydraulics, and chemistry—collectively influence the removal of nitrate in natural and urban catchments. Mulholland et al. also noted that a significant fraction of stream nitrate uptake was associated with storage in the sediment bed, either in the form of biomass or particulate material. Incorporating kinetics for nitrate storage into the PASS model is therefore an obvious target for future research.

3.8. Model Limitations and Future Directions

Beyond the limitations already noted, the PASS model does not account for a number of processes known to affect nitrogen budgets in aquatic systems. We plan to address three such limitations in future evolutions of the model: (1) influence of flow fields operating over different scales (e.g., bedform exchange coupled with regional upwelling of groundwater); (2) formation of redox microzones in heterogeneous sediments; and (3) spatially variable patterns of organic carbon and respiration rates. First, Boano and co-workers demonstrated that the superposition of groundwater-stream interactions (e.g., associated with gaining or losing streams) alters the RTD of bedform exchange, in part by limiting the depth over which bedform exchange can occur [Boano et al., 2008, 2009]. Thus, upwelling groundwater, for example, could affect nitrate concentrations in rivers both directly by adding nitrate (if the groundwater is contaminated with nitrate) and indirectly by altering the biogeochemical transformations that depend on the RTD of water parcels in the sediment (note that nitrate flux into the sediment depends explicitly on the hyporheic zone RTD, see equation (9b)). Second, bedforms are heterogeneous relative to sediment grain sizes [Cardenas et al., 2004] and flowpaths [Menichino et al., 2014,2015]. This heterogeneity can lead to mixing across streamlines [Sawyer, 2014; Triska et al., 1989] and facilitate the formation of redox microzones (e.g., localized pockets of denitrification embedded within well-oxygenated downwelling regions) that enhance coupled nitrification-denitrification and overall nitrate removal rates in natural sediments [Briggs et al., 2015; Sawyer, 2014]. Third, organic carbon and microbial respiration rates are spatially variable, not homogeneous as assumed in the present modeling effort. For example, bulk organic carbon concentration often declines with depth into the sediment bed [Cook et al., 2006] and/or can be locally concentrated, for example, in the form of buried fecal pellets [Jørgensen, 1977].

Appendix B. Derivations and supplemental figures and tables

References

A model set-up for an oxygen and nutrient flux model for Aarhus Bay (Denmark) (2004), NERI Technical Report No. 483; National Environmental Research Institute, Denmark.

Bardini, L.; Boano, F.; Cardenas, M. B.; Revelli, R.; Ridolfi, L. Nutrient Cycling in Bedform Induced Hyporheic Zones (2012), Geochim. Cosmochim. Acta, 84, 47–61.

Berg, P.; Long, M.H.; Huettel, M.; Rheuban, J.E.; McGlathery, K.J.; Howarth, R.W.; Foreman, K.H.; Giblin, A.E.; Marino, R. (2013), Eddy Correlation Measurements of Oxygen Fluxes in Permeable Sediments Exposed to Varying Current Flow and Light. Linol. Oceangr., 58, 1329-1343.

Boano, F; Revelli, R; Ridolfi, L. (2008), Reduction of the hyporheic zone volume due to the stream-aquifer interaction. Geophys. Res. Lett., 35, L09401, doi: 10.1029/2008GL033554.

Boano, F; Revelli, R; Ridolfi, L. (2009), Quantifying the impact of groundwater discharge on the surface-subsurface exchange. Hydrol. Process, 23, 2108-2116.

Boano, F.; Harvey, J.; Marion, A.; Packman, A.I.; Revelli, R.; Ridolfi, L.; Worman, A. (2014), Hyporheic Flow and Transport Processes: Mechanisms, Models, and Biogeochemical Implications. Rev. Geophys, 52, 1-77.

Briggs, M.A.; Day-Lewis, F.D.; Arnetske; J.P.; Harvey, J.W. (2015), A physical explanation for the development of redox microzones in hyporheic flow. Geophys. Res. Lett., 42, doi:10.1002/2015GL064200.

Brunke, M.; Gonser, T. (1997), The Ecological Significance of Exchange Processes between Rivers and Groundwater. Freshw. Biol., 37, 1–33.

Cardenas, M. B.; Wilson, J. L.; Zlotnik, V. A. (2004), Impact of heterogeneity, bed forms, and stream curvature on subchannel hyporheic exchange. Water Resour. Res., 40, W08307, doi: 10.1029/2004WR003008.

Cardenas, M. B.; Wilson, J. L. (2007), Dunes, Turbulent Eddies, and Interfacial Exchange with Permeable Sediments. Water Resour. Res., 43, W08412.

Cardenas, M. B. and Jiang, H. (2011), Wave-driven porewater and solute circulation through rippled elastic sediment under highly transient forcing, Limon. Oceanog. : Fluids and Environments, 1, 23-37, doi:10.1215/21573698.

Cook, P. L. M., F. Wenzhofer, S. Rysgaard, O.S. Galaktionov, F.J.R. Meysman, B.D. Eyre, J. Cornwell, M. Huettel, and R.N. Glud (2006), Quantification of denitrification in permeable sediments : Insights from a two-dimensional simulation analysis and experimental data, Limnol. Oceanogr. Methods, 4, 294–307.

David, M.; Wall, L.; Royer, T.; Tank, J. (2006), Denitrification and the Nitrogen Budget of a Reservoir in an Agricultural Landscape. Ecol. Appl., 16, 2177–2190.

David, A.; Perrin, J.L.; Rosain, D.; Rodier, C.; Picot, B.; Tournoud, M.G. (2011), Implications of Two In-Stream Processes in the Fate of Nutrients Discharged by Sewage Systems into a Temporary River. Environ. Monit. Assess., 181, 491-507.

Elliott, A. H.; Brooks, N. H. (1997), Transfer of Nonsorbing Solutes to a Streambed with Bed Forms: Laboratory Experiments. Water Resour. Res., 33, 137–151.

Elliott, A. H.; Brooks, N. H. (1997), Transfer of Nonsorbing Solutes to a Streambed with Bed Forms: Theory. Water Resour. Res., 33, 123–136.

Evrard, V., Glud, R.N.; Cook, P.L.M. (2013), The kinetics of denitrification in permeable sediments. Biogeochemistry, 113, 563-572.

Fischer, H.; List, J.; Koh, C.; Imberger, J.; Brooks, N. (1979), Mixing in inland and coastal waters, Academic Press: San Diego, New York, Boston, London, Sydney, Tokyo, Toronto.

Galloway, J.N., F.J. Dentener, D.G. Capone, E.W. Boyer, R.W. Howarth, S.P. Seitzinger, G.P. Asner, C.C. Clevland, P.A. Green, E.A. Holland, D.M. Karl, A.F. Michaels, J.H. Porter, A.R. Townsend, and C. J. Voosmarty (2004), Nitrogen Cycles: Past, Present, and Future, Biogeochemistry, 70, 153–226.

Gandy, C. J.; Smith, J. W. N.; Jarvis, A. P. (2007), Attenuation of Mining-Derived Pollutants in the Hyporheic Zone: A Review. Sci. Total Environ., 373, 435–446.

Grant, S. B.; Litton-Mueller, R. M.; Ahn, J. H. (2011), Measuring and Modeling the Flux of Fecal Bacteria across the Sediment-Water Interface in a Turbulent Stream. Water Resour. Res., 47, W05517.

Grant, S. B.; Marusic, I. (2011), Crossing Turbulent Boundaries: Interfacial Flux in Environmental Flows. Environ. Sci. Technol., 45, 7107–7113.

Grant, S. B.; Stolzenbach, K.; Azizian, M.; Stewardson, M. J.; Boano, F.; Bardini, L. (2014), First-Order Contaminant Removal in the Hyporheic Zone of Streams: Physical Insights from a Simple Analytical Model. Environ. Sci. Technol., 48, 11369-11378.

Haggard, B.E.; Stanley, E.H.; Storm, D.E. (2005), Nutrient Retention in a Point-Source-Enriched Stream. J. N. Am. Benthol. Soc., 24, 29-47.

Hall, S. J. (2002), The Continental Shelf Benthic Ecosystem: Current Status, Agents for Change and Future Prospects. Environ. Conserv., 29, 350–374.

Hester, E.T.; Gooseff, M.N. (2010), Moving beyond the banks: hyporheic restoration is fundamental to restoring ecological services and functions of streams. Environ. Sci. Technol., 44, 1521-1525.

Hill, C.G. (1977), An Introduction to Chemical Engineering Kinetics and Reactor Design, Chapter 11, John Wiley and Sons: New York, U.S..

Howarth, R.W.; et al. (1996), Regional Nitrogen Budgets and Riverine N and P Fluxes for the Drainages to the North Atlantic Ocean: Natural and Human Influences. Biogeochemistry, 35, 75-139.

Howarth, R.; Sharpley, A.; Walker, D. (2002), Sources of Nutrient Pollution to Coastal Waters in the United States: Implications for Achieving Coastal Water Quality Goals. Estuaries, 25, 656–676.

Huettel, M.; Berg, P.; Kostka, J. E. (2014), Benthic Exchange and Biogeochemical Cycling in Permeable Sediments. Ann. Rev. Mar. Sci., 6, 23–51.

Janssen, F.; Cardenas, M.B.; Sawyer, A.H.; Dammrich, T.; Krietsch, J. de Beer, D. (2012), A comparative experimental and multiphysics computational fluid dynamics study of coupled surface-subsurface flow in bedforms. Water Resour. Res., 48, W08514, doi: 10.1029/2012WR011982.

Jørgensen, B. B. (1977), Bacterial sulfate reduction within reduced microniches of oxidized marine sediments, Mar. Biol., 41(1), 7–17.

Kessler, A.J.; Glud, R.N.; Cardenas, M.B.; Larsen, M.; Bourke, M.F.' Cook, P.L.M. (2012), Quantifying Denitrification in Rippled Permeable Sands through Combined Flume Experiments and Modeling. Limnol. Oceanogr., 57, 1217-1232, doi:10.4319/lo.2012.57.4.1217.

Kessler, A.J.; Glud, R.N.; Cardenas, M.B.; Cook, P.L.M. (2013), Transport Zonation Limits Coupled Nitrification-Denitrification in Permeable Sediments. Environ. Sci. Technol., 47, 13404-13411.

Lawrence, J.E.; Skold, M.E.; Hussain, F.A.; Silverman, D.R.; Resh, V.H.; Sedlak, D.L.; Luthy, R.G.; McCray, J. E. (2013), Hyporheic Zone in Urban Streams: A Review and Opportunities for Enhancing Water Quality and Improving Aquatic Habitat by Active Management. Environ. Eng. Sci., 30, 480-501.

Levenspiel, O. (1972), Chemical Reaction Engineering, Wiley: New York, U.S..

Litton, R.M.; Ahn, J.H.; Sercu, B.; Holden, P.A.; Sedlak, D.L.; Grant, S.B. (2010), Evaluation of Chemical, Molecular, and Traditional markers of Fecal Contaminantion in an Effluent Dominated Urban Stream. Environ. Sci. Technol., 44, 7369-7375.

Marchant, H.K.; Lavik, G.; Holtappels, M.; Kuypers, M.M.M. (2014), The fate of nitrate in intertidal permeable sediments PLoS One, 9, e104517.

Marzadri, A.; Tonina, D.; Bellin, A. (2011), A Semianalytical Three-Dimensional Process-Based Model for Hyporheic Nitrogen Dynamics in Gravel Bed Rivers. Water Resour. Res., 47, W11518.

Menichino, G. T.; Ward, A. S.; Hester, E. T. (2014), Macropores as preferential flow paths in meander bends, Hydrol. Process., 28, 482-495.

Menichino, G. T.; Scott, D. T.; Hester, E. T. (2015), abundance and dimensions of naturally occuring macropores along stream channels and the effects of artificially constructed large macropores on transient storage. Freashwater Science, 34, 125-138.

Meysman, F. J. R.; Galaktionov, O. S.; Cook, P. L. M.; Janssen, F.; Huettel, M.; Middelburg, J. J. (2007), Quantifying Biologically and Physically Induced Flow and Tracer Dynamics in Permeable Sediments. Biogeosciences, 4, 627–646.

Mulholland, P.J., A. M. Helton, G. C. Poole, R. O. Hall Jr, S K. Hamilton, B. J. Peterson, J. L. Tank, L. R. Ashkenas, L. W. Cooper, C. N. Dahm, W. K. Dodds, S. E. G. Findlay, S. V. Gregory, N. B. Grimm, S. L. Johnson, W. H. McDowell, J. L. Meyer, H. M. Valett, J. R. Webster, C. P. Arango, J. J. Beaulieu, M. J. Bernot, A. J. Burgin, C. L. Crenshaw, L. T. Johnson, B. R. Niederlehner, J. M. O'Brien, J. D. Potter, R. W. Sheibley, D. J. Sobota, and S. M. Thomas (2008), Stream denitrification across biomes and its response to anthropogenic nitrate loading. Nature, 452, 202-205.

Pinay, G.; O'Keefe, T. C.; Edwards, R. T.; Naiman, R. J. (2009), Nitrate Removal in the Hyporheic Zone of a Salmon River in Alaska. River Res. Appl., 25, 367–375.

Potter, J.D.; McDowel, W.H.; Helton, A.M.; Daley, M.L. (2014), Incorporating urban infrastructure into biogeochemical assessment of urban tropical streams in Puerto Rico. Biogeocehmistry, 121, 271-286.

Rutherford, J.C.; Boyle, J.D.; Elliott, A.H.; Hatherell, T.V.J.; Chiu, T.W. (1995), Modeling benthic oxygen uptake by pumping. ASCE J. Environ. Eng., 121, 84-95.

Sawyer, A.H. (2014), Enhanced removal of groundwater-borne nitrate in heterogeneous aquatic sediments. Geophys. Res. Lett., 42, 403-410.

Santos, I. R.; Eyre, B. D.; Huettel, M. (2012), The Driving Forces of Porewater and Groundwater Flow in Permeable Coastal Sediments: A Review. Estuar. Coast. Shelf Sci., 98, 1–15.

Searcy, E.; Packman, A.I.; Atwill, E.R.; Harter, T. (2006), Deposition of Cryptosporidium Oocysts in Streambeds. Appl. Environ. Microbiol., 72, 1810-1816.

Seitzinger, S.; Harrison, J. A.; Bohlke, J. K.; Bouwman, A. F.; Lowrance, R.; Peterson, B.; Tobias, C.; Van Dretch, G. (2006), Denitrification across landscapes and waterscapes: a synthesis. Ecological Applications, 16 (6), 2064-2090.

Sinigalliano, C.D.; Gidley, M.L.; Shibata, T.; Whitman, D.; et al. (2007), Impacts of Hurricanes Katrina and Rita on the Microbial Landscape of the New Orleans Area. Proceedings of the National Academy of Sciences USA, 104, 9029-9034.

Stonedahl, S. H.; Harvey, J. W.; Wörman, A.; Salehin, M.; Packman, A. I. (2010), A Multiscale Model for Integrating Hyporheic Exchange from Ripples to Meanders. Water Resour. Res., 46, W12539.

Stonedahl, S. H.; Harvey, J. W.; Detty, J.; Aubeneau, A.; Packman, A. I. (2012), Physical Controls and Predictability of Stream Hyporheic Flow Evaluated with a Multiscale Model. Water Resour. Res., 48, W10513.

Stream Solute Workshop (1990), Concepts and Methods for Assessing Solute Dynamics in Stream Ecosystem. J. N. Am. Benthol. Soc., 9, 95-119.

Triska, F. J.; Kennedy, V. C.; Avanzino, R. J.; Zellweger, G. W.; Bencala, K. E. (1989), Retention and transport of nutrients in a third-order stream in northwestern California: Hyporheic processes. Ecology, 70 (6), 1893-1905.

Young, B. a.; Norris, R. H.; Sheldon, F. (2011), Is the Hyporheic Zone a Refuge for Macroinvertebrates in Drying Perennial Streams? Mar. Freshw. Res., 62, 1373-1382.

Zarnetske, J. P.; Haggerty, R.; Wondzell, S. M.; okil, V.A.; Gonzales-Pinzon, R. (2012), Coupled transport and reaction kinetics control the nitrate source-sink function of hyporheic zones. Water Resour. Res.,48, W11508.

Chapter 4

Ambient Groundwater Flow Diminishes Nitrate Processing in the Hyporheic Zone of Streams[1]

Abstract

Modeling and experimental studies demonstrate that ambient groundwater reduces hyporheic exchange, but the implications of this observation for stream N-cycling is not yet clear. Here we utilize a simple process-based model (the Pumping and Streamline Segregation or PASS model) to evaluate N-cycling over two scales of hyporheic exchange (fluvial ripples and riffle-pool sequences), ten ambient groundwater and stream flow scenarios (five gaining and losing conditions and two stream discharges), and three biogeochemical settings (identified based on a principal component analysis of previously published measurements in streams throughout the United States). Model-data comparisons indicate that our model provides realistic estimates for direct denitrification of stream nitrate, but overpredicts nitrification and coupled nitrification-denitrification. Riffle-pool sequences are responsible for most of the N-processing, despite the fact that fluvial ripples generate 3-11 times more hyporheic exchange flux. Across all scenarios, hyporheic exchange flux and the Damköhler number emerge as primary controls on stream N-cycling; the former regulates trafficking of nutrients and oxygen across the sediment-water interface, while the latter quantifies the relative rates of organic carbon mineralization and advective transport in streambed sediments. Vertical groundwater flux

---

[1] A version of this chapter was published as [Azizian, M.; F. Boano; P.L.M. Cook; R. Detwiler; M.A. Rippy; S. B. Grant (2017), Ambient Groundwater Flow Diminishes Nitrate Processing in Hyporheic Zone of Streams, Water Resources Research, 53(5),3941-3967, doi:10.1002/2016WR020048].

modulates both of these master variables in ways that tend to diminish stream N-cycling. Thus, anthropogenic perturbations of ambient groundwater flows (e.g., by urbanization, agricultural activities, groundwater mining, and/or climate change) may compromise some of the key ecosystem services provided by streams.

4.1. Introduction

Humans more than doubled the annual terrestrial input of bioavailable nitrogen over the past century, from 155 Tg N y^{-1} in 1900 to 345 Tg N y^{-1} in 2000 [Galloway et al., 2004; Seitzinger et al., 2006]. This number is projected to increase another 18-48% (from 408 to 510 Tg N y^{-1}) by the year 2030 [Bouwman et al., 2005]. Much of this anthropogenic nitrogen finds its way to rivers and streams through point and non-point source pollution, including return flows from irrigated agriculture, runoff from confined animal feeding operations, septic tank leachates, and partially treated municipal wastewater discharges, to name a few [Jongbloed and Lenis, 1998; Carey and Migliaccio, 2009; Morée et al., 2013]. As nitrate loading increases, streams less efficiently remove nitrate by biological assimilation and denitrification [Bernot and Dodds, 2005; Mulholland et al., 2008] and disproportionately more nitrate escapes to downstream receiving waters where it threatens both human and ecosystem health [Smith et al., 1999; Powlson et al., 2008; Canfield et al., 2010]. An alarming example is currently playing out in the Gulf of Mexico, where nitrate discharged from the Mississippi and Atchafalaya Rivers is responsible, at least in part, for a seasonal hypoxic region (or "dead zone") the size of the U.S. State of Connecticut [Coppess, 2016].

As nitrogen is transported downstream upwards of 70% is removed from the stream by biological assimilation and denitrification [Peterson et al., 2001; Galloway et al., 2004; Birgand et al., 2007], and much of this ecosystem service is thought to occur in the hyporheic zone [Groffman et al., 2005; Bohlke et al., 2009; Zarnetske et al., 2011, 2012; Kiel and Cardenas, 2014] and riparian zone [McClain et al., 2003]. The hyporheic zone is often defined as the portion of the streambed where hydrological flow paths start and terminate at the stream [Gooseff, 2010; Boano et al., 2014]. The cycling of water, oxygen, and nutrients between the stream and hyporheic zone ("hyporheic exchange") drives a number of biological processes that influence stream water quality, including stream nitrate concentrations [Huettel et al., 2014; Rode et al., 2015]. Water and solutes are "pumped" into and out of the sediment by static and dynamic pressure variations over the sediment-water interface [Thibodeaux and Boyle, 1987; Grant and Marusic, 2011; Boano et al., 2014]. Water and mass move from the stream to the sediment in high-pressure regions (downwelling zones) and from the sediment to the stream in low-pressure regions (upwelling zones). Hyporheic exchange can also occur due to variations in streambed hydraulic conductivity [Herzog et al., 2015], bed form migration [Rutherford et al., 1993; Elliott and Brooks, 1997a, 1997b; Ahmerkamp et al., 2015], and bioirrigation [Vaughn and Hakenkamp, 2001; Meysman et al., 2006a, 2006b].

The pumping of water through submerged ripples and riffle-pool sequences, in particular, appears to dominate hyporheic exchange fluxes and nutrient turnover in many streams [Gomez-Velez and Harvey, 2014; Gomez-Velez et al., 2015]. Because hyporheic exchange across ripples and riffle-pool sequences occurs over different time scales (minutes-to-hours versus hours-to-days, respectively) [Boano et al., 2014], these two bed form scales could also serve different functional roles relative to N-cycling; e.g., producing nitrate at one scale and consuming nitrate at another, depending on the local balance between transport and respiration rates [Groffman et al., 2005; Zarnetske et al., 2011,2012; Azizian et al., 2015].

At the reach scale, the net removal (or generation) of stream nitrate can be quantified with the nitrate uptake velocity (v_f , units m s^{-1}), defined here as the flux of nitrate out of the streambed divided by the nitrate concentration in the stream [Stream Solute Workshop, 1990; Wollheim et al., 2006]. The nitrate uptake velocity is favored over other metrics of nitrate attenuation (e.g., the uptake length scale) [Peterson et al., 2001], because it isolates the influence of biological processes on nitrate removal in the streambed [Wollheim et al., 2006]. In a review of nitrate pollution in agriculturally impacted streams, Birgand et al. [2007] concluded that the uptake velocity "is a powerful concept that should be henceforth commonly used in studies of nitrogen removal" (pg. 469). For the sign convention adopted here, the nitrate uptake velocity is negative (or positive) when the streambed is a sink (or a source) of nitrate, respectively.

There is an urgent need for modeling tools that can provide realistic estimates for the nitrate uptake velocity in support of regulatory, ecological, and sustainability goals, including implementation of total maximum daily loads for nitrogen impaired streams [French et al., 2006], stream restoration efforts to improve the retention and removal of bioavailable nitrogen [Craig et al., 2008], and long-term forecasts of the effects of land-use and climate change on water resources at the watershed scale [Grathwohl et al., 2013]. To this end, several process-based models for v_f have been proposed, but these: (1) do not consider the multiscale nature of hyporheic exchange flows and, in particular, the impact of ambient groundwater flow on hyporheic exchange; (2) rely on simplified conceptualizations of mixing within streambed sediments (e.g., a well-mixed box); (3) neglect important steps in the N-cycle (e.g., nitrification and ammonification); and/or (4) adopt pseudo-first-order kinetic descriptions of denitrification [Stream Solute Workshop, 1990; Runkel, 2007; Yang and Wang, 2010]. The first limitation is particularly concerning given that groundwater resources are increasingly under stress from urbanization, agricultural activities, groundwater mining, and climate change [Walsh et al., 2005; Green et al., 2011; Askarizadeh et al., 2015]. The effects of ambient groundwater flow on in-stream ecosystem services are largely unknown [Boulton et al., 2010; Grathwohl et al., 2013; Wondzell, 2015].

In this chapter, we develop and test a simple and scalable process-based model for estimating the nitrate uptake velocity that addresses the limitations identified above. In particular, our model accounts for: (1) hyporheic exchange at multiple scales together with ambient groundwater flow in gaining or losing streams; (2) the broad residence time distributions characteristic of hyporheic exchange; (3) key biogeochemical reactions associated with N-cycling, including respiration, ammonification, nitrification, and denitrification; and (4) the nonlinear nature of the pertinent biogeochemical reaction rates, including Monod kinetics for aerobic respiration and denitrification, and second-order kinetics for nitrification. Using this modeling framework we systematically evaluate how changing ambient groundwater flow is likely to affect N-cycling in the hyporheic zone of streams, and compare our predictions to previously published reach-scale measurements of nitrate removal.

The chapter is organized as follows. We begin by presenting our modeling framework, which we refer to as the Pumping and Streamline Segregation or PASS model (**section 4.2**). Information needed to implement the PASS model is then described, including (1) a biokinetic model for the evolution of nitrate concentration with travel time through the hyporheic zone (**section 4.3**); (2) physical models for the hyporheic exchange of water through ripples and riffle-pool sequences (**section 4.4**); and (3) physical models for the residence time distributions associated with these two bed form scales (**section 4.5**). These results are then combined through the PASS modeling framework to predict nitrate uptake velocities for a variety of scenarios related to stream chemistry, bed form scale, stream discharge, and ambient groundwater flow (**section 4.6**). We end with a discussion of how these nitrate uptake velocity predictions might be scaled-up to watersheds (**section 4.7**) and model limitations and future directions (**section 4.8**).

4.2. Pumping and Streamline Segregation (PASS) Model for Nitrate Uptake

4.2.1. PASS Model Formulation

Numerous studies have documented that advection is the dominant mechanism by which mass is exchanged across the sediment-water interface in permeable streambeds, defined as streambeds with permeability $>10^{-12}$ m [Grant and Marusic, 2011; Kessler et al., 2013a, 2013b; Boano et al., 2014; Huettel et al., 2014]. Here we conceptualize this advective exchange as flow through a bundle of small diameter tubes (referred to as hyporheic zone tubes or HZTs) that collectively represent the various flow paths stream water takes as it moves through the hyporheic zone (**Figure 4.1**). Biogeochemical reactions in the sediment cause nutrient and oxygen concentrations to evolve continuously along the HZTs; e.g., sediment-associated microbial biofilms consume oxygen, causing the oxygen concentration in a water parcel to decline with travel time through the hyporheic zone [Zarnetske et al., 2011, 2012; Kessler et al., 2013a, 2013b]. As a water parcel exits the HZT and returns to the stream, its final nitrate concentration (denoted here by the function $C_{\text{HZT-NO}_3^-}(\tau;\text{"chemistry"})$, units mol m^{-3}) will depend on the water parcel's travel time through the hyporheic zone (τ, units s) conditioned on subsurface biogeochemical reactions that consume and produce nitrate (denoted here by the shorthand "chemistry"). Provided there is no mixing of mass across or within HZTs (i.e., mass transport occurs only by advection through the HZT, discussed further in **section 4.2.2**), mass balance over a single submerged and periodic bed form yields the PASS model for nitrate uptake velocity [Rutherford et al., 1993, 1995; Grant et al., 2014; Azizian et al., 2015; Tonina et al., 2015]:

$$v_{\text{f}} = q_{\text{H}}\left[\bar{C}_{\text{HZT-NO}_3^-} - 1\right] \tag{1a}$$

$$\bar{C}_{\text{HZT-NO}_3^-} = \frac{1}{C_{\text{S-NO}_3^-}}\int_0^\infty C_{\text{HZT-NO}_3^-}(\tau;\text{"chemistry"}) \times E(\tau)\,d\tau \tag{1b}$$

Variables appearing in these equations include: (1) the volume of stream water pumped through the hyporheic zone per streambed area per time ("hyporheic exchange flux", q_{H}, units m s^{-1}); (2) the residence time distribution (RTD) of water in the hyporheic zone $E(\tau)$ (units s^{-1}), where $E(\tau)d\tau$ represents the fraction of hyporheic exchange flux with a

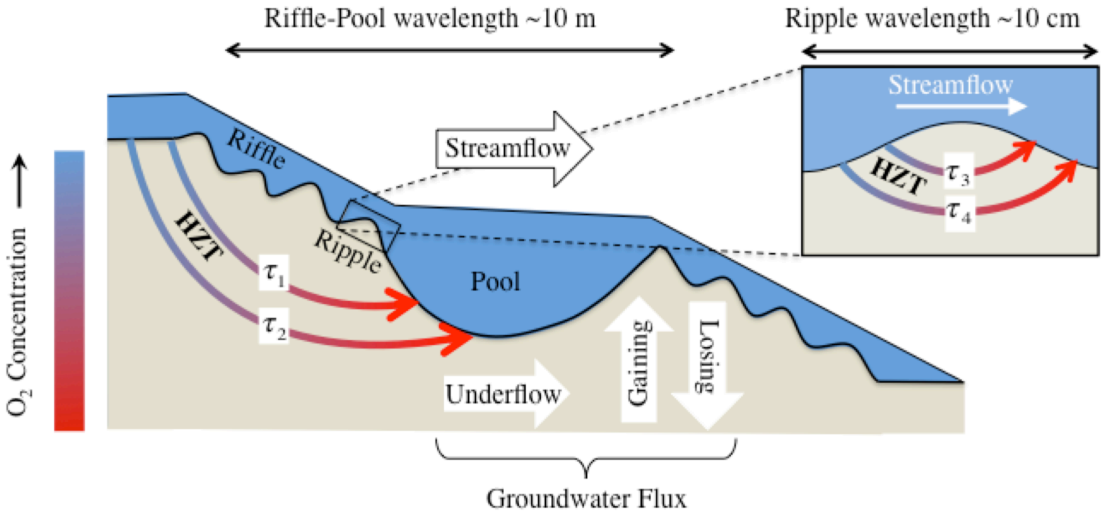

Figure 4.1. Hyporheic exchange and ambient groundwater flux influence nitrogen cycling in the hyporheic zone of a stream. Here, ambient groundwater flux has both vertical (gaining or losing) and horizontal (underflow) components. Hyporheic zone tubes (HZTs) with different residence times (denoted by the labels τ_1 through τ_4) represent the various flow paths stream water takes as it undergoes hyporheic exchange through submerged bed forms. Two submerged bed form scales are illustrated here: riffle-pool sequences (wavelength ~10 m) and fluvial ripples (wavelength ~10 cm). As water travels through a HZT, microbial respiration of organic carbon consumes oxygen and creates anoxic conditions favorable for denitrification, as indicated by the transition in color from blue to red.

HZT travel time within $d\tau$ of τ [Levenspiel, 1972; Hill, 1977]; (3) the stream nitrate concentration $C_{\text{S-NO}_3^-}$ (units mol m^{-3}); and (4) the normalized "breakthrough" concentration of nitrate in an upwelling zone ($\bar{C}_{\text{HZT-NO}_3^-}$, unitless). The last quantity is calculated from the ratio of the flow-weighted nitrate concentration returning to the stream in an upwelling zone (integral term in equation (1b)) and the stream nitrate concentration $C_{\text{S-NO}_3^-}$ [Grant et al., 2014; Azizian et al., 2015; McCluskey et al., 2016].

To illustrate how the PASS model captures the physics and chemistry of N-cycling in the hyporheic zone, consider the hypothetical example where all water leaving the hyporheic zone has a single residence time, denoted here by the variable τ^*. In this event, the RTD reduces to the Dirac delta function, $E(\tau) = \delta(\tau - \tau^*)$, and the PASS model simplifies:

$$v_\mathrm{f} = q_\mathrm{H}\left[F_\mathrm{N}\left(\tau^*\right) - 1\right] \tag{2a}$$

$$F_\mathrm{N}\left(\tau^*\right) = \frac{C_{\mathrm{HZT\text{-}NO_3^-}}\left(\tau^*;\text{"chemistry"}\right)}{C_{\mathrm{S\text{-}NO_3^-}}} \tag{2b}$$

Following Zarnetske et al. [2012], the variable F_N represents the fraction of nitrate remaining after a water parcel spends a time τ^* traveling through the hyporheic zone. From equation (2) we can identify several limits of interest. First, if all nitrate is removed (e.g., by denitrification), then the fraction of nitrate remaining is zero ($F_\mathrm{N} = 0$). In this "mass transfer limit", or MTL, nitrate uptake by the streambed depends solely on the hyporheic exchange flux: $v_\mathrm{f,MTL} = -q_\mathrm{H}$. Alternatively, for values of fractional removal less than unity ($0 < F_\mathrm{N} \le 1$), the nitrate uptake velocity depends on the magnitude of both q_H and F_N, a condition we refer to as reaction-limited nitrate uptake. An extreme example is when $F_\mathrm{N} = 1$, and hyporheic exchange plays no functional role relative to nitrate generation or removal ($v_\mathrm{f} = 0$). Finally, in sediments that are net nitrifying (i.e., the generation of nitrate by nitrification exceeds the removal of nitrate by other processes, $F_\mathrm{N} > 1$), the nitrate uptake velocity will be positive ($v_\mathrm{f} > 0$) and its magnitude will depend both on the hyporheic exchange flux q_H and the extent to which the nitrate concentration increases during passage through the hyporheic zone.

Which of these limits apply to a particular stream may depend on the magnitude of the dimensionless Damköhler number (Da, unitless), defined here as the ratio of the characteristic travel time scale of water undergoing hyporheic exchange (τ_T) and the timescale for mineralization of organic carbon within the streambed (τ_R): $\mathrm{Da} = \tau_\mathrm{T}/\tau_\mathrm{R}$. The MTL condition, for example, is most likely to occur when the Damköhler number is large ($\mathrm{Da} >> 1$), because long transport timescales together with short mineralization timescales are associated with anaerobic conditions in the sediments and nitrate removal by denitrification [Boano et al., 2010; Mazadri et al., 2011; Zarnetske et al., 2011, 2012; Kessler et al, 2013a, 2013b; Azizian et al. 2015]. On the other hand, for intermediate ($\mathrm{Da} \approx 1$) or small ($\mathrm{Da} << 1$) values of the Damköhler number, the sediments may serve as a reaction-limited sink of nitrate ($-q_\mathrm{H} < v_\mathrm{f} \leq 0$) or as a net source of nitrate through the nitrification of ammonium ($v_\mathrm{f} > 0$) [Zarnetske et al., 2012]. The ammonium, in turn, may be downwelled from the stream or generated in situ by the respiration of sediment organic carbon (i.e., ammonification) [Cook et al., 2006; Azizian et al., 2015]. In practice, hyporheic exchange exhibits a broad range of residence times (not a single residence time, as assumed in the hypothetical example above), and thus the integral form of the nitrate uptake velocity (equation (1)) must be used in place of equation (2).

4.2.2. The Segregated Streamline Hypothesis

The PASS model assumes that all HZTs are completely segregated; i.e., there is no mixing of mass across or within HZTs. The concept of complete segregation can be traced back to chemical engineering reactor design, where a distinction is made between macromixing and micromixing within a chemical reactor [Rawlings and Ekerdt, 2013]. In the present context, macromixing refers to the diversity of flow paths water parcels take as they pass through the hyporheic zone, represented here by the RTD function $E(\tau)$. Micromixing, on the other hand, refers to the exchange of mass between individual water parcels during their residence times, and falls along a spectrum from complete segregation (adopted here) to maximum-mixedness [Rawlings and Ekerdt, 2013]. In the complete segregation limit, mixing across HZTs occurs at the last possible moment as water exits the hyporheic zone and returns to the stream. In the maximum mixedness limit, mixing occurs as soon as possible while accounting for the fact that water parcels cannot be mixed for longer than their residence time. A key result of this theory is that the magnitude (and sign) of error introduced by adopting a particular micromixing model depends on the order of the underlying reaction. For example, the micromixing model has no effect on substrate conversion if the underlying reaction is first-order [Rawlings and Ekerdt, 2013]. Micromixing can also be thought of in terms of idealized reactors; e.g., the complete segregation limit is equivalent to assuming that a water parcel behaves like a batch reactor as it travels along a HZT. Importantly, different types (and combinations) of idealized reactors can be used to characterize the influence of micromixing on chemical transformations. Elucidating the most appropriate such model for the hyporheic zone is an interesting topic for future study [e.g., see Feinberg and Hildebrandt, 1997].

4.2.3. Stream Bed and Ambient Flow Scenarios

In the analysis presented below we use the PASS model to estimate the nitrate uptake velocity under a variety of ambient flow conditions. These calculations are carried out assuming that the stream in question has a sandy streambed of constant hydraulic conductivity ($K_{\mathrm{h}} = 5 \times 10^{-4}$ m s^{-1}), mean slope of $S = 2\%$, and porosity $\theta = 0.3$. Ten ambient flow conditions are evaluated, including two choices of stream discharge ($Q =$ 17.47 m^3 s^{-1} and 7.40 m^3 s^{-1}, denoted "H-Q" and "L-Q", respectively), five choices of vertical groundwater flux ($q_{\mathrm{V}} =$ 0, $\pm 5.8 \times 10^{-6}$, and $\pm 2.3 \times 10^{-5}$ m s^{-1}), and a single horizontal groundwater flux or "underflow" ($q_{\mathrm{U}} = K_{\mathrm{h}} S = 10^{-5}$ m s^{-1}) (**Table 4.1**). Collectively, these ten scenarios cover a realistic range of ambient stream and groundwater flows [e.g., Schmidt et al., 2006; Kennedy et al., 2009; Englelhardt et al., 2011] and were specifically chosen so that we could incorporate into our study the results of a previously published computational fluid dynamics (CFD) study of hyporheic exchange across riffle-pool sequences [Trauth et al., 2013, 2014].

4.3. Nitrate Evolution Along a HZT

4.3.1. Model of Subsurface Biogeochemistry

Our biokinetic model tracks the evolution of three chemical constituents (nitrate, oxygen, and ammonium) as a water parcel travels along a HZT. These three chemical constituents are produced and/or consumed by a coupled set of microbially mediated redox reactions, including aerobic respiration (AR), ammonification (AM), nitrification (NI), and denitrification (DN) ["National Environmental Research Institute, 2004; Cook et al., 2006; Evrard et al., 2012]:

Table 4.1. Physical Parameter Values Used for the PASS Model Simulations (Variables Defined in Notation Section).

Parameters (units)	Value	
Alluvium characteristics		
K_h (m s^{-1})	5×10^{-4}	
S (-)	0.02	
q_U (m s^{-1})	10^{-5}	
q_V (m s^{-1})	$0, \pm5.8\times10^{-6}, \pm23\times10^{-6}$	
θ	0.3	
Riffle-Pool dimensions		
Period (m)	10	
Amplitude (m)	0.5	
Ripple dimensions		
H (m)	0.02	
λ (m)	0.15	
a	0.16	
m	3/8	
Stream flow characteristics	High stream discharge	Low stream discharge
Q (m^3 s^{-1})	17.47	7.40
d_s (m)	1	0.7
U (m s^{-1})	1.95	1.15

$$\mathrm{AR: CH_2O + O_2 \rightarrow CO_2 + H_2O} \tag{3a}$$

$$\mathrm{DN: CH_2O + 0.8\,NO_3^- + 0.8\,H^+ \rightarrow CO_2 + 0.4\,N_2 + 1.4\,H_2O} \tag{3b}$$

$$\mathrm{NI: NH_4^+ + 2\,O_2 \rightarrow NO_3^- + 2H^+ + H_2O} \tag{3c}$$

$$\mathrm{AM:}\ \{\mathrm{NH_3}\}_{\mathrm{OM}} + \mathrm{H^+} \rightarrow \mathrm{NH_4^+} \tag{3d}$$

The temporary storage of N in microbial or plant biomass (assimilation) is not included, which is reasonable provided a steady state balance exists between N uptake by assimilation and N release by biomass decomposition and die-off (e.g., over weeks or longer timescales) [Peterson et al., 2001]; however, up to a third of the N assimilated in plant tissues can be stored in stream sediments as refractory soil organic material [Birgand et al., 2007]. Indeed, one of the goals of our study is to evaluate the importance of N assimilation—relative to the other components of the N cycle captured by equations (3a)-(3d)—by comparing our model predictions (which do not account for assimilation) with nitrate uptake velocities observed in reach-scale field experiments (**section 4.6**). Our biokinetic model also neglects anaerobic ammonium oxidation (Anammox) and dissimilatory nitrate reduction to ammonium (DNRA). Although important in some estuarine and marine settings, these alternative pathways for nitrate reduction are thought to be of secondary importance (relative to respiratory denitrification, equation (3b)) in rivers and streams [Burgin and Hamilton, 2007; Hu et al., 2011; Lansdown et al., 2016].

To translate the above redox reactions into predictions for the evolution of oxygen, nitrate, and ammonium concentration along a HZT we invoke the following two assumptions: (1) water parcels behave like well-mixed batch reactors as they travel along a HZT (see the streamline segregation discussion in **section 4.2.2**); and (2) at any particular location in the sediment the concentration field and flow field are steady-state (i.e., they do not change with time). Given these two assumptions, mass balance over a single water parcel yields the following set of coupled ordinary differential equations for the concentrations (units of mol m^{-3}) of molecular oxygen ($C_{\mathrm{HZT\text{-}O_2}}$), nitrate ($C_{\mathrm{HZT\text{-}NO_3^-}}$), and ammonium ($C_{\mathrm{HZT\text{-}NH_4^+}}$) as function of travel time (τ) through a HZT:

$$\frac{dC_{\mathrm{HZT\text{-}O_2}}}{d\tau} = -R_{\mathrm{AR}} - 2R_{\mathrm{NI}} \tag{4a}$$

$$\frac{dC_{\mathrm{HZT\text{-}NO_3^-}}}{d\tau} = R_{\mathrm{NI}} - R_{\mathrm{DN}} \tag{4b}$$

$$\frac{dC_{\text{HZT-NH}_4^+}}{d\tau} = R_{\text{AM}} - R_{\text{NI}} \tag{4c}$$

Variables on the right hand side of these equations represent rates (units of mol m^{-3} s^{-1}) of aerobic respiration (R_{AR}), nitrification (R_{NI}), denitrification (R_{DN}), and ammonification (R_{AM}).

Following the procedure outlined in Van Cappellenn and Wang [1996] and Berg et al. [2003], we assume AR and DN follow saturation-type (Monod) rate expressions, NI is second-order in oxygen and ammonium concentrations, and AM is zero-order and proportional to the organic carbon mineralization rate ($R_{\min}$, units mol m^{-3} s^{-1}) [see also Cook et al., 2006; Kessler et al. 2013a, 2013b]. The organic carbon mineralization rate can be represented as the product of a first-order mineralization rate constant ($k_{\min}$, units s^{-1}) and the interstitial concentration of dissolved organic carbon (C_{DOC}, units mol m^{-3}) [Pett, 1989; Zarnetske et al., 2012]: $R_{\min} = k_{\min} C_{\text{DOC}}$. Thus, the potential effects of organic carbon limitation on denitrification [e.g., see Taylor and Townsend, 2010] are embodied in the value of $R_{\min}$, which in our biokinetic model is assumed to be constant throughout the hyporheic zone:

$$R_{\text{AR}} = \frac{R_{\min} C_{\text{HZT-O}_2}}{C_{\text{HZT-O}_2} + K_{\text{O}_2}^{\text{sat}}} \tag{5a}$$

$$R_{\text{AM}} = \frac{1}{\gamma_{\text{CN}}} R_{\min} \tag{5b}$$

$$R_{\text{NI}} = k_{\text{NI}} C_{\text{HZT-O}_2} C_{\text{HZT-NH}_4^+} \tag{5c}$$

$$R_{\text{DN}} = \theta_{\text{O}_2}^{\text{inh}} \kappa \frac{R_{\min} C_{\text{HZT-NO}_3^-}}{C_{\text{HZT-NO}_3^-} + K_{\text{NO}_3^-}^{\text{sat}}} ; \theta_{\text{O}_2}^{\text{inh}} = \frac{K_{\text{O}_2}^{\text{inh}}}{C_{\text{HZT-O}_2} K_{\text{O}_2}^{\text{inh}}} \tag{5d}$$

New variables appearing here include a fixed constant for the production of dissolved ammonium by the mineralization of organic carbon (γ_{CN}, unitless); a second-order nitrification rate constant (k_{NI}, units m^3 mol^{-1} s^{-1}); half-saturation constants for aerobic respiration ($K_{\mathrm{O_2}}^{\mathrm{sat}}$, units mol m^{-3}), denitrification ($K_{\mathrm{NO_3^-}}^{\mathrm{sat}}$, units mol m^{-3}), and oxygen inhibition of denitrification ($K_{\mathrm{O_2}}^{\mathrm{inh}}$, units mol m^{-3}); coefficient for the noncompetitive inhibition of denitrification by molecular oxygen ($\theta_{\mathrm{O_2}}^{\mathrm{inh}}$); and a parameter ($\kappa$, unitless) that indicates the relative rate at which organic carbon is oxidized by aerobic respiration and respiratory denitrification.

Combining equations (4a) through (5d) and normalizing all variables to a dimensionless form, we arrive at the following set of coupled rate equations for the coevolution of molecular oxygen, nitrate, and ammonium with travel time through the hyporheic zone:

$$\frac{d\hat{C}_{\mathrm{HZT\text{-}O_2}}}{d\hat{\tau}_{\mathrm{R}}} = -\frac{\hat{C}_{\mathrm{HZT\text{-}O_2}}}{\hat{C}_{\mathrm{HZT\text{-}O_2}} \big/ \hat{K}_{\mathrm{O_2}}^{\mathrm{sat}} + 1} - 2\delta \hat{C}_{\mathrm{HZT\text{-}O_2}} \hat{C}_{\mathrm{HZT\text{-}NH_4^+}}, \hat{C}_{\mathrm{HZT\text{-}O_2}}\left(\hat{\tau}_{\mathrm{R}} = 0\right) = 1 \tag{6a}$$

$$\begin{gathered}\frac{d\hat{C}_{\mathrm{HZT\text{-}NO_3^-}}}{d\hat{\tau}_{\mathrm{R}}} = \delta \hat{C}_{\mathrm{HZT\text{-}O_2}} \hat{C}_{\mathrm{HZT\text{-}NH_4^+}} - \frac{\kappa \hat{K}_{\mathrm{O_2}}^{\mathrm{inh}} \hat{K}_{\mathrm{O_2}}^{\mathrm{sat}} \hat{C}_{\mathrm{HZT\text{-}NO_3^-}}}{\left(\hat{C}_{\mathrm{HZT\text{-}O_2}} + \hat{K}_{\mathrm{O_2}}^{\mathrm{inh}}\right)\left(\hat{C}_{\mathrm{HZT\text{-}NO_3^-}} + \hat{K}_{\mathrm{NO_3^-}}^{\mathrm{sat}}\right)}, \\ \hat{C}_{\mathrm{HZT\text{-}NO_3^-}}\left(\hat{\tau}_{\mathrm{R}} = 0\right) = \beta\end{gathered} \tag{6b}$$

$$\frac{d\hat{C}_{\mathrm{HZT\text{-}NH_4^+}}}{d\hat{\tau}_{\mathrm{R}}} = \frac{1}{\gamma_{\mathrm{CN}}} \hat{K}_{\mathrm{O_2}}^{\mathrm{sat}} - \delta \hat{C}_{\mathrm{HZT\text{-}O_2}} \hat{C}_{\mathrm{HZT\text{-}NH_4^+}}, \hat{C}_{\mathrm{HZT\text{-}NH_4^+}}\left(\hat{\tau}_{\mathrm{R}} = 0\right) = \alpha \tag{6c}$$

In these equations, all variables with units of concentration have been normalized by the concentration of molecular oxygen in the stream: $\hat{C}_{\mathrm{HZT\text{-}O_2}} = C_{\mathrm{HZT\text{-}O_2}} \big/ C_{\mathrm{S\text{-}O_2}}$, $\hat{C}_{\mathrm{HZT\text{-}NO_3^-}} = C_{\mathrm{HZT\text{-}NO_3^-}} \big/ C_{\mathrm{S\text{-}O_2}}$, $\hat{C}_{\mathrm{HZT\text{-}NH_4^+}} = C_{\mathrm{HZT\text{-}NH_4^+}} \big/ C_{\mathrm{S\text{-}O_2}}$, $\hat{K}_{\mathrm{O_2}}^{\mathrm{sat}} = K_{\mathrm{O_2}}^{\mathrm{sat}} \big/ C_{\mathrm{S\text{-}O_2}}$, $\hat{K}_{\mathrm{NO_3^-}}^{\mathrm{sat}} = K_{\mathrm{NO_3^-}}^{\mathrm{sat}} \big/ C_{\mathrm{S\text{-}O_2}}$,

$\hat{K}_{\mathrm{O}_2}^{\mathrm{inh}} = K_{\mathrm{O}_2}^{\mathrm{inh}} / C_{\text{S-O}_2}$, $\alpha = C_{\text{S-NH}_4^+}(\hat{\tau}_{\mathrm{R}} = 0) / C_{\text{S-O}_2}$, and $\beta = C_{\text{S-NO}_3^-}(\hat{\tau}_{\mathrm{R}} = 0) / C_{\text{S-O}_2}$. The dimensionless parameters δ and $\hat{\tau}_{\mathrm{R}}$ represent the relative rates of nitrification and respiration ($\delta = k_{\mathrm{NI}} C_{\text{S-O}_2} \tau_{\mathrm{R}}$) and normalized travel time along a HZT ($\hat{\tau}_{\mathrm{R}} = \tau / \tau_{\mathrm{R}}$), the variable $\tau_{\mathrm{R}} = K_{\mathrm{O}_2}^{\mathrm{sat}} / R_{\mathrm{min}}$ (units s) is the timescale for organic carbon mineralization.

The benefit of rewriting our model in dimensionless form is that, by doing so, we reduce the number of model parameters by the number of physical units [Buckingham, 1914]. Because our biokinetic model has two physical units (mass concentration and time), we reduced its dimensionality from ten parameters ($C_{\text{S-O}_2}$, $C_{\text{S-NO}_3^-}$, $C_{\text{S-NH}_4^+}$, R_{min}, $K_{\mathrm{NO}_3^-}^{\mathrm{sat}}$, $K_{\mathrm{O}_2}^{\mathrm{sat}}$, $K_{\mathrm{O}_2}^{\mathrm{inh}}$, k_{NI}, γ_{CN}, κ) to eight parameters (δ, $\hat{K}_{\mathrm{O}_2}^{\mathrm{sat}}$, $\hat{K}_{\mathrm{NO}_3^-}^{\mathrm{sat}}$, $\hat{K}_{\mathrm{O}_2}^{\mathrm{inh}}$, α, β, γ_{CN}, κ). Once these eight dimensionless parameters are specified, equations (6a) through (6c) are numerically solved to yield the interstitial nitrate concentration as a function of travel time along a HZT; (see equation (1b) and **Appendix C**, **Code C.1**). Next we describe the process by which we chose three sets of parameter values to represent a spectrum streams, from pristine to polluted.

4.3.2. Selection of Biokinetic Model Parameters

4.3.2.1. In-Stream Concentrations and Ecosystem Respiration

In-stream concentrations of oxygen, nitrate, ammonium, and organic carbon tend to covary across different streams (i.e., they are not statistically independent, see Taylor and Townsend [2010]), and this covariance should be accounted for if we are to select realistic model parameters. To this end, we performed a principal component analysis

(PCA) of $C_{\text{S-O}_2}$, $C_{\text{S-NO}_3^-}$, $C_{\text{S-NH}_4^+}$, and ecosystem respiration (ER, units mol m^{-2} s^{-1}) values measured in 70 stream sites across the United Sates (including reference streams, urban impacted streams, and agriculture impacted streams) as part of the Second Lotic Intersite Nitrate Experiment (LINX II) [Mulholland et al., 2008, 2009; Beaulieu et al., 2011]. The PCA was performed on log-transformed, mean-centered and scaled (z-scored) data (details in **Appendix C**, **Text C.1**), with the goal of identifying the dominant patterns, or PC modes, for these four chemical parameters across all 70 sites. A resampling-based stopping rule [Peres-Neto et al., 2005; Rippy et al., 2017] was used to identify PC modes that explained more variance in stream biogeochemistry than expected by chance (significant at $p < 0.1$). A nonparametric bootstrap approach [Babamoradi et al., 2013] was used to determine the statistical uncertainty about significant PC modes and their corresponding scores: i.e., the location of individual reference, agricultural, and urban streams relative to the first two PC modes.

PCA identified two marginally significant PC modes ($p < 0.1$) that together capture approximately 67% of the biogeochemical variability in the LINX II data set (**Figure 4.2** and **Appendix C, Figure C.1**). PC Mode 1 (our primary pattern, 38% variance explained) predominantly reflects the ambient in-stream concentration of ammonium (i.e., PC Mode 1 aligns with the loading vector for NH_4^+), and separates reference streams (typically low $C_{\text{S-NH}_4^+}$) from urban and agriculture-impacted streams (low to high $C_{\text{S-NH}_4^+}$). PC Mode 2 (our secondary pattern, 29% variance explained) primarily reflects ER (i.e., PC Mode 2 aligns with the loading vector for ER), but does not obviously separate the streams by type (i.e., reference, agriculture, or urban). The loading vector for molecular

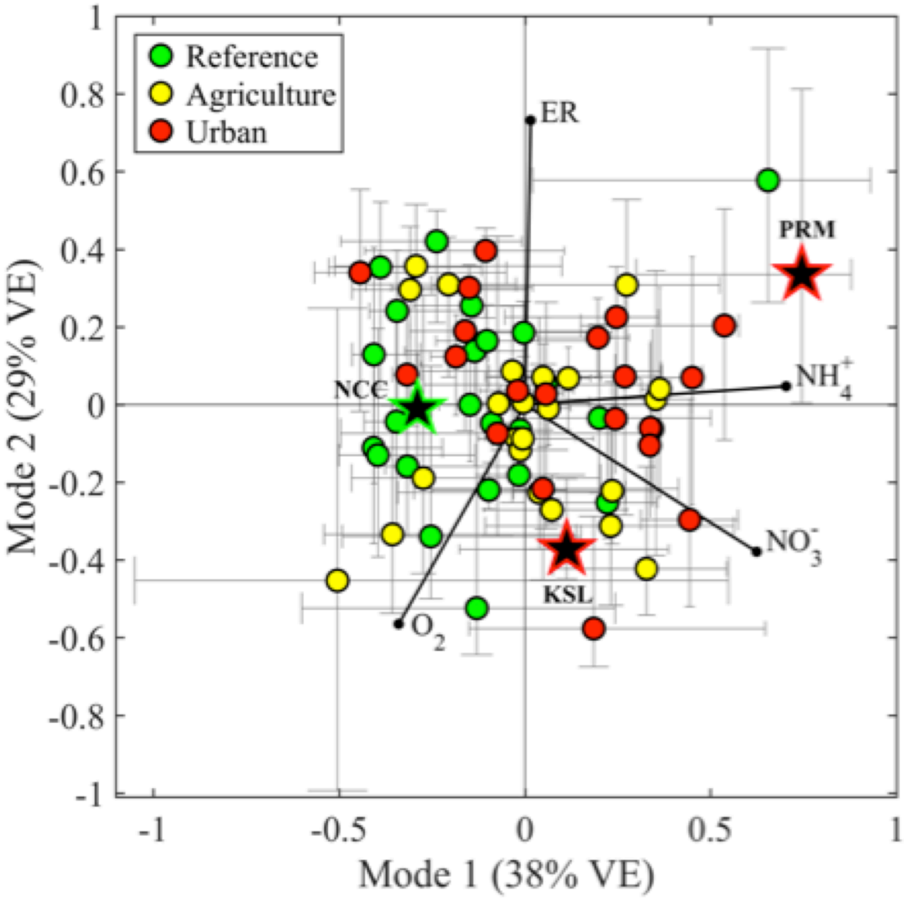

Figure 4.2. Principle Component Analysis (PCA) of ambient stream data measured at 70 stream sites included in the second Lotic Intersite Nitrogen Experiments (LINX II) study (data reproduced from Mulholland et al. [2008, 2009]; Beaulieu et al. [2011]. Sites include pristine or reference streams (green circles), agriculture impacted streams (yellow circles), and urban impacted streams (red circles); the error bars about these points are 95% resampling-based confidence intervals. The first two PCA modes explain 67% of the variance in log-transformed, z-scored measurements of ecosystem respiration (ER) and in-stream concentrations of ammonium (NH_4^+), nitrate (NO_3^-), and oxygen (O_2). Biogeochemical loading vectors for these four stream parameters are shown in black. Three sites were selected for biokinetic modeling (large colored stars), including Cunningham Creek in North Carolina (NCC), Rio Maymeyes Tributary in Puerto Rico (PRM), and Little Kitten Creek in Kansas (KSL).

oxygen is associated with low $C_{\text{S-NH}_4^+}$ (negative values of Mode 1) and low ER (negative values of Mode 2). The loading vector for nitrate is associated with high ammonium concentrations (postive values of Mode 1) and low ER (negative values of Mode 2).

Overall, these PCA results are qualitatively consistent with the structure of our biokinetic model and previously published assessments of N-cycling in streams [e.g., Birgand et al., 2007]. In particular, the following patterns are evident (**Figure 4.2**): (1) oxygen concentrations are low in streams with high ER, reflecting high organic carbon mineralization rates (large R_{min}) and high rates of aerobic respiration (large R_{AR}) (see equation (5a)); (2) nitrate concentrations are low in streams with high ER, reflecting high organic carbon mineralization rates (large R_{min}) and high denitrification rates (large R_{DN}) (see equation (5d)); and (3) ammonium concentrations are low in streams with high molecular oxygen concentrations, reflecting high rates of nitrification (large R_{NI}) (see equation (5c)). Intriguingly, the loading vector for nitrate is located midway between the oxygen and ammonium loading vectors, perhaps reflecting the importance of nitrification (which requires both oxygen and ammonium, see equation (5c)) in nitrate generation.

Based on the results presented in **Figure 4.2**, we selected three stream sites that collectively capture a diversity of biogeochemical settings (see colored stars): (1) Cunningham Creek in North Carolina (NCC) is characterized by low ammonium and nitrate concentrations, moderate molecular oxygen concentration, and moderate ER ($C_{\text{S-O}_2} = 2.91\times10^{-1}$ mol m^{-3}, $C_{\text{S-NH}_4^+} = 2.14\times10^{-4}$ mol m^{-3}, $C_{\text{S-NO}_3^-} = 7.14\times10^{-4}$ mol m^{-3}, $\text{ER} = 1.88\times10^{-6}$ mol m^{-2} s^{-1}; (2) Rio Mameyes Tributary in Puerto Rico (PRM) is characterized by high ammonium, moderate nitrate, and low molecular oxygen concentrations, together with high ER ($C_{\text{S-O}_2} = 1.34 \times 10^{-1}$ mol m^{-3}, $C_{\text{S-NH}_4^+} = 1.57 \times 10^{-1}$ mol m^{-3}, $C_{\text{S-NO}_3^-} = 1.24 \times 10^{-2}$ mol m^{-3}, $\text{ER} = 2.68 \times 10^{-6}$ mol m^{-2} s^{-1}); and (3) Little Kitten Creek in Kansas (KSL) is characterized by moderate ammonium and nitrate concentrations, high oxygen concentration, and low ER ($C_{\text{S-O}_2} = 2.60 \times 10^{-1}$ mol m^{-3}, $C_{\text{S-NH}_4^+} = 1.71 \times 10^{-3}$ mol m^{-3}, $C_{\text{S-NO}_3^-} = 1.20 \times 10^{-2}$ mol m^{-3}, $\text{ER} = 3.26 \times 10^{-7}$ mol m^{-2} s^{-1}). While several LINX II sites had higher nitrate concentrations than KSL (i.e., plotted closer to the end of the NO_3^- loading vector), these were not selected for further study because: (1) nitrate uptake velocities were not measured or (2) sediment characteristics differed substantially from NCC and PRM (A. Marzadri, personal communication, 2017). Organic carbon mineralization rates at these three sites were calculated by dividing reported ER values by an order-of-magnitude estimate of the streambed depth over which mineralization occurs (~10 cm): $R_{\min} = \text{ER}/d$ where $d = 0.1$ m. Accordingly, we adopted the following mineralization rates for NCC, PRM, and KSL, respectively: $R_{\min} = 1.88 \times 10^{-5}$ mol m^{-3} s^{-1}, $R_{\min} = 2.68 \times 10^{-5}$ mol m^{-3} s^{-1}, and $R_{\min} = 3.26 \times 10^{-6}$ mol m^{-3} s^{-1} (**Table 4.2**).

4.3.2.2. Half-Saturation Constants

Garcia-Ruiz et al. [1998] measured half-saturation constants for denitrification ($K_{\text{NO}_3^-}^{\text{sat}}$) in intact sediment cores collected from five sites along the Swale-Ouse river system in northeastern England, including one from a highly polluted tributary. The half-saturation

Table 4.2. In-Stream and Hyporheic Zone "Chemistry" for Three Sites Selected From LINX II Data Set[a]

	NCC	PRM	KSL
Dimensional parameters (units)			
$C_{\text{S-O}_2}$ (mol m^{-3})	2.91E-01	1.34E-01	2.60E-01
$C_{\text{S-NH}_4^+}$ (mol m^{-3})	2.14E-04	1.57E-01	1.71E-03
$C_{\text{S-NO}_3^-}$ (mol m^{-3})	7.14E-04	1.24E-02	1.20E-02
$K_{\text{O}_2}^{\text{inh}}$ (mol m^{-3})	3.00E-03	3.00E-03	3.00E-03
$K_{\text{NO}_3^-}^{\text{sat}}$ (mol m^{-3})	1.30E-02	9.00E-02	9.00E-02
$K_{\text{O}_2}^{\text{sat}}$ (mol m^{-3})	6.00E-03	6.00E-03	6.00E-03
k_{NI} (m^3 mol^{-1} s^{-1})	4.00E-04	4.00E-04	4.00E-04
R_{min} (mol m^{-3} s^{-1})	1.88E-05	2.68E-05	3.26E-06
$\tau_{\text{R}} \equiv K_{\text{O}_2}^{\text{sat}} \big/ R_{\text{min}}$ (s)	319	224	1840
Non-dimensional parameters (unitless)			
$\delta \equiv \tau_{\text{R}} k_{\text{NI}} C_{\text{S-O}_2}$	3.72E-02	1.20E-02	1.91E-01
$\hat{K}_{\text{O}_2}^{\text{sat}} \equiv K_{\text{O}_2}^{\text{sat}} \big/ C_{\text{S-O}_2}$	2.06E-02	4.48E-02	2.31E-02
$\hat{K}_{\text{NO}_3^-}^{\text{sat}} \equiv K_{\text{NO}_3^-}^{\text{sat}} \big/ C_{\text{S-O}_2}$	4.46E-02	6.72E-01	3.47E-01
$\hat{K}_{\text{O}_2}^{\text{inh}} \equiv K_{\text{O}_2}^{\text{inh}} \big/ C_{\text{S-O}_2}$	1.03E-02	2.24E-02	1.16E-02
$\alpha \equiv C_{\text{S-NH}_4^+} \big/ C_{\text{S-O}_2}$	7.35E-04	1.17E+00	6.60E-03
$\beta \equiv C_{\text{S-NO}_3^-} \big/ C_{\text{S-O}_2}$	2.45E-03	9.25E-02	4.62E-02
$\kappa \cong v_{\text{f,Dw}} \left(C_{\text{S-NO}_3^-} + K_{\text{NO}_3^-}^{\text{sat}} \right) \Big/ \text{ER}$	0.11	0.36	0.38
γ_{CN}	14	14	14

---

[a] Cunningham Creek in North Carolina (NCC), Rio Mameyes Tributary in Puerto Rico (PRM), and Little Kitten Creek in Kansas (KSL) (variables defined in Notation section)

constants range from $K_{\mathrm{NO}_3^-}^{\mathrm{sat}}$ = 0.013 mol m^{-3} at the headwater site to $K_{\mathrm{NO}_3^-}^{\mathrm{sat}}$ = 0.09 mol m^{-3} at the downstream site; the most polluted site had a half-saturation constant of $K_{\mathrm{NO}_3^-}^{\mathrm{sat}}$ = 0.64 mol m^{-3}. These authors noted that their measured half-saturation constants increased along the river continuum (i.e., as ambient stream nitrate concentration increased), consistent with the idea that denitrifying microorganisms in streambed sediments have reduced nitrate affinity (i.e., higher half-saturation constants) at sites with high ambient stream nitrate concentrations. The authors also noted that their experimental approach (measuring denitrification rates after adding a fixed concentration of nitrate to the water overlying an intact sediment core) tends to overestimate the half-saturation constant [Garcia-Ruiz et al, 1998]. Alternatively, Evrard et al. [2012] conducted denitrification measurements in flow through reactors specifically designed to mimic advective flow through permeable sediments; their half-saturation constants ($K_{\mathrm{NO}_3^-}^{\mathrm{sat}}$ = 0.0015 to 0.0198 mol m^{-3}) are generally lower than the values reported by Garcia-Ruiz et al. (0.013-0.09 mol m^{-3}, excluding the most polluted site). While the different ranges reported in these two studies could reflect methodological differences (static incubations with intact cores versus flow through experiments in sediment columns), the ambient nitrate concentrations were also quite different; indeed, the highest ambient nitrate concentration used in Evrard et al.'s study (0.00493 mol m^{-3}) is more than twofold lower than the nitrate concentrations measured at our PRM and KSL sites (0.0124 and 0.0120 mol m^{-3}, respectively). In the end, we adopted Garcia-Ruiz et al.'s highest half saturation constant (excluding the most polluted site) for our two urban impacted stream sites ($K_{\mathrm{NO}_3^-}^{\mathrm{sat,KSL}} = K_{\mathrm{NO}_3^-}^{\mathrm{sat,PRM}}$ = 0.09 mol m^{-3}) and Garcia-Ruiz et al.'s lowest half-saturation constant for our pristine site ($K_{\mathrm{NO_3^-}}^{\mathrm{sat,NCC}} = 0.013$ mol m^{-3}) (**Table 4.2**). A single set of half-saturation constants was adopted for aerobic respiration ($K_{\mathrm{O_2}}^{\mathrm{sat}} = 0.006$ mol m^{-3}) and noncompetitive oxygen inhibition of denitrification ($K_{\mathrm{O_2}}^{\mathrm{inh}} = 0.003$ mol m^{-3}) [Sawyer, 2015] (**Table 4.2**).

4.3.2.3. Ammonification, Denitrification, and Nitrification.

Ammonification was taken as a fixed fraction ($\gamma_{\mathrm{CN}} = 14$) of the organic carbon mineralization rate [Kessler et al., 2013b]. The denitrification rate depends on $R_{\min}$, $K_{\mathrm{NO_3^-}}^{\mathrm{sat}}$, $K_{\mathrm{O_2}}^{\mathrm{inh}}$ (discussed above), as well as the constant κ . Given the stoichiometry of AR and DN (see equations (3a) and (3b)), aerobic respiration should consume one mole of organic carbon for every mole of molecular oxygen reduced, while denitrification should consume κ = 1/ 0.8 = 1.25 moles of organic carbon for every mole of nitrate reduced.

However, recent laboratory and field observations of respiratory denitrification in coastal marine sediments indicate that κ is 25 times smaller (κ = 0.05) than the stoichiometric value (κ = 1.25) [Evrard et al., 2012; Kessler et al., 2013a, 2013b], perhaps reflecting the dominance of benthic algal metabolism in these systems [Bourke et al., 2017]. To determine where along this spectrum (from κ = 0.05 to 1.25) our stream sites fall, we estimated κ as follows. Assuming the sediment is well-mixed and oxygen inhibition of denitrification in the bulk sediment is minimal ($\theta_{\mathrm{O_2}}^{\mathrm{inh}} \approx 1$), equation (5d) can be rearranged as follows: $\kappa \approx \left(R_{\mathrm{DN}}/R_{\min}\right)\left(C_{\mathrm{S\text{-}NO_3^-}} + K_{\mathrm{NO_3^-}}^{\mathrm{sat}}\right)\big/C_{\mathrm{S\text{-}NO_3^-}}$. The ratio $R_{\mathrm{DN}}/R_{\min}$ can be approximated from the ratio of the flux of stream nitrate into the streambed by denitrification (U_{DN} , units mol m^{-2} s^{-1}) and the ecosystem respiration rate: $R_{\text{DN}}/R_{\min} \approx U_{\text{DN}}/\text{ER}$. This last equality follows by multiplying the top and bottom of the ratio $R_{\text{DN}}/R_{\min}$ by the sediment depth d over which denitrification occurs, and recognizing that $U_{\text{DN}} \approx R_{\text{DN}}d$ and $\text{ER} \approx R_{\min}d$ (see earlier discussion of estimating $R_{\min}$ from ER). Combining these results, we obtain the formula: $\kappa \approx v_{\text{f,Dw}}\left(C_{\text{S-NO}_3^-} + K_{\text{NO}_3^-}^{\text{sat}}\right)\big/\text{ER}$ where $v_{\text{f,Dw}}$ (units m s^{-1}) is the uptake velocity of stream nitrate by direct denitrification: $v_{\text{f,Dw}} \equiv U_{\text{DN}}\big/C_{\text{S-NO}_3^-}$. From $^{15}\text{NO}_3^-$-seeding experiments, Mulholland et al. [2008] estimated values for $v_{\text{f,Dw}}$ for most of the LINX II sites (note that $v_{\text{f,Dw}}$ is notated as v_{fden} in their paper). Thus, all of the variables needed to estimate κ for our three sites were either known ($v_{\text{f,Dw}}$, $C_{\text{S-NO}_3^-}$, ER) or previously estimated from the literature (see last section, $K_{\text{NO}_3^-}^{\text{sat}}$). After substituting these values into our formula we obtain: $\kappa = 0.11$, 0.38, and 0.36 for NCC, KSL, and PRM, respectively (**Table 4.2**); these values were adopted in the modeling studies presented below. Intriguingly, these estimates of κ are skewed toward the previous estimate for permeable marine sediments ($\kappa = 0.05$), perhaps signalling the importance of benthic algal metabolism in both freshwater streams and coastal marine systems. Finally, the second-order nitrification rate constant was estimated from the nitrification parameters reported by Zarnetske et al [2012] for Drift Creek, Oregon (USA): $k_{\text{NI}} = 0.0004$ m^3 mol^{-1} s^{-1} (**Table 4.2**).

4.3.3. Biokinetic Model Predictions for the Evolution of Nitrate Along a HZT

Biokinetic model predictions for the evolution of $\mathrm{NO_3^-}$ with travel time through the hyporheic zone are presented in **Figure 4.3**. These results are presented in terms of the fraction $F_\mathrm{N}(\tau)$ (introduced in **section 4.2.1**), which represents the fraction of nitrate remaining after a water parcel travels through a HZT of residence time τ (see equation (2b)). For very short travel times ($\tau < 100$ s), there is insufficient time for biogeochemical reactions to occur and the interstitial nitrate concentration is unchanged (i.e. $F_\mathrm{N} = 1$). For larger travel times, the nitrate concentration evolves in a similar manner across the three sites, first increasing above ambient stream concentrations ($F_\mathrm{N} > 1$, due to the net production of nitrate by nitrification) and then declining after the oxic-anoxic transition ($F_\mathrm{N} < 1$, as microbial metabolism switches from aerobic respiration to respiratory denitrification). The primary source of new nitrate at KSL is nitrification of ammonium downwelled into the hyporheic zone from the stream. The primary source of new nitrate at NCC is nitrification of ammonium produced within the hyporheic zone by ammonification (i.e., respiration of sediment organic material). The new nitrate at PRM is generated by nitrification of both stream-borne ammonium and ammonium generated in situ by ammonification. The residence time at which F_N drops below unity decreases in order: KSL > NCC > PRM. This sequence precisely matches the respiration timescales for these three environments ($\tau_\mathrm{R} = 1840, 319, 224$ s, respectively; see **Table 4.2**).

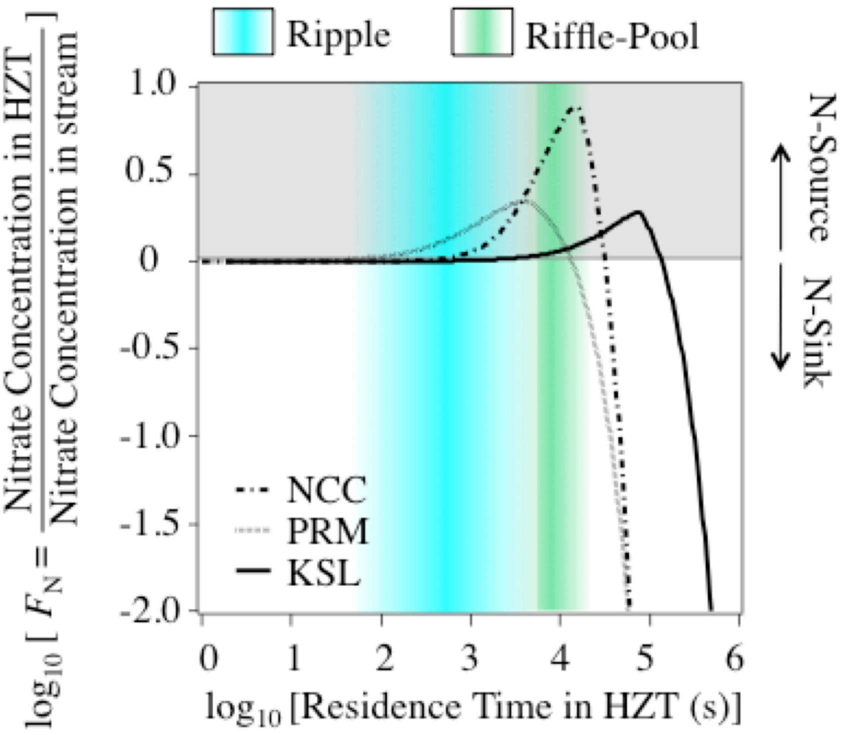

Figure 4.3. Fraction of stream nitrate remaining (F_N) as a function of travel time through a HZT, as predicted by our biokinetic model (equations (6a) through (6c)). Different curves correspond to three LINX II stream sites: NCC, PRM, and KSL (see caption for Figure 2 for details). The vertical bands of color indicate the distribution of residence times for fluvial ripples (turquoise) and riffle-pool sequences (green).

4.4. Hyporheic Exchange Flux and Ambient Groundwater

Hyporheic exchange flux (q_H) refers to the volume of water per unit streambed area per time that circulates between the hyporheic zone and the stream; it excludes vertical ambient groundwater flux (q_V) that moves in only one direction, either from the stream to the sediment under losing conditions or vice versa under gaining conditions. The hyporheic exchange flux is particularly important in the PASS model, because it is the only mechanism by which mass is transported across the sediment-water interface. Also, as noted in **section 4.2.1**, in the limit where all nitrate is removed by denitrification (i.e., the MTL, $\bar{C}_{\text{HZT-NO}_3^-} = 0$), the magnitude of the nitrate uptake velocity is determined solely by the hyporheic exchange flux: $v_{\text{f,MTL}} = -q_{\text{H}}$. Below we examine how ambient groundwater conditions affect the value of q_{H} across two bed form scales; namely riffle-pool sequences and fluvial ripples.

4.4.1. Riffle-Pool Sequences

4.4.1.1. Trauth et al.'s CFD Analysis.

Trauth et al. [2013, 2014] performed CFD simulations of steady state turbulent stream flow over an idealized three-dimensional and fully submerged riffle-pool sequence with a bed slope of S = 2% and a stream width of W = 10 m (streambed topography is reproduced in **Figure 4.4**, lower surface). The period and amplitude of the riffle-pool features were 10 m and 0.5 m, respectively, while the average depth and velocity of the stream were 0.7 m and 1.15 m s^{-1} (for the low discharge scenario, L-Q) and 1 m and 1.95 m s^{-1} (for the high discharge scenario, H-Q) (**Table 4.1**). These CFD simulations yielded pressure distributions over the sediment-water interface, from which Trauth et al. calculated from Darcy's Law hyporheic exchange flow fields subject to an imposed upward ($q_{\text{V}} > 0$, gaining stream) or downward ($q_{\text{V}} < 0$, losing stream) vertical groundwater flux and constant underflow ($q_{\text{U}} = K_{\text{h}} S = 10^{-5}$ m s^{-1}).

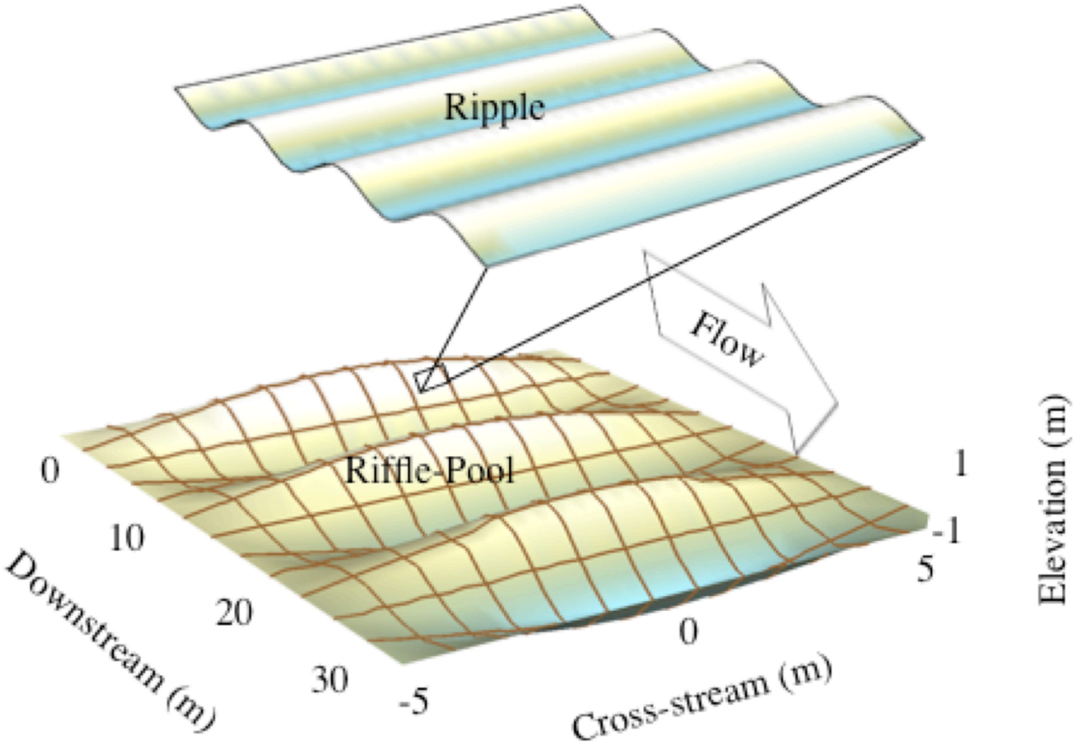

Figure 4.4. Idealized bed form topography assumed for submerged riffle-pool sequences (bottom surface) and fluvial ripples (inset). It should be noted that, depending on sediment grain size and stream velocity, fluvial ripples and riffle-pool sequences may not cooccur in natural streams [Leeder, 2012].

4.4.1.2. Hyporheic Exchange Flux across Riffle-Pool Sequences

Trauth et al.'s simulations of hyporheic exchange flux (q_H, units m s^{-1}) for the ten flow scenarios are reproduced in **Figure 4.5** (dark green and dark orange bars). All else being equal, the hyporheic exchange flux across riffle-pool sequences: (1) is approximately 25% larger for simulations conducted at higher discharge (compare dark orange and dark green bars), and (2) declines sharply with vertical ambient groundwater flux (see reduction in dark orange and dark green bars as the magnitude of q_V increases). The reduction in q_H is similar (although not identical) for gaining ($q_V > 0$) and losing ($q_V < 0$)

conditions. The slight asymmetry arises because, for a three-dimensional streambed, hyporheic flow paths are suppressed by groundwater flux in different parts of the sediment-water interface under gaining and losing conditions [Trauth et al., 2013, 2014].

4.4.2. Fluvial Ripples

4.4.2.1. Boano et al.'s Advective Pumping Model

Elliott and Brooks derived an analytical solution for hyporheic exchange across fluvial ripples [Elliott and Brooks, 1997a, 1997b]. Their so-called advective pumping model, which assumes that hyporheic exchange is driven by a sinusoidal pressure variation over a flat sediment-water interface, was modified by Boano et al. [2008, 2009] to account for vertical (q_{V}) and horizontal (q_{U}) ambient groundwater fluxes (see **Appendix C**, **Text C.2** for details). Boano et al.'s formula for the hyporheic exchange flux is given as follows:

$$q_{\mathrm{H}} = q_{\mathrm{H},0}\sqrt{1-\left(q_{\mathrm{V}}/\pi q_{\mathrm{H},0}\right)^2} + \left(\left|q_{\mathrm{V}}\right|/\pi\right)\sin^{-1}\left(\left|q_{\mathrm{V}}\right|/\pi q_{\mathrm{H},0}\right) - \left(\left|q_{\mathrm{V}}\right|/2\right) \quad (7a)$$

$$q_{\mathrm{H},0} = 2K_{\mathrm{h}}h_0/\lambda \quad (7b)$$

$$h_0 = a\frac{U^2}{2g}\left(\frac{H}{0.34d_s}\right)^m \quad (7c)$$

$$\tau_{\mathrm{T}} = \lambda\theta\big/\left(2\pi^2 q_{\mathrm{H},0}\right) \quad (7d)$$

New variables appearing here include: a characteristic hyporheic exchange flux ($q_{\mathrm{H},0}$); the amplitude of the dynamic pressure head perturbation over the ripple (h_0, units m); the ripple height (*H*, units of m) and wavelength (λ, units of m); stream depth (d_{s}, units m) and mean velocity (*U*, units m s^{-1}); the gravitational constant (g = 9.81 m s^{-2}); two empirical constants (a, m, both unitless); and a characteristic transport timescale for hyporheic exchange (τ_T, units s). Equation (7c) is based on flume measurements of the dynamic pressure head over the surface of triangular dunes submerged in a turbulent stream [Fehlman, 1985]. While Boano et al.'s solution assumes that the streambed is infinitely deep, analogous solutions have been derived for a sediment bed of finite depth with [Marzadri et al., 2015] or without [Packman et al., 2000] vertical ambient groundwater flow.

The hyporheic exchange flux across fluvial ripples was calculated from equation (7a) for the ten ambient flow scenarios described earlier. To this end we adopted ripple dimensions ($H = 0.02$ m and $\lambda = 0.15$ m) and empirical constants ($a = 0.16$ and $m = 3/8$) reported in an experimental flume study by Fox et al. [2014] (see inset, **Figure 4.4**). All other variables were chosen to be consistent with the Trauth et al.'s CFD simulations described earlier (see **section 4.1.1**), including stream depth ($d_s = 1$ and 0.7 m for H-Q and L-Q, respectively), average stream velocity ($U = 1.95$ and 1.15 units m s^{-1} for H-Q and L-Q, respectively), stream slope ($S = 2\%$), porosity ($\theta = 0.3$), ambient groundwater flow ($q_U = 10^{-5}$ m s^{-1} and $q_V = 0, \pm 5.8\times10^{-6}, \pm 23\times10^{-6}$ m s^{-1}), and streambed hydraulic conductivity ($K_h = 5\times10^{-4}$ m s^{-1}) (**Table 4.1**).

4.4.2.2. Hyporheic Exchange Flux across Fluvial Ripples

All else being equal and despite their much smaller size, fluvial ripples generate three to eleven times more hyporheic exchange flux than riffle-pool sequences (**Figure 4.5**, compare light and dark-colored bars). Compared to riffle-pool sequences, the hyporheic

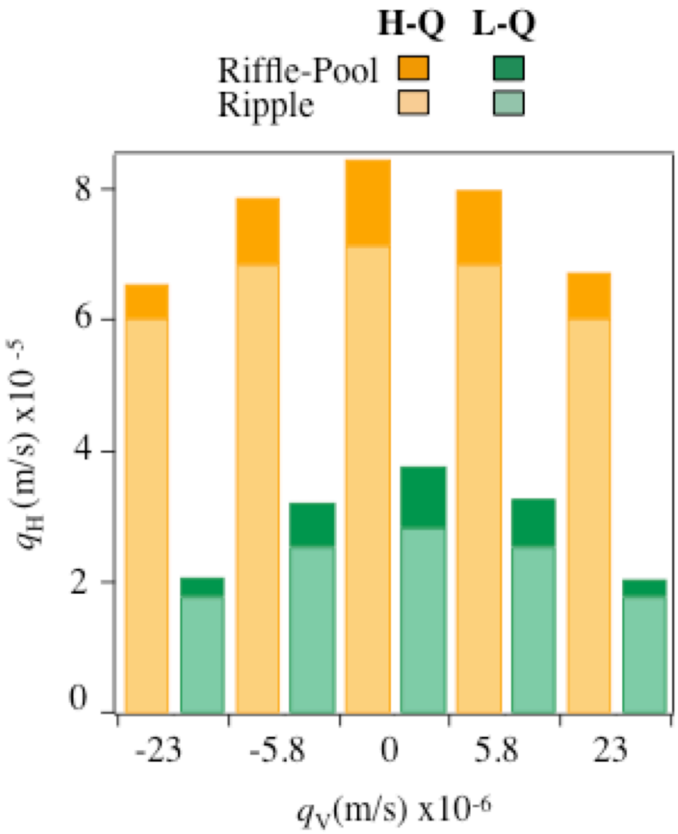

Figure 4.5. Hyporheic exchange flux (q_H) predicted for riffle-pool sequences (dark shades) and fluvial ripples (light shades) in the presence of ambient vertical groundwater flux ($q_V = 0$, $q_V > 0$, and $q_V < 0$ denote neutral, gaining, and losing conditions, respectively), a constant groundwater underflow ($q_U = 10^{-5}$ m s^{-1}), and two stream discharges (Q = 7.4 m^3 s^{-1} (L-Q, green bars) and 17.47 m^3 s^{-1} (H-Q, orange bars)). Hyporheic exchange fluxes reported for the riffle-pool sequences are reproduced from Trauth et al. [2013]; hyporheic exchange fluxes reported for fluvial ripples were calculated from equations (7a) through (7c) in this chapter.

exchange flux across ripples is more sensitive to stream discharge (compare light orange and light green bars) and less sensitive to vertical ambient groundwater flow (increasing magnitude of q_V). Because Boano et al.'s model assumes that the sediment-water interface is flat, the hyporheic exchange flux calculated from equation (7a) declines symmetrically under gaining or losing conditions (see **Appendix C**, **Text C.3** for a discussion of the symmetry properties of Boano et al.'s model).

4.5. Residence Time Distributions.

The PASS model also requires specification of the RTD of water parcels undergoing hyporheic exchange, expressed as a probability density function (PDF) ($E(\tau)$, units s^{-1}, see equation (1b)). As mentioned earlier, $E(\tau)d\tau$ represents the fraction of water circulating through the hyporheic zone with a residence time within $d\tau$ of τ. Likewise, we can define a cumulative distribution function (CDF) form of the RTD (F_{RTD}, unitless), which represents the fraction of water circulating through the hyporheic zone with a residence time τ or younger. The PDF and CDF forms of the RTD are related in the usual way: $E(\tau) = dF_{\text{RTD}}/d\tau$.

As will be seen shortly, the residence time of water parcels undergoing hyporheic exchange varies over many orders of magnitude. The question then arises: what is the best way to represent such probability distributions graphically? An analogous situation arises for environmental particle size distributions (for example aerosols), and such distributions are routinely displayed by dividing the PDF into evenly spaced logarithmic increments of particle diameter [Friedlander, 2000]. Applied to our RTDs, this approach requires the specification of a new PDF (designated here as $E(\log_{10}\tau)$) that divides the fraction of water circulating through the hyporheic zone into equally spaced logarithmic intervals of residence time:

$$E\left(\log_{10}\tau\right)=\frac{dF_{\mathrm{RTD}}}{d\log_{10}\tau}=2.303\tau E\left(\tau\right) \tag{8}$$

The second equal sign in equation (8) follows from evaluating the derivative in the denominator, and then substituting the definition of $E(\tau)$. There are several advantages associated with representing the hyporheic zone RTDs as plots of $E\left(\log_{10}\tau\right)$ against $\log_{10}\tau$: (1) the RTD can be evaluated over many log-cycle changes in residence time τ; (2) the area under such curves is always unity, which allows for the direct comparison of RTDs associated with different scales of hyporheic exchange and different ambient flow conditions; and (3) the physical interpretation of such plots is straightforward, because the height of the curve at any point represents the probability density associated with a particular logarithmic interval of residence time. Below we adopt this approach to investigate the effects of changing ambient groundwater on the RTDs for riffle-pool sequences and fluvial ripples.

4.5.1. RTD of Water Circulating through Riffle-Pool Sequences

Using numerical particle-tracking techniques, Trauth et al. generated RTDs for each of the ten CFD simulations described earlier (see **sections 4.1.1.** and **4.1.2.**). These RTDs, which are reproduced in **Figure 4.6A** and **4.6B**, have a primary mode at around 3 hours

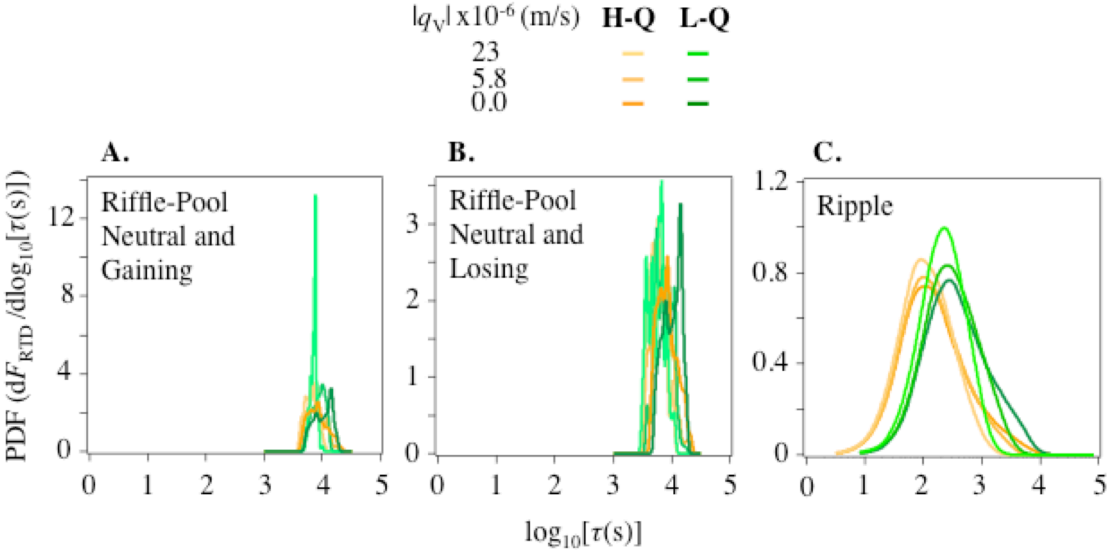

Figure 4.6. Simulated residence time distributions (RTDs) for: (**A**) riffle-pool sequences under neutral and gaining conditions; (**B**) riffle-pool sequences under neutral and losing conditions; and (**C**) fluvial ripples under neutral, gaining, and losing conditions. The curves are colored to represent the ten ambient flow scenarios described in the text. RTDs in **Figures 4.6A** and **4.6B** are reproduced from Trauth et al. [2013]; RTDs in panel **Figure 4.6C** were calculated from the formula derived in this chapter (see equations (9a) through (9c)).

($\tau \approx 10^4$ s) and are confined to a relatively narrow range of log-transformed residence times ($\tau \approx 10^{3.6}$ to $10^{4.3}$ s). The RTDs shift leftward (toward shorter residence times) when vertical groundwater flux is "turned on" (i.e., when the groundwater flux is changed from neutral to losing or gaining). This pattern is particularly apparent at low discharge (see dark to light green curves in **Figure 4.6A** and **4.6B**).

4.5.2. RTD of Water Circulating through Fluvial Ripples

4.5.2.1. Derivation of a New Analytical Solution for the RTD of Fluvial Ripples

Elliott and Brooks derived a formula for the RTD of water parcels undergoing hyporheic exchange; however, their formula does not account for ambient groundwater flow [Elliott and Brooks, 1997a, 1997b]. Here we derive a new RTD formula that is based on Boano et al.'s model of hyporheic exchange (see **section 4.2.1**) and explicitly accounts for ambient groundwater flow of arbitrary orientation and magnitude.

Before we present the new RTD formula, however, it is important to understand how ambient groundwater flow affects the hyporheic exchange flow field. To illustrate, in **Figure 4.7** we present an example of the subsurface flow field predicted by Boano et al.'s model for one of ten ambient flow conditions; namely low stream discharge (L-Q) and vertical and horizontal groundwater flow of $q_{\mathrm{V}} = 2.3\times10^{-5}$ m s^{-1} and $q_{\mathrm{U}} = 10^{-5}$ m s^{-1}, respectively. Noteworthy features of this hyporheic exchange flow field include: (1) when groundwater flow cannot be neglected (i.e., $q_{\mathrm{V}} \neq 0$ and/or $q_{\mathrm{U}} \neq 0$) hyporheic exchange occurs within a defined region of the sediment bed referred to as the interfacial exchange zone (IEZ, see the portion of the sediment bed contained within the thick black curve in the figure) [Cardenas and Wilson, 2007a, 2007b; Cardenas, 2008; Cardenas et al., 2008]; (2) within the IEZ, there are two flow cells, one located on the upstream side of the IEZ, and another located on the downstream side of the IEZ (denoted "upstream cell" and "downstream cell" in the figure); (3) the upstream and downstream flow cells are symmetrical when there is no underflow (i.e., when $q_{\mathrm{U}} = 0$), and asymmetrical otherwise (the upstream and downstream cells in **Figure 4.7** are asymmetrical because $q_{\mathrm{U}} \neq 0$ in this case); and (4) because the upstream and downstream circulation cells are not, in general, symmetrical, the overall RTD (F_{RTD}) has contributions from both the upstream

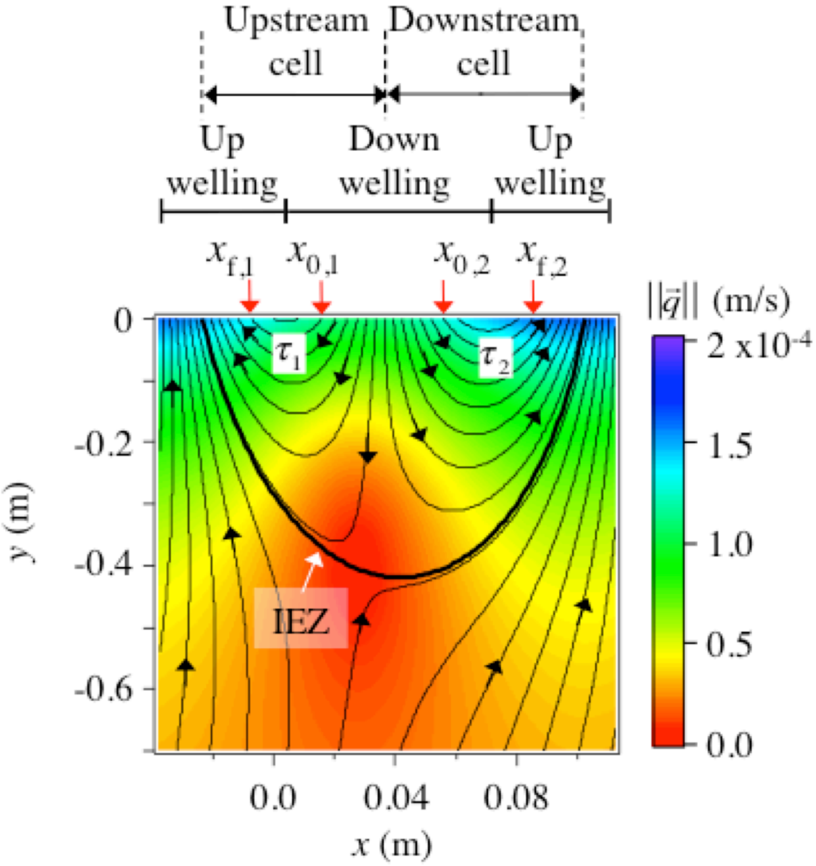

Figure 4.7. Hyporheic exchange in the presence of ambient groundwater flow, as predicted by Boano et al.'s model [2008, 2009]. In this example, streamflow above the sediment-water interface ($y > 0$) is from left to right, the wavelength of the fluvial ripple is 0.15 m, the stream discharge is 7.4 m^3 s^{-1}, and the vertical and underflow groundwater fluxes are 2.3×10^{-5} and 10^{-5} m s^{-1}, respectively. Negative y values represent depth into the sediment bed, x is distance parallel to sediment-water interface (which is assumed to be flat), and color represents the modulus of the Darcy flux. Stream water is pumped into the sediment in high-pressure regions ("downwelling") and back into the stream in low-pressure regions ("upwelling"). Hyporheic exchange is confined to an Interfacial Exchange Zone (IEZ, bold black curve) that includes upstream and downstream flow cells. All streamlines (represented by the thin black curves) have a unique residence time (τ), starting point (x_0), and ending point (x_f); two streamlines have been labeled with subscripts "1" and "2" in the upstream and downstream flow cells, respectively. In this rendering, the volumetric flow rate per unit width between any two adjacent streamlines is the same and equal to $0.2\lambda q_{H,0}$. Functionally, HZTs are equivalent to streamlines (see **Appendix C**, **Text C.3** for further details).

(F_1) and downstream (F_2) circulation cells (see **Appendix C**, **Text C.4** for derivation):

$$F_{\text{RTD}}\left(\overline{\tau}\right) = F_1\left(\overline{\tau}\right) + F_2\left(\overline{\tau}\right) \tag{9a}$$

$$F_1\left(\overline{\tau}\right) = \frac{\left|\overline{q}_{\text{V}}\right|\left(\overline{x}_0^{\text{up-cell}}\left(\overline{\tau}\right) - \sin^{-1}\left|\overline{q}_{\text{V}}\right|\right) - \sqrt{1-\left|\overline{q}_{\text{V}}\right|^2} + \cos\left[\overline{x}_0^{\text{up-cell}}\left(\overline{\tau}\right)\right]}{2\left(\left|\overline{q}_{\text{V}}\right|\left(\pi/2 - \sin^{-1}\left|\overline{q}_{\text{V}}\right|\right) - \sqrt{1-\left|\overline{q}_{\text{V}}\right|^2}\right)} \tag{9b}$$

$$F_2\left(\overline{\tau}\right) = \frac{-\left|\overline{q}_{\text{V}}\right|\left(\overline{x}_0^{\text{down-cell}}\left(\overline{\tau}\right) + \sin^{-1}\left|\overline{q}_{\text{V}}\right| - \pi\right) - \sqrt{1-\left|\overline{q}_{\text{V}}\right|^2} - \cos\left[\overline{x}_0^{\text{down-cell}}\left(\overline{\tau}\right)\right]}{2\left(\left|\overline{q}_{\text{V}}\right|\left(\pi/2 - \sin^{-1}\left|\overline{q}_{\text{V}}\right|\right) - \sqrt{1-\left|\overline{q}_{\text{V}}\right|^2}\right)} \tag{9c}$$

New variables appearing here include a normalized form of the vertical groundwater flux ($\overline{q}_{\text{V}} = q_{\text{V}}/\left(\pi q_{\text{H},0}\right)$) and the location along the sediment-water interface where water first enters the hyporheic zone in the upstream ($\overline{x}_0^{\text{up-cell}} = 2\pi x_0^{\text{up-cell}}/\lambda$) or downstream ($\overline{x}_0^{\text{down-cell}} = 2\pi x_0^{\text{down-cell}}/\lambda$) flow cells.

As currently written, our RTD formula (equations (9a) through (9c)) is expressed as a function of the streamline starting positions $\overline{x}_0^{\text{up-cell}}$ and $\overline{x}_0^{\text{down-cell}}$; these two variables are, in turn, a function of residence time τ. Indeed, as illustrated for two streamlines in **Figure 4.7**, each HZT passing through the upstream or downstream flow cell has a unique: (1) starting position (where water from the stream first enters the HZT, $\overline{x}_0$); (2) final position (where water exits the HZT and returns to the stream, $\overline{x}_{\text{f}} = 2\pi x_{\text{f}}/\lambda$); and (3) travel time ($\tau$) between these two locations. For any starting position ($\overline{x}_0$) in the upstream or downstream flow cell, the corresponding value of τ can be calculated by numerically solving the following set of coupled ordinary differential equations for the trajectory of a water parcel through the hyporheic zone, and recording the residence time τ at which the water parcel crosses the sediment-water interface and returns to the stream:

$$\bar{x}'(\bar{\tau}) = -\cos\bar{x}(\bar{\tau})e^{\bar{y}(\bar{\tau})} + \bar{q}_{\mathrm{U}} \tag{10a}$$

$$\bar{y}'(\bar{\tau}) = -\sin\bar{x}(\bar{\tau})e^{\bar{y}(\bar{\tau})} + \bar{q}_{\mathrm{V}} \tag{10b}$$

$$\bar{x}(0) = \bar{x}_0, \bar{y}(0) = 0 \tag{10c}$$

New variables appearing here include normalized forms of the horizontal ($\bar{x} = 2\pi x/\lambda$) and vertical ($\bar{y} = 2\pi y/\lambda$) coordinates, horizontal groundwater flux ($\bar{q}_{\mathrm{U}} = q_{\mathrm{U}}/(\pi q_{\mathrm{H},0})$), and travel time through the hyporheic zone ($\bar{\tau} = \tau/\tau_{\mathrm{T}} = 2\pi^2 q_{\mathrm{H},0}\tau/(\lambda\theta)$, where τ_{T} (units, s) is a characteristic travel time). A procedure for numerically implementing our RTD solution is described in **Appendix C** (see **Text C.5** and **Code C.2**), along with a comparison of RTDs generated with our formula and new and previously published particle tracking results (**Appendix C**, **Text C.6**).

4.5.2.2. The RTD Results

When our new formula (equations (9) and (10)) is applied to the ten ambient flow conditions described earlier, the resulting RTDs span a very broad range of residence times, from 10 to 10,000 s (**Figure 4.6C**). Each of these RTDs has a single mode (centered around $10^{2.4}$ and $10^{1.9}$ s for the L-Q and H-Q scenarios, respectively); interestingly, the RTDs display only a single mode, despite the fact that hyporheic exchange in this case involves circulation through separate (upstream and downstream) circulation cells (see **Figure 4.7** and discussion thereof). Increasing stream discharge (from L-Q to H-Q) shifts the mode to shorter residence times (compare green and orange RTDs, **Figure 4.6C**). Increasing the ambient groundwater flow, on the other hand, has relatively little effect on either the shape or location of the RTDs, other than to slightly truncate the upper tail and increase the probability density associated with the mode. It should be noted that, for the largest vertical groundwater flux tested ($|q_\mathrm{V}| = 23\times10^{-6}$ m s^{-1}), the ratio $|q_\mathrm{V}|/q_\mathrm{H}$ ranged from 0.38 to 1.3. Thus, our observation that increasing vertical groundwater flux has little impact on the RTD cannot be dismissed as an artifact of choosing vertical groundwater fluxes that are much smaller than the hyporheic exchange flux. Indeed, Fox et al. [2016] reached a similar conclusion, based on flume measurements of hyporheic exchange in the presence of an imposed vertical groundwater flux. These authors noted that the mean residence time of water undergoing hyporheic exchange varies only modestly when the groundwater flux is increased in either a gaining or losing configuration.

4.6. PASS Model Predictions for the Nitrate Uptake Velocity

We now have all of the information—evolution of the nitrate concentration with residence time, hyporheic exchange fluxes, and RTDs—required to calculate nitrate uptake velocities from the PASS model (see equations (1a) and (1b)). In the discussion below we present results for three different forms of the nitrate uptake velocity: (1) total uptake defined as the flux of nitrate out of the sediment ($U_{\mathrm{NO}_3^-}$, units mol m^{-2} s^{-1}) normalized by the in-stream concentration of nitrate ($v_\mathrm{f} = U_{\mathrm{NO}_3^-}/C_{\text{S-NO}_3^-}$, units of m s^{-1}); (2) direct denitrification of stream nitrate, defined as two times the flux of nitrogen gas generated by the denitrification of stream nitrate ($2U_{\mathrm{N}_2,\mathrm{Dw}}$, units mol m^{-2} s^{-1}) normalized by the in-stream concentration of nitrate ($v_{\mathrm{f,Dw}} = 2U_{\mathrm{N}_2,\mathrm{Dw}}/C_{\text{S-NO}_3^-}$, units of m s^{-1}) (note that the factor of two is included here because, during denitrification, two molecules of nitrate are reduced for every molecule of N_2 generated); and (3) coupled nitrification-denitrification of ammonium downwelled from the stream or generated in situ by ammonification, defined as two times the flux of dinitrogen gas generated by the denitrification of new nitrate ($2U_{\mathrm{N_2,Dn}}$, units mol m^{-2} s^{-1}) normalized by the in-stream concentration of nitrate ($v_{\mathrm{f,Dn}} = 2U_{\mathrm{N_2,Dn}} \big/ C_{\mathrm{S\text{-}NO_3^-}}$, units of m s^{-1}).

Together these three forms of the nitrate uptake velocity provide a complete accounting of the ways nitrate is generated and removed in the hyporheic zone, and are useful in different contexts. For example, the total nitrate uptake velocity (v_{f}) is of great practical interest, because the sign and magnitude of this quantity indicates whether, and to what extent, the sediments are a net source of nitrate (by net nitrification, $v_{\mathrm{f}} > 0$) or a net sink of nitrate (by net denitrification, $v_{\mathrm{f}} < 0$). On the other hand, field studies that quantify the rate at which stream nitrate is denitrified to N_2 (e.g., as v_{fden} values estimated from the LINX II $^{15}\mathrm{NO_3^-}$ seeding studies [Mulholland et al., 2008], see **section 4.3.2**) will be directly comparable to our model-predictions of $v_{\mathrm{f,Dw}}$. Finally, studies of coupled nitrification-denitrification (e.g., using $^{15}\mathrm{NH_4^+}$ seeing experiments as in Peterson et al. [2001], or the isotope pairing method of Nielsen and Sloth [1994]) will be directly comparable to our model-predictions of $v_{\mathrm{f,Dn}}$. A Mathematica script for calculating the three forms of uptake velocity is presented in **Appendix C** (**Code C.3**). Our model-predictions for the three uptake velocities (v_{f}, $v_{\mathrm{f,Dw}}$, $v_{\mathrm{f,Dn}}$) are tabulated for all scenarios in the **Appendix C**, **Table C.2** and **C.3** and described below.

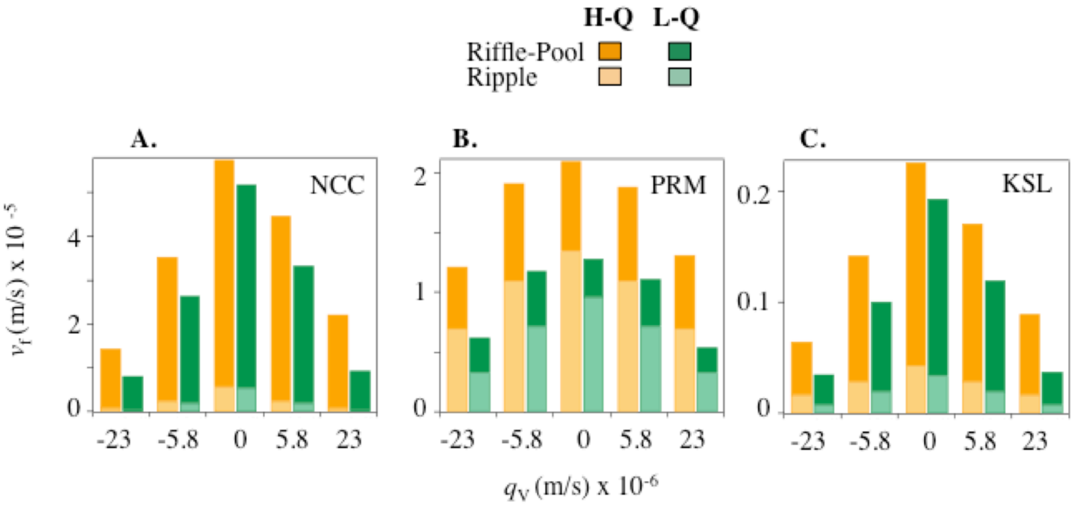

Figure 4.8. Model-predicted response of the total nitrate uptake velocity (v_f) to stream discharge (orange and green bars), bed form scale (light and dark shades), vertical ambient groundwater flux (horizontal axes), and biogeochemistry at the three LINX II stream sites: **(A)** NCC, **(B)** PRM, and (**C**) KSL (compare with **Figure 4.5**).

4.6.1. Effect of Stream Chemistry

Our model simulations predict that streambed sediments are a net source of nitrate at all three sites ($v_f > 0$, net nitrification), with v_f decreasing in order: NCC > PRM > KSL (**Figure 4.8**, compare vertical axes). At first glance, it is surprising that the pristine site (NCC) would have the largest v_f value. This can be explained by the site's low nitrate concentration ($C_{\text{S-NO}_3^-} = 0.0007$ mol m^{-3}, see **Table 4.2**), which makes even a small nitrate flux manifest as a large positive nitrate uptake velocity (recall, $v_f \propto 1/C_{\text{S-NO}_3^-}$).

Uptake velocities for direct denitrification of stream nitrate ($v_{f,Dw}$, **Figure 4.9A-C**) and coupled nitrification-denitrification ($v_{f,Dn}$, **Figure 4.9D-F**) varies across the three sites, declining in order: PRM > NCC > KSL. Respiration time scales exhibit the opposite

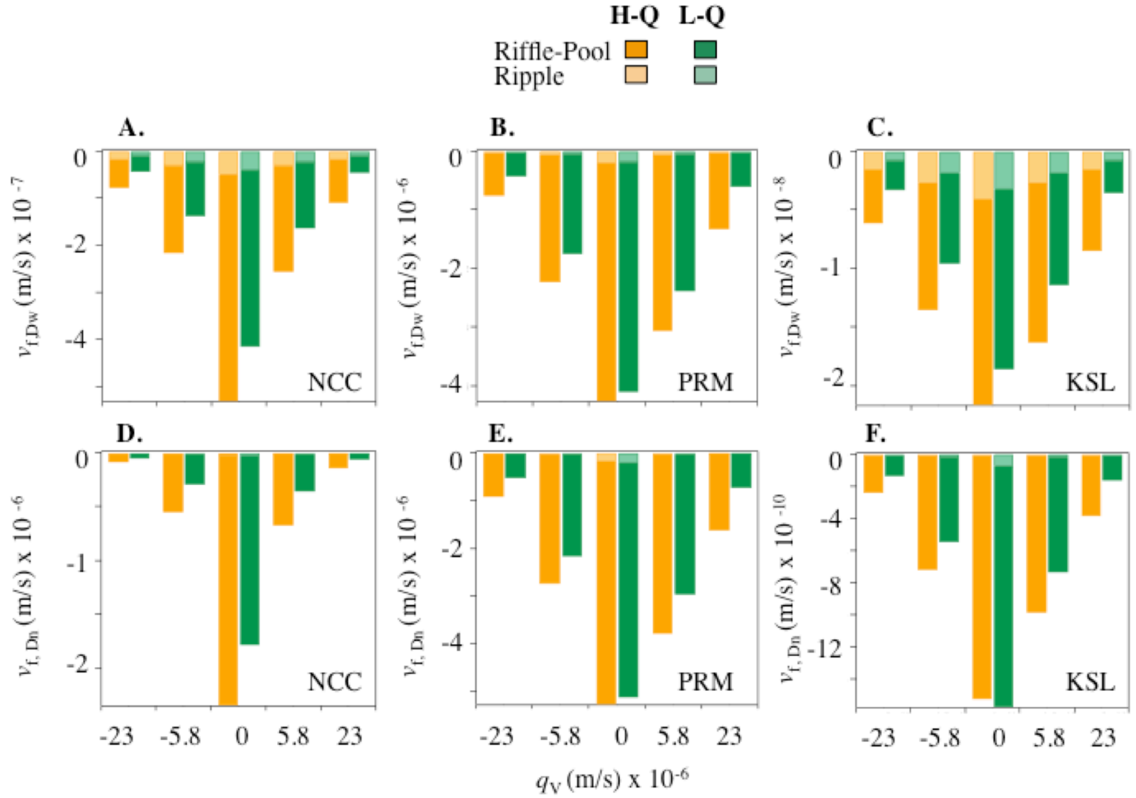

Figure 4.9. (A-C) Model-predicted response of the uptake velocities for direct denitrification of stream nitrate ($v_{f,Dw}$) and **(D-F)** coupled nitrification-denitrification ($v_{f,Dn}$) to stream discharge (orange and green bars), bed form scale (light and dark shades), vertical ambient groundwater flux (horizontal axes), and biogeochemistry at the three LINX II stream sites: (**A** and **D**) NCC, (**B** and **E**) PRM, and (**C** and **F**) KSL (compare with **Figure 4.8**).

order (KSL >> NCC > PRM, see **Tabe 4.2**), which is expected given that denitrification occurs faster at sites with shorter respiration timescales.

Our prediction that streambed sediments are a net source of nitrate ($v_f > 0$, **Figure 4.8**) is contrary to the general observation that streambeds are a net sink of nitrate [Birgand et al., 2007], although there are notable exceptions [Holmes et al., 1994; Ribot et al., 2012]. There are at least two possible explanations for this discrepancy. First, as noted earlier, our model does not account for assimilation of nitrate by benthic autotrophic and heterotrophic organisms, and assimilation is known to dominate uptake velocities in many streams. For example, Mulholland et al. [2008] found that assimilation accounted for between 57 and 84% of the nitrate uptake observed in the LINX II $^{15}NO_3^-$-seeding studies, although some of the assimilated nitrate will be remineralized and released back to the stream over time scales of weeks to years [Peterson et al., 2001; Mulholland et al., 2000]. Second, our model may overestimate the generation of nitrate, either by overestimating in situ nitrification rates and/or over-estimating the generation of ammonium by ammonification.

In a multimethod study of N-cycling in the upper Mississippi River basin (USA), Bohlke et al. [2009] found that most of the nitrate being denitrified in streambed sediments was downwelled from the stream (direct denitrification of stream nitrate), and to a lesser extent supplied by in situ nitrification of ammonium (coupled nitrification-denitrification). These authors went on to note that coupled nitrification-denitrification is more common in estuarine or marine systems, which have "lower NO_3^- concentrations, higher sediment NH_4^+ concentrations, and steeper sub-bottom redox gradients." With the exception of the KSL site, our model predictions for $v_{f,Dn}$ (**Figure 4.9D** and **4.9E**) are similar (PRM) or larger (NCC) in magnitude than model predictions for $v_{f,Dw}$ (**Figure 4.9A** and **4.9B**). Thus, at PRM and NCC our model predicts that coupled nitrification-denitrification is a significant fraction of total denitrification, in violation of field observations for freshwater streams.

There are a several reasons our model may overestimate nitrification rates. Our biokinetic model assumes that the organic carbon mineralization rate (R_{min}) is constant, whereas in reality R_{min} declines with travel time through the hyporheic zone [Zarnetske et al., 2015]. Our model also assumes that all ammonium produced by ammonification or downwelled from the stream is available for nitrification, when in reality a portion of the ammonium will sorb to stream sediments or undergo biological assimilation. Indeed, based on $^{15}\mathrm{NH}_4^+$ stream seeding studies, Peterson et al. [2001] concluded that ammonium is removed primarily by assimilation and sorption to sediments, and "secondarily by nitrification." These model limitations can be addressed by increasing model complexity, for example by adding: (1) an additional term to the mass balance equation for nitrate (equation (4b)) to account for the kinetics of nitrate assimilation [e.g., see Birgand et al., 2007]; (2) a rate equation to the biokinetic model for the evolution of dissolved and/or particulate organic carbon concentration with travel time [Zarnetske et al., 2012]; and (3) additional terms to the mass balance equation for ammonium (equation (4c)) to account for adsorption and assimilation [Thibodeaux and Mackay, 2011].

While our model appears to overestimate v_{f} and $v_{\mathrm{f,Dn}}$, estimates of direct denitrification ($v_{\mathrm{f,Dw}}$) fall within the range measured by Mulholland et al. [2008] during the LINX II studies (**Figure 4.10**). It should be stressed that the physical parameters adopted for these simulations, such as stream flow and the hydraulic conductivity of the streambed sediments (see **Table 4.1**), were not tailored to the LINX II sites. Thus we do not expect model predictions for $v_{\mathrm{f,Dw}}$ to align precisely with the experimentally observed values at NCC, PRM, and KSL (indicated in the figure by large stars).

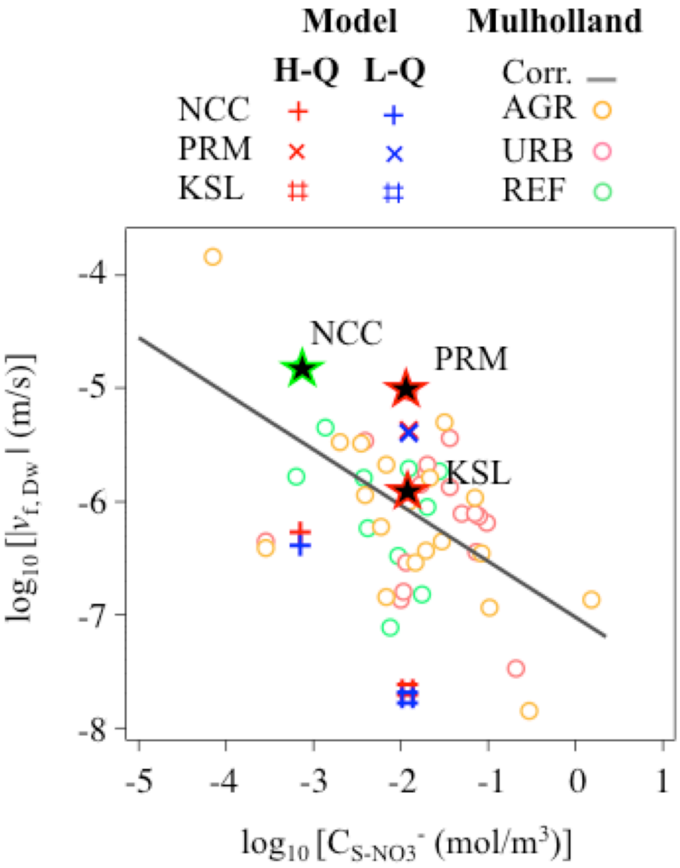

Figure 4.10. Comparison of model-predicted (blue and red crosses and hatchmarks) and field-measured (colored circles and stars) uptake velocities for the direct denitrification of stream nitrate ($v_{f,Dw}$) plotted against in-stream nitrate concentration ($C_{S\text{-}NO_3^-}$). The stars correspond to LINX II sites (NCC, PRM, KSL) and the black line is an empirical correlation proposed by Mulholland et al. [2008] between denitrification velocity and in-stream nitrate concentration proposed. Data reproduced from Mulholland et al. [2008].

4.6.2. Effect of Bedform Scale

4.6.2.1. Bedform Scale and Nitrification Rates

Despite the fact that ripples generate up to 11 times more hyporheic exchange flux than riffle-pool sequences (see **section 4.4**), the nitrate uptake velocities predicted for the NCC and KSL sites indicate that more nitrate is produced by riffle-pool sequences than by fluvial ripples (compare light and dark color shades, **Figure 4.8A** and **4.8C**). This result can be understood by noting that riffle-pool sequences have relatively long residence times, which in well-oxygenated sediments favor nitrate generation by nitrification. Indeed, comparing F_N curves (predicted by our biokinetic model, **Figure 4.3**) with the range of residence times estimated for ripples and riffle-pool sequences (turquoise and green bands of color in the figure) supports the idea that the longer residence times associated with riffle-pools should result in net nitrate generation in NCC and KSL; i.e., the peak in the F_N curve coincides with the range of residence times for water circulating through the riffle pool sequences. On the other hand, ripples and riffle-pool sequences contribute roughly equally to nitrate generation at PRM (compare light and dark color shades, **Figure 4.8B**), consistent with the partial overlap between the peak of the F_N curve for this site and the RTDs of both ripples and riffle-pool sequences (**Figure 4.3**).

4.6.2.2. Bedform Scale and Denitrification Rates

Not surprisingly given their longer residence times, riffle-pools also dominate N removal by direct denitrification (**Figure 4.9A-9C**) and coupled nitrification-denitrification (**Figure 4.9D-9F**). Indeed, according to our model simulations, ripples have virtually no functional role relative to nitrate generation or removal, despite their outsized role in flushing water through the hyporheic zone (**Figure 4.5**). It should be noted that bed forms can be net producers of nitrate (i.e., $v_f > 0$) even while they remove N by direct denitrification ($v_{f,Dw} < 0$) and coupled nitrification-denitrification ($v_{f,Dn} < 0$). In such cases, the generation of nitrate by nitrification exceeds the removal of nitrate by one or more pathways.

4.6.3 Effect of Ambient Groundwater Flow and Stream Discharge

The model-predicted uptake velocities (v_f, $v_{f,Dw}$, and $v_{f,Dn}$) decline sharply with increasing vertical ambient groundwater flow under both gaining and losing conditions (**Figures 4.8 and 4.9**). This occurs because the nitrate uptake velocities are proportional to q_H (see equation (1a)) and q_H declines as the magnitude of q_V is increased (**Figure 4.5**). The magnitude of the nitrate uptake velocity is almost always larger at higher stream discharge (compare dark orange and green bars for riffle-pool sequences, and light orange and green bars for ripples, **Figures 4.8** and **4.9**), reflecting the importance of stream discharge as a primary driver of hyporheic exchange flux.

4.6.4. The Damköhler Number

As noted earlier, the Damköhler number has been proposed as a master variable for nitrate removal and generation in the hyporheic zone of streams. For example, Zarnetske et al. [2012] reported that, across a wide range of randomly selected biokinetic model parameter values, the fractional reduction in nitrate concentration along a single flow path through the hyporheic zone (F_N, see equation (2b)) exhibited a general pattern in which net denitrifying conditions ($F_N < 0$) coincided with Da > 1, whereas net nitrifying conditions ($F_N > 0$) coincided with Da < 10.

To see if a similar pattern applies to our results, we compared model-predicted v_f, $v_{f,Dw}$, and $v_{f,Dn}$ values against their corresponding Da values. As applied here, the Damköhler number is the ratio of timescales for transport and organic carbon mineralization in the hyporheic zone: Da = $\tau_{\mathrm{T}}/\tau_{\mathrm{R}}$. The respiration timescale is the ratio of the half-saturation constant for aerobic respiration and the organic carbon mineralization rate ($\tau_{\mathrm{R}} = K_{\mathrm{O_2}}^{\mathrm{sat}}/R_{\mathrm{min}}$). The definition of τ_{T}, on the other hand, varies by bedform scale. For fluvial ripples, we set τ_{T} equal to the characteristic transport timescale described earlier for Boano et al.'s advective pumping model (see equation (7d)). For riffle-pool sequences, we first fit Trauth et al.'s RTDs (obtained from particle tracking experiments) to a lognormal distribution, and equated τ_{T} to the geometric means thus obtained (see **Appendix C**, **Table C.3**).

When normalized by the hyporheic exchange flux (q_{H}), the uptake velocities exhibit a simple functional dependence on Da (**Figure 4.11**). For Da < 10, the uptake velocities are a negligible fraction of the hyporheic exchange flux (i.e., $v_{\mathrm{f}}/q_{\mathrm{H}} \approx v_{\mathrm{f,Dw}}/q_{\mathrm{H}} \approx v_{\mathrm{f,Dn}}/q_{\mathrm{H}} \approx 0$). Under such conditions the sediment bed has no functional role relative to the consumption or generation of nitrate. Above Da = 10, v_{f} increases with Da, while $v_{\mathrm{f,Dw}}$ and $v_{\mathrm{f,Dn}}$ decrease with Da. Even at the largest Da tested (~10), direct denitrification and coupled nitrification-denitrification are reaction limited (i.e., $v_{\mathrm{f,Dn}}/q_{\mathrm{H}}, v_{\mathrm{f,Dw}}/q_{\mathrm{H}} > -1$). Furthermore, nitrate generation by nitrification outcompetes nitrate removal by both direct denitrification and coupled nitrification-denitrification; as a result, v_{f} is a positive increasing function of Da. While the results presented in **Figure 4.11** are broadly consistent with those reported by Zarnetske et al. [2012], there are several important differences. Zarnetske et al.'s relationship between F_{N} and Da is relatively diffuse; i.e., the simulations for various random choices of biokinetic model parameters broadly fall into two categories—net denitrifying for Da > 1 and net nitrifying for Da <10,

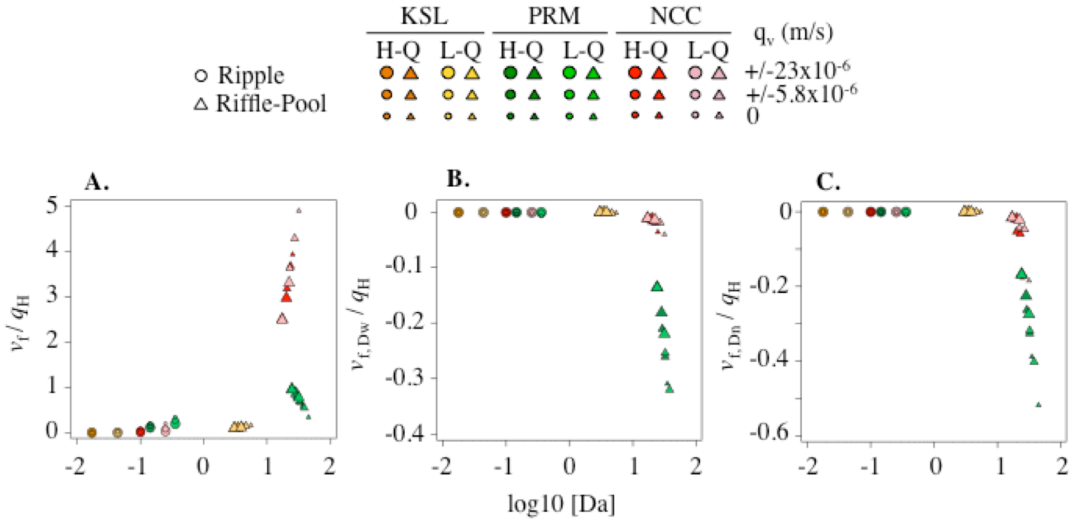

Figure 4.11. Model predictions for (**A**) total uptake velocity, (**B**) uptake velocity for direct denitrification of stream nitrate, and (**C**) uptake velocity for coupled nitrification-denitrification. When normalized by the hyporheic exchange flux (q_H), the respective uptake velocities exhibit a relatively monotonic dependence on the Damköhler number (Da, horizontal axis). The circles and triangles denote ripples and riffle-pool sequences, respectively; their color denotes biogeochemical setting (KSL, PRM, NCC); and their size denotes the magnitude of the vertical groundwater flux.

see Figure 4 in their paper. By contrast, our model-predicted uptake velocities exhibit a nearly monotonic dependence on Da (**Figure 4.11**). There are several possible explanations. First, in preparing **Figure 4.11** we normalized our uptake velocities by their corresponding hyporheic exchange fluxes. Any variation in uptake velocity attributable solely to variation in advective mass transfer across the sediment-water interface (e.g., brought on by changing vertical groundwater flux, see **Figure 4.5**) has been removed by normalization. Second, as revealed by our earlier PCA analysis (see **Figure 4.2** and **section 4.3.2.2**) the various parameters characterizing stream biogeochemistry strongly co-vary across stream sites. Hence, some of the scatter in Zarnetske et al.'s F_N versus Da relationship may result from treating the biokinetic model parameters as statistically independent—an intrinsic assumption in the Monte Carlo sampling approach these authors employed to generate realizations of F_N. Finally, we have accounted for the in situ generation of ammonium by oxidation of organic matter (ammonification). By contrast, the only source of ammonium in Zarnetske et al.'s simulations is ammonium downwelled from the stream. As a result, our simulations indicate that streambed sediments can be net nitrifying well above Da = 10, whereas nitrification is ammonium-limited at values of Da > 10 in Zarnetske et al.'s simulations.

Our model simulations also suggest that vertical groundwater flux can affect the balance of nitrification and denitrification by altering hyporheic zone RTDs. For example, increasing $|q_V|$ at the PRM site causes the riffle-pool RTD to shift leftward (**Figure 4.6A** and **4.6B**), increases the overlap between the F_N peak and the riffle-pool RTD (**Figure 4.3**), and thereby increases the net generation of nitrate (i.e., v_f/q_H becomes more positive with increasing $|q_V|$, see green triangles in **Figure 4.11A**). The opposite pattern prevails at NCC, where increasing the vertical groundwater flux decreases the overlap between the F_N peak and the riffle-pool RTD (**Figure 4.3**) and reduces the net generation of nitrate (v_f/q_H declines with increasing $|q_V|$, red triangles in **Figure 4.11A**). These groundwater-induced shifts in the hyporheic zone RTD can also affect denitrification rates. For example, at PRM the magnitudes of $v_{f,Dw}$ and $v_{f,Dn}$ decline with increasing vertical groundwater flux (green triangles in **Figure 4.11B** and **4.11C**). In this case, vertical groundwater flux induces a leftward shift in the RTD, increases the oxygen content of the hyporheic zone, and thereby suppresses both direct denitrification and coupled nitrification-denitrification.

In summary, the results presented in **Figure 4.11** suggest that hyporheic exchange flux and the Damköhler number exert a primary control on N-cycling in streams. In turn, these two controls on N-cycling are strongly influenced by the vertical groundwater flux. Hyporheic exchange flux controls trafficking of mass and water across the sediment-water interface, and therefore as q_H decreases so does the magnitude of v_f, $v_{f,Dw}$, and $v_{f,Dn}$ (see equation (1a)). All else being equal, increasing the Damköhler number increases denitrification rates, but can also increase ammonification rates in oxygenated sediments, and provided that the rate of ammonification is proportional to the mineralization rate of organic carbon, as assumed here. The biogeochemical setting (as reflected in the choice of biokinetic model parameters) will ultimately determine which of these two opposing processes—increased nitrate production by ammonification and nitrification versus increased nitrate removal by denitrification—dominates as Da increases. Finally, the vertical groundwater flux can affect nitrate processing in at least two ways, by attenuating the hyporheic exchange flux (q_H, see **Figure 4.5**) and by inducing a leftward shift in the RTD of water passing through the hyporheic zone (see **Figure 4.6**).

4.7. Scaling-Up to Stream Reaches and Watersheds

In this section, we translate our model-predicted nitrate uptake velocities into the fraction f (unitless) of nitrate load removed or added by hyporheic exchange over a stream reach. From a steady state mass balance over a differential length of stream and assuming uniform flow and neglecting longitudinal dispersion, the following differential equation describes the change in nitrate concentration with downstream distance x associated with

N-cycling in the hyporheic zone (all variables defined previously also see notation section):

$$\frac{dC_{\text{S-NO}_3^-}}{dx} = \frac{v_\text{f}}{d_\text{s}U} C_{\text{S-NO}_3^-} \tag{11}$$

For a stream reach of length ℓ equation (11) can be integrated to yield the following expression for the evolution of nitrate concentration over the stream reach:

$$\frac{C_{\text{S-NO}_3^-}(x=\ell)}{C_{\text{S-NO}_3^-}(x=0)} = \exp\frac{v_\text{f}\ell}{d_\text{s}U} = \exp\frac{v_\text{f}}{H_\text{L}} \tag{12}$$

The hydraulic loading rate (units m s^{-1}) is defined as $H_\text{L} = Q/(W\ell)$ and stream discharge is given by $Q = UWd_\text{s}$. If the hyporheic zone is a net sink of nitrate ($v_\text{f} < 0$), then the fraction of nitrate load removed (f_R, unitless) from the stream by hyporheic exchange over the stream reach ℓ can be written as follows:

$$f_\text{R} = \frac{L_{x=0} - L_{x=\ell}}{L_{x=0}} = 1 - \exp\frac{v_\text{f}}{H_\text{L}}, v_\text{f} < 0 \tag{13}$$

Where $L_{x=0}$ and $L_{x=\ell}$ (both units of mol s^{-1}) are loading rate of nitrate at $x = 0$ and $x = \ell$, respectively. Conversely, if the sediments are a net nitrate source ($v_\text{f} > 0$), then the fraction of nitrate load added (f_A, unitless) by hyporheic exchange over the stream reach ℓ becomes:

$$f_A = \frac{L_{x=\ell} - L_{x=0}}{L_{x=0}} = \exp\frac{v_\text{f}}{H_\text{L}} - 1, v_\text{f} > 0 \tag{14}$$

Equations (13) and (14) can be consolidated into a single expression for the fraction f (unitless) of nitrate load removed or added by hyporheic exchange:

$$f = \left|1 - \exp\frac{v_\text{f}}{H_\text{L}}\right| \tag{15}$$

Equation (15) makes clear that the fate and transport of nitrate in streams depends on the relative strength of biological processes in the hyporheic zone (as quantified by the nitrate uptake velocity v_f) and horizontal transport in the stream (as quantified by hydraulic loading rate, H_L). For a 1 km reach of a 10 m wide stream with discharge of 7.4 m^3 s^{-1} (corresponding to our L-Q scenario), under neutral conditions our estimates of v_f imply that stream nitrate load is increased by 0.7%, 0.2%, and 0.03% in NCC, PRM, and KSL, respectively. For our maximum gaining condition (q_V = $+23\times10^{-6}$ m s^{-1}) these numbers become 0.1%, 0.07%, and 0.005%, respectively.

Scaling such calculations up to an entire watershed (e.g., using a stream network model) [Wollheim et al., 2006] will require estimating q_H and $E(\tau)$ for each stream reach in the network. In the case of ripples, these two quantities can be estimated from equation (7a), and equations (9a) through (9c) given reach-by-reach values for: (1) vertical q_V and horizontal q_U groundwater flux (e.g., based on stream slope, sediment hydraulic conductivity, and estimates of groundwater flux across the sediment-water interface) [Caruso et al., 2016]; (2) stream discharge, width, and depth (e.g., based on stream network model calculations together with appropriate scaling-laws) [see Mulholland et al. [2008]; and (3) the amplitude and wavelength of submerged bed forms responsible for hyporheic exchange. Because small bedforms will likely dominate hyporheic exchange flux (see **Figure 4.5**), restricting such calculations to fluvial ripples may be sufficient in cases where nitrate removal is transport limited and therefore $v_f \approx v_{f,MTL} = -q_H$. However, virtually all of our model simulations suggest that, while ripples dominate hyporheic exchange flux, riffle-pool sequences dominate nitrate processing. In this case, it is probably not feasible to conduct reach-by-reach CFD simulations of hyporheic exchange, like those reported by Trauth et al. [2013]. Instead, scaling laws [e.g., Marzadri et al., 2010; Tonina, 2013] could provide estimates for q_{H} and $E(\tau)$ at the riffle-pool scale under neutral conditions. Further research is needed to determine how such scaling relationships should be modified to account for ambient groundwater flow.

4.8. Modeling Limitations and Future Directions

Beyond the limitations already identified with our biokinetic model (see **section 4.6.1.2**), there are several aspects of the PASS modeling framework that could be improved moving forward. One potential limitation is that denitrification can only occur once oxygen is depleted along the HZT; i.e., for travel times past the oxic-anoxic transition. Several recent studies suggest that small-scale heterogeneities, or "microzones", within the hyporheic zone can be hotspots for denitrification, even when the bulk sediment is aerobic [Harvey et al., 2013; Aubeneau et al., 2014, 2015a, 2015b; Briggs, 2015; Sawyer, 2015]. On the other hand, experimental studies of buried macroalgae within sand ripples indicate that this type of heterogeneity may not affect denitrification rates [Bourke et al., 2014]. Microzones may arise from: (1) physical heterogeneities (such as internal porosity within sediment grains) where water parcels become trapped for long periods of time [Kessler et al., 2014]; and (2) spatial variations in reaction rates caused by, for example, variable biofilm density and organic carbon inclusions (e.g., leaf litter or benthic diatoms). Within the HZT framework, physical heterogeneities can be represented by heavy tailed RTD functions, where the "heavy" part of the tail accounts for the trapping of water parcels in immobile zones. Indeed, so-called "mobile-immobile" (MIM) models have been developed to represent reactive mass transport through porous media with slow and fast transport pathways [e.g., Schumer et al., 2001, 2003, and 2009]. Presumably, MIM models could be used to represent heterogeneous transport within individual HZTs, along the lines reported in Sanz-Prat et al. [2015]. Accounting for biogeochemical heterogeneities, on the other hand, may require adopting a probabilistic, rather than deterministic, description of hyporheic zone reaction fields [e.g., see Rawlings and Ekerdt 2013]. N-cycling can also occur in other components of the stream (i.e., other than the hyporheic zone), such as the stream's water column or in hydraulically disconnected surface storage zones [Stewart et al., 2011].

Finally, while we have focused here on the processing of stream-borne nitrate by hyporheic exchange, it is important to acknowledge that groundwater can also be a significant source of nitrate, particularly in agricultural areas [Hinkle et al., 2001; Smith et al., 2009]. Upwelling of nitrate-contaminated groundwater can affect stream water quality both directly by adding nitrate to the stream, and indirectly by altering features of the hyporheic zone that influence denitrification (as illustrated in this study). Indeed, groundwater upwelling can create conditions favorable for denitrification and the removal of groundwater-borne nitrate, for example, by limiting the depth of aerobic respiration within the streambed and harnessing the denitrification potential of deeper sediments [Hester et al., 2013; Lansdown et al., 2015].

Appendix C. Numerical codes, derivations, and supplemental figures and tables

4.9. Notation

a	empirical pre-factor in the Fehlman [1985] correlation between hyporheic exchange flux, stream velocity, water depth, and bed form geometry (see equation (7c)) (-)
α	normalized in-stream concentration of ammonium by in-stream concentration of oxygen (-)
AM	ammonification
Anammox	anaerobic ammonium oxidation
AR	aerobic respiration
β	normalized in-stream concentration of nitrate by in-stream concentration of oxygen (-)
C_{DOC}	interstitial concentration of dissolved organic carbon (mol m^{-3})
"chemistry"	subsurface biogeochemical reactions that consume and produce nitrate
CDF	cumulative distribution function (-)
CFD	computational fluid dynamics
CH_2O	formaldehyde representing dissolved organic carbon
$C_{\text{HZT-NH}_4^+}$	interstitial concentration of ammonium along a HZT (mol m^{-3})
$\hat{C}_{\text{HZT-NH}_4^+}$	interstitial concentration of ammonium along a HZT normalized by in-stream concentration of molecular oxygen (-)
$C_{\text{HZT-NO}_3^-}$	interstitial concentration of nitrate along a HZT (mol m^{-3})
$\hat{C}_{\text{HZT-NO}_3^-}$	interstitial concentration of nitrate normalized by in-stream concentration of molecular oxygen (-)
$\bar{C}_{\text{HZT-NO}_3^-}$	normalized "breakthrough" concentration of nitrate in an upwelling zone (see equation (1b)) (-)
$C_{\text{HZT-O}_2}$	interstitial concentration of molecular oxygen along a HZT (mol m^{-3})
$\hat{C}_{\text{HZT-O}_2}$	normalized interstitial concentration of molecular oxygen by in-stream concentration of molecular oxygen (-)
CO_2	carbon dioxide
$C_{\text{S-NH}_4^+}$	in-stream concentration of ammonium (mol m^{-3})
$C_{\text{S-NO}_3^-}$	in-stream concentration of nitrate (mol m^{-3})
$C_{\text{S-O}_2}$	in-stream concentration of oxygen (mol m^{-3})
Da	Damköhler number
DN	denitrification
DNRA	dissimilatory nitrate reduction to ammonium
DOC	dissolved organic carbon
d	approximate depth over which mineralization of organic carbon and respiratory denitrification occur (m)
d_s	depth of stream (m)
δ	relative rates of nitrification and respiration
$\delta\left(\tau-\tau^*\right)$	Dirac delta function representation of an RTD with single residence time τ^* (s^{-1})
ER	ecosystem respiration (mol m^{-2} s^{-1})
$E(\tau)$	PDF form of the hyporheic zone RTD (s^{-1})

f	fraction of nitrate load removed or added by hyporheic exchange over a stream reach (-)
f_{R}	fraction of nitrate load removed from the stream by hyporheic exchange over a stream reach (-)
f_{A}	fraction of nitrate load added to the stream by hyporheic exchange over a stream reach (-)
F_1	contribution of the upstream flow cell to the ripple RTD (-)
F_2	contribution of the upstream flow cell to the ripple RTD (-)
F_{N}	fraction of nitrate remaining in HZT after a water parcel travels through the hyporheic zone (-)
F_{RTD}	CDF function (-)
g	gravitational constant (m s^{-2})
γ_{CN}	moles of ammonium released per mole of carbon mineralized (-)
H	height of ripples (m)
H_{L}	hydraulic loading rate (m s^{-1})
H-Q	high stream discharge scenario
h_0	amplitude of the dynamic pressure head perturbation over a ripple (m)
HZT	hyporheic zone tube
IEZ	interfacial Exchange Zone
κ	moles of carbon oxidized per mole of nitrate reduced during respiratory denitrification (-)
K_{h}	hydraulic conductivity (m s^{-1})
KSL	Little Kitten Creek in Kansas; an urban-impacted site selected from LINX II data set
k_{min}	first-order mineralization rate constant (s^{-1})
k_{NI}	nitrification rate constant (m^3 mol^{-1} s^{-1})
$K^{\mathrm{sat}}_{\mathrm{NO}_3^-}$	half-saturation constant for denitrification (mol m^{-3})
$\hat{K}^{\mathrm{sat}}_{\mathrm{NO}_3^-}$	half-saturation constant for denitrification normalized by in-stream concentration of oxygen (-)
$K^{\mathrm{inh}}_{\mathrm{O}_2}$	oxygen inhibition of denitrification (mol m^{-3})
$\hat{K}^{\mathrm{inh}}_{\mathrm{O}_2}$	oxygen inhibition of denitrification normalized by in-stream concentration of oxygen (-)
$K^{\mathrm{sat}}_{\mathrm{O}_2}$	half-saturation constant for aerobic respiration (mol m^{-3})
$\hat{K}^{\mathrm{sat}}_{\mathrm{O}_2}$	half-saturation constant for aerobic respiration normalized aerobic by in-stream concentration of oxygen (-)
ℓ	length of a stream reach (m)
$L_{x=0}$	loading rate of nitrate at start of a reach (mol s^{-1})
$L_{x=\ell}$	loading rate of nitrate at length ℓ of a reach (mol s^{-1})
L-Q	low stream discharge scenario
LINX II	second lotic intersite nitrate experiment
λ	wavelength of a ripple (m)
m	empirical exponent in the Fehlman [1985] correlation between hyporheic exchange flux, stream velocity, water depth, and bedform geometry (see equation (7c)) (-)
MTL	mass transfer limited

NCC	Cunningham Creek in North Carolina; a reference site selected from the LINX II data set
NI	nitrification
$\{NH_3\}_{OM}$	ammonia associated with Organic Matter
$^{15}NH_4^+$	labeled ammonium molecule with ^{15}N-isotope
$^{15}NO_3^-$	labeled nitrate molecule with ^{15}N-isotope
OM	organic matter
PASS	pumping and streamline segregation model
PDF	probability density function (s^{-1})
PRM	Rio Mameyes Tributary in Puerto Rico; an urban-impacted site selected from LINX II data set
Q	stream flow discharge ($m^3\ s^{-1}$)
q_H	hyporheic exchange flux ($m\ s^{-1}$)
$q_{H,0}$	characteristic hyporheic exchange flux ($m\ s^{-1}$)
q_U	horizontal component of ambient groundwater flux ($m\ s^{-1}$)
q_V	vertical component of ambient groundwater flux ($m\ s^{-1}$)
R_{AM}	rate of ammonification ($mol\ m^{-3}\ s^{-1}$)
R_{AR}	rate of aerobic respiration ($mol\ m^{-3}\ s^{-1}$)
R_{DN}	rate of denitrification ($mol\ m^{-3}\ s^{-1}$)
R_{min}	rate of mineralization of sediment organic matter ($mol\ m^{-3}\ s^{-1}$)
R_{NI}	rate of nitrification ($mol\ m^{-3}\ s^{-1}$)
RTD	residence time distribution
S	slope of alluvium (-)
τ	travel time through the hyporheic zone (s)
τ_T	characteristic travel time through a bedform by hyporheic exchange (s)
τ^*	a hypothetical travel time through a bedform by hyporheic exchange (s)
$\bar{\tau}$	normalized travel time through the HZT (-)
τ_R	aerobic mineralization time scale (s)
$\hat{\tau}_R$	travel time along a HZT normalized by the mineralization time scale (-)
θ	porosity (-)
$\theta_{O_2}^{inh}$	inhibition coefficient of denitrification with oxygen (-)
U	stream flow velocity ($m\ s^{-1}$)
U_{DN}	flux of stream nitrate out of the streambed associated with direct denitrification ($mol\ m^{-2}\ s^{-1}$)
$U_{N_2,Dw}$	flux of nitrogen gas out of the streambed by the direct denitrification of stream nitrate ($mol\ m^{-2}\ s^{-1}$)
$U_{N_2,Dn}$	flux of nitrogen gas out of the streambed by coupled denitrification-denitrification ($mol\ m^{-2}\ s^{-1}$)
$U_{NO_3^-}$	flux of nitrate out of the sediment ($mol\ m^{-2}\ s^{-1}$)
v_f	total nitrate uptake velocity ($m\ s^{-1}$)
v_{fden}	uptake velocity of stream nitrate by direct denitrification as reported by Mulholland et al. [2008] ($m\ s^{-1}$)
$v_{f,Dn}$	uptake velocity for coupled nitrification-denitrification ($m\ s^{-1}$)
$v_{f,Dw}$	uptake velocity of stream nitrate by direct denitrification ($m\ s^{-1}$)
$v_{f,MTL}$	total nitrate uptake velocity under MTL conditions ($m\ s^{-1}$)

W	stream width (m)
x	horizontal coordinate (m)
$\overline{x}$	normalized horizontal coordinate (-)
x_0	starting position of a HZT (m)
$\overline{x}_0$	normalized starting position of a HZT (-)
$x_0^{\text{down-cell}}$	location along the sediment-water interface where water first enters the hyporheic zone in the downstream flow cell of ripples (m)
$\overline{x}_0^{\text{down-cell}}$	normalized location along the sediment-water interface where water first enters the hyporheic zone in the downstream flow cell of ripples (-)
$x_0^{\text{up-cell}}$	location along the sediment-water interface where water first enters the hyporheic zone in the upstream flow cell of ripples (m)
$\overline{x}_0^{\text{up-cell}}$	normalized location along the sediment-water interface where water first enters the hyporheic zone in the upstream flow cell of ripples (-)
x_{f}	final position where water exits the HZT and returns to the stream (-)
$\overline{x}_{\text{f}}$	normalized final position where water exits the HZT and returns to the stream (-)
y	vertical coordinate (m)
$\overline{y}$	normalized vertical coordinate (-)

References

Ahmerkamp, S., C Winter, F. Janssen, M. M. Kuypers, and M. Holtappels (2015), The impact of bedform migration on benthic oxygen fluxes, J. Geophys. Res. Biogeosci., 120, 2229–2242, doi:10.1002/2015JG003106.

Askarizadeh, A., et al. (2015), From rain tanks to catchments: Use of low-impact development to address hydrologic symptoms of the urban stream syndrome, Environ. Sci. Technol., 49(19), 11,264–11,280.

Aubeneau, A. F., B. Hanrahan, D. Bolster, and J, L. Tank (2014), Substrate size and heterogeneity control anomalous transport in small streams, Geophys. Res. Lett., 41, 8335–8341, doi:10.1002/2014GL061838.

Aubeneau, A. F., J. D. Drummond, R. Schumer, D. Bolster, J. L. Tank, and A. I. Packman (2015a), Effects of benthic and hyporheic reactive transport on breakthrough curves, Freshwater Sci., 34(1), 301–315.

Aubeneau, A. F., R. L. Martin, D. Bolster, R. Schumer, D. Jerolmack, and A. Packman (2015b), Fractal patterns in riverbed morphology pro- duce fractal scaling of water storage times, Geophys. Res. Lett., 42, 5309–5315, doi:10.1002/2015GL064155.

Azizian, M., S.B. Grant, A.J. Kessler, P.L.M. Cook, M.A. Rippy, M. Stewardson (2015), Bedforms as biocatalytic filters: A Pumping and Stream- line Segregation (PASS) model for nitrate removal in permeable sediments, Environ. Sci. Technol., 49(18), 10,993–11,002, doi: 10.1021/ acs.est.5b01941.

Babamoradi, H., F. Van den Berg, and A. Rinnan (2013), Bootstrap based confidence limits in principal component analysis: A case study, Chemometr. Intell. Lab. 120, 97–105.

Beaulieu, J.J., et al. (2011) Nitrous oxide emission from denitrification in stream and river networks, Proc. Natl. Acad. Sci. U. S. A., 108(1), 214–219.

Berg, P., S. Rysgaard, and B. Thamdrup (2003), Dynamic modeling of early diagnosis and nutrient cycling. A case study in an Arctic marine sediment, Am. J. Sci., 303, 905–955.

Bernot, M. J., and W. K. Dodds (2005) Nitrogen retention, removal, and saturation in lotic ecosystems, Ecosystems, 8, 442–453.

Bird, R. B., W. E. Stewart, and E. W. Lightfoot (2007), Transport Phenomena, John Wiley, New York.

Birgand, F., R. W. Skaggs, G. M. Chescheir, and J. W. Gilliam (2007), Nitrogen removal in streams of agricultural catchments: A literature review, Crit. Rev. Environ. Sci. Technol. 37(5) 381–487.

Boano, F., R. Revelli, and L. Ridolfi (2008), Reduction of the hyporheic zone volume due to the stream-aquifer interaction, Geophys. Res. Let., 35, L09401, doi:10.1029/2008GL033554.

Boano, F., R. Revelli, and L. Ridolfi (2009), Quantifying the impact of groundwater discharge on the surface-subsurface exchange, Hydrol. Processes, 23, 2108–2116.

Boano, F. R., A. Demaria, R. Revelli, and L. Ridolfi (2010), Biogeochemical zonation due to intrameander hyporheic flow, Water Resour. Res. 46, W02511, doi:10.1029/2008WR007583.

Boano, F., J. W. Harvey, A. Marion, A. I. Packman, R. Revelli, L. Ridolfi, and A. Worman (2014), Hyporheic flow and transport processes: Mech- anisms, models, and biogeochemical implications, Rev. Geophys., 25, 603–679, doi:10.1002/2012RG000417.

Bohlke, J. K., R. C. Antweiler, J. W. Harvey, A. E. Laursen, L. K. Smith, R. L. Smith, and M. A. Voytek (2009), Multi-scale measurements and modeling of denitrification in streams with varying flow and nitrate concentration in the upper Mississippi River basin, USA, Biogeochemistry, 93, 117–141.

Boulton, A. J., T. Datry, T. Kasahara, M. Mutz, and J. A. Stanford (2010), Ecology and management of the hyporheic zone: Stream- groundwater interactions of running waters and their floodplains, J. N. Am. Benthol. Soc., 29(1), 26–40.

Bourke, M. F., A. J. Kessler, and P. L. M. Cook (2014), The influence of the buried macroalgae Ulva lactuca on denitrification in permeable sediments, Mar. Ecol. Prog. Ser., 498, 85–94.

Bourke, M. F., P. J. Marriott, R. N. Glud, H. Hassler-Sheetal, M. Kamalanathang, J. Beardall, C. Greening, and P. L. M. Cook (2017), Metabolism in anoxic permeable sediments is dominated by eukaryotic dark fermentation, Nat. Geosci., 10, 30–35.

Bouwman, A. F., G. Van Drecht, and K. W. Van der Hoek (2005), Global and Regional Surface Nitrogen Balances in Intensive Agricultural Pro- duction Systems for the Period 1970-2030, Pedosphere, 15, 137–155.

Briggs, M. A., F. D. Day-Lewis, J. P, Zarnetske, and J. W. Harvey (2015), A physical explanation for the development of redox microzones in hyporheic flow, Geophys. Res. Lett., 42, 4402–4410, doi:10.1002/2015GL064200.

Buckingham, E. (1914), On physically similar systems; illustration of the use of dimensional equations, Phys. Rev., 4(4), 345, doi:10.1103/ physrev.4.345.

Burgin, A. J., and S. K. Hamilton (2007), Have we overemphasized the role of denitrification in aquatic ecosystems? A review of nitrate removal pathways, Front. Ecol. Environ., 5(2), 89–96.

Canfield, D. E., A. N. Glazer, and P. G. Falkowski (2010), The evolution and future of earth's nitrogen cycle, Science, 330, 192–196.

Cardenas, M. B. (2008), Surface water-groundwater interface geomorphology leads to scaling of residence times, Geophys. Res. Lett., 35, L08402, doi:10.1029/2008GL033753.

Cardenas, M. B., and J. L. Wilson (2007a), Exchange across a sediment-water interface with ambient groundwater discharge, J. Hydrol., 346(3–4), 69–80, doi:10.1016/j.jhydrol.2007.08.019, 69-80.

Cardenas, M. B., and J. L Wilson (2007b), Hydrodynamics of coupled flow above and below a sediment-water interface with triangular bed forms: Underflow case, Adv. Water. Res., 30(3), 301–313, doi:10.1016/j.advwaters.2006.06.009.

Cardenas, M., J. L. Wilson, and R. Haggerty (2008), Residence time of bedform-driven hyporheic exchange. Adv. Water Res., 31, 1382–1386.

Carey, R. O., and K. W. Migliaccio (2009), Contribution of wastewater treatment plant effluents to nutrient dynamics in aquatic systems: A review, Environ. Manage., 44, 205–217.

Caruso, A., Ridolfi, L., Boano, F. (2016), Impact of watershed topography on hyporheic exchange. Adv. Water Res., 94, 400–411.

Cook, P. L. M., F. Wenzhofer, S. Rysgaard, O. S. Galaktionov, F. J. R. Meysman, B. D. Eyre, J. Cornwell, M. Huettel, and R. N. Glud (2006), Quantification of denitrification in permeable sediments: Insights from a two-dimensional simulation analysis and experimental data, Limnol. Oceanogr. Methods, 4, 294–307.

Coppess, J. (2016), Dead Zones and Drinking Water, Part 1: RCPP and Review, farmdoc daily, 6(6), 37.

Craig, L. S., et al. (2008), Stream restoration strategies for reducing river nitrogen loads, Front. Ecol. Environ., 6(10), 529–538.

Elliott, A. H., and N. H. Brooks (1997a), Transfer of nonsorbing solutes to a streambed with bed forms: Theory, Water Resour. Res., 33, 123-136.

Elliott, A. H., and N. H. Brooks (1997b), Transfer of nonsorbing solutes to a streambed with bed forms: Laboratory experiments. Water Resour. Res., 33, 137-151.

Engelhardt, I., M. Piepenbrink, N. Trauth, S. Stadler, C. Kludt, M. Schulz, C. Schu€th, and T. A. Ternes (2011), Comparison of tracer methods to quantify hydrodynamic exchange within the hyporheic zone. J. Hydrol., 400, 255–266.

Evrard, V., R. N. Glud, and P. L. M. Cook (2012), The kinetics of denitrification in permeable sediments, Biogeochemistry, 113, 563–572, doi: 10.1007/s10533-012-9789-x.

Fehlman, H. (1985), Resistance components and velocity distributions of open channel flows over bedforms, MS thesis, Colo. State Univ., Fort Collins.

Feinberg, M., and D. Hildebrandt (1997), Optimal reactor design from a geometric viewpoint—I. Universal properties of the attainable region, Chem. Eng. Sci., 52(10), 1637–1665.

Fox, A., F. Boano, and S. Arnon (2014), Impact of losing and gaining streamflow conditions on hyporheic exchange fluxes induced by dune-shaped bedforms, Water Resour. Res., 50, 1895–1907, doi:10.1002/2013WR014668.

Fox, A., G. Laube, C. Schmidt, J. H. Fleckenstein, and S. Arnon (2016), The effect of losing and gaining flow conditions on hyporheic exchange in heterogeneous streambeds, Water Resour. Res., 52, 7460–7477, doi:10.1002/2016WR018677.

French, C., L. Wu, T. Meixner, D. Haver, J. Kabashima, and W.A. Jury (2006), Modeling nitrogen transport in the Newport Bay/San Diego Creek watershed of Southern California, Agric. Water Manage., 81, 199–215.

Friedlander, S. K. (2000), Smoke, dust, and haze: Fundamentals of aerosol dynamics, in Topics in Chemical Engineering, edited by K. E. Gubbins, Oxford Univ. Press, New York.

Galloway, J. N., et al.(2004), Nitrogen cycles: Past, present, and future, Biogeochemistry, 70, 153–226.

Garcia-Ruiz, R., S. N. Pattinson, and B. A.Whitton (1998), Kinetic parameters of denitrification in a river continuum, Appl. Environ. Microbiol., 64, 2533–2538.

Gomez-Velez, J. D., and J. W. Harvey (2014), A hydrogeomorphic river network model predicts where and why hyporheic exchange is important in large basins, Geophys. Res. Lett., 41, 6403–6412, doi:10.1002/2014GL061099.

Gomez-Velez, J. D., J. W. Harvey, M. B. Cardenas, and B. Kiel (2015), Denitrification in the Mississippi River network controlled by flow through river bedforms, Nat. Geosci., 8, 941–945, doi:10.1038/ngeo2567.

Gooseff, M. N. (2010), Defining hyporheic zones: Advancing our conceptual and operational definitions of where stream water and ground- water meet, Geogr. Compass, 4(8), 945–955, doi:10.1111/j.1749-8198.2010.00364.x.

Grant, S. B., and I. Marusic (2011), Crossing turbulent boundaries: Interfacial flux in environmental flows, Environ. Sci. Technol., 45, 7107–7113.

Grant, S. B., K. Stolzenbach, M. Azizian, M. J. Stewardson, F. Boano, and L. Bardini (2014), First-order contaminant removal in the hyporheic zone of streams: Physical insights from a simple analytical model, Environ. Sci. Technol., 48, 11,369–11, 378.

Grathwohl, P., et al. (2013), Catchments as reactors: A comprehensive approach for water fluxes and solute turnover, Environ. Earth Sci., 69, 317–333.

Green, T. R., M. Taniguchi, H. Kooi, J. J. Gurdak, D. M. Allen, K. M. Hiscock, H. Treidel, and A. Aureli (2011), Beneath the surface of global change: Impacts of climate change on groundwater, J. Hydrol., 405(3), 532–560.

Groffman, P. M., A. M. Dorsey, and P. M. Mayer (2005), N processing within geomorphic structures in urban streams, J. N. Am. Benthol. Soc., 24(3), 613–625.

Harvey, J. W., J. K. Bohlke, M. A. Voytek, D. Scott, and C. R. Tobias (2013), Hyporheic zone denitrification: Controls on effective reaction depth and contribution to whole-stream mass balance, Water Resour. Res., 49, 6298–6316, doi:10.1002/wrcr.20492.

Herzog, S. P., C. P. Higgins, and J. E. McCray (2015), Engineered streambeds for induced hyporheic flow: Enhanced removal of nutrients, pathogens, and metals from urban streams, ASCE J. Environ. Eng., 142(1), 04015053.

Hester, E. T., K. I. Young, and M. A. Widdowson (2013), Mixing of surface and groundwater induced by riverbed dunes: Implications for hyporheic zone definitions and pollutant reactions, Water Resour. Res., 49, 5221–5237, doi:10.1002/wrcr/20399.

Hill, C. G. (1977), An Introduction to Chemical Engineering Kinetics and Reactor Design, chap. 11, John Wiley, New York.

Hinkle, S.R., J. H. Duff, F. J. Triska, A. Laenen, E. B. Gates, K. E. Bencala, D. A. Wents, and S. R. Silva (2001), Linking hyporheic flow and nitrogen cycling near the Willamette River: A large river in Oregon, USA, J. Hydrol., 244, 157–180.

Holmes, R. M., S. G. Fisher, and N. B. Grimm (1994), Parafluvial nitrogen dynamics in a desert stream ecosystem. J. N. Am. Benthol. Soc., 13(4), 468–478.

Hu, B. L., L. D. Shen, X. Y. Xu, and P. Zheng (2011), Anaerobic ammonium oxidation (anammox) in different natural ecosystems, Biochem. Soc. Trans., 39(6), 1811–1816.

Huettel, M., P. Berg, and J. E. Kostka (2014), Benthic exchange and biogeochemical cycling in permeable sediments, Annu. Rev. Mar. Sci., 6, 23–51.

Jongbloed, A. W., and N. P. Lenis (1998), Environmental concerns about animal manure, J. Anim. Sci., 76(10), 2641–2648.

Kennedy, C. D., D. P. Genereux, D. R. Corbett, and H. Mitasova (2009), Spatial and temporal dynamics of coupled groundwater and nitrogen fluxes through a streambed in an agricultural watershed, Water Resour. Res., 45, W09401, doi:10.1029/2008WR007397.

Kessler, A. J., R. N. Glud, M. B. Cardenas, and P. L. M. Cook (2013a), Transport zonation limits coupled nitrification-denitrification in permeable sediments, Environ. Sci.

Technol., 47, 13,404–13,411.

Kessler, A. J., R. N. Glud, M. B. Cardenas, M. Larsen, M. F. Bourke, and P. L. M. Cook (2013b), Quantifying denitrification in rippled permeable sands through combined flume experiments and modeling, Limnol. Oceanogr., 57, 1217–1232.

Kessler, A. J., M. B. Cardenas, I. R. Santos, and P. L. M. Cook (2014), Enhancement of denitrification in permeable carbonate sediment due to intra-granular porosity: A multi-scale modelling analysis, Geochim. Cosmochim. Acta, 141, 440–453.

Kiel, B. A., and M. B. Cardenas (2014), Lateral hyporheic exchange throughout the Mississippi River network, Nat. Geosci., 7(6), 413–417.

Lansdown, K., C. M. Heppell, M. Trimmer, A. Binley, A. L. Heathwaite, P. Byrne, and H. Zhang (2015), The interplay between transport and reaction rates as controls on nitrate attenuation in permeable streambned sediments, J. Geophys. Res. Biogeosci.s, 120, 1093–1109, doi: 10.1002/2014JG002874.

Lansdown, K., B. A. McKew, C. Whitby, C. M. Heppell, A. J. Dumbrell, A. Binley, L. Olde, and M. Trimmer (2016), Importance and controls of anaerobic ammonium oxidation influenced by riverbed geology, Nat. Geosci., 9, 357–360, doi:10.1038/ngeo2684.

Leeder, M. R. (2012), Sedimentology: Process and Product, Springer, London.

Levenspiel, O. (1972), Chemical Reaction Engineering, John Wiley, New York.

Marzadri, A., D. Tonina, A. Bellin, G. Vignoli, and M. Tubino (2010), Semianalytical analysis of hyporheic flow induced by alternate bars, Water Resour. Res., 46, W07531, doi:10.1029/2009WR008285.

Mazadri, A., D. Tonina, and A. Bellin (2011), A semi-analytical three-dimensional process-based model for hyporheic nitrogen dynamics in gravel bed rivers, Water Resour. Res., 47, W11518, doi:10.1029/2011WR010583.

Marzadri, A., D. Tonina, A. Bellin, and A. Valli (2015), Mixing interfaces, fluxes, residence times and redox conditions of the hyporheic zones induced by dune-like bedforms and groundwater flows, Adv. Water Resour., 88, 139–151, doi: 10.1016/j.advwatres.2015.12.014.

McClain, M. E., et al. (2003), Biogeochemical hot spots and hot moments at the interface of terrestrial and aquatic ecosystems, Ecosystems, 6, 301–331.

McCluskey, A. H., S. B. Grant, M. J. Stewardson (2016), Flipping the thin film model: Mass transfer by hyporheoc exchange in gainng and losing streams, Water. Resour. Res., 52, 7806–7818, doi:10.1002/2016WR018972

Meysman, F. J. R., O. S. Galaktionov, P. L. M Cook, F. J. J. G. Janssen, M. Huettel, and

J. J. Middelburg (2006a), Quantifying biologically and physically induced flow and tracer dynamics in permeable sediments, Biogeosci. Discuss., 3(6), 1809–1858.

Meysman, F. J. R., O. S. Galaktionov, B. Gribsholt, and J. J. Middelburg (2006b), Bioirrigation in permeable sediments: Advective pore water transport induced by burrow ventilation, Limnol. Oceanogr., 51, 142–156.

Morée, A. L., A. H. W. Beusen, A. F. Bouwman, and W. J. Willems (2013), Exploring global nitrogen and phosphorus flows in urban wastes during the twentieth century, Global Biogeochem. Cycles, 27, 836–846, doi:10.1002/gbc.20072.

Mulholland, P. J., J. L. Tank, D. M. Sanzone, W. M. Wollheim, B. J. Peterson, J. R. Webster, and J. L. Meyer (2000), Nitrogen cycling in a forest stream determined by a 15N tracer addition, Ecol. Monogr., 70(3), 471–493.

Mulholland, P. J., et al. (2008), Stream denitrification across biomes and its response to anthropogenic nitrate loading, Nature, 452, 202–205. Mulholland, P. J., et al. (2009), Nitrate removal in stream ecosystems measured by 15N addition experiments: Denitrification, Limnol. Oceanogr., 54(3), 666–680.

National Environmental Research Institute (2004), A model set-up for an oxygen and nutrient flux model for Aarhus Bay (Denmark), NERI Tech. Rep. 483, Denmark.

Nielsen, L. P., and N. P. Sloth (1994), Denitrification, nitrification and nitrogen assimilation in photosynthetic microbial mats, in Microbial Mats: Structure, Development and Environmental Significance, edited by L. J. Stal, and P. Caumette, NATO ASI Ser., vol. 35, pp. 319–324, Springer, New York.

Packman, A. I., N. H. Brooks, and J. J. Morgan (2000), A physiochemical model for colloid exchange between a stream and a sand stream-bed with bed forms, Water Resour. Res., 36, 2351–2361, doi:10.1029/2000WR900059.

Peres-Neto, P. R., D. A. Jackson, K. M. Somers (2005), How many principal components? Stopping rules for determining the number of non- trivial axes revisited, Comput. Stat. Data Anal. 49, 974–997.

Peterson, B. J., et al. (2001), Control of nitrogen export from watersheds by headwater streams, Science, 292(5514), 86–90.

Pett, R. J. (1989), Kinetics of microbial mineralization of organic carbon from detrital Skeletonema costatum cells, Mar. Ecol. Prog. Se., 52(2), 123–128.

Powlson, D. S., T. M. Addiscott, N. Benjamin, K. G. Cassman, and T. M. de Kok (2008), When does nitrate become a risk for humans?, J. Envi- ron. Qual., 37, 291–295.

Rawlings, J. B., and J. G. Ekerdt (2013), Chemical Reactor Analysis and Design Fundamentals, chap. 8, Nob Hill Publ., Madison, Wis.

Ribot, M., E. Mart ı, D. von Schiller, F. Sabater, H. Daims, and T. J. Battin (2012), Nitrogen processing and the role of epilithic biofilms down- stream of a wastewater treatment plant, Freshwater Sci., 31(4), 1057–1069.

Rippy, M. A., A. Deletic, J. Black, R. Aryal, J.-L. Lampard, J. Y.M. Tang, D. McCarthy, P. Kolotelo, J. Sidhu, and W. Gernjak (2017), Pesticide occurrence and spatiotemporal variability in urban run-off across Australia, Water Res., 115, 245–255.

Rode, M., M. Hartwig, D. Wagenschein, T. Kebede, and D. Borchardt (2015), The importance of hyporheic zone processes on ecological functioning and solute transport of streams and rivers, in Ecosystem Services and River Basin Ecohydrology, edited by L. Chicharo, pp. 57–82, Springer, Netherlands.

Runkel, R. L. (2007), Toward the transport-based analysis of nutrient spiraling and uptake in streams, Limnol. Oceanogr. Methods, 5, 50–62. Rutherford, J. C., G. J. Latimer, and R. K. Smith (1993), Bedform mobility and benthic oxygen uptake, Water Res., 27(10), 1545–1558.

Rutherford, J. C., J. D. Boyle, A. H. Elliott, T. V. J. Hatherell, and T. W. Chiu (1995), Modeling benthic oxygen uptake by pumping, ASCE J. Envi- ron. Eng., 121(1), 7216.

Sanz-Prat, A., C. Lu, M. Finkel, and O. Cirpka (2015), On the validity of travel-time based nonlinear bioreactive transport models in steady- state flow, J. Contam. Hydrol., 175, 26–43, doi:10.1016/j.jconhyd.2015.02.003.

Sawyer, A. H. (2015), Enhanced removal of groundwater-borne nitrate in heterogeneous aquatic sediments, Geophys. Res. Lett., 42, 403– 410, doi:10.1002/2014GL062234.

Schmidt, C., M. Bayer-Raich, and M. Schirmer (2006), Characterization of spatial heterogeneity of groundwater-stream water interactions using multiple depth streambed temperature measurements at the reach scale, Hydrol. Earth Syst. Sci., 10(6), 849–859.

Schumer R., D. A. Benson, M. M. Meerschaert, and S. W. Wheatcraft (2001), Eulerian derivation of the fractional advection-dispersion equation, J. Contam. Hydrol., 48, 69–88.

Schumer, R., D. A. Benson, M. M. Meerschaert, and B. Baeumer (2003), Fractal mobile/immobile solute transport, Water Resour. Res., 39(10), 1296, doi:10.1029/2003WR002141.

Schumer R., M. M. Meerschaert, and B. Baeumer (2009) Fractional advection-dispersion equations for modeling transport of the Earth surface, J. Geophys. Res., 114, F00A07, doi:10.1029/2008JF001246.

Seitzinger, S., J. A. Harrison, J. K. Bohlke, A.F. Bouwman, R. Lowrance, B. Peterson, C. Tobias, and G. Van Drecht (2006), Denitrification across Landscapes and Waterscapes: A Synthesis, Ecol. Appl., 16, 2064–2090.

Smith, V. H., G. D. Tilman, and J. C. Nekola (1999), Eutrophication: Impacts of excess nutrient inputs on freshwater, marine, and terrestrial ecosystems, Environ. Pollut., 100, 179–196.

Smith, J. W. N., B. W. Surridge, T. H. Haxton, and D. N. Lerner (2009), Pollutant attenuation at the groundwater–surface water interface: A classification scheme and statistical analysis using national-scale nitrate data, J. Hydrol., 369(3), 392–402.

Stewart, R. J., W. M. Wollheim, M. N. Gooseff, M. A. Briggs, J. M. Jacobs, B. J. Peterson, and C. S. Hopkinson (2011), Separation of river network-scale nitrogen removal among the main channel and two transient storage compartments, Water Resour. Res., 47, W00J10, doi: 10.1029/2010WR009896.

Stream Solute Workshop (1990), Concepts and methods for assessing solute dynamics in stream ecosystem, J. N. Am. Benthol. Soc., 9, 95–119.

Taylor, P. G., and A. R. Townsend (2010), Stoichiometric control of organic carbon–nitrate relationships from soils to the sea, Nature, 464(7292), 1178–1181.

Thibodeaux, L. J., and J. D. Boyle (1987) Bedform-generated convective transport in bottom sediment, Nature, 325(22) 341–343.

Thibodeaux, L. J., and D. Mackay (2011), Handbook of Chemical Mass Transport in the Environment, CRC Press, Boca Raton, Fla.

Tonina, D., A. Marzadri, and A. Bellin (2015), Benthic uptake rate due to hyporheic exchange: The effects of streambed morphology for constant and sinusoidally varying nutrient loads, Water, 7(2), 398–419, doi:10.3390/w7020398.

Trauth, N., C. Schmidth, U. Maier, M. Wieweg, and J. H. Fleckenstein (2013), Coupled 3-D stream flow and hyporheic flow model under varying stream and ambient groundwater flow conditions in a pool-riffle system, Water Resour. Res., 49, 5834–5850, doi:10.1002/wrcr.20442.

Trauth, N., J. C. Schmidt, M. Vieweg, U. Maier, and J. H. Fleckenstein (2014), Hyporheic transport and biogeochemical reactions in pool-riffle systems under varying ambient groundwater flow conditions, J. Geophys. Res. Biogeosci., 119, 910–928, doi:10.1002/2013JG002586.

Vaughn, C. C., and C. C. Hakenkamp (2001) The functional role of burrowing bivlaves in freshwater ecosystems, Freshwater Biol., 46, 1431. Van Cappellen, P., and Y. Wang (1996), Cycling of iron and manganese in surface sediments, A general theory for the coupled transport and reaction of carbon oxygen, nitrogen, sulfur, iron, and manganese, Am. J. Sci., 296(3) 197–243, doi:10.2475/ajs.296.3.197.

Walsh, C. J., A. H. Roy, J. W. Feminella, P. D. Cottingham, P. M. Groffman, and R. P. Morgan II (2005), The urban stream syndrome: Current knowledge and the search for a cure, J. N. Am. Benthol. Soc., 24(3), 706–723.

Wollheim, W. M., C. J. Vorosmarty, B. J. Peterson, S. P Seitzinger, and C. S. Hopkinson (2006), Relationship between river size and nutrient removal, Geophys. Res. Lett., 33, L06410, doi:10.1029/2006GL025845.

Wondzell, S. M. (2015), Groundwater–surface-water interactions: perspectives on the development of the science over the last 20 years, Freshwater Sci., 34(1), 368–376.

Yang, Y. S., and L. Wang (2010), A review of modeling tools for implementation of the EU Water Framework Directive in handling diffuse water pollution, Water Resour. Manage. 24, 1819–1843.

Zarnetske, J. P., R. Haggerty, S. M. Wondzell, and M. A. Baker (2011), Dynamics of nitrate production and removal as a function of residence time in the hyporheic zone, J. Geophys. Res., 116, G01025, doi:10.1029/2010JG001356.

Zarnetske, J. P., R. Haggerty, S. M. Wondzell, V. A. Bokil, and R. Gonzalez-Pinzon (2012), Coupled transport and reaction kinetics control the nitrate source-sink function of hyporheic zones, Water Resour. Res., 48, W11508, doi:10.1029/2012WR011894.

Zarnetske, J. P., R. Haggerty, and S. M. Wondzell (2015), Coupling multiscale observations to evaluate hyporheic nitrate removal at the reach scale, Freshwater Sci., 34(1), 172–186.

Chapter 5[1]

Factoring Physics into Local and Global Assessments of Nitrogen Pollution

Abstract

The discharge of excess nitrogen to streams and rivers poses an existential threat to both humans and ecosystems. A seminal study of headwater streams across the U.S. conclude that in-stream removal of nitrate is controlled primarily by stream chemistry and biology, and only weakly by stream physics. A reanalysis of these data reveals that stream physics (in particular, turbulent mass transfer across the concentration boundary layer) imposes a previously unrecognized upper limit on the rate nitrate is removed from streams. The upper limit represents the potential (mass-transfer limited) capacity of a stream to remove nitrate, while the fraction of that potential realized in practice is determined by stream chemistry, biology, and hydrology. Physics alone closely reproduces measured distributions of nitrate removal in headwater streams, a discovery that should inform stream restoration designs and efforts to assess the impacts of nitrogen pollution on receiving water quality and the global nitrogen cycle.

---

[1] A version of this chapter is undergoing review in Science as [Grant, S.B., M. Azizian, P. Cook; F. Boano, M.A. Rippy (2017), Factoring Physics into Local and Global Assessments of Nitrogen Pollution].

Over the past century humans have dramatically increased nitrogen loading to streams and rivers, primarily from the over-application of fertilizer for food production. The environmental consequences of this nitrogen pollution are evident in both developed and developing countries, and include eutrophication of inland and coastal waters, ocean acidification, and greenhouse gas generation [Galloway et al., 2004; Marzadri et al., 2017]. Thousands of stream, river, lake, groundwater, and coastal sites across the U.S. are classified as impaired for nitrogen by the U.S. Environmental Protection Agency [U.S. E.P.A., 2017]. In a recent assessment of critical earth systems required for the continued development of human societies, nitrate pollution was identified as one of only three planetary boundaries (along with phosphate pollution and loss of genetic diversity) that have already been crossed [Steffen et al., 2015]. According to the U.S. National Academy of Engineering, restoring balance to the nitrogen cycle is one of the 14 Grand Challenges facing engineers in the 21st Century [U.S. N.A.E., 2017].

Streams have a natural capacity to remove dissolved inorganic nitrogen (DIN, including nitrate, nitrite, and ammonium) through a coupling of physical transport processes and biologically mediated reactions in streambed sediments (**Figure 5.1A**). DIN is assimilated by autotrophs growing at the sediment-water interface (benthic algal layer) and heterotrophic microbial populations in the hyporheic zone, a region of the sediment bed where hydrologic flow paths begin and end in the stream [Hall et al., 2009]. As DIN travels through the hyporheic zone it undergoes a variety of microbially mediated redox reactions including oxidation of ammonium to nitrate (nitrification) and reduction of nitrate to nitrite, nitrous oxide, and di-nitrogen gas (denitrification). Of these, only

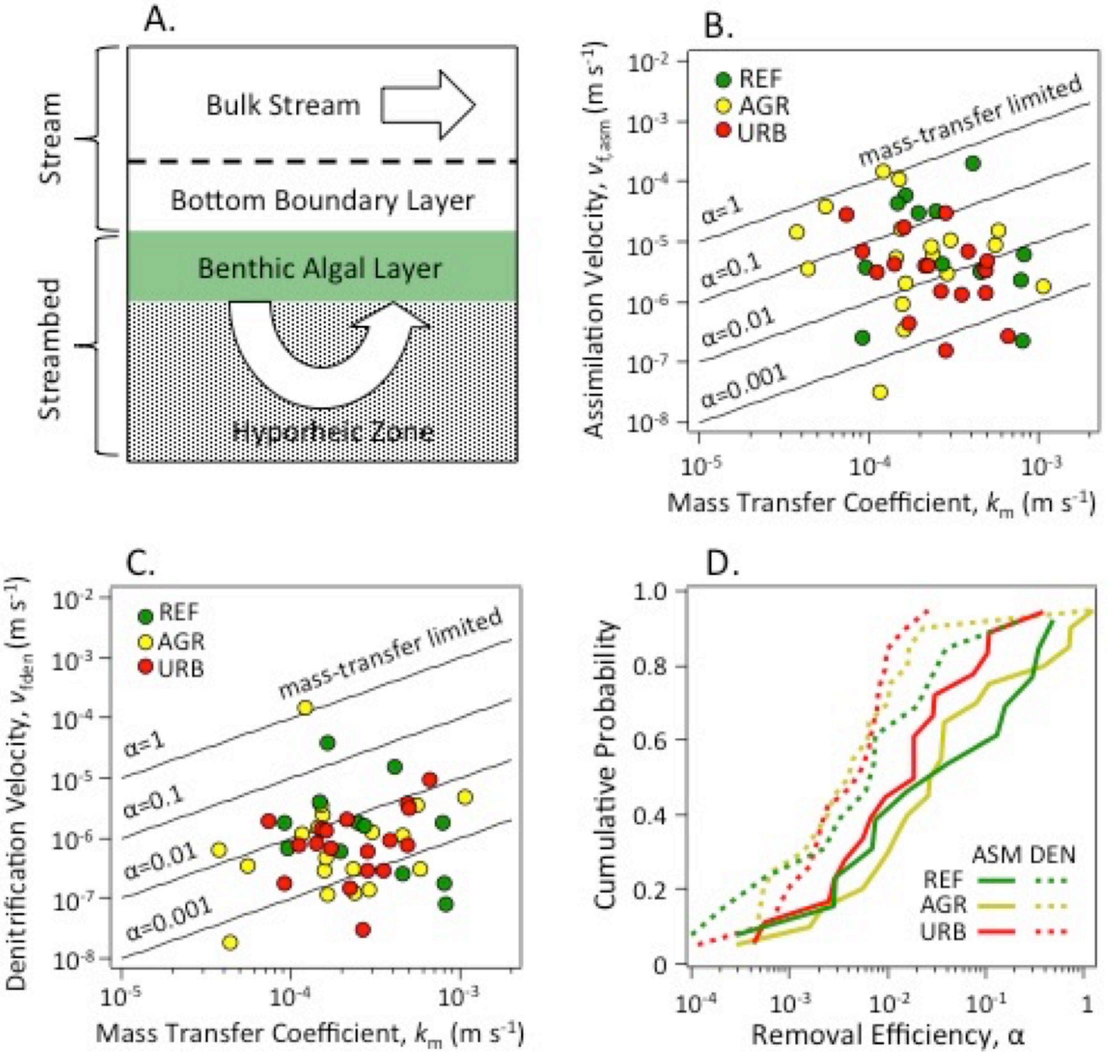

Figure 5.1. Nitrate uptake in streams by assimilation and denitrification is limited by turbulent transport across the concentration boundary layer. (**A**) Conceptual model of how nitrate is transported from the bulk stream, across the concentration boundary layer, and into the streambed where it is removed by assimilation and denitrification in the benthic algal layer and hyporheic zone. (**B**) Assimilation velocities measured during the LINX II field campaign plotted against the mass transfer coefficient calculated from equation (2a). Colors denote surrounding land-use for the stream site as reference (REF), agriculture (AGR), or urban (URB). (**C**) Same as (**B**) except that the vertical axis is denitrification velocity. (**D**) Cumulative distribution functions (CDFs) of the removal efficiencies for assimilation (solid curves) and denitrification (dashed curves) separated by land-use type (REF, AGR, or URB). Efficiencies were calculated from the ratio of the uptake velocity and mass transfer coefficient. The mass-transfer limit corresponds to the case where all nitrate is removed instantly by the streambed ($\alpha = 1$) and nitrate uptake depends only on the mass transfer coefficient ($v_f = k_m$).

denitrification permanently removes nitrogen from the stream through the evasion of nitrous oxide or di-nitrogen gas. Indeed, the production of nitrous oxide by streams is approximately 10% of global anthropogenic emissions of this potent greenhouse gas [Beaulieu et al, 2011], of which headwater streams account for a disproportionate fraction [Marzadri et al., 2017]. Of the DIN that is assimilated, a fraction is stored (for >1 year) as particulate nitrogen in streambed sediments or in adjacent riparian vegetation [Hall et al., 2009] while the rest is re-mineralized and released back to the stream.

The local efficiency with which DIN is removed from a stream can be quantified by one of several nutrient spiraling metrics [Ensign and Doyle, 2006]. In this study we focus specifically on nitrate (because of its mobility, recalcitrance, and environmental impacts) and quantify its removal with the nitrate uptake velocity $v_f \geq 0$ (units m s^{-1}), defined as the flux of nitrate into the streambed divided by the concentration of nitrate in the overlying water column.

The second Lotic Intersite Nitrogen eXperiment (LINX II), which was conducted over five years from 2001 to 2006, remains one of the most comprehensive studies of nitrate uptake in headwater streams to-date [Hall et al., 2009; Beaulieu et al., 2011; Mulholland et al., 2008; 2009]. LINX II included ^{15}N-labeled nitrate seeding experiments in 72 streams across eight regions of the U.S., collectively representing eight different biomes (temperate rain forest, chaparral, northern mixed forest, deciduous forest, montane coniferous forest, temperate grassland, shrub desert and tropical forest) and three different land-use types (reference sites, urban-impacted sites, and agriculture-impacted). Based on regression and structural equation modeling of these data, LINX II researchers concluded that the nitrate uptake velocity is controlled primarily by streams chemistry (ambient concentrations of nitrate and ammonium concentrations) and biology (gross primary production and ecosystem respiration), and only weakly by stream physics (a measure of residence time in the hyporheic zone). Similarly, a meta-analysis of nutrient spiraling experiments conducted over the past three decades confirms that the evidence for physical controls on nutrient uptake in streambed sediments is “equivocal” [Ensign and Doyle, 2006].

Evaluation of physical controls on nitrate uptake in streams have been focused on hyporheic exchange (circulation of water through the hyporheic zone), quantified based on transient storage analysis of conservative tracer injection experiments [Bencala and Walters, 1983] or physical models of the pumping of water through streambed sediments by static and dynamic pressure variations [Boano et al., 2014]. Missing from these previous assessments is turbulent mass transport across the concentration boundary layer at the bottom of a stream. This transport mechanism is a key control on the delivery of oxygen to fine-grained (non-permeable) sediments [Hondzo et al., 1998], although its importance in streams with coarser (permeable) sediments (like most of the headwater streams included in the LINX II study) is not clear [Grant et al., 2011].

Given its position between the stream and streambed (**Figure 5.1A**), we hypothesized that nitrate uptake by permeable sediment beds might be “bottlenecked” by turbulent transport across the concentration boundary layer. In that event, the uptake velocity can be expressed as the product of a mass transfer coefficient k_m that depends solely on stream physics (the velocity with which mass is "squeezed" across the concentration boundary layer by turbulence, units m s^{-1}) and an efficiency α that captures the coupled physics and biogeochemistry of nitrate uptake in the benthic algal layer and hyporheic zone (the fraction of nitrate delivered to the streambed removed by assimilation and denitrification, unitless) (derivation in **Appendix D**):

$$v_\mathrm{f} = \alpha k_\mathrm{m},\ v_\mathrm{f} \geq 0,\ 0 \leq \alpha \leq 1,\ k_\mathrm{m} \geq 0 \tag{1a}$$

$$\alpha = \left(1 - \frac{1}{\psi + 1}\right),\ 0 \leq \psi < \infty \tag{1b}$$

$$\psi = \frac{v_\mathrm{algae} + v_\mathrm{HZ}}{k_\mathrm{m}} = \frac{\text{nitrate uptake velocities in the streambed}}{\text{turbulent mass transport across concentration boundary layer}} \tag{1c}$$

Conceptually, the mass transfer coefficient k_m represents the potential (mass-transfer limited) uptake velocity of a stream while the efficiency α indicates the fraction of that potential realized in practice. The efficiency depends on a dimensionless number ψ representing the balance of nitrate uptake by the streambed (uptake velocities in the benthic algae layer (v_algae, units m s^{-1}) and hyporheic zone (v_HZ, units m s^{-1})) and mass transfer across the concentration boundary layer. Because efficiency α varies from zero ($\psi \to 0$) to 1 ($\psi \to \infty$), if our hypothesis is correct the uptake velocity should always be less than or equal to the mass transfer coefficient: $v_\mathrm{f} \leq k_\mathrm{m}$ (see equation (1a)).

As a test of our hypothesis, we estimated values of the mass transfer coefficient at all LINX II sites where uptake velocities for nitrate assimilation ($v_{\mathrm{f,asm}}$, units m s^{-1}) and denitrification ($v_{\mathrm{f,den}}$, units m s^{-1}) were reported (49 of the 72 LINX II sites) [Mulholland et al., 2008]. Site-specific values of the transfer coefficient k_{m} were estimated from surface renewal theory, assuming mass transport across the concentration boundary layer occurs by sweep and ejection events associated with coherent turbulence in the stream together with molecular diffusion of mass into the streambed [O'Connor and Hondzo, 2008]. The theory predicts that k_{m} can be calculated from routinely measured features of a stream including slope (S) and depth (h), together with temperature corrected values for the kinematic viscosity (υ, units m^2 s^{-1}) and the molecular diffusion coefficient of nitrate (D_{m}, units m^2 s^{-1}):

$$k_{\mathrm{m}} = 0.17 u_* \mathrm{Sc}^{-2/3} \tag{2a}$$

$$\mathrm{Sc} = \upsilon / D_{\mathrm{m}} \tag{2b}$$

$$u_* = \sqrt{g h S} \tag{2c}$$

The Schmidt number (Sc, unitless) represents the relative importance of molecular diffusion of momentum and mass, the shear velocity (u_*, units m s^{-1}) is a measure of stream turbulence, and the gravitational constant is given by $g = 9.81$ m s^{-2}. Very similar formulae for calculating the mass transfer coefficient (equation (2a)) are obtained for different conceptual models of sediment-water interface (e.g., rough versus smooth) (reviewed in Grant and Marusic [2011]).

With one exception, the LINX II uptake velocities conform to the inequality $v_\mathrm{f} \le k_\mathrm{m}$ predicted by surface renewal theory (**Figures 5.1B** and **5.1C**), as does the total uptake velocity ($v_\mathrm{f,tot} = v_\mathrm{f,den} + v_\mathrm{f,asm}$, **Figure D.1** in **Appendix D**). The implied efficiencies (computed from the ratio $\alpha = v_\mathrm{f}/k_\mathrm{m}$) span approximately four orders of magnitude ($10^{-4} < \alpha_\mathrm{asm} \le 1$) for assimilation and approximately three orders of magnitude ($10^{-4} < \alpha_\mathrm{den} < 0.1$) for denitrification. The reduced range for α_den probably reflects the more restrictive nature of denitrification, which requires the presence of microbial populations capable of catalyzing the relevant redox reactions, anoxic conditions in the sediment, and sufficient electron donor and nitrate concentrations [Mulholland et al., 2008; 2009]. The uptake velocity for the one exceptional site (Headquarters Stream in the Teton National Park, Wyoming) exceeds the mass transfer coefficient by about 20%, which is within the error of the methods used to estimate uptake velocities [Mulholland et al., 2008]. Removal efficiencies calculated from the LINX II data are generally lowest in urban impacted streams and highest in reference and agriculture-impacted streams (**Figure 5.1D**). Estimates of the turbulent mass transfer coefficient are generally highest at reference sites (**Figure D.2** in **Appendix D**).

Our hypothesis implies a simple scaling relationship for the fraction of nitrate removed ($0 \le f \le 1$) over a stream reach of length L (units m) (derivation in **Appendix D**).

$$f = 1 - \exp\left(-0.17\alpha\sqrt{\frac{f_\mathrm{D}}{8}}\left(\frac{L}{h}\right)\mathrm{Sc}^{-2/3}\right) \tag{3}$$

If the goal is to enhance nitrate removal by manipulating stream physics (e.g., through stream restoration) equation (3) indicates that the Darcy Weisbach friction factor $f_{\mathrm{D}} = 8u_*^2/U^2$ (where U (units m s^{-1}) is the average velocity of the stream) and the length-to-depth ratio of the reach L/h should be maximized; e.g., using conventional hydraulic relationships [Ferguson, 2007]. The fraction of that potential realized in practice (i.e., the magnitude of α) can be estimated from empirical, modeling, and/or statistical approaches. The small-value limit of ψ (i.e., $\psi \approx \alpha \approx v_{\mathrm{f}}/k_{\mathrm{m}}$ when $\psi \ll 1$ (see **Appendix D**)) implies that α can be estimated by substituting empirical relationships for v_{f} into equation (1b), such as the negative power-law dependence of nitrate uptake on stream nitrate concentration proposed by Mulholland et al. [2008]. Alternatively, nitrate uptake in the benthic algal layer and hyporheic zone (v_{algae} and v_{HZ}) can be estimated from computational models (e.g., Gomez-Valez and Harvey [2014] and Azizian et al. [2017]) and then substituted into equations (1b) and (1c) to obtain the efficiency α . Given the inherent spot-to-spot and moment-to-moment variability associated with denitrification rates [Groffman et al., 2009] a statistical approach for estimating the efficiency may be warranted; e.g., by adopting measures of central tendency for α (such as the median) or Monte Carlo sampling the distributions presented in **Figure 5.1D**.

Remarkably, trialing the simplest of these three approaches (fixed median values for the efficiency of denitrification and assimilation across all land-use categories: $\alpha_{\mathrm{den}} = 0.0045$ and $\alpha_{\mathrm{asm}} = 0.0183$, see stars in **Figure 5.2A**) we find that equation (3) closely reproduces probability distributions of the fraction of nitrate removed at LINX II sites (**Figure 5.2B**)

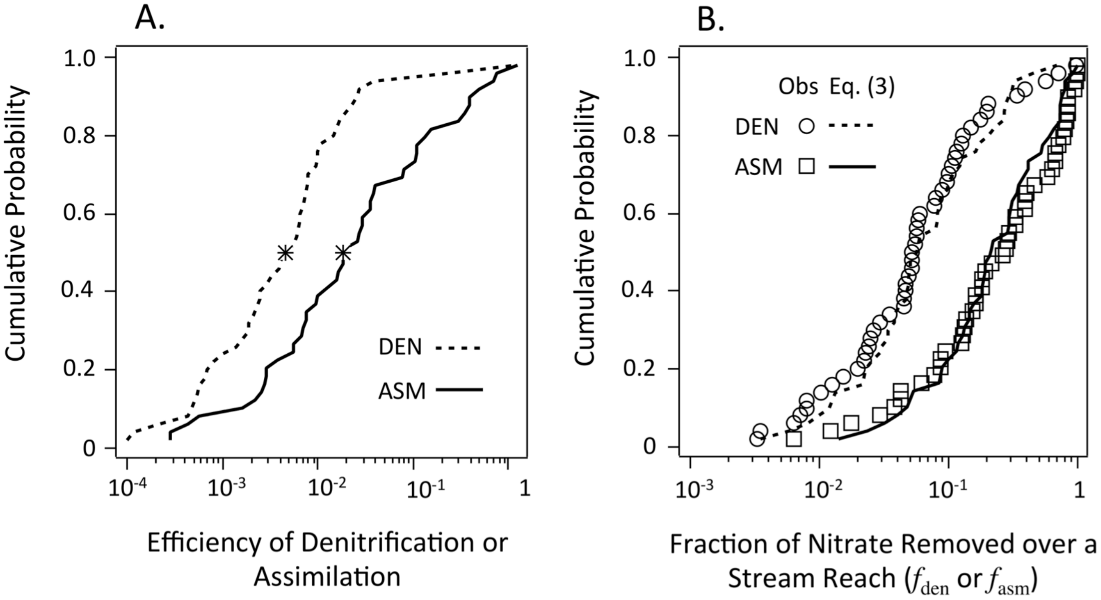

Figure 5.2. A "physics only" test of the scaling law (equation (3)) derived in this study. **(A)** Probability distributions for denitrification and assimilation efficiencies measured across all LINX II sites (median values denoted by stars). **(B)** Probability distributions of the measured (symbols) and predicted (curves) fraction of nitrate removed by denitrification (f_{den}). Predicted values were calculated from equation (3) using the median denitrification and assimilation efficiencies.

(see **Appendix D**). Not surprisingly, the performance of this "physics only" approach is mixed when evaluated on a site-by-site basis (**Figure D.3** in **Appendix D**); i.e., equation (3) correctly predicts the fraction of nitrate removed at sites where the efficiency is close to the median value, but not otherwise. While the probability of nitrate removal can be estimated by substituting median efficiency values into equation (3) (**Figure 5.2B**), locally tailored values of α (obtained from the empirical or modeling approaches described above) should improve the theory's utility for site-specific estimates of nitrate removal as well. Collectively, these results support the use of equation (3) in conjunction with stream network models, like the one recently prepared for the Mississippi River

Basin [Kiel and Cardenas, 2014], to estimate the fate and transport of nitrate pollution at watershed, continental, and global scales.

Appendix D. Derivations.

References

Azizian, M., F. Boano, P.L.M. Cook, R.L. Detwiler, M.A. Rippy, S.B. Grant (2017) Ambient groundwater flow diminishes nitrate processing in the hyporheic zone of streams. Wat. Resour. Res. 53, doi:10.1002/2016WR020048.

Beaulieu J. J., et al., (2011) Nitrous oxide emission from denitrification in stream and river networks. Proc. Natl. Acad. Sci. U.S.A. 108, 214-219.

Bencala, K.E., R.A. Walters (1983). Simulation of solute transport in a mountain pool-and-riffle stream: a transient storage model. Wat. Resour. Res. 19, 718-725.

Boano, F., J.W. Harvey, A. Marion, A.I. Packman, R. Revelli, L. Ridolfi, A. Worman (2014) Hyporheic flow and transport processes: Mechanisms, models, and biogeochemical implications. Rev. Geophys. 52, doi:10.1002/2012RG000417.

Ensign, S.H., M.W. Doyle (2006) Nutrient spiraling in streams and river networks. J. Geophys. Res. 111, G04009.

Ferguson, R. (2007), Flow resistance equations for gravel and boulder-bed streams. Water Resour. Res., 43, W05427.

Galloway, J. N., et al. (2004), Nitrogen cycles: Past, present, and future, Biogeochemistry, 70, 153–226.

Gomez-Velez, J.D., J.W. Harvey (2014) A hydrogeomorhpic network model predicts where and why hyporheic exchange is important in large basins. Geophys. Res. Lett. 41, 6403-6412.

Grant, S.B., I. Marusic (2011) Crossing turbulent boundaries: Interfacial flux in environmental flows. Environ. Sci. Technol. 45, 7107-7113.

Groffman, P.M. et al. (2009) Challenges to incorporating spatially and temporally explicit phenomena (hotspots and hot moments) in denitrification models Biogeochem. **93**, 49-77.

Hall, R.O., et al. (2009), Nitrate removal in stream ecosystems measured by 15N addition experiments: total uptake. Limnol. Oceanogr. 54, 653-665.

Hall, R.O., M.A. Baker, C.D. Arp, B.J. Koch (2009) Hydrologic control of nitrogen removal, storage, and export in a mountain stream. Limnol. Oceanogr. 54, 2128-2142.

Hondzo , M. (1998), Dissolved oxygen transfer at the sediment-water interface in a turbulent flow. Wat. Resour. Res. 34, 3525-3533.

Kiel, B.A., M.B. Cardenas (2014) Lateral hyporheic exchange through the Mississippi River network. Nature Geosci. 7, NGEO2157.

Marzadri, A., M.M. Dee, D. Tonina, A. Bellin, J.L.Tank (2017), Role of surface and subsurface processes in scaling N2O emissions along riverine networks. Proc. Natl. Acad. Sci. U.S.A. 114, 4330-4336.

Mulholland, P.J. et al. (2008) Stream denitrification across biomes and its response to anthropogenic nitrate loading. Nature 452, 202-206.

Mulholland P.J. et al. (2009) Nitrate removal in stream ecosystems measured by 15N addition experiments: Denitrification. Limnol. Oceanogr. 54, 666-680.

National Academy of Engineering (2017), NAE Grand Challenges for Engineering. [online] Available at: http://www.engineeringchallenges.org/challenges.aspx [Accessed 30 May, 2017].

O'Connor, B.L., M. Hondzo (2008) Dissolved oxygen transfer to sediments by sweep and eject motions in aquatic environments. Limnol. Oceanogr. 53, 566-578.

Steffen, W. et al. (2015), Planetary boundaries: guiding human development on a changing planet. Science, 347, 1259855. doi: 10.1126/science.1259855.

U.S. Environmental Protection Agency, (EPA), "Water quality assessment and total maximum daily loads information: assessment, TMDL tracking and implementation system (ATTAINS)" (https://www.epa.gov/waterdata/assessment-and-total-maximum-daily-load-tracking-and-implementation-system-attains).

Chapter 6

Summary and Conclusions, Future Research Directions

6.1. Summary and Conclusions

In this thesis I focus on developing and testing process-based models of nutrient transformations in streams and coastal waters, which then can be used to better manage point and non-point sources of nutrients within urban and agriculturally impacted watersheds. More specifically, I focus on mitigation of nitrogen pollution by in-stream treatment; i.e. the natural ability of streams to remove inorganic nitrogen (ammonium, nitrate, and nitrite) by nitrification and denitrification. Much of this in-stream treatment occurs in the hyporheic zone, defined as the portion of the streambed where hydrologic flow paths begin and end in the stream. My process-based model, also called Pumping And Streamline Segregation (PASS) model, provides a simple framework to combine both physical (i.e. hyporheic exchange flux and residence time distribution) and biogeochemical (i.e. concentration profile along the hyporheic zone flow paths) components underlying the transport and fate of nutrients in the hyporheic zone of streams. Therefore, it can provide mechanistic explanations for some of previously published labor- and data- intensive experimental correlations, laboratory observations, and numerical simulations. Below I present the evolution of the PASS model over the course of this dissertation and provide key findings of each study included in this thesis.

In **Chapter 2**, a simple analytical model is presented for the removal of stream-borne contaminants by hyporheic exchange across duned or rippled streambeds. The model assumes a steady-state balance between contaminant supply from the stream and first-order reaction in the sediment. Hyporheic exchange occurs by bed form pumping, in which water and contaminants flowed into bed forms in high-pressure regions (downwelling zones) and out of bed forms in low-pressure regions (upwelling zones). Model-predicted contaminant concentrations are higher in downwelling zones than upwelling zones, reflecting the strong coupling that exists between transport and reaction in these systems. When flow-averaged, the concentration difference across upwelling and downwelling zones drive a net contaminant flux into the sediment bed proportional to the average downwelling velocity. The downwelling velocity is functionally equivalent to a mass transfer coefficient, and can be estimated from stream state variables including stream velocity, bed form geometry, and the hydraulic conductivity and porosity of the sediment. Increasing the mass transfer coefficient increases the fraction of stream water cycling through the hyporheic zone (per unit length of stream) but also decreases the time contaminants undergo first-order reaction in the sediment. As a consequence, small changes in stream state variables can significantly alter the performance of hyporheic zone treatment systems.

Bedforms are a focal point of carbon and nitrogen cycling in streams and coastal marine ecosystems. Therefore, in **Chapter 3,** I develop and test a mechanistic model—the "pumping and streamline segregation" or PASS model—for nitrate removal in bedforms. The PASS model dramatically reduces the computational overhead associated with modeling nitrogen transformations in bedforms and reproduces (within a factor of 2 or better) previously published measurements and models of biogeochemical reaction rates, benthic fluxes, and in-sediment nutrient and oxygen concentrations. Application of the PASS model in a diverse set of marine and freshwater biogeochemical settings indicates that (1) physical controls on nitrate removal in a bedform included the pore water flushing rate, residence time distribution, and relative rates of respiration and transport (as represented by the Damköhler number); (2) the biogeochemical pathway for nitrate removal is an environment-specific combination of direct denitrification of stream nitrate and coupled nitrification-denitrification of stream and/or sediment ammonium; and (3) permeable sediments are almost always a net source of dissolved inorganic nitrogen. The PASS model also provides a mechanistic explanation for previously published empirical correlations showing denitrification velocity (N_2 flux divided by nitrate concentration) declines as a power law of nitrate concentration in a stream [Mulholland et al., 2008].

Modeling and experimental studies demonstrate that ambient groundwater reduces hyporheic exchange, but the implications of this observation for stream N-cycling is not yet clear. In **Chapter 4**, I utilize a simple process-based model (the Pumping and Streamline Segregation or PASS model) to evaluate N-cycling over two scales of hyporheic exchange (fluvial ripples and riffle-pool sequences), ten ambient groundwater and stream flow scenarios (five gaining and losing conditions and two stream discharges), and three biogeochemical settings (identified based on a principal component analysis of previously published measurements in streams throughout the United States). Model-data comparisons indicate that my model provide realistic estimates for direct denitrification of stream nitrate, but over-predict nitrification and coupled nitrification-denitrification. Riffle-pool sequences are responsible for most of the

N-processing, despite the fact that fluvial ripples generate 3-11 times more hyporheic exchange flux. Across all scenarios, hyporheic exchange flux and the Damköhler number emerge as primary controls on stream N-cycling; the former regulates trafficking of nutrients and oxygen across the sediment-water interface, while the latter quantifies the relative rates of organic carbon mineralization and advective transport in streambed sediments. Vertical groundwater flux modulates both of these master variables in ways that tended to diminish stream N-cycling. Thus, anthropogenic perturbations of ambient groundwater flows (e.g., by urbanization, agricultural activities, groundwater mining, and/or climate change) may compromise some of the key ecosystem services provided by streams.

The seminal study of Mulholland et al. [2008] on headwater streams across the U.S. conclude that in-stream removal of nitrate is controlled primarily by stream chemistry and biology, and only weakly by stream physics. In **Chapter 5**, my reanalysis of these data reveals that stream physics (in particular, turbulent mass transfer across the concentration boundary layer) imposes a previously unrecognized upper limit on the rate nitrate is removed from streams. The upper limit represents the potential (mass-transfer limited) capacity of a stream to remove nitrate, while the fraction of that potential realized in practice is determined by stream chemistry, biology, and hydrology. Physics alone closely reproduces measured distributions of nitrate removal in headwater streams, a discovery that should inform stream restoration designs and efforts to assess the impacts of nitrogen pollution on receiving water quality and the global nitrogen cycle.

6.2. Future Research Directions

The simplicity of the modeling framework that is presented in this dissertation is both its strength and weakness. Stripping the problem to its essential elements (hyporheic exchange flux, residence time distribution, and concentration profile of the chemicals along the hyporheic zone flow paths) allows for explicit evaluations of the effect of the key controlling variables on the contaminant removal in hyporheic zone of streams. However, in so doing I neglect many hydrological, biophysical, and chemical processes that can influence contaminant fate and transport in streams. Below I present some of the limitations that can be diagnosed in this dissertation and provide some recommendations for future research direction.

In this dissertation I only account for hyporheic exchange process due to the bed form pumping across ripples and riffle-pool sequences, which is only one of many transport mechanisms that can induce hyporheic exchange. Turbulent eddies in the water column of a stream, for example, can cause flow across the sediment-water interface in the presence or absence of bed forms. Also larger scale geomorphic features of a stream such as debris dams and meander bends can influence hyporheic exchange. Therefore, one of the opportunities for future research is to account for other types of hyporheic exchange processes and investigate their effects on contaminant removal in the hyporheic sediments.

The research presented in this dissertation does not account for a number of biogeochemical factors known to affect nitrogen budgets in aquatic systems. For example, there are some chemical pathways other than nitrification and denitrification through which nitrate can be produced or reduced in the hyporheic sediments (such as anaerobic ammonium oxidation (Anammox) or dissimilatory nitrate reduction to ammonium (DNRA)) (see Chapters 3 and 4). Also, patterns of organic carbon and respiration rates can be spatially variable. Bulk organic carbon concentration often declines with depth into the sediment bed [Cook et al., 2006] and/or can be locally concentrated, for example, in the form of buried fecal pellets [Jørgensen, 1977] (see Chapters 4 and 5). All of the above items are limitations of the current biokinetic model that I implement in this dissertation that can be improved moving forward.

Hyporheic sediments are heterogeneous relative to sediment grain sizes [Cardenas et al., 2004] and flow paths [Menichino et al., 2014,2015]. This heterogeneity can lead to mixing across streamlines [Sawyer, 2014; Triska et al., 1989] and facilitate the formation of redox microzones (e.g., localized pockets of denitrification embedded within well-oxygenated downwelling regions) that enhance coupled nitrification-denitrification and overall nitrate removal rates in natural sediments [Briggs et al., 2015; Sawyer, 2014]. In the context of the PASS modeling framework, physical heterogeneities can be represented by heavy tailed RTD functions (presumably through so-called “mobile-immobile” (MIM) models; see Schumer et al., 2001, 2003, and 2009). Further research on this topic should be promising as well.

Plants and animals colonizing the hyporheic zone can also exert profound impacts on stream-sediment exchange, by forming mounds across which pumping occurs, inducing pore-water flow within sediments, and structuring the permeability field with burrows and roots (reviewed in Meysman et al. [2007]). Different animals or plants also have different tendency to remove certain types of nutrient or pollutant. Therefore, through changing both biogeochemical settings of the environment as well as the physics of the hyporheic exchange, hyporheic plants and animals can influence a stream's potential for contaminant removal. This topic should be fruitful for future research.

Finally, while I have focused here on the processing of stream-borne nitrate by hyporheic exchange, it is important to acknowledge that groundwater can also be a significant source of nitrate, particularly in agricultural areas [Hinkle et al., 2001; Smith et al., 2009] and N-cycling and contaminant removal can also occur in other components of the stream (i.e., other than the hyporheic zone), such as the stream's water column or in hydraulically disconnected surface storage zones [Stewart et al., 2011]. Finding ways to account for introduction of nitrate pollution to the hyporheic zone from the groundwater component and also including other components of the stream is another interesting topic for future research.

References

Briggs, M.A.; Day-Lewis, F.D.; Arnetske; J.P.; Harvey, J.W. (2015), A physical explanation for the development of redox microzones in hyporheic flow. Geophys. Res. Lett., 42, doi:10.1002/2015GL064200.

Cardenas, M. B.; Wilson, J. L.; Zlotnik, V. A. (2004), Impact of heterogeneity, bed forms, and stream curvature on subchannel hyporheic exchange. Water Resour. Res., 40, W08307, doi: 10.1029/2004WR003008.

Cook, P. L. M., F. Wenzhofer, S. Rysgaard, O. S. Galaktionov, F. J. R. Meysman, B. D. Eyre, J. Cornwell, M. Huettel, and R. N. Glud (2006), Quantification of denitrification in permeable sediments: Insights from a two-dimensional simulation analysis and experimental data, Limnol. Oceanogr. Methods, 4, 294–307.

Elliott, A. H., and N. H. Brooks (1997a), Transfer of nonsorbing solutes to a streambed with bed forms: Theory, Water Resour. Res., 33, 123-136.

Elliott, A. H., and N. H. Brooks (1997b), Transfer of nonsorbing solutes to a streambed with bed forms: Laboratory experiments. Water Resour. Res., 33, 137-151.

Hinkle, S.R., J. H. Duff, F. J. Triska, A. Laenen, E. B. Gates, K. E. Bencala, D. A. Wents, and S. R. Silva (2001), Linking hyporheic flow and nitrogen cycling near the Willamette River: A large river in Oregon, USA, J. Hydrol., 244, 157–180.

Jørgensen, B. B. (1977), Bacterial sulfate reduction within reduced microniches of oxidized marine sediments, Mar. Biol., 41(1), 7–17.

Menichino, G. T.; Ward, A. S.; Hester, E. T. (2014), Macropores as preferential flow paths in meander bends, Hydrol. Process., 28, 482-495.

Menichino, G. T.; Scott, D. T.; Hester, E. T. (2015), abundance and dimensions of naturally occuring macropores along stream channels and the effects of artificially constructed large macropores on transient storage. Freashwater Science, 34, 125-138.

Meysman, F. J. R.; Galaktionov, O. S.; Cook, P. L. M.; Janssen, F.; Huettel, M.; Middelburg, J. J. (2007), Quantifying Biologically and Physically Induced Flow and Tracer Dynamics in Permeable Sediments. Biogeosciences, 4, 627–646.

Mulholland, P. J., et al. (2008), Stream denitrification across biomes and its response to anthropogenic nitrate loading, Nature, 452, 202–205. Mulholland, P. J., et al. (2009), Nitrate removal in stream ecosystems measured by 15N addition experiments: Denitrification, Limnol. Oceanogr., 54(3), 666–680.

Rutherford, J. C., J. D. Boyle, A. H. Elliott, T. V. J. Hatherell, and T. W. Chiu (1995), Modeling benthic oxygen uptake by pumping, ASCE J. Envi- ron. Eng., 121(1), 7216.

Sawyer, A.H. (2014), Enhanced removal of groundwater-borne nitrate in heterogeneous aquatic sediments. Geophys. Res. Lett., 42, 403-410.

Schumer R., D. A. Benson, M. M. Meerschaert, and S. W. Wheatcraft (2001), Eulerian derivation of the fractional advection-dispersion equation, J. Contam. Hydrol., 48, 69–88.

Schumer, R., D. A. Benson, M. M. Meerschaert, and B. Baeumer (2003), Fractal mobile/immobile solute transport, Water Resour. Res., 39(10), 1296, doi:10.1029/2003WR002141.

Schumer R., M. M. Meerschaert, and B. Baeumer (2009) Fractional advection-dispersion equations for modeling transport of the Earth surface, J. Geophys. Res., 114, F00A07, doi:10.1029/2008JF001246.

Smith, V. H., G. D. Tilman, and J. C. Nekola (1999), Eutrophication: Impacts of excess nutrient inputs on freshwater, marine, and terrestrial ecosystems, Environ. Pollut., 100, 179–196.

Stewart, R. J., W. M. Wollheim, M. N. Gooseff, M. A. Briggs, J. M. Jacobs, B. J. Peterson, and C. S. Hopkinson (2011), Separation of river network-scale nitrogen removal among the main channel and two transient storage compartments, Water Resour. Res., 47, W00J10, doi: 10.1029/2010WR009896.

Triska, F. J.; Kennedy, V. C.; Avanzino, R. J.; Zellweger, G. W.; Bencala, K. E. (1989), Retention and transport of nutrients in a third-order stream in northwestern California: Hyporheic processes. Ecology, 70 (6), 1893-1905.

Appendix A

First-Order Contaminant Removal in the Hyporheic Zone of Streams: Physical Insights from a Simple Analytical Model

Text A.1. Numerical Simulations to Assess the Flatbed Assumption in the Elliott and Brooks Model of Hyporheic Exchange

EB model predictions of the modulus of the Darcy flux were compared with numerical simulations that explicitly account for the affect of bed form geometry on both the pressure distribution at the sediment-water interface and flow through the bed form. Numerical simulations were performed following the same approach and hydraulic modeling scheme used by Bardini et al. [2012] in **Chapter 2** (see **Figure A.1**). A Cartesian reference system was adopted, with x and y coordinates taken as the streamwise and upward coordinates, respectively; the origin of the y-axis was placed at the bed form trough (i.e., $y = 0$ corresponds to the base of the bed form). Two different types of surfaces were modeled: (1) flatbed (to closely mimic the EB model assumptions); and (2) a bed consisting of triangular and asymmetric 2D bed forms, with the crest position shifted towards the downstream end of the bed form. Bed form height Δ and length λ were 0.075 m and 1 m respectively, and the crest was located at $x = 0.9m$. For both simulations the stream velocity U and water depth H were set to 0.33 m/s and 0.5 m, respectively.

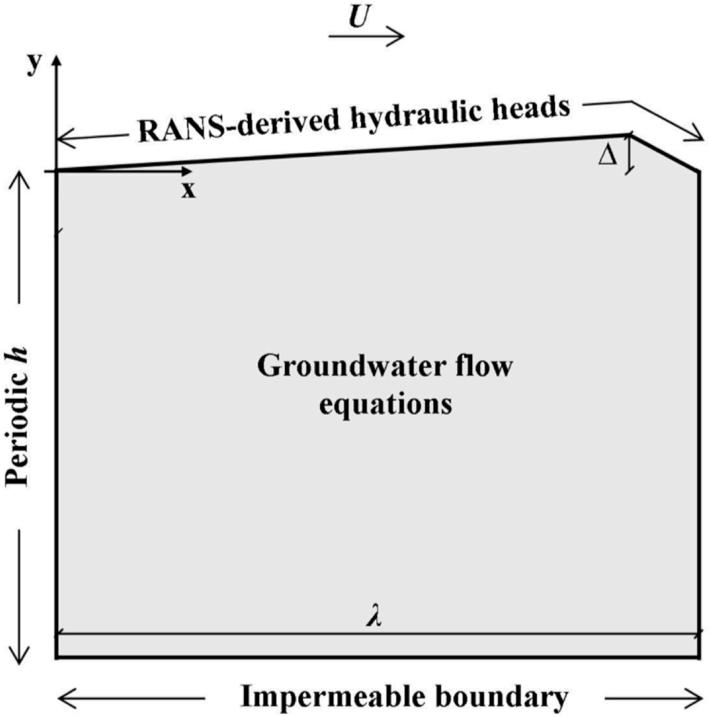

Figure A.1. Numerical domain for numerical simulations carried out to evaluate potential issues associated with the assumed flatbed geometry in the Elliott and Brooks velocity model.

On the surface boundary a Dirichlet condition was prescribed using a Reynolds-Averaged Navier-Stokes (RANS)-derived hydraulic head distribution. Specifically, the hydraulic head values were taken from open channel flow simulations conducted by Sawyer and Cardenas [2009], who numerically solved, in steady state conditions, the RANS equations for incompressible and homogeneous fluids with the k – ω closure scheme for eddy viscosity. Lateral boundaries were periodic in head, with a head drop due to the stream slope. The bottom boundary was assigned a no-flow condition. The steady-state

Darcy flow in the sediment was simulated by solving the groundwater flow equations, i.e. the Darcy's law and the continuity equation for incompressible fluids:

$$u = -K\nabla h \text{ and } \nabla \cdot \mathbf{u} = 0 \qquad \text{(A1)}$$

where $\mathbf{u} = \left(u_x, u_y\right)$ is the Darcy velocity vector, $K = 9.8 \times 10^{-4} ms^{-1}$ is the hydraulic conductivity and h is the hydraulic head. The Darcy velocity **u** included both the flow induced by the hydraulic head distribution at the streambed surface (the so called "bedform pumping flow") and the regional groundwater flow. The "turnover" process was not considered, because the bed forms modeled here were stationary. Equations (A1) were numerically solved with COMSOL, a generic multi-physics finite element solver, with adaptive meshing and error control. From the simulated velocity field, horizontally averaged values of the modulus of the Darcy flux (see equation 2d in **Chapter 2**) were computed:

$$\|\bar{\mathbf{u}}\| = \frac{1}{L}\int_0^L \|\mathbf{u}\| dx \qquad \text{(A2)}$$

where L is the horizontal space of integration. For the simulation involving a bedform-shaped sediment-water interface $L > \lambda$ for $y > 0$ and $L = \lambda$ for $y \leq 0$. For the simulation involving a flat sediment-water interface, $L = \lambda$ for $y \leq 0$.

The horizontally averaged Darcy flux obtained from the numerical RANS/Darcy Flow simulations is plotted against depth in **Figure A.2**. It is important to note that the horizontally averaged Darcy flux computed for the flatbed and bed form cases cannot be compared quantitatively, because it is not clear how datums for the two solutions should be aligned relative to each other. Specifically, it is not clear if the datum (i.e., position of

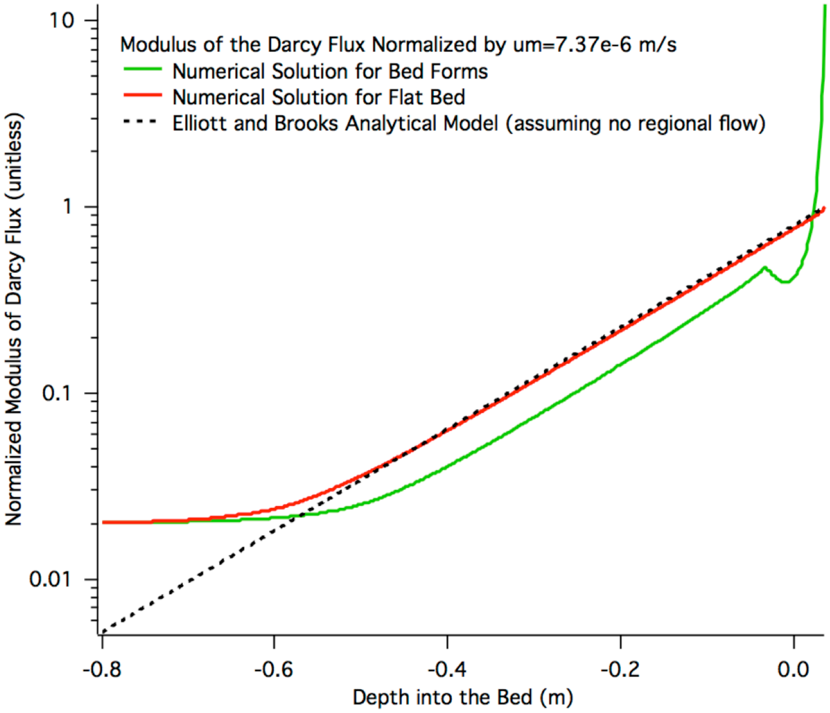

Figure A.2. Comparison of numerical simulations for a triangular bed form (green curve), flat bed (red curve), and the Elliott and Brooks velocity model (black dashed line).

$y=0$) for the flat bed solution should be located at the base of the bed form, at the top of the bed form, or somewhere in between. For the comparison presented here we arbitrarily assigned the datum of the flatbed solution to the base of the bed form, but any other choice would be equally valid, and would give a different relative (vertical) positioning of the red and green curves shown in **Figure A.2**. Although the magnitudes cannot be compared, their functional dependence on the y-coordinate can be compared. When plotted in a log-linear format, both the flatbed and bed form solutions for $\|\bar{\mathbf{u}}\|/u_m$ appear linear below the base of the bed form (i.e., $y<0$) implying that both solutions exhibit an exponential decay with depth in this region—a result consistent with the predictions of the EB model (compare dashed line with red and green lines, **Figure A.2**). For elevations between the base and crest of the dune ($0 < y < 0.04m$) the bed-form solution exhibits a non-exponential functional dependence on y. For depths $y < -0.6m$ both the flatbed and bed form numerical simulations converge to a constant horizontally-averaged Darcy flux of $\|\bar{\mathbf{u}}\|/u_m = 0.02$, which corresponds to the regional groundwater flow. Note the EB model continues to decay exponentially for $y < -0.6m$ because it does not account for regional groundwater flow (dashed black line in **Figure A.2**).

As a final test of the EB model (and specifically how well it approximates the advective flux across bed forms) we computed the average normal Darcy flux across the surface of the dune, and compared it to the EB estimate of $\bar{q}_{EB} = u_{m,EB}/\pi$ (see discussion of the mass transfer coefficient in **Chapter 2**). The bed form simulation yields $\bar{q}_{sim} = 2.08 \times 10^{-6} ms^{-1}$ while the EB model predicts $\bar{q}_{EB} = 2.35 \times 10^{-6} ms^{-1}$, a difference of approximately 11%. The $u_{m,EB}$ value used to estimate the above value of $\bar{q}_{EB}$ was obtained from a rearranged version of equation (14a) in **Chapter 2**, which was based on pressure measurements over artificial dunes by Fehlman [1985]. If instead we use the expression proposed by Cardenas and Wilson (equation (14b)) the predicted average Darcy flux across the sediment-water interface is again very close to the simulated value: $\bar{q}_{CW} = u_{m,CW}/\pi = 1.54 \times 10^{-6} ms^{-1}$. However, if we utilize the modified form of the Cardenas and Wilson expression proposed in **Chapter 2** (based on its better match with experimental mass transfer limited flux measurements, see **Figure 2.4C** in **Chapter 2**) the average Darcy flux is approximately a factor of 6 larger than the simulated value:

$\bar{q}_{CW,\mathrm{mod}} = 1.2 \times 10^{-5} m s^{-1}$. While the original CW mass transfer coefficient exhibits a systematic bias with respect to measured mass transfer coefficients (see **Figure 2.4B** in **Chapter 2**), it matches relatively well our simulated estimates of flux across a triangular dune. Conversely, the modified CW expression better matches experimental values, but does a relatively poor job of predicting the simulated Darcy flux above.

There are several explanations for the apparent contradiction outlined above. First, our simulated flux utilizes a pressure distribution obtained from RANS simulations reported in Sawyer and Cardenas [2009]. The simulated pressure distribution was generated by the same group (using the same methods) as proposed the original Cardenas and Wilson correlation, which may explain why the simulation and correlation are in relatively good agreement. Second, the RANS simulations reported here were carried out using a set of parameter values (e.g., $U = 0.34 m s^{-1}$, $K_h = 9.81 \times 10^{-4} m s^{-1}$, $\lambda = 1m$) near (or outside of) the range of values applicable to the experimental data plotted in **Figure 2.4** in **Chapter 2**, which may explain why the original Cardenas and Wilson correlation does not predict the experimental flux measurements in **Figure 2.4B**. A thorough reconciliation of numerical simulations and experimental estimates of flux across the sediment-water interface is an interesting topic for future investigation.

Text A.2. Relative Importance of Mechanical Dispersion and Advective Transport

The solute transport and reaction equation (equation 3 in **Chapter 2**) has separate terms for advection and mechanical dispersion, and molecular diffusion, but only one of these may dominate in practice. To assess their relative importance, here we perform an order-of-magnitude analysis on a simplified geometry; namely, the steady-state one-dimensional transport and reaction of a solute in a fully saturated sediment column of constant porosity. Assuming the mechanical dispersive flux (J_{Disp}) is much smaller than the advective flux (J_{adv}), solute concentration at any location x in the one-dimensional column can be derived from mass balance. For a constant concentration boundary condition at the entrance ($C(x=0)=C_0$) mass balance yields the following result: $C=C_0\exp(-\theta k_r x/u)$ where u is the Darcy flux in the x-direction. While this solution neglects dispersive flux, it can still be used to estimate the dispersive flux provided $J_{Disp} << J_{adv}$. Substituting the solution for C into the definition of the dispersive flux ($J_{Disp}=-(\alpha_L u)dC/dx$) and dividing by the advective flux ($J_{adv}=uC$) yields a quantitative estimate for the relative importance of these two flux terms: $J_{Disp}/J_{adv}=\alpha_L\theta k_r/u$. Again, this expression is only valid if $J_{Disp} << J_{adv}$. For the parameter values used to generate **Figure 2.2A** (see **Table A.1**) and assuming a Darcy flux of $u=u_m$ (which will overestimate the magnitude of the dispersive flux), the dispersive flux is roughly 500 times smaller than the advective flux ($J_{Disp}/J_{Adv}\approx 2.1\times10^{-3}$). Therefore mechanical dispersion can be neglected in this case.

Text A.3. Relative Importance of Molecular Diffusion and Advective Transport

A similar analysis can be carried out to assess the relative importance of advective transport and transport by molecular diffusion. For the one-dimensional column analogy introduced above, mass flux by molecular diffusion is: $J_{Mol}=-\beta D_m\,dC/dx$ where β is

Table A.1. Primary variables used for simulations of contaminant removal in the hyporheic zone of a stream (see **Figure 2.2A** and **2.2B** in **Chapter 2**). Values are from Bardini et al. [2012].

k_r [a] $\left[\mathrm{s}^{-1}\right]$	U [b] $\left[\mathrm{ms}^{-1}\right]$	θ [c] $[-]$	λ [d] $[\mathrm{m}]$	K_h [e] $\left[\mathrm{m\,s}^{-1}\right]$	H [f] $[\mathrm{m}]$	Δ [g] $[\mathrm{m}]$	α_{L} [h] $[\mathrm{m}]$	α_{T} [i] $[\mathrm{m}]$	D_{m} [j] $\left[\mathrm{m}^2\mathrm{s}^{-1}\right]$	β [k] $[-]$	u_m [l] $\left[\mathrm{m\,s}^{-1}\right]$
5x10^{-6}	0.21	0.4	1.0	9.81x10^{-4}	0.5	0.075	0.003	0.0003	1.97x10^{-9}	0.19	2.9x10^{-6}

[a] first-order reaction rate constant; [b] stream velocity; [c] sediment porosity; [d] dune wavelength; [e] hydraulic conductivity; [f] stream depth; [g] dune amplitude; [h] longitudinal dispersivity; [i] transverse dispersivity; [j] molecular diffusion coefficient (appropriate for oxygen in water at 20C); [k] tortuosity; [l] amplitude of the maximum Darcy velocity (calculated using the expression developed by Elliott and Brooks [1997a]).

tortuosity and D_m is the molecular diffusion coefficient of a solute in water. Substituting the above solution for C and dividing by the advective flux yields: $J_{Mol}/J_{adv} = \theta\beta D_m k_r/u^2$. For the set of parameter values listed in **Table A.1** (and again substituting u_m for u) we obtain $J_{mol}/J_{adv} = 10^{-3}$, lower than the above estimate for J_{Disp}/J_{adv}. Note that we assumed a value for the molecular diffusion coefficient (D_m = 1.97x10^{-9} m^2 s^{-1}) that would be typical for a rapidly diffusing molecule such as O_2 in water at 20C. Therefore, the value of J_{mol}/J_{adv} calculated here is conservative; i.e., for more slowly diffusing compounds, the ratio will be even smaller.

Text A.4. Numerical Artifacts Associated with Imposing A Constant-concentration (Dirichlet) Boundary Condition at the Sediment-stream Interface

Most numerical simulations of biogeochemical transformations in the hyporheic zone adopt a constant concentration boundary condition at the sediment-stream boundary. On its face, this choice of boundary condition raises several concerns. First, in upwelling zones, water flowing into the stream from the hyporheic zone should have a chemical signature reflective of the hyporheic zone (i.e., the concentration at the sediment-stream boundary should not be equal to C_0 there). Second, by forcing the concentration to be constant everywhere along the sediment-stream boundary, if there is no loss or gain of water by the stream, advection can contribute no net mass flux across the sediment-stream boundary. This would appear to contradict one of the major conclusions above: that for the set of parameter values listed in **Table A.1** mass transport is dominated by advection, not mechanical dispersion nor molecular diffusion. All of this begs the question: does the constant concentration boundary conditions adversely affect numerical simulations of mass transport in the hyporheic zone? For numerical simulations that include both advection and mechanical dispersion, advection confines the effect of the boundary condition to a region of length scale α_L near the sediment surface, where α_L represents longitudinal dispersivity. The numerical simulations illustrated in **Figure 2.2B** obviously has this characteristic (i.e., contaminant-depleted waters make it very close, but not all the way, to the sediment-stream boundary in the upwelling zone, see **Figure 2.2A**). However, in the numerical simulation the length scale α_L is probably over-estimated because of the finite grid size used in the finite element scheme employed by COMSOL.

To understand how the Dirichlet boundary condition affects (or not) the numerical simulation results, we return to the column analogy used earlier to assess the relative importance of dispersive and advective fluxes. At the end of the one-dimensional column (say at $x = L$) advection attempts to push a flux $u_x C_0 \exp(-\theta k_r L / u_x)$ out of the column, which is smaller than the advective flux $u_x C_0$ entering the column at $x = 0$. This results in a net advective flux into the column of $u_x \Delta C$, where $\Delta C = C_0 \left[1 - \exp\left(-\theta k_r L / u_x \right) \right]$. The equivalent of enforcing a constant concentration at the sediment-stream boundary (in numerical simulations of hyporheic exchange) is forcing $C = C_0$ at $x = L$ (in the one-dimensional column analogy). If $C = C_0$ at $x = L$ and advection pushes the non-dispersive concentration distribution within a distance α_L of the end of the column, then the concentration gradient near the column exit is roughly $\Delta C / \alpha_L$. This implies a dispersive flux into the column at $x = L$ of $u_x \alpha_L \Delta C / \alpha_L = u_x \Delta C$; i.e. just enough to balance the net advective flux and thus satisfy the imposed boundary condition at $x = L$. The supply of mass to the sediment is the advective inflow flux $u_x C_0$, a fraction $\Delta C / C_0$ of which reacts in the sediment, thereby determining the average concentration in the sediment. In conclusion, the constant-concentration boundary condition at the end of the column has little effect on the overall concentration field, and is unlikely to adversely affect estimates of the net flux across the sediment-stream boundary.

Text A.5. Proof that the x-component of the Velocity Is Everywhere Constant along a Single Streamline in the EB Flow Model

This can be demonstrated by noting that, for any two-dimensional steady flow field, the slope of the streamline is equal to the ratio of the x - and y -components of the velocity vector:

$$\frac{dy\left(\bar{x} \middle| \bar{x}_0\right)}{dx} = \frac{u_y}{u_x} = \tan \bar{x} \qquad \text{(A3)}$$

Here the notation "$\bar{x}|\bar{x}_0$" denotes the $\bar{x}$ position along the $\bar{x}_0$ streamline. Integration of equation (A3) yields an equation for the streamline; namely how the depth ($\bar{y}$) of the $\bar{x}_0$ streamline varies as a function of horizontal coordinate ($\bar{x}$):

$$y\left(\bar{x}|\bar{x}_0\right)=\frac{\lambda}{2\pi}\ln\left|\frac{\cos\bar{x}_0}{\cos\bar{x}}\right| \tag{A4}$$

Substituting equation (A4) into the x-component of the Elliott and Brooks velocity vector (equation (2b)) yields the x-component of the velocity along the $\bar{x}_0$ streamline (equation (8) in **Chapter 2**).

Text A.6. Proof that C_{exit} Represents the Flow-weighted Concentration of Water Parcels Exiting the Hyporheic Zone

From the Elliott and Brooks velocity field, the flow-average concentration of contaminant flowing out of the hyporheic zone is represented by Equation (A5):

$$\frac{u_m\int\limits_{-\lambda/4}^{0} C_f\left(2\pi x/\lambda\right)\sin\left(2\pi x/\lambda\right)dx}{u_m\int\limits_{-\lambda/4}^{0}\sin\left(2\pi x/\lambda\right)dx}=\frac{2\pi}{\lambda}\int\limits_{0}^{-\lambda/4} C_f\left(2\pi x/\lambda\right)\sin\left(2\pi x/\lambda\right)dx \tag{A5}$$

Combining equations (7) and (9) and (A5) we obtain:

$$\frac{2\pi}{\lambda}\int\limits_{0}^{-\lambda/4} C_f\left(2\pi x/\lambda\right)\sin\left(2\pi x/\lambda\right)dx=\frac{2\pi}{\lambda}\int\limits_{0}^{-\lambda/4} C_0\exp\left[\frac{k_r\lambda\theta 2\pi x/\lambda}{\pi u_m\cos 2\pi x/\lambda}\right]\sin\left(2\pi x/\lambda\right)dx \tag{A6}$$

Making the variable transformations: $x=-x_0\Rightarrow dx=-dx_0$, $\bar{x}_0=2\pi x_0/\lambda\Rightarrow dx_0=\frac{\lambda d\bar{x}_0}{2\pi}$ and $\mathrm{Da}=k_r\lambda\theta\pi/u_m$ we obtain the expression for C_{exit} in **Chapter 2** (equation (10b)):

$$C_{exit} = C_0 \int_0^{\pi/2} \exp\left[-\frac{\mathrm{Da}\bar{x}_0}{\pi^2 \cos\bar{x}_0}\right] \sin\bar{x}_0 \, d\bar{x}_0 \qquad \text{(A7)}$$

Therefore, equation (10b) represents the flow-weighted concentration of contaminant exiting the upwelling zone.

Text A.7. Derivation of the Exact Solution for Contaminant Concentration in the Hyporheic Zone

This can be shown by rewriting equations (7) and (9) so they represent the solute concentration and residence time of a water parcel located at any position $\bar{x}$ along the streamline that begins at $\bar{x} = \bar{x}_0$:

$$C(\bar{x}|\bar{x}_0) = C_0 \exp\left[-k_r \tau(\bar{x}|\bar{x}_0)\right] \qquad \text{(A8)}$$

$$\tau(\bar{x}|\bar{x}_0) = \lambda\theta(\bar{x}_0 - \bar{x})/(2\pi u_m \cos\bar{x}_0) \qquad \text{(A9)}$$

The variable $\bar{x}_0$ can be eliminated from these equations by rearranging equation (A4):

$$\bar{x}_0 = \cos^{-1}\left[e^{\bar{y}} \cos\bar{x}\right], \; -\pi/2 < \bar{x} < \pi/2, \; \bar{y} < 0 \qquad \text{(A10)}$$

Combining equations (A8), (A9), and (A10) we arrive at the final result shown in **Chapter 2** (equation (11)).

Text A.8. Calculation of Normalized Root Mean Square Deviance (NRMSD)

To assess the model fit, we computed a normalized root mean square deviance for each model as follows:

$$\mathrm{NRMSD} = \frac{\sqrt{\sum_i \left(\log k_{m,i}^{\mathrm{pred}} - \log k_{m,i}^{\exp}\right)^2}}{\left|\log k_{m,\max}^{\exp} - \log k_{m,\min}^{\exp}\right|} \qquad \text{(A11)}$$

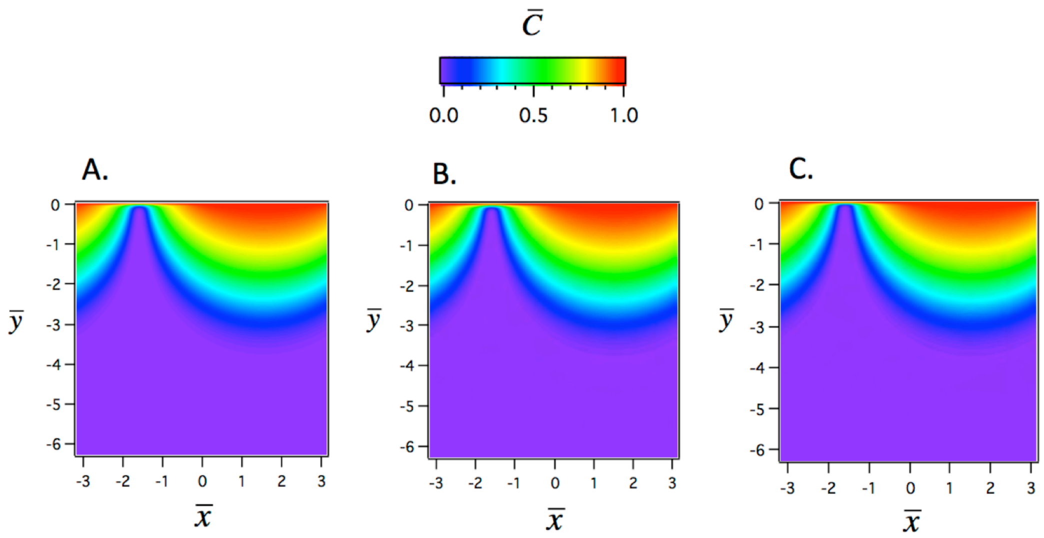

Figure A.3. Numerical simulation of the concentration filed assuming first-order reaction, advection, and the following: (A) both numerical diffusion and mechanical dispersion; (B) only mechanical dispersion; (C) only molecular diffusion. All three simulations used the set of parameter values listed in **Table A.1**.

The NRMSD represents the average deviance of a model relative to the range of observations. Because the k_m values vary over multiple orders of magnitude, in all cases the NRMSD calculation was performed on log-transformed mass-transfer coefficients.

References

Sawyer, A.H.; Cardenas, M.B. (2009) Hyporheic flow and residence time distributions in heterogeneous cross-bedded sediment. Wat. Resour. Res., 45, W08406.

Bedforms as Biocatalytic Filters:

A Pumping and Streamline Segregation (PASS) Model for Nitrate Removal in Permeable Sediments

Text B.1. APM Stream Function

Here we derive a stream function for the Elliott and Brooks APM flow field, and explain how the stream function was used to generate the streamlines plotted in **Figures 1B**, **C**, and **E**. For any steady-state two-dimensional flow field, the stream function $\psi(\bar{x},\bar{y})$ is related to velocity components in the x and y directions as follows [Bird et al., 2002]:

$$u_x = -\frac{\partial\psi}{\partial y} \tag{B1a}$$

$$u_y = \frac{\partial\psi}{\partial x} \tag{B1b}$$

In this equation u_x and u_y represent velocities in the x and y directions, respectively.

Substituting the APM velocity components $\bar{u}_x = u_x/\pi k_m = -\cos\bar{x}e^{\bar{y}}$ and $\bar{u}_y = u_y/\pi k_m = -\sin\bar{x}e^{\bar{y}}$ (Elliott and Brooks [1997], and where $k_m\left[\mathrm{m\,s^{-1}}\right]$ is pore water flushing rate) and integrating the resulting differential equations yields the following stream function for the APM:

$$\psi(\bar{x},\bar{y}) = (\lambda k_m/2)\cos\bar{x}e^{\bar{y}} \tag{B2}$$

Streamlines are obtained by setting the stream function equal to a constant, $\psi(\bar{x},\bar{y}) = C_1$. The difference between any two stream function constants $\Delta\psi = C_2 - C_1$ represents the volumetric flow rate per unit width of sediment bed [$\mathrm{m^3 m^{-1} s^{-1}}$] flowing between the streamlines represented by $\psi(\bar{x},\bar{y}) = C_1$ and $\psi(\bar{x},\bar{y}) = C_2$. For the APM, the stream function constant can be written in terms of the horizontal position ($\bar{x} = \bar{x}_0$) where the streamline crosses the sediment-water interface (at $\bar{y} = 0$) in the downwelling zone:

$$C = \frac{\lambda k_m}{2}\cos\bar{x}_0, \quad 0 \le \bar{x}_0 \le \pi/2 \tag{B3}$$

Combining equations (B2) and (B3), we arrive at an equation for the streamline that intersects the sediment-water interface in the downwelling zone at $\bar{x} = \bar{x}_0$:

$$\bar{y}\left(\bar{x}\middle|\bar{x}_0\right) = \ln\left|\frac{\cos\bar{x}_0}{\cos\bar{x}}\right|, \quad \bar{y} \le 0, \quad 0 \le \bar{x}_0 \le \pi/2 \tag{B4}$$

Here the notation "$\bar{x}|\bar{x}_0$" denotes the $\bar{x}$ position along the streamline that intersects the sediment-water interface at $\bar{x} = \bar{x}_0$ (denoted here as the "$\bar{x}_0$ streamline"). This last equation was used to plot the streamlines shown in **Figure 3.1B**, **C**, and **E** of **Chapter 3**. The five streamlines shown in the figures were selected so that the volumetric flow rate per unit width between any two adjacent streamlines was the same and equal to $\Delta\psi = 0.25\lambda k_m/2$. For **Figure 3.1E**, we chose $\lambda = 0.1\text{m}$ and $k_m = 1.64\times10^{-6}\text{ms}^{-1}$ (see **Table B.1**) which corresponds to $\Delta\psi = 2.05\times10^{-8}\text{m}^2\text{s}^{-1}$ or 1.7 liters per meter (of stream width) per day.

Table B.1. Seven non-dimensional parameters of rate equations, oxygen initial concentration, reaction time scale for **Kessler et al.** and **Six Scenarios** in “Riverine waters”: **A.** Agricultural runoff impacted river, **B.** Urban runoff impacted river, **C.** Sewage impacted river; and in “Coastal waters”: **D.** Oligotrophic marine coastal water, **E.** Marine coastal waters with low O_2 bottom water, **F.** Eutrophic marine coastal water.

	Kessler	A	B	C	D	E	F
Non-dimensional parameters							
$\delta[-] \equiv \dfrac{k_{NI} C_{O_2}(0)}{R_{\min} / K^{sat}_{O_2}}$	0.12	0.0214	0.0713	0.0021	0.0595	0.0007	0.0018
$\bar{K}^{sat}_{O_2}[-] \equiv K^{sat}_{O_2} / C_{O_2}(0)$	0.18	0.0333	0.0333	0.2000	0.0400	1.0000	0.0400
$\bar{K}^{sat}_{NO_3^-}[-] \equiv K^{sat}_{NO_3^-} / C_{O_2}(0)$	0.18	0.0333	0.0713	0.0400	0.0600	1.0000	0.0080
$\bar{K}^{inh}_{O_2}[-] \equiv K^{inh}_{O_2} / C_{O_2}(0)$	0.02	0.0167	0.0167	0.1000	0.0200	0.5000	0.0200
$\alpha[-] \equiv C_{NH_4^+}(0) / C_{O_2}(0)$	0.02	0.0003	0.0003	2.0000	0.0004	0.5000	0.0004
$\beta[-] \equiv C_{NO_3^-}(0) / C_{O_2}(0)$	0.23	4.0000	0.2333	0.0200	0.0004	2.0000	0.0004
$\gamma_{CN}[-]$	18.00	14.000	14.000	14.000	14.000	14.000	14.000
In-stream concentration of O_2							
$C_{O_2}(0)\left[\text{mol m}^{-3}\right]$	0.220	0.300	0.300	0.050	0.250	0.010	0.250
Reaction time scale							
$\tau_R[\text{s}] = K^{sat}_{O_2} / R_{\min}$	1379	360.000	36.000	1200.00	360.000	36.000	1200.00

Text B.2. APM Water Parcel Age

In this section we derive equation (1a) in **Chapter 3**, which represents the age $\tau(\bar{x},\bar{y})$ of a water parcel as it travels from the point where the water parcel crosses into the sediment from the stream to any location $(\bar{x},\bar{y})$ in the sediment. We begin by noting that, in the APM flow field, the $x-$component velocity of a water parcel is constant everywhere along any streamline. This can be demonstrated by substituting the equation for a streamline (equation (B4)) into the $x-$ component of the APM velocity ($\bar{u}_x = u_x / \pi k_m = -\cos\bar{x} e^{\bar{y}}$):

$$u_x(x_0) = -\pi k_m \cos\bar{x}_0, \quad 0 \le \bar{x}_0 \le \pi/2 \tag{B5}$$

Once the pore water flushing rate (k_m) and starting position (x_0) of the streamline are specified, the $x-$ component of the velocity is a fixed constant (i.e., it does not change with position $\bar{x}$ and $\bar{y}$). For the representative downwelling and upwelling zones analyzed in **Chapter 3** ($-\pi/2 \le \bar{x}_0 \le \pi/2$), each streamline begins and ends at $\bar{x}_0$ and $-\bar{x}_0$, respectively. Thus, the age of a water parcel at any position $\bar{x}$ can be calculated from the ratio of the $x-$ distance traveled ($\bar{x}-\bar{x}_0$) and the constant velocity $u_x(\bar{x}_0)/\theta$, where θ denotes sediment porosity:

$$\tau(\bar{x}|\bar{x}_0) = \frac{(\bar{x}-\bar{x}_0)\lambda/2\pi}{-u_x(\bar{x}_0)/\theta}, \quad \bar{y} \le 0, \quad 0 \le \bar{x}_0 \le \pi/2 \tag{B6}$$

The notation $\tau(\bar{x}|\bar{x}_0)$ denotes the age of a water parcel located at position $\bar{x}$ along the streamline that originated in the downwelling zone at $\bar{x} = \bar{x}_0$. An expression for the variable $\bar{x}_0$ appearing in the last equation can be obtained by rearranging equation (B4):

$$\bar{x}_0 = \cos^{-1}\left[e^{\bar{y}}\cos\bar{x}\right], \quad \bar{y} \le 0, \quad -\pi/2 \le \bar{x} \le \pi/2 \tag{B7}$$

Combining equations (B7), (B5), and (B6), we arrive at equation (1a) in **Chapter 3**.

Text B.3. APM Residence Time Distribution Function

Here we derive equations (3a) and (3b) in **Chapter 3**, which together represent the residence time distribution (RTD) of water parcels in the APM flow field. In this paper we adopt the standard chemical engineering definition of the RTD ($F_{RTD}(\bar{\tau}_f)$) as the fraction of water volume exiting the reactor with a reduced final age of $\bar{\tau}_f$ or younger

[Levenspiel, 1972; Hill, 1977]. Recalling that every streamline has a unique final age $\bar{\tau}_f$, this chemical engineering definition of the RTD can be written mathematically as:

$$F_{RTD}\left(\bar{\tau}_f\right) \equiv \int_0^{\bar{x}_0\left(\bar{\tau}_f\right)} \left|\frac{dQ}{Q}\right|, \quad 0 \le \bar{x}_0 \le \pi/2 \tag{B8}$$

Here dQ represents the differential volumetric flow rate of water moving along the streamline intersecting the sediment-water interface between $\bar{x} = \bar{x}_0$ and $\bar{x} = \bar{x}_0 + d\bar{x}_0$ $\left(0 \le \bar{x}_0 \le \pi/2\right)$ and $Q = k_m \lambda W$ represents the total volumetric flow rate of water across the entire bedform where W represents the width of the stream (all other variables have been defined above). The differential volumetric flow rate along any streamline can be written:

$$dQ = 2u_y\left(x_0\right)dx_0 W, \quad 0 \le \bar{x}_0 \le \pi/2 \tag{B9}$$

The factor of two on the right hand side of the last equation is included to account for the fact that there are two downwelling zones per dune wavelength λ (see **Figure 3.1B** in **Chapter 3**). Substituting the vertical component of the APM velocity field at the sediment-water interface ($u_y(\bar{x}_0) = -\pi k_m \sin(\bar{x}_0)$) and combining equations (B8) and (B9) we arrive at the RTD presented in **Chapter 3** (equation (3a)). However, the right hand side of equation (3a) contains an unknown function $\bar{x}_0\left(\bar{\tau}_f\right)$. We can derive this function (for the same upwelling/downwelling zone considered in **Chapter 3**, $-\pi/2 \le \bar{x} \le \pi/2$) by noting that each water parcel entering the sediment at $\bar{x} = \bar{x}_0$ in the downwelling zone ($0 \le \bar{x}_0 \le \pi/2$) exits the sediment at $\bar{x} = -\bar{x}_0$ in the adjacent upwelling zone ($-\pi/2 \le \bar{x}_0 \le 0$). Substituting $\bar{x} = -\bar{x}_0$ and the *x*-component of the APM velocity along a streamline ($u_x\left(x_0\right) = -\pi k_m \cos\bar{x}_0, \quad 0 \le \bar{x}_0 \le \pi/2$) into equation (B6) we obtain the implicit form of the

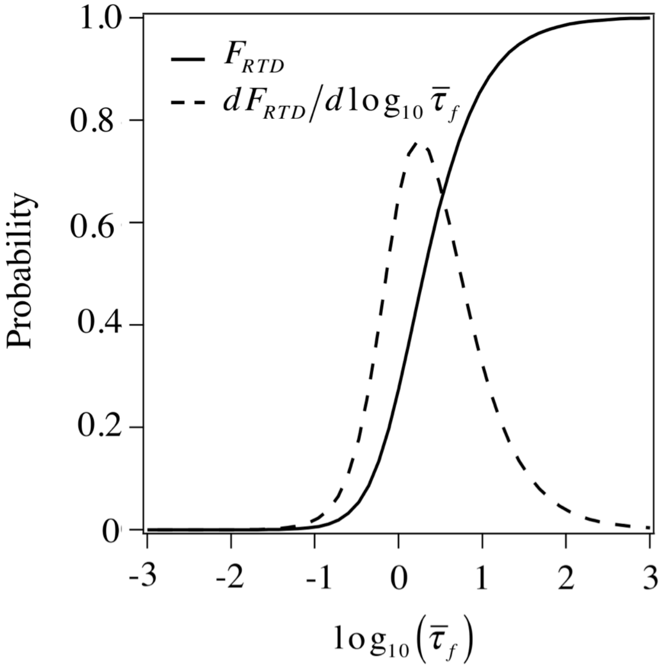

Figure B.1. CDF and PDF forms of the residence time distribution (RTD) function for the Advective Pumping Model (APM).

function $\overline{x}_0(\overline{\tau}_f)$ (equation (3b) in **Chapter 3**). A graphical representation of the APM RTD is presented in **Figure B.1**. The two curves in the figure correspond to two different representations of the RTD: a cumulative distribution function (CDF) representation (F_{RTD}) and a probability distribution function (PDF) representation ($dF_{RTD}/d\log_{10}\overline{\tau}_f$). We have presented the PDF in terms of logarithmic change in the reduced final age ($\overline{\tau}_f$) for two reasons: (1) the final exit age of water parcels varies over many orders of magnitude; and (2) when plotted against $\log_{10}\overline{\tau}_f$ the area under the $dF_{RTD}/d\log_{10}\overline{\tau}_f$ curve is unity.

Text B.4. Comparison to Residence Time Function Derived by Elliott and Brooks

Here we demonstrate that the RTD derived above is equivalent to the "average residence time function" $\bar{R}(\tau)$ derived for the APM by Elliott and Brooks [1997]. As defined by Elliott and Brooks, $\bar{R}(\tau)$ represents "the fraction of solute which entered the bed in a short time near $t=0$ and remains in the bed at time τ." By contrast, the RTD defined in our study (equation (3a)) represents the fraction of solute that entered the bed in a short time near $t=0$ and exited the bed by time τ. These two definitions of residence time must sum to unity, because a solute that entered the bed near time $t=0$ is either still in the bed or has exited the bed by time τ (i.e., there is no other place the solute could be). Therefore, the following relationship applies:

$$\bar{R} = 1 - F_{RTD}\left(\bar{\tau}_f\right) \tag{B10}$$

Combining equations (3a) and (B10) we obtain equation (B11):

$$\bar{\tau}_f = \frac{\cos^{-1}\bar{R}}{\bar{R}} \tag{B11}$$

This is precisely the result derived by Elliott and Brooks for the APM (equation (15b) in Elliott and Brooks [1997]), where our $\bar{\tau}_f$ is equivalent to Elliott and Brooks $t^*/2\theta$, where $t^* = \left(2\pi^2 k_m/\lambda\right)t$.

Text B.5. Normalized Mass Balance Equations for Oxygen, Nitrate, and Ammonium

A coupled set of mass balance equations for the evolution of oxygen, nitrate, and ammonium along a streamline can be derived by substituting the reaction rate equations (equations 6a-d) into the mass balance equations (equations 5a-c), and writing the resulting equations in a non-dimensional form:

$$\frac{d\bar{C}_{O_2}}{d\bar{\tau}_R}=-\frac{\bar{C}_{O_2}}{\bar{C}_{O_2}/\bar{K}_{O_2}^{sat}+1}-2\delta\bar{C}_{O_2}\bar{C}_{NH_4^+},\ \bar{C}_{O_2}\left(\bar{\tau}_R=0\right)=1 \tag{B12a}$$

$$\frac{d\bar{C}_{NO_3^-}}{d\bar{\tau}_R}=\delta\bar{C}_{O_2}\bar{C}_{NH_4^+}-0.05\times\frac{\bar{K}_{O_2}^{inh}\bar{K}_{O_2}^{sat}\bar{C}_{NO_3^-}}{\left(\bar{C}_{O_2}+\bar{K}_{O_2}^{inh}\right)\left(\bar{C}_{NO_3^-}+\bar{K}_{NO_3^-}^{sat}\right)},\ \bar{C}_{NO_3^-}\left(\bar{\tau}_R=0\right)=\beta \tag{B12b}$$

$$\frac{d\bar{C}_{NH_4^+}}{d\bar{\tau}_R}=\frac{1}{\gamma_{CN}}\bar{K}_{O_2}^{sat}-\delta\bar{C}_{O_2}\bar{C}_{NH_4^+},\ \bar{C}_{NH_4^+}\left(\bar{\tau}_R=0\right)=\alpha \tag{B12c}$$

All concentrations, saturation rate constants, and the inhibition rate constant are reduced by in-stream concentration of oxygen ($C_{O_2}\left(\bar{\tau}_R=0\right)$); furthermore, travel time along a streamline is reduced by the characteristic respiration time scale ($\bar{\tau}_R[-]=\tau/\tau_R$, where $\tau_R=K_{O_2}^{sat}/R_{\min}$). The reason these equations are written in non-dimensional (or "reduced") form is that by doing so we minimize the number of parameters that need to be specified before solving the equations numerically; i.e., the equations and associated variables are said to have been *reduced* to their most parsimonious form [Buckingham, 1914]. In order to numerically integrate the above set of differential equations the following seven reduced parameters must be specified:

$$\delta[-]\equiv\frac{k_{NI}C_{O_2}(0)}{R_{\min}/K_{O_2}^{sat}} \tag{B13a}$$

$$\bar{K}_{O_2}^{sat}[-]\equiv K_{O_2}^{sat}/C_{O_2}(0) \tag{B13b}$$

$$\bar{K}_{NO_3^-}^{sat}[-]\equiv K_{NO_3^-}^{sat}/C_{O_2}(0) \tag{B13c}$$

$$\bar{K}_{O_2}^{inh}[-]\equiv K_{O_2}^{inh}/C_{O_2}(0) \tag{B13d}$$

$$\alpha[-]\equiv C_{NH_4^+}(0)/C_{O_2}(0) \tag{B13e}$$

$$\beta[-]\equiv C_{NO_3^-}(0)/C_{O_2}(0) \tag{B13f}$$

$$\gamma_{CN}[-] \tag{B13g}$$

Parameters appearing in these equations are defined in **Chapter 3** and specified for six different environmental scenarios in **Table B.1** (and the experimental flume studies presented by Kessler et al. [2013], see **Chapter 3**). We numerically integrated this coupled set of 3 differential equations (using Wolfram Mathematica, version 10.0) to obtain the reduced concentrations of oxygen, nitrate, and ammonium as a function of reduced travel time ($\overline{\tau}_R$) along any streamline through the bedform (**Figure B.2**).

Text B.6. Kessler et al.'s Numerical Flume Studies

Kessler et al. [2012, 2013] estimated pore fluid concentrations of oxygen, nitrate, and ammonium beneath a single ripple using an experimentally calibrated numerical flow and reactive transport model. Their so-called "numerical flume" studies involved the following steps: (1) a computational grid was prepared to mimic the two-dimensional geometry (i.e., dune shape and water depth) measured in their flume experiments (involving sediments and water collected from Port Phillip Bay, Melbourne, Australia); (2) the pressure distribution at the sediment-water interface was estimated by solving a $k-\omega$ RANS formulation of the Navier-Stokes equation for turbulent flow over the ripple, consistent with flow conditions measured in the flume experiments; (3) from the two-dimensional pressure distribution at the sediment-water interface (obtained from the last step) the interstitial flow field in the sediment was solved using Darcy's Law and the continuity equation; (4) the steady-state velocity field was then combined with a flow and reactive transport model which accounts for advection, molecular diffusion, mechanical dispersion, and a set of reaction rate laws for ammonification, nitrification, and

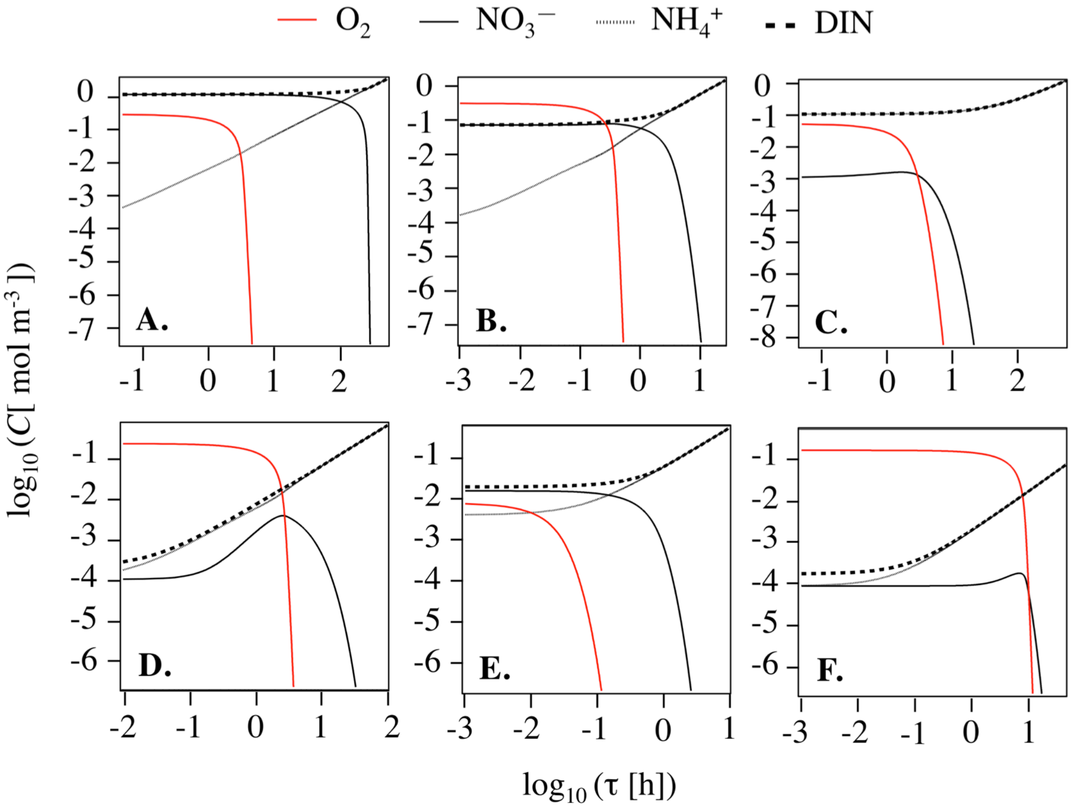

Figure B.2. Predicted concentrations of oxygen, nitrate, ammonium, and dissolved inorganic nitrogen (DIN) along a streamline calculated from a numerical solution of equations (B12a) through (B12c). The different panels correspond to different hypothetical environments. The top row corresponds to streams impacted by (**A**) agricultural runoff; (**B**) urban runoff; and (**C**) sewage. The bottom row corresponds to coastal marine environments with bottom waters that are: (**D**) oligotrophic; (**E**) low oxygen; and (**F**) eutrophic.

denitrification; and finally (5) the flow and reactive transport model obtained from step (4) was solved numerically to yield steady-state pore fluid concentrations for ammonium, nitrate, and oxygen beneath a single ripple.

Note that in Step (4), Kessler et al. used piece-wise linear rate laws based on experimental data, while in the PASS model (equations (B12a) through (B12c)) we have adopted saturation-type rate formulations fitted to those experimental data, which are likely to be more universally applicable (equations (6a), (6d) in **Chapter 3**). PASS model predictions were not significantly altered by the substitution of piece-wise linear rate laws with non-linear saturation type rate laws (**Figure B.3**), although the values of $R_{\min}$ and γ_{CN} had to be adjusted slightly to make the two different kinetic formulations comparable (see rows 15 through 25, **Table B.2**). Kessler et al.'s numerical flume simulations and our PASS model (see discussion of **Figures B.4** through **B.7** in **Chapter 3**) were compared over the horizontal region between two troughs of a single ripple (see the outline of the ripple surface in all panels that appear in the last two rows of **Figures B.4** through **B.6**). This domain in Kessler et al.'s model corresponds to a single wavelength in our pass model ($\lambda = 0.1$ m) extending over the horizontal domain from one pressure peak ($\bar{x} = -3\pi/2$) to the next pressure peak ($\bar{x} = \pi/2$). Translated into physical distance (given the known wavelength of the ripple) that horizontal distance becomes $x = -0.075$ to 0.025 m (see x-values plotted in **Figures B.4** through **B.7**).

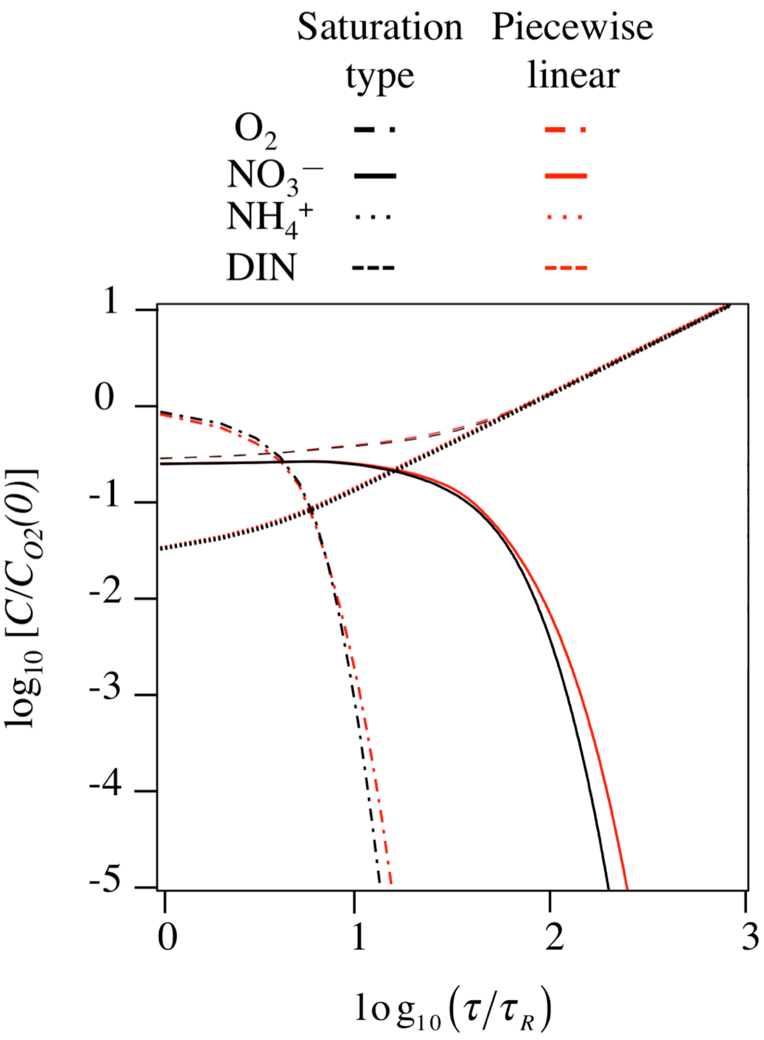

Figure B.3. Comparison of oxygen, nitrate, ammonium, and total inorganic nitrogen DIN concentration along a streamline calculated using saturation-type (black curves) and piecewise linear (red curves) biogeochemical reaction rate formulations. The vertical axis represents normilized concentration of a solute with respect to the in-stream concentration of oxygen. The horizontal axis represents the normalized age of a water parcel relative to the respiration time scale.

Table B.2. Parameter values used for comparison of PASS model with Kessler et al.'s model.

	Description	Value
Physical parameters		
$\lambda[\mathrm{m}]$	Dune wave length	1.00 E-01
$\Delta[\mathrm{m}]$	Dune height	1.00 E-02
$H[\mathrm{m}]$	Water depth	1.30 E-01
$U\left[\mathrm{m\ s^{-1}}\right]$	Stream velocity	1.60 E-01
$\theta[-]$	Porosity	3.50 E-01
$k_p\left[\mathrm{m^2}\right]$	Permeability	4.00 E-11
$K_h\left[\mathrm{m\ s^{-1}}\right]=k_p g/\nu_w$	Hydraulic conductivity	3.92 E-04
$\nu_w\left[\mathrm{m^2\ s^{-1}}\right]$	Water kinematic viscosity at 20 ºC	1.00 E-06
$h_m[\mathrm{m}]$	Maximum pressure head (APM)	2.09 E-04
$u_m\left[\mathrm{m\ s^{-1}}\right]$	Maximum velocity (APM)	5.16 E-06
$k_m\left[\mathrm{m s^{-1}}\right]=u_m/\pi$	Flushing rate	1.64 E-06
$\alpha_L[\mathrm{m}]$	Longitudinal dispersivity	1.00 E-02
$\alpha_T[\mathrm{m}]$	Transverse dispersivity	1.00 E-03
$\tau_T[\mathrm{s}]=\lambda\theta/\pi^2 k_m$	Solute transport time scale	2159

		Saturation-Type	Piece-Wise
Chemical parameters			
$K_{O_2}^{sat}\left[\mathrm{mol\ m^{-3}}\right]$	Half saturation constant for $\mathrm{O_2}$ limitation of oxic mineralization	4.00 E-02	-
$K_{NO_3^-}^{sat}\left[\mathrm{mol\ m^{-3}}\right]$	Half saturation constant for $\mathrm{NO_3^-}$ limitation of denitrification	4.00 E-02	-
$K_1\left[\mathrm{s^{-1}}\right]$	First constant for AR and DN rate	-	1.09 E-04
$K_2\left[\mathrm{mol\ m^{-3}\ s^{-1}}\right]$	Second constant for AR and DN rate	-	8.28 E-06
$K_3\left[\mathrm{s^{-1}}\right]$	Third constant for AR and DN rate	-	5.22 E-04
$C_{crit}\left[\mathrm{mol\ m^{-3}}\right]$	Critical concentration	-	2.00 E-02
$K_{O_2}^{inh}\left[\mathrm{mol\ m^{-3}}\right]$	Half saturation constant for $\mathrm{O_2}$ inhibition of DN	5.00 E-03	5.00 E-03
$k_{NI}\left[\mathrm{m^3\ mol^{-1}\ s^{-1}}\right]$	NI rate constant	3.96 E-04	3.96 E-04
$\gamma_{CN}[-]$	Net mineralization of C relative to production of $\mathrm{NH_4^+}$	18	14
$R_{\min}\left[\mathrm{mol\ m^{-3}s^{-1}}\right]$	Maximum rate of organic matter oxidation and denitrification (as C	2.90 E-05	2.27 E-05

	equivalents)	
$C_{O_2}(0)\left[\text{mol m}^{-3}\right]$	In-stream concentration of O_2	2.20 E-01
$C_{NO_3^-}(0)\left[\text{mol m}^{-3}\right]$	In-stream concentration of NO_3^-	5.10 E-02
$C_{NH_4^+}(0)\left[\text{mol m}^{-3}\right]$	In-stream concentration of NH_4^+	5.00 E-03
$D_{m,O_2}\left[\text{m}^2\text{s}^{-1}\right]$	Molecular diffusion coefficient of O_2	1.97 E-09
$D_{m,NO_3^-}\left[\text{m}^2\text{s}^{-1}\right]$	Molecular diffusion coefficient of NO_3^-	1.40 E-09
$D_{m,NH_4^+}\left[\text{m}^2\text{s}^{-1}\right]$	Molecular diffusion coefficient of NH_4^+	1.45 E-09
$D'_{m,O_2}=\left(1-2\ln\theta\right)^{-1}D_{m,O_2}\left[\text{m}^2\text{s}^{-1}\right]$	Effective diffusion coefficient of O_2	6.35 E-10
$D'_{m,NO_3^-}=\left(1-2\ln\theta\right)^{-1}D_{m,NO_3^-}\left[\text{m}^2\text{s}^{-1}\right]$	Effective diffusion coefficient of NO_3^-	4.53 E-10
$D'_{m,NH_4^+}=\left(1-2\ln\theta\right)^{-1}D_{m,NH_4^+}\left[\text{m}^2\text{s}^{-1}\right]$	Effective diffusion coefficient of NH_4^+	4.68 E-10
$\tau_R[\text{s}]=K_{O_2}^{sat}/R_{\text{min}}$	Reaction time scale for mineralization of organic carbon	1379
$\text{Da}=\tau_T/\tau_R$	Damkohler number	1.6

All of the “physical parameter” values listed in this table were extracted or calculated based on values reported by Kessler et al. [2013], except dispersivity coefficients which were taken from Cardenas et al. [2008]. Kinematic viscosity of the water was calculated at 20ºC. “Chemical parameter” values were separated into “saturation” and “piece-wise” types. Piece-wise values were reported in Kessler et al. [2013], and saturation type values were set to the Kessler el al.’s values or fitted based on the discussion presented in **Text B.6**. Stream concentrations were taken from Kessler et al. [2013]. The effective diffusion coefficients are corrected for tortuosity following Boudreau [1996], and molecular diffusion coefficients were calculated as a function of temperature and salinity using the relations given by Boudreau [1997] (assuming zero salinity and temperature of 25ºC).

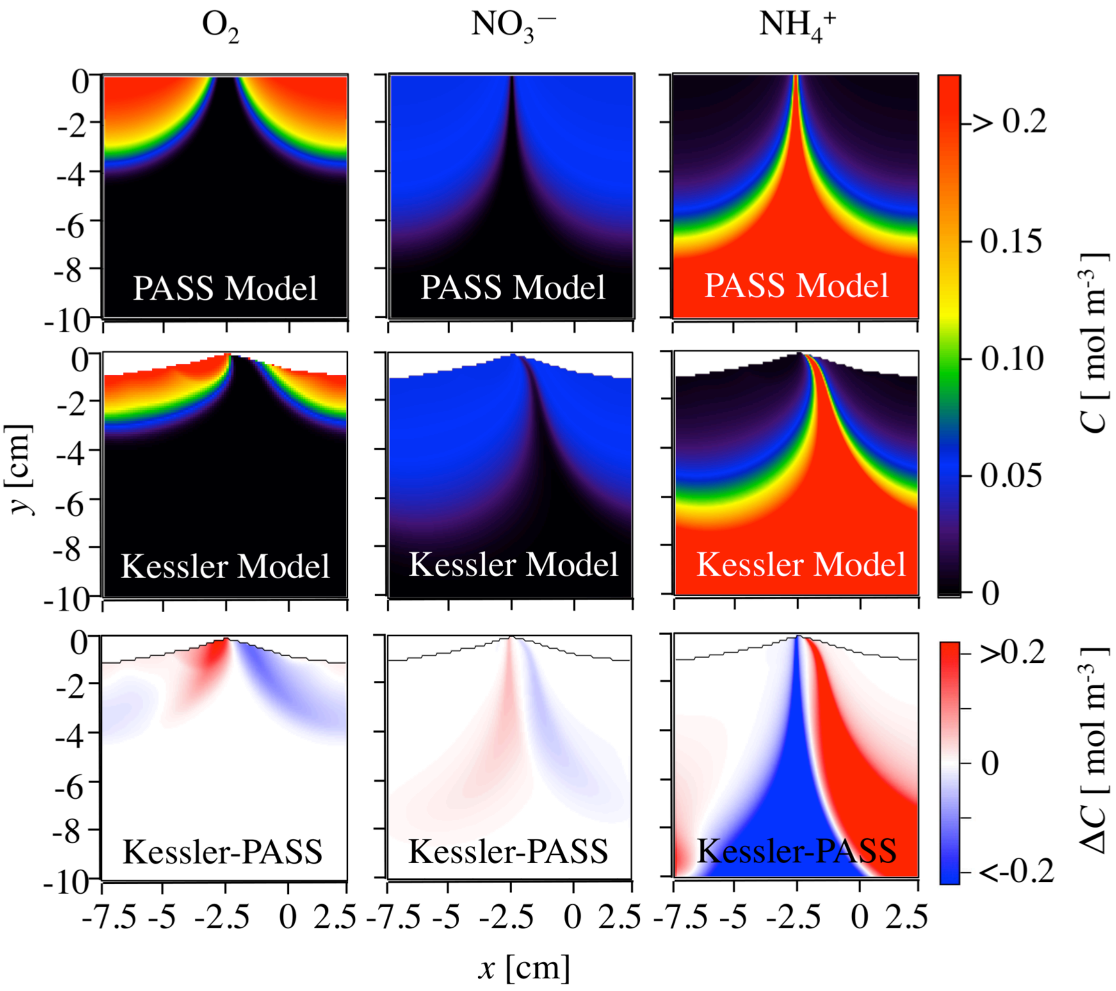

Figure B.4. Pore fluid concentrations predicted by the PASS model (top row), Kessler's numerical flume model (middle row), and the difference between the two (bottom row). Shown are the predicted concentrations of oxygen (left column), nitrate (middle column), and ammonium (right column).

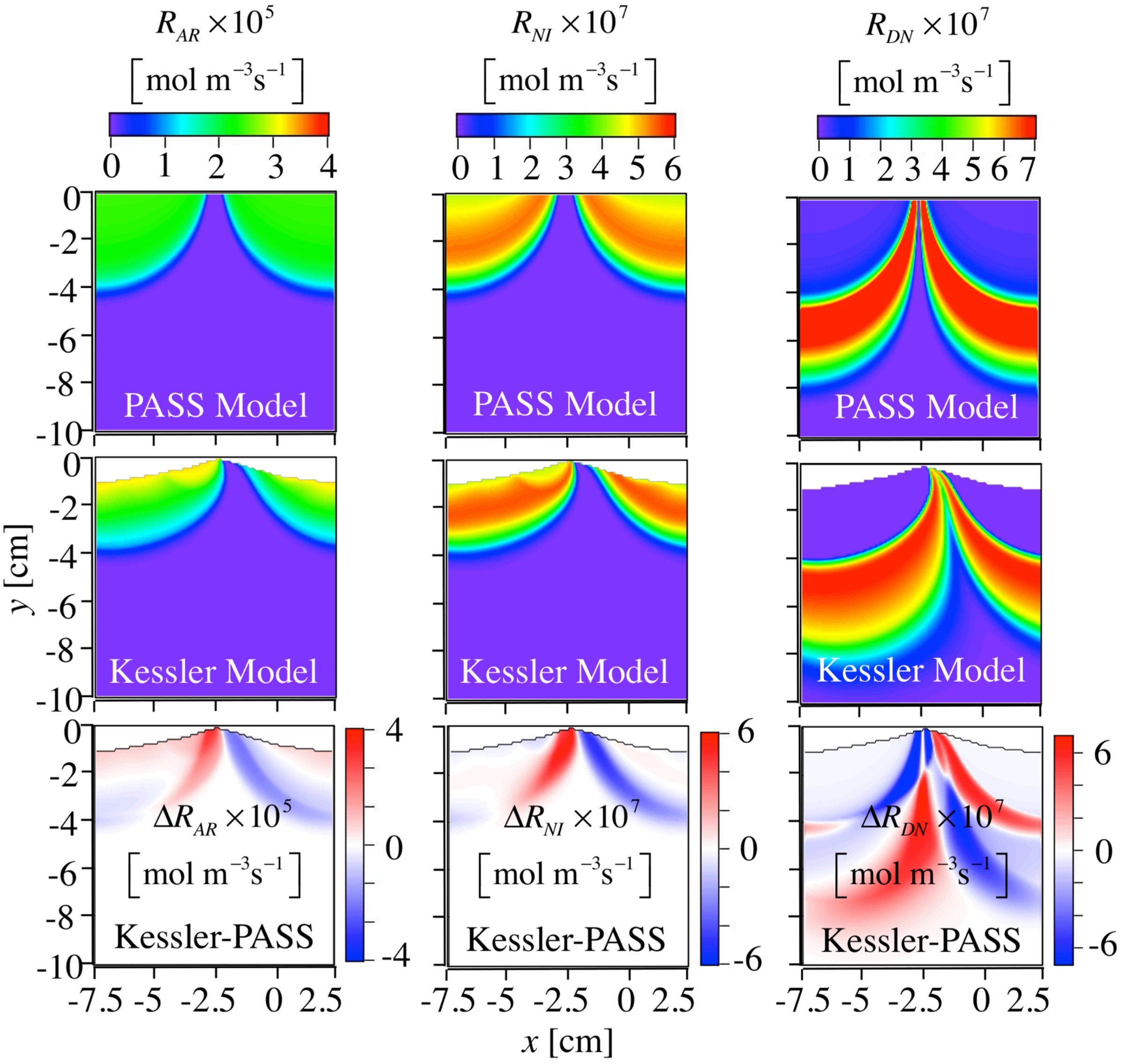

Figure B.5. Rates of aerobic respiration (first column), nitrification (second column), and denitrification predicted by the PASS model (top row), Kessler's numerical flume model (middle row), and the difference between the two (bottom row).

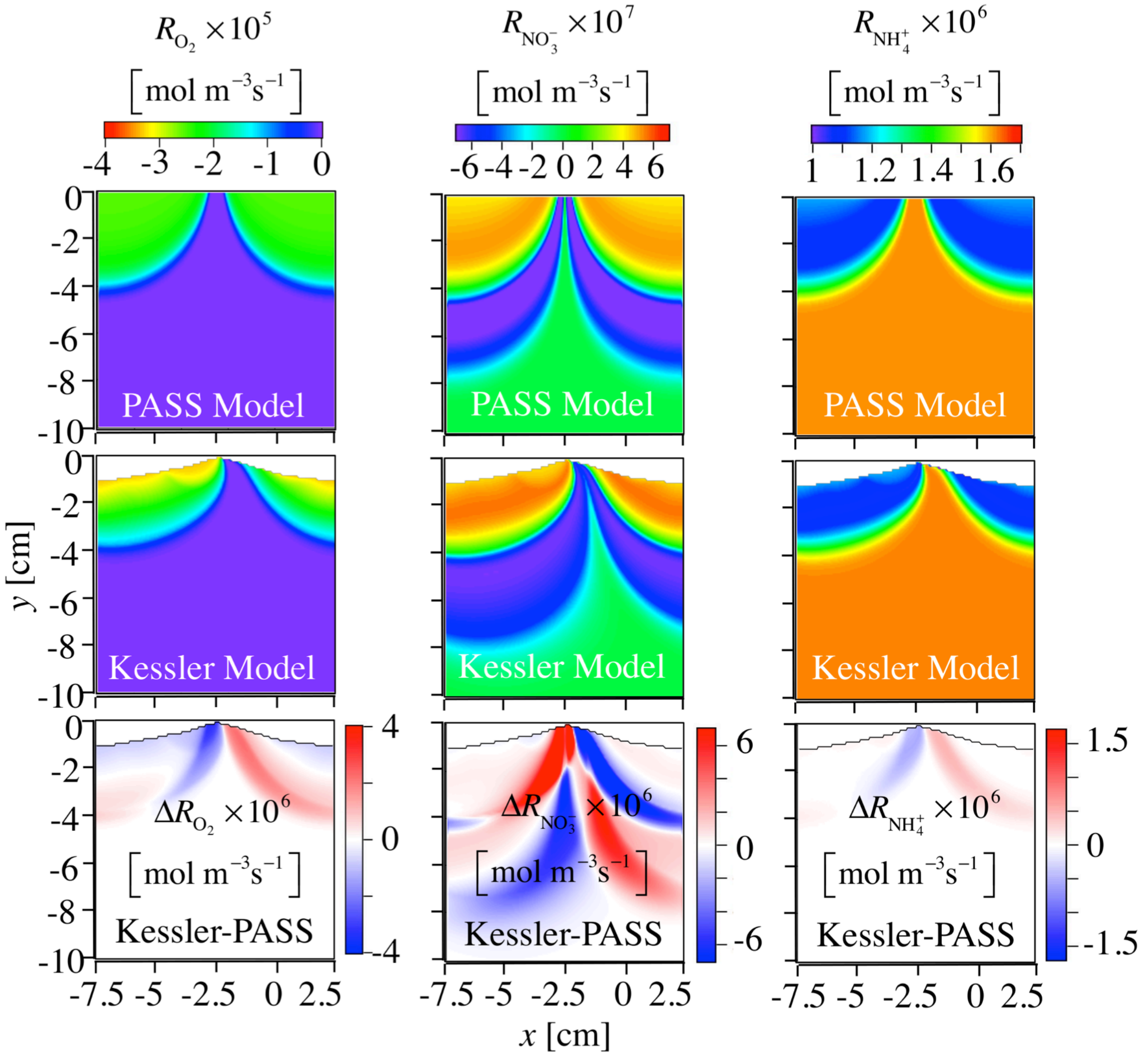

Figure B.6. Reaction rates for oxygen (first column), nitrate (second column), and ammonium predicted by the PASS model (top row), Kessler's numerical flume model (middle row), and the difference between the two (bottom row).

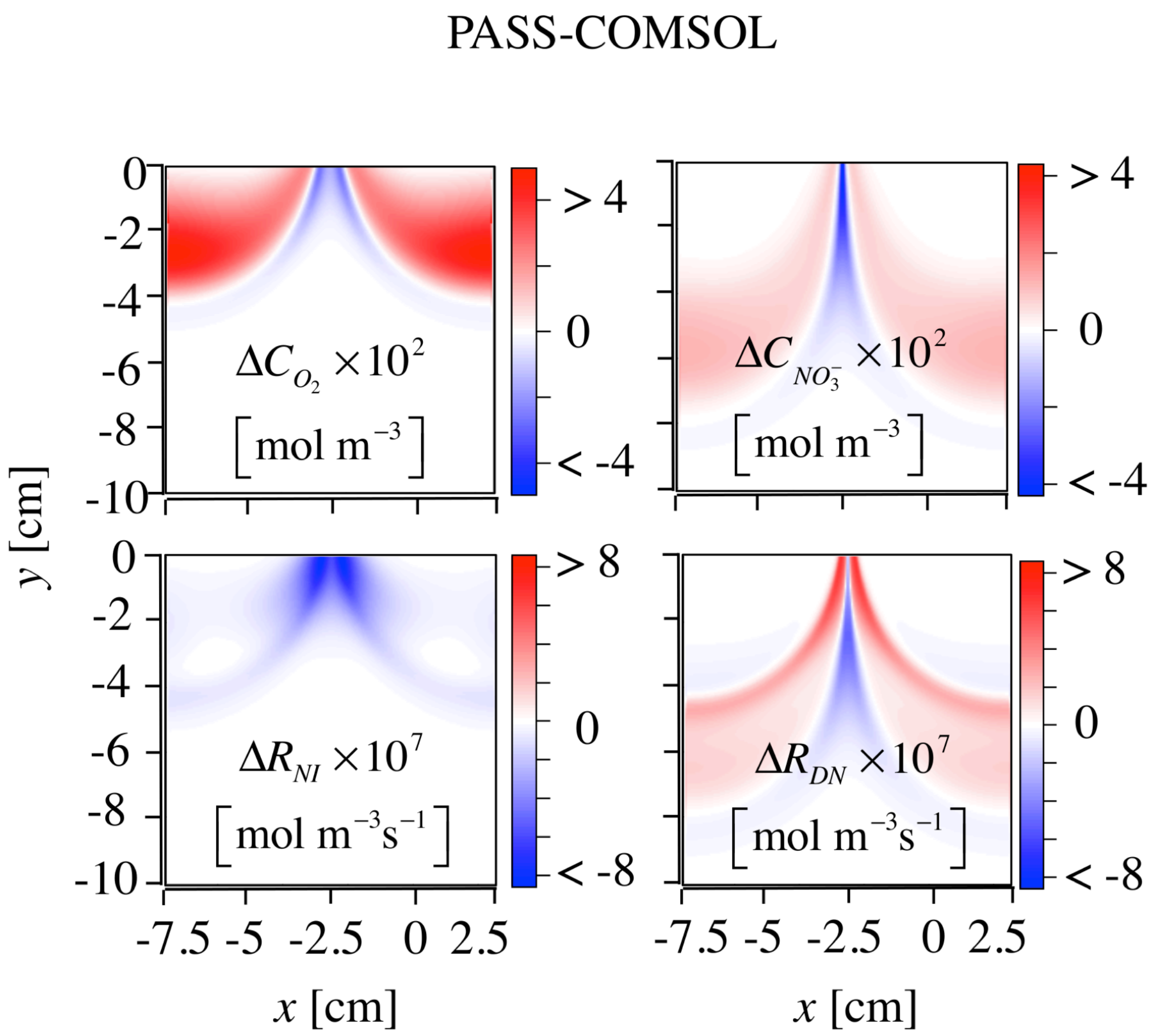

Figure B.7. Difference between PASS model and COMSOL model simulations of oxygen concentration (upper left panel), nitrate concentration (upper right panel), nitrification rate (lower left panel), and denitrification rate (lower right panel). Note that molecular diffusion and mechanical dispersion (turned on in the COMSOL simulation) cause a pronounced increase and decrease in the rates of nitrification and denitrification, respectively, in the anoxic chimney.

Text B.7. Relaxing the Segregated Streamline Hypothesis

Here we conduct a numerical simulation in COSMOL Multiphysics (version 4.4) in which all features of PASS model were unchanged except that solutes were allowed to mix by molecular diffusion and mechanical dispersion (difference between PASS and COMSOL model simulations of oxygen, nitrate, nitrification and denitrification is shown in **Figure B.7**). A steady-state form of the mass balance equation that accounts for reaction, advection, mechanical dispersion, and molecular diffusion can be written as follows [Bardini et al., 2012]:

$$R_i = \nabla . \left(\frac{\mathbf{u}}{\theta} C_i - \mathbf{D}_i \cdot \nabla C_i \right) \tag{B14}$$

In this equation i represents a chemical species (oxygen, nitrate, and ammonium), R_i is the reaction rate of species i (defined in equations 6a-d of **Chapter 3**), $\mathbf{u}\left[\mathrm{m\,s^{-1}}\right]$ is Darcy's velocity field (defined by the APM in this case), θ is porosity, $C_i\left[\mathrm{mol\,m^{-3}}\right]$ is concentration of species i, $\mathbf{D}_i\left[\mathrm{m^2 s^{-1}}\right]$ represent dispersion-diffusion tensor (which can be calculated from the APM—see equation (4b) in Grant et al., [2014]]:

$$\mathbf{D}_i = \begin{bmatrix} \frac{u_m e^{\bar{y}}}{\theta}\left(\alpha_L \cos^2 \bar{x} + \alpha_T \sin^2 \bar{x}\right) + D'_{m,i} & \frac{u_m e^{\bar{y}}}{\theta}\left(\alpha_L - \alpha_T\right)\frac{\sin 2\bar{x}}{2} \\ \frac{u_m e^{\bar{y}}}{\theta}\left(\alpha_L - \alpha_T\right)\frac{\sin 2\bar{x}}{2} & \frac{u_m e^{\bar{y}}}{\theta}\left(\alpha_L \sin^2 \bar{x} + \alpha_T \cos^2 \bar{x}\right) + D'_{m,i} \end{bmatrix} \tag{B15}$$

New variables include longitudinal α_L and transverse α_T dispersivities, and an effective molecular diffusion coefficient $D'_{m,i}$ of species i in water modified by tortuosity parameter $\beta[-]$: $D'_{m,i} = \beta D_{m,i} = \left(1 - 2\ln\theta\right)^{-1} D_{m,i}$ [Iversen and Jorgensen, 1993]. The horizontal domain was identical to the one used for the comparison between PASS model and Kessler et al.'s model ($x = -0.075$ to 0.025 m, see discussion at the end of the **Text B.6**). Boundary conditions employed for the COMSOL simulations include: (1) a periodic boundary condition at the left and right vertical boundaries ($x = -0.075$ and 0.025 m, respectively); (2) an outflow boundary condition ($-\mathbf{n} . D_i \nabla C_i = 0$) at the bottom boundary ($y = -0.1$ m); (3) an outflow boundary condition ($-\mathbf{n} . D_i \nabla C_i = 0$) in the upwelling zone of the upper boundary ($-0.05m \le x \le 0m$); and (4) constant concentration boundary conditions at two locations along the upper boundary (corresponding to the two downwelling zones, see **Figures B.4** through **B.6**), one between $-0.075m \le x \le -0.05m$ and another between $0m \le x \le 0.025m$. Parameter values utilized for the COMSOL simulation are reported in **Table B.2**.

Text B.8. Benthic Flux

In this section, we derive the equation for benthic flux, equation (9) in **Chapter 3**. We assume that the concentration of the *i*th species at the sediment water interface ($\bar{y} = 0$) in the down-welling zone ($0 \le \bar{x} \le \pi/2$) is constant and equal to the in-stream concentration of the *i*th species, $C_i(0)$. Therefore, the flux of the *i*th species into the sediment bed (in the downwelling zone) is: $U_{i,in} = -k_m C_i(0)$ where k_m is the pore-water flushing rate (see **Chapter 3**). Water parcels traveling through the sediments will chemically evolve until they exit the sediment with a final age $\bar{\tau}_f$ in the upwelling zone. The fraction of total volumetric flow rate through the bedform that has final ages between $\bar{\tau}_f$ and $\bar{\tau}_f + d\bar{\tau}_f$ is, by definition, equal to differential of the RTD: dF_{RTD}. The differential flux (of the *i*th species) associated with this fraction of the volumetric flow rate is

$dU_{i,out} = k_m C_i\left(\overline{\tau}_R\right)\left(dF_{RTD}/d\overline{\tau}_f\right)d\overline{\tau}_f$ where $\left(dF_{RTD}/d\overline{\tau}_f\right)$ represents the PDF of the RTD. To calculate the total flux of the *i*th species leaving the bedform we integrate over all streamlines:

$$U_{i,out} = k_m \int_0^{\infty} C_i\left(\overline{\tau}_R = \mathbf{Da}\,\overline{\tau}_f\right)\frac{dF_{RTD}}{d\overline{\tau}_f}d\overline{\tau}_f \qquad \text{(B16a)}$$

This integral can also be expressed in terms of the logarithmic change in final water parcel age (by doing so we facilitate numerical integration, because the RTD ranges over many orders of magnitude, see **Figure B.1**):

$$U_{i,out} = k_m \int_{-\infty}^{\infty} C_i\left(\overline{\tau}_R = \mathbf{Da}\times 10^{\log_{10}\overline{\tau}_f}\right)\frac{dF_{RTD}}{d\log_{10}\overline{\tau}_f}d\log_{10}\overline{\tau}_f \qquad \text{(B16b)}$$

The difference between mass flux into and out of the sediment bed yields the final net flux expression presented as equation (9) (see **Chapter 3**).

Text B.9. Rate Equations Solved for Different Sources of Nitrate, Ammonium, and Nitrogen Gas

To determine the dominant pathways for removal and generation of nitrate in the bedform, we derived a set of coupled mass conservation equations that track how nitrate from different nitrogen sources evolves with water parcel age along a streamline through the sediment. In particular, we mathematically "tagged" the following nitrate molecules: (1) nitrate from the stream ($\overline{C}_{NO_3^-}^{stream}$); (2) nitrate generated from nitrification of stream ammonium ($\overline{C}_{NO_3^-}^{NH_4^+-stream}$); and (3) nitrate generated from the nitrification of sediment ammonium ($\overline{C}_{NO_3^-}^{NH_4^+-sed}$). The reduced rate equations for the chemical evolution of these molecules along a streamline is given as follows:

$$\frac{d\bar{C}_{NO_3^-}^{stream}}{d\bar{\tau}_R}=-0.05\times\frac{\bar{K}_{O_2}^{inh}\bar{K}_{O_2}^{sat}\bar{C}_{NO_3^-}^{stream}}{\left(\bar{C}_{O_2}+\bar{K}_{O_2}^{inh}\right)\left(\bar{C}_{NO_3^-}^{stream}+\bar{C}_{NO_3^-}^{NH_4^+-stream}+\bar{C}_{NO_3^-}^{NH_4^+-sed}+\bar{K}_{NO_3^-}^{sat}\right)},\ \bar{C}_{NO_3^-}^{stream}\left(\bar{\tau}_R=0\right)=\beta$$

(B17a)

$$\frac{d\bar{C}_{NO_3^-}^{NH_4^+-stream}}{d\bar{\tau}_R}=\delta\bar{C}_{O_2}\bar{C}_{NH_4^+}^{stream}-0.05\times\frac{\bar{K}_{O_2}^{inh}\bar{K}_{O_2}^{sat}\bar{C}_{NO_3^-}^{NH_4^+-stream}}{\left(\bar{C}_{O_2}+\bar{K}_{O_2}^{inh}\right)\left(\bar{C}_{NO_3^-}^{stream}+\bar{C}_{NO_3^-}^{NH_4^+-stream}+\bar{C}_{NO_3^-}^{NH_4^+-sed}+\bar{K}_{NO_3^-}^{sat}\right)},\ \bar{C}_{NO_3^-}^{NH_4^+-stream}\left(\bar{\tau}_R=0\right)=0$$

(B17b)

$$\frac{d\bar{C}_{NO_3^-}^{NH_4^+-sed}}{d\bar{\tau}_R}=\delta\bar{C}_{O_2}\bar{C}_{NH_4^+}^{sed}-0.05\times\frac{\bar{K}_{O_2}^{inh}\bar{K}_{O_2}^{sat}\bar{C}_{NO_3^-}^{NH_4^+-sed}}{\left(\bar{C}_{O_2}+\bar{K}_{O_2}^{inh}\right)\left(\bar{C}_{NO_3^-}^{stream}+\bar{C}_{NO_3^-}^{NH_4^+-stream}+\bar{C}_{NO_3^-}^{NH_4^+-sed}+\bar{K}_{NO_3^-}^{sat}\right)},\ \bar{C}_{NO_3^-}^{NH_4^+-sed}\left(\bar{\tau}_R=0\right)=0$$

(B17c)

where $\bar{C}_{NH_4^+}^{stream}$ and $\bar{C}_{NH_4^+}^{sed}$ represent the concentration of ammonium originating in the stream and sediment, respectively. Importantly, the overall concentration of nitrate at any location along a streamline is simply the sum of these different nitrate species: $\bar{C}_{NO_3^-}\left(\tau\right)=\bar{C}_{NO_3^-}^{stream}\left(\tau\right)+\bar{C}_{NO_3^-}^{NH_4^+-stream}\left(\tau\right)+\bar{C}_{NO_3^-}^{NH_4^+-sed}\left(\tau\right)$.

Likewise, the chemical evolution of stream and sediment ammonium can be tracked as a water parcel travels through the sediment:

$$\frac{d\bar{C}_{NH_4^+}^{stream}}{d\bar{\tau}_R}=-\delta\bar{C}_{O_2}\bar{C}_{NH_4^+}^{stream},\ \bar{C}_{NH_4^+}^{stream}\left(\bar{\tau}_R=0\right)=\alpha \tag{B18a}$$

$$\frac{d\bar{C}_{NH_4^+}^{sed}}{d\bar{\tau}_R}=\frac{1}{\gamma_{CN}}\bar{K}_{O_2}^{sat}-\delta\bar{C}_{O_2}\bar{C}_{NH_4^+}^{sed},\ \bar{C}_{NH_4^+}^{sed}\left(\bar{\tau}_R=0\right)=0 \tag{B18b}$$

We can also derive a set of coupled differential equations for the nitrogen gas generated from the different species of nitrate; specifically, the N_2 generated from: (1) direct denitrification of stream nitrate ($\bar{C}_{N_2}^{stream}$); (2) coupled nitrification-denitrification of stream ammonium ($C_{N_2}^{NH_4^+-stream}$); and (3) coupled nitrification-denitrification of sediment ammonium ($\bar{C}_{N_2}^{NH_4^+-sed}$):

$$\frac{d\bar{C}_{N_2}^{NO_3^--stream}}{d\bar{\tau}_R}=\frac{1}{2}\times 0.05\times\frac{\bar{K}_{O_2}^{inh}\bar{K}_{O_2}^{sat}\bar{C}_{NO_3^-}^{stream}}{\left(\bar{C}_{O_2}+\bar{K}_{O_2}^{inh}\right)\left(\bar{C}_{NO_3^-}^{stream}+\bar{C}_{NO_3^-}^{NH_4^+-stream}+\bar{C}_{NO_3^-}^{NH_4^+-sed}+\bar{K}_{NO_3^-}^{sat}\right)},\quad \bar{C}_{N_2}^{stream}\left(\bar{\tau}_R=0\right)=0$$

(B19a)

$$\frac{d\bar{C}_{N_2}^{NH_4^+-stream}}{d\bar{\tau}_R}=\frac{1}{2}\times 0.05\times\frac{\bar{K}_{O_2}^{inh}\bar{K}_{O_2}^{sat}\bar{C}_{NO_3^-}^{NH_4^+-stream}}{\left(\bar{C}_{O_2}+\bar{K}_{O_2}^{inh}\right)\left(\bar{C}_{NO_3^-}^{stream}+\bar{C}_{NO_3^-}^{NH_4^+-stream}+\bar{C}_{NO_3^-}^{NH_4^+-sed}+\bar{K}_{NO_3^-}^{sat}\right)},\quad C_{N_2}^{NH_4^+-stream}\left(\bar{\tau}_R=0\right)=0$$

(B19b)

$$\frac{d\bar{C}_{N_2}^{NH_4^+-sed}}{d\bar{\tau}_R}=\frac{1}{2}\times 0.05\times\frac{\bar{K}_{O_2}^{inh}\bar{K}_{O_2}^{sat}\bar{C}_{NO_3^-}^{NH_4^+-sed}}{\left(\bar{C}_{O_2}+\bar{K}_{O_2}^{inh}\right)\left(\bar{C}_{NO_3^-}^{stream}+\bar{C}_{NO_3^-}^{NH_4^+-stream}+\bar{C}_{NO_3^-}^{NH_4^+-sed}+\bar{K}_{NO_3^-}^{sat}\right)},\quad C_{N_2}^{NH_4^+-sed}\left(\bar{\tau}_R=0\right)=0$$

(B19c)

The factor of 1/2 appearing on the right hand side of the last set of equations is included because, during denitrification, one-half mole of nitrogen gas is produced from reduction of one mole of nitrate. The consumption of oxygen along a streamline becomes:

$$\frac{d\bar{C}_{O_2}}{d\bar{\tau}_R}=-\frac{\bar{C}_{O_2}}{\bar{C}_{O_2}/\bar{K}_{O_2}^{sat}+1}-2\delta\bar{C}_{O_2}\left(\bar{C}_{NH_4^+}^{stream}+\bar{C}_{NH_4^+}^{\mathrm{sed}}\right),\ \bar{C}_{O_2}\left(\bar{\tau}_R=0\right)=1 \tag{B20}$$

All concentrations appearing in these equations have been reduced by the in-stream concentration of oxygen; i.e., the reduced concentration for the *i*th species is $\bar{C}_i\equiv C_i/C_{O_2}(0)$. We numerically integrated this coupled set of 9 equations (using Wolfram Mathematica, version 10.0) to obtain the reduced concentration of all species of interest as a function of reduced travel time ($\bar{\tau}_R$) through the bedform. By so doing we were able to generate the uptake velocities included in **Figures 3.2** and **3.3** of **Chapter 3** (small

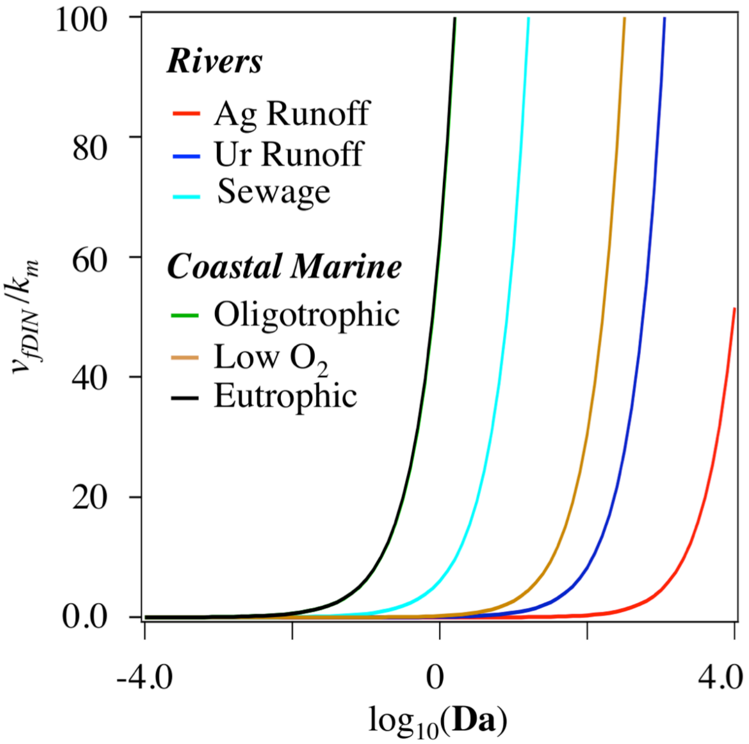

Figure B.8. Uptake velocity of dissolved inorganic nitrogen (DIN) plotted as a function of the Damköhler number for each of the six environments considered in this study.

panels). We were also able to calculate the uptake velocity of dissolved inorganic nitrogen (DIN, see **section 3.6.4** of **Chapter 3** for definition). The uptake velocities for DIN are plotted against Damköhler number for each of the six environments considered in this study (**Figure B.8**).

Text B.10. Limiting Behavior of Denitrification Uptake Velocity

In this section we derive two exact solutions for the denitrification velocity v_{fden} in the limits of high and low in-stream nitrate concentration ($C_{NO_3^-}(0)$). Neglecting nitrification and oxygen inhibition of denitrification we can approximate the rate of nitrate and nitrogen gas production along a streamline as follows (derived from equations (5b) and (6d) assuming $\theta_{O_2}^{inh} = 1$ and $R_{NI} << R_{DN}$):

$$\frac{dC_{N_2}}{d\overline{\tau}_f} = -\frac{1}{2}\frac{dC_{NO_3^-}}{d\overline{\tau}_f} \approx \frac{1}{2}\frac{\mathbf{Da}\,\kappa K_{O_2}^{sat} C_{NO_3^-}}{C_{NO_3^-} + K_{NO_3^-}^{sat}} \qquad \text{(B21a)}$$

When the initial concentration of nitrate is much lower than the half-saturation rate constant for denitrification ($C_{NO_3^-}(0) \ll K_{NO_3^-}^{sat}$), production rates of nitrate and nitrogen gas are first-order behavior with respect to nitrate concentration:

$$\frac{dC_{N_2}}{d\overline{\tau}_f} = -\frac{1}{2}\frac{dC_{NO_3^-}}{d\overline{\tau}_f} = \frac{1}{2}\frac{\mathbf{Da}\,\kappa K_{O_2}^{sat}}{K_{NO_3^-}^{sat}} C_{NO_3^-} \qquad \text{(B21b)}$$

On the other hand, when the initial concentration of nitrate is much larger than the half-saturation rate constant for denitrification ($C_{NO_3^-}(0) \gg K_{NO_3^-}^{sat}$), production rates of nitrate and nitrogen gas are zero-order with respect to nitrate concentration:

$$\frac{dC_{N_2}}{d\overline{\tau}_f} = -\frac{1}{2}\frac{dC_{NO_3^-}}{d\overline{\tau}_f} = \frac{1}{2}\mathbf{Da}\,\kappa \bar{K}_{O_2}^{sat} \qquad \text{(B21c)}$$

Equations B21b and B21c have the following explicit solutions for nitrogen gas and nitrate concentrations:

$$\text{if } C_{NO_3^-}(0) \ll K_{NO_3^-}^{sat} \Rightarrow \frac{C_{NO_3^-}(\overline{\tau}_f)}{C_{NO_3^-}(0)} = e^{-\mathbf{Da}\,\kappa K_{O_2}^{sat}\overline{\tau}_f / K_{NO_3^-}^{sat}} \text{ and } \frac{C_{N_2}(\overline{\tau}_f)}{C_{NO_3^-}(0)} = \frac{1}{2}\left(1 - e^{-\mathbf{Da}\,\kappa K_{O_2}^{sat}\overline{\tau}_f / K_{NO_3^-}^{sat}}\right) \qquad \text{(B22a)}$$

$$\text{if } C_{NO_3^-}(0) \gg K_{NO_3^-}^{sat} \Rightarrow \frac{C_{NO_3^-}(\overline{\tau}_f)}{C_{NO_3^-}(0)} = 1 - \frac{\mathbf{Da}\,\kappa K_{O_2}^{sat}\overline{\tau}_f}{C_{NO_3^-}(0)} \text{ and } \frac{C_{N_2}(\overline{\tau}_f)}{C_{NO_3^-}(0)} = \frac{1}{2}\frac{\mathbf{Da}\,\kappa K_{O_2}^{sat}\overline{\tau}_f}{C_{NO_3^-}(0)} \qquad \text{(B22b)}$$

Substituting these expressions for C_{N_2} into equation (9a) we obtain the following two solutions for v_{fden}:

$$\text{if } C_{NO_3^-}(0) \ll K_{NO_3^-}^{sat} \Rightarrow \frac{v_{fden}}{k_m} = 2\int_0^{\pi/2} \frac{C_{N_2}(\overline{x}_0)}{C_{NO_3^-}(0)} \sin\overline{x}_0 d\overline{x}_0 = \int_0^{\pi/2} \left(1 - e^{-\frac{\mathbf{Da}\,\kappa K_{O_2}^{sat}\overline{x}_0}{K_{NO_3^-}^{sat}\cos\overline{x}_0}}\right) \sin\overline{x}_0 d\overline{x}_0 \qquad \text{(B23a)}$$

$$\text{if } C_{NO_3^-}(0) \gg K_{NO_3^-}^{sat} \Rightarrow \frac{v_{fden}}{k_m} = 2\int_0^{\pi/2} \frac{C_{N_2}(\overline{x}_0)}{C_{NO_3^-}(0)} \sin\overline{x}_0 d\overline{x}_0 = \frac{\mathbf{Da}\,\kappa K_{O_2}^{sat}}{C_{NO_3^-}(0)} \int_0^{\pi/2} \frac{\overline{x}_0}{\cos\overline{x}_0} \sin\overline{x}_0 d\overline{x}_0 \qquad \text{(B23b)}$$

The integral expression in equation (B23b) can be numerically integrated:

$$\int_0^{\pi/2} \frac{\overline{x}_0}{\cos\overline{x}_0} \sin\overline{x}_0 d\overline{x}_0 = 57.6 \qquad \text{(B24a)}$$

Furthermore, the integral in equation (B23a) can be numerically evaluated for any choice of the quantity $v = \left(\mathbf{Da}\,\kappa K_{O_2}^{sat}\right) / \left(K_{NO_3^-}^{sat}\right)$:

$$G(v) = \int_0^{\pi/2} \left(1 - e^{-\frac{v\overline{x}_0}{\cos\overline{x}_0}}\right) \sin\overline{x}_0 d\overline{x}_0 \qquad \text{(B24b)}$$

Combining equations (B23a), (B23b), (B24a), and (B24b) we arrive at equations (11a) and (11b) in **Chapter 3**.

Text B.11. Non-parametric Bootstrap Analysis

Non-parametric bootstrap statistics were used to estimate 95% confidence intervals for the slope of the power law regression between nitrate concentration ($C_{NO_3^-}$) and the denitrification uptake velocity (v_{fden}) in streams. The data evaluated here are from Mulholland et al.'s Supplementary Table 1 [Mulholland et al., 2008]. 49 streams from multiple biomes in 8 regions of the US are represented, including those with urban, agricultural, and "reference" catchments where the surrounding land was predominantly native forest, grassland, or shrubs. A residual-based resampling (or fixed x) approach was employed for this analysis. Briefly, a line (first order polynomial) was fit to log transformed data: $C_{NO_3^-}$ (x values) and v_{fden} (y values). The residuals were calculated and bootstrapped 10,000 times, producing 10,000 realizations of error. Each realization of error was added to the original linear fit and then re-fit. The slope estimates (b) from these 10,000 fits were retained, and used to calculate (1) the average slope and (2) 95% confidence intervals about that average. Because the probability distribution of the slopes was observed to be symmetric, confidence intervals were calculated using a basic percentile approach where the 10,000 slope estimates were sorted and the 250th value (2.5%) and 9,750th value (97.5%) selected as the lower and upper confidence bounds, respectively.

References

Bardini, L.; Boano, F.; Cardenas, M. B.; Revelli, R.; Ridolfi, L. Nutrient cycling in bed form induced hyporheic zones. Geochim. Cosmochim. Acta **2012**, 84, 47–61.

Bird, R. B.; Stewart W. E.; Lightfoot E. N. Transport Phenomena, Wiley: New York, U.S., 2002.

Boudreau, B. P.; The diffusive tortuosity of fine-grained unlithified sediment. Geochim. Cosmochim. Acta **1996,** 60, 3139-3142.

Boudreau, B. P.; Diagenetic Models and their implementation: modeling transport reactions in aquatic sediment. Springer, Hiedelberg Germany, 1997.

Buckingham, E. On Physically Similar Systems; Illustrations of the use of dimensional Equations. Phys. Rev. **1914**, 4, 345-376, doi:10.1103/physRev.4.345.

Cardenas et al. 2008: Cardenas, M.B.; Cook, P. L. M.; Jiang, H.; Traykovski, P. Constraining denitrification in permeable wave-influenced marine sediment using linked hydrodynamic and biogeochemical modeling. Earth and Planetary Science Letters **2008**, 275, 127-137.

Elliott, A. H.; Brooks, N. H. Transfer of Nonsorbing Solutes to a Streambed with Bed Forms: Theory. Water Resour. Res. **1997**, 33, 123–136.

Grant, S. B.; Stolzenbach, K.; Azizian, M.; Stewardson, M. J.; Boano, F.; Bardini, L. First-Order Contaminant Removal in the Hyporheic Zone of Streams: Physical Insights from a Simple Analytical Model. Environ. Sci. Technol. **2014**, 48, 11369-11378.

Hill, C.G. An Introduction to Chemical Engineering Kinetics and Reactor Design, Chapter 11, John Wiley and Sons: New York, U.S., 1977.

Iversen, N.; Jorgensen, B. B. Diffusion coefficients of sulfate and methane in marine sediments: Influence of porosity. Geochim. Cosmochim. Acta **1993**, 57, 571–578.

Kessler, A.J.; Glud, R.N.; Cardenas, M.B.; Larsen, M.; Bourke, M.F.' Cook, P.L.M. Quantifying Denitrification in Rippled Permeable Sands through Combined Flume Experiments and Modeling. Limnol. Oceanogr. **2012**, 57, 1217-1232, doi:10.4319/lo.2012.57.4.1217.

Kessler, A.J.; Glud, R.N.; Cardenas, M.B.; Cook, P.L.M. Transport Zonation Limits Coupled Nitrification-Denitrification in Permeable Sediments. Environ. Sci. Technol. **2013**, 47, 13404-13411.

Levenspiel, O. Chemical Reaction Engineering, Wiley: New York, U.S., 1972.

Mulholland et al. Stream denitrification across biomes and its response to anthropogenic nitrate loading. Nature **2008**, 452, 202-205.

Appendix C

Ambient Groundwater Flow Diminishes Nitrate Processing in the Hyporheic Zone of Streams

Text C.1. Principal Component Analysis Methods

The resampling-based stopping rule employed in Peres-Neto et al. [2005] was used to identify principal component (PC) modes that explained marginally significantly ($p < 0.1$) more variance in stream biogeochemical characteristics than expected by chance. The stopping rule was implemented as follows:

1) Principal Component Analysis (PCA) was performed on log transformed, mean-centered and scaled (i.e., z-scored) stream biogeochemistry data (ecosystem respiration, CNH_3, CNO_3, and O_2 concentration), and the eigenvalues associated with each PC mode (EIG_{data}) were saved;

2) Variables (e.g., biogeochemical characteristics) within our stream biogeochemistry matrix were randomized 10,000 times;

3) PCA was conducted on these randomized matricies and the eigenvalues for each PC mode (EIG_{rand}) were saved;

4) Percentile-based 90% confidence intervals were calculated for each PC mode using the generated EIG_{rand} values (10,000 realizations per mode); and

5) Modes where EIG_{data} was $\geq$ the 90th percentile value of EIG_{rand} were retained as dominant modes (see **Figure C.1**).

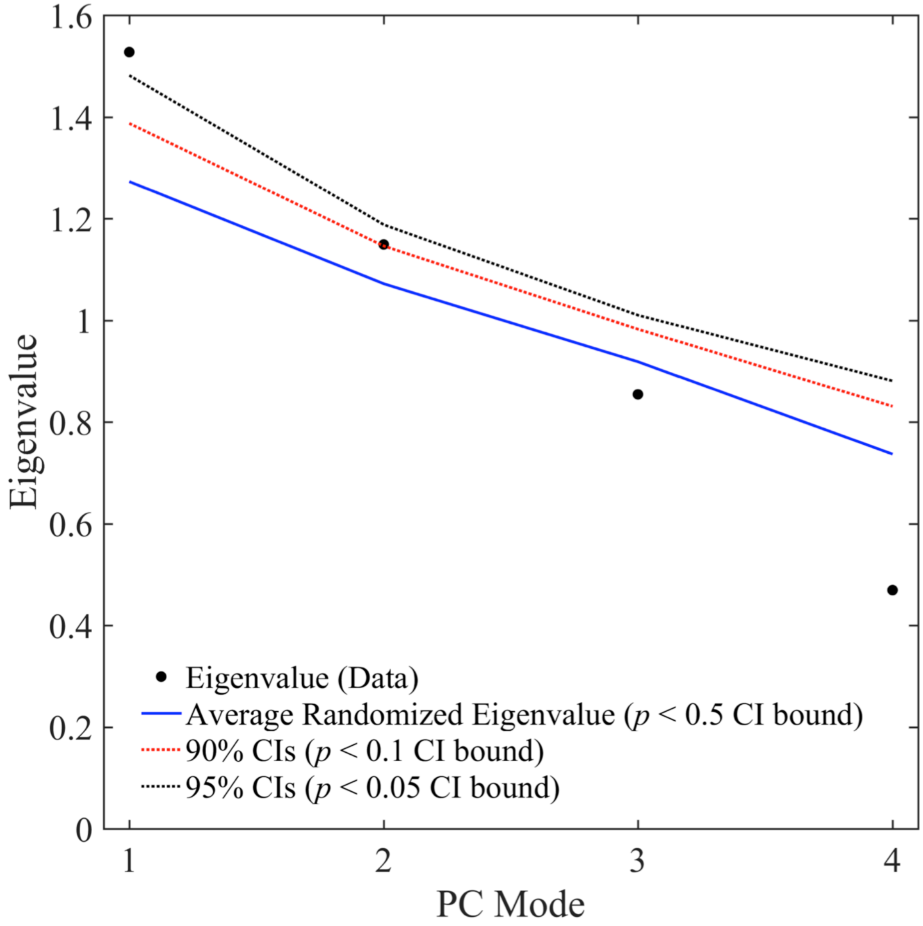

Figure C.1. Principal component modes 1 through 4 (*x*-axis) ranked by their eigenvalue (*y*-axis). Resampling-based stopping rule results are depicted as lines; the blue line is the average eigenvalue expected if stream biogeochemical characteristics were completely random, the black dashed line is the upper 90% confidence bound, and the red dashed line is the upper 95% confidence bound. PC modes that exceed the red (Mode 1) or black (Mode 1 and 2) dashed lines are significantly different from random at a $p < 0.05$ or $p < 0.1$ level, respectively.

Text C.2. Boano et al.'s Advective Pumping Model (APM) Solution

In this section we summarize Boano et al.'s [2009] Advective Pumping Model (APM), which accounts for hyporheic exchange across a flat sediment-water interface, given a sinusoidal pressure variation over the sediment-water interface together with groundwater flux in the horizontal (underflow, q_{U}, units m s^{-1}) and vertical (gaining $q_{\mathrm{V}} > 0$, losing $q_{\mathrm{V}} < 0$, or neutral $q_{\mathrm{V}} = 0$, units m s^{-1}) directions.

C.2.1. Solution for the Hyporheic Exchange Flow Field

Boano et al.'s solution for the hyporheic exchange velocity field is as follows, where q_{x}, q_{y}, and $\|\vec{q}\|$ represent the horizontal component, vertical component, and modulus of the Darcy fluxes (all units m s^{-1}):

$$q_{\mathrm{x}} = -\pi q_{\mathrm{H},0} \cos\bar{x} e^{\bar{y}} + q_{\mathrm{U}} \tag{C1a}$$

$$q_{\mathrm{y}} = -\pi q_{\mathrm{H},0} \sin\bar{x} e^{\bar{y}} + q_{\mathrm{V}} \tag{C1b}$$

$$\|\vec{q}\| = \sqrt{q_{\mathrm{x}}^2 + q_{\mathrm{y}}^2} = \sqrt{\left(\pi q_{\mathrm{H},0} e^{\bar{y}}\right)^2 + q_{\mathrm{U}}^2 + q_{\mathrm{V}}^2 - 2\pi q_{\mathrm{H},0} e^{\bar{y}} \left(q_{\mathrm{V}} \sin\bar{x} + q_{\mathrm{U}} \cos\bar{x}\right)} \tag{C1c}$$

In these equations, $\bar{x} = 2\pi x/\lambda$ and $\bar{y} = 2\pi y/\lambda$ (unitless) are normalized forms of the horizontal and vertical coordinates x and y (units of m), respectively. The sediment-water interface corresponds to $y = 0$, and the y-coordinate is directed upwards; therefore, the inequalities $y > 0$ and $y < 0$ correspond to regions above and below the sediment-water interface, respectively. The variable λ (units m) represents the wavelength of the sinusoidal pressure variation at the sediment-water interface (assumed equal to the wavelength of a bedform), and $q_{\mathrm{H},0}$ (units m s^{-1}) is a characteristic hyporheic exchange flux (see equations (7b) and (7c) in **Chapter 4**).

C.2.2. Stream Function Representation of Boano et al.'s Flow Field

For steady-state conditions, the velocity components of a two-dimensional flow field in the x and y-directions can be represented by a stream function $\psi(x,y)$ [Bird et al., 2007]:

$$q_{\mathrm{x}} = -\frac{\partial \psi}{\partial y} \tag{C2a}$$

$$q_{\mathrm{y}} = \frac{\partial \psi}{\partial x} \tag{C2b}$$

Applied to Boano's velocity field, the stream function is as follows (note that, in these equations, the vertical and horizontal components of the ambient groundwater flux (q_{V} and q_{U}) have been normalized by the characteristic hyporheic exchange velocity $q_{\mathrm{H},0}$):

$$\psi(\bar{x},\bar{y}) = \frac{\lambda q_{\mathrm{H},0}}{2}\left[\cos\bar{x}\, e^{\bar{y}} + \bar{q}_{\mathrm{V}}\bar{x} - \bar{q}_{\mathrm{U}}\bar{y}\right] \tag{C3a}$$

$$\bar{q}_{\mathrm{V}} = q_{\mathrm{V}} \big/ \left(\pi q_{\mathrm{H},0}\right) \tag{C3b}$$

$$\bar{q}_{\mathrm{U}} = q_{\mathrm{U}} \big/ \left(\pi q_{\mathrm{H},0}\right) \tag{C3c}$$

Streamlines (which are functionally equivalent to hyporheic zone tubes (HZTs), see main text) can be calculated from Equation (C3a) by setting the stream function equal to a constant C. The magnitude of the constant determines the streamline being plotted. Here we express the constant C in terms of the x-coordinate where water first enters the sediment bed from the stream, a location we refer to as the "starting position" of the streamline ($\bar{x}_0 = 2\pi x_0/\lambda$):

$$C = \frac{\lambda q_{\mathrm{H},0}}{2}\left[\cos\bar{x}_0 + \bar{q}_{\mathrm{V}}\bar{x}_0\right] \tag{C4}$$

This last equation can be derived from equation (C3a) by setting $\bar{y} = 0$ (corresponding to the sediment-water interface) and letting $\bar{x} = \bar{x}_0$.

C.2.3. Flow Fields for the Ten Ambient Flow Conditions

Figure C.2 presents the hyporheic exchange flow fields predicted by Boano et al.'s model (equations (C1a) – (C1c)) for the ten ambient flow scenarios described in **Chapter 4**, including two choices of stream discharge ($Q =$ 17.47 and 7.40 $\mathrm{m^3\,s^{-1}}$, denoted by "H-Q" and "L-Q", respectively), five ambient vertical groundwater fluxes ($q_{\mathrm{V}} = 0$, $\pm 5.8\times 10^{-6}$, and $\pm 2.3\times 10^{-5}$ $\mathrm{m\,s^{-1}}$), and one ambient horizontal groundwater flux ($q_{\mathrm{U}} = 10^{-5}$ $\mathrm{m\,s^{-1}}$).

All else being equal, the modulus of the hyporheic exchange velocity (see color contours) is larger for H-Q than L-Q, reflecting the quadratic dependence of the hyporheic exchange flux on stream discharge (see equation (7c) in **Chapter 4**). The Interfacial

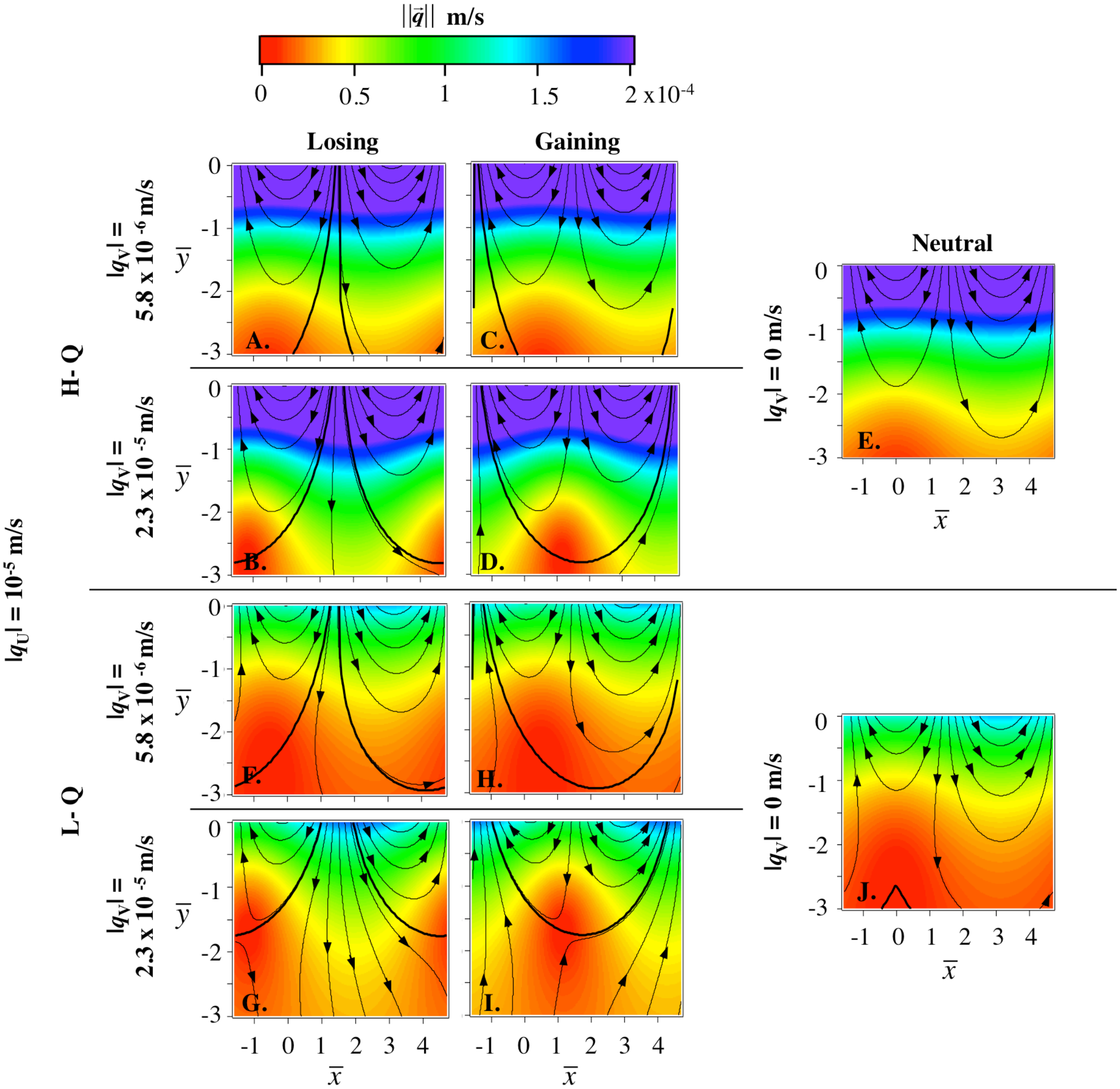

Figure C.2. Velocity fields predicted by Boano et al.'s model for the ten different ambient flow conditions described in **Chapter 4**, including five different scenarios of groundwater ambient flows ($q_V = \pm 5.8 \times 10^{-6}$ (**A, C, F, H**), $q_V = \pm 2.3 \times 10^{-5}$ (**B, D, G, I**), and $q_V = 0$ (**E, J**) m s^{-1}), a fixed groundwater underflow ($q_U = 10^{-5}$ m s^{-1}), and two different stream discharges ($Q = 17.47$ m^3 s^{-1} (H-Q, upper panels) and $Q = 7.4$ (L-Q, lower panels)). The sediment-water interface corresponds to $\bar{y} = 0$, and streamflow (above the sediment-water interface, $\bar{y} > 0$) is from left to right. The color contours, thin black curves with arrows, and thick black curves represent the modulus of the velocity $\|\vec{q}\|$ (units m s^{-1}), streamlines, and the boundary of the Interfacial Exchange Zone (IEZ), respectively. Streamlines were chosen so that volumetric flow rate per unit width between any two adjacent streamlines is the same and equal to $0.2\lambda q_{H,0}$ m^2 s^{-1}.

Exchange Zone (IEZ)—the region of the sediment through which hyporheic exchange occurs—contracts as the magnitude of the vertical groundwater flux increases (in the figure the boundary of the IEZ is indicated by a thick black curve). This effect is most pronounced at the lower stream discharge (L-Q simulations), reflecting the weaker hyporheic exchange flows that occur at lower stream discharge (**Figure C.2**).

Text C.3. Symmetry of Gaining and Losing Velocity Fields

As noted in **Chapter 4**, Boano et al.'s solution for the residence time distribution F_{RTD} and the hyporheic exchange flux q_{H} do not change when the sign of the vertical groundwater flux is changed from gaining to losing or vice versa. In this section we explore the gaining/losing symmetry properties of Boano et al.'s solution relative to: (i) the modulus of the velocity field; (ii) streamlines; (iii) upwelling and downwelling regions; and (iv) hyporheic exchange flux. The symmetry of the residence time distribution is discussed in **Text C.4**, where we derive the F_{RTD} solution presented in **Chapter 4**.

C.3.1. Gaining/Losing Symmetry of the Velocity Modulus

Consider two hyporheic exchange velocity fields that are identical in all respects, except the vertical groundwater flux is directed downward in the first case (i.e., the stream is losing) and the vertical groundwater flux is directed upwards in the second case (i.e., the stream is gaining):

Losing: $q_{\mathrm{x},l} = -\pi q_{\mathrm{H},0} \cos \bar{x} e^{\bar{y}} + q_{\mathrm{U}}$ and $q_{\mathrm{y},l} = -\pi q_{\mathrm{H},0} \sin \bar{x} e^{\bar{y}} - |q_{\mathrm{V}}|$ (C5a)

Gaining: $q_{\mathrm{x},g} = -\pi q_{\mathrm{H},0} \cos \bar{x} e^{\bar{y}} + q_{\mathrm{U}}$ and $q_{\mathrm{y},g} = -\pi q_{\mathrm{H},0} \sin \bar{x} e^{\bar{y}} + |q_{\mathrm{V}}|$ (C5b)

The subscripts "*l*" and "*g*" refer to losing and gaining conditions, respectively. Equations (C5a) and (C5b) follow directly from Boano et al.'s solution for the hyporheic exchange velocity field (compare with equations (C1a) and (C1b)). Now let $\bar{x}_{\mathrm{R}} = -\bar{x}$ represent a new horizontal coordinate that has been reflected around the $\bar{y}$-axis (i.e., around $\bar{x} = 0$). Performing this coordinate transformation on equation (C5b) we obtain a new set of equations for the reflected and gaining velocity field:

Reflected & Gaining: $q^{\mathrm{R}}_{\mathrm{x},g} = -\pi q_{\mathrm{H},0} \cos \bar{x}_{\mathrm{R}} e^{\bar{y}} + q_{\mathrm{U}}$ and $q^{\mathrm{R}}_{\mathrm{y},g} = \pi q_{\mathrm{H},0} \sin \bar{x}_{\mathrm{R}} e^{\bar{y}} + |q_{\mathrm{V}}|$ (C6)

Comparing equations (C5a) and (C6) we observe that the following equalities hold when $\bar{x}_{\mathrm{R}}$ is substituted for $\bar{x}$ or vice versa: $q^{\mathrm{R}}_{\mathrm{x},g} = q_{\mathrm{x},l}$ and $q^{\mathrm{R}}_{\mathrm{y},g} = -q_{\mathrm{y},l}$. In words, when the gaining velocity field is reflected around the $\bar{y}$-axis the: (1) x-component of the velocity field is unchanged; and (2) y-component of the reflected gaining velocity field becomes equal to the negative of the y-component of the losing velocity field. An important consequence is that the modulus of the reflected gaining velocity field is equal to the modulus of the losing velocity field: $\left\|\vec{q}^{\,\mathrm{R}}_{g}\right\| = \left\|\vec{q}_{l}\right\|$, where by definition $\left\|\vec{q}^{\,\mathrm{R}}_{g}\right\| = \sqrt{\left(q^{\mathrm{R}}_{\mathrm{x},g}\right)^2 + \left(q^{\mathrm{R}}_{\mathrm{y},g}\right)^2}$ and $\left\|\vec{q}_{l}\right\| = \sqrt{q^2_{\mathrm{x},l} + q^2_{\mathrm{y},l}}$. This last result is illustrated in **Figure C.3**, where the moduli of gaining and losing velocity fields are clearly reflected about the $\bar{y}$-axis (indicated by the vertical dashed line).

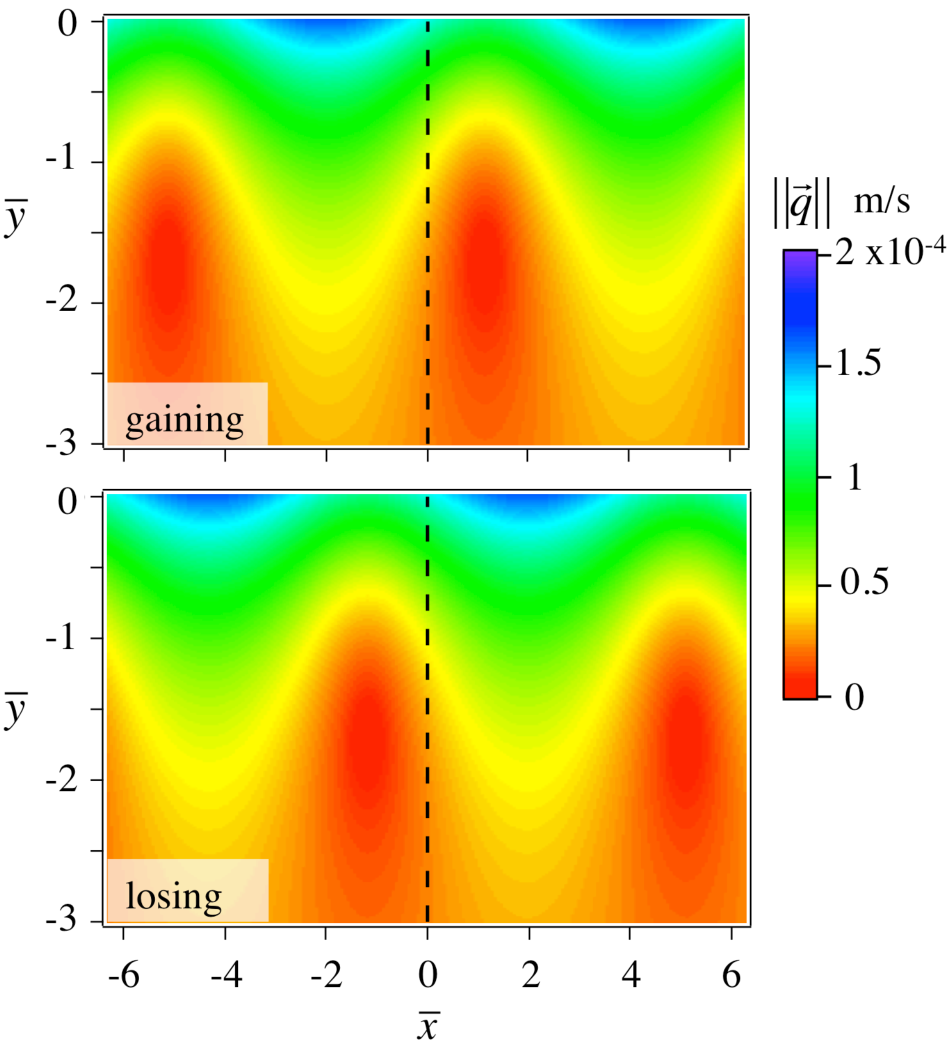

Figure C.3. Moduli of the velocity field for a gaining stream (top panel) and losing stream (bottom panel). The color scale and dashed line represent modulus of the Darcy flux $\|\vec{q}\|$ (units m s^{-1}) and $\bar{y}$-axis (at $\bar{x}=0$), respectively. In this example, the stream discharge is $Q = 7.4$ m^3 s^{-1} (corresponding to L-Q), and the magnitude of vertical and horizontal groundwater fluxes are $|q_V| = 2.3\times10^{-5}$ m s^{-1} and $q_U = 10^{-5}$ m s^{-1}, respectively. Comparing the gaining and losing velocity fields we see that moduli of the two velocity fields are reflected about the vertical dashed line (corresponding to the $\bar{y}$-axis)

C.3.2. Streamline Symmetry

As a next step, we set out to determine if the streamlines of the reflected gaining velocity field are identical to the streamlines of the unreflected losing velocity field. The equation for a streamline can be obtained by equating equations (C3a) and (C4):

$$\cos\bar{x}\, e^{\bar{y}} + \bar{q}_{\mathrm{V}}\bar{x} - \bar{q}_{\mathrm{U}}\bar{y} = \cos\bar{x}_0 + \bar{q}_{\mathrm{V}}\bar{x}_0 \tag{C7}$$

Setting $\bar{q}_{\mathrm{V}} = |\bar{q}_{\mathrm{V}}|$ (to assure that the vertical groundwater flux is always positive) we have from equation (C7) the equation for a streamline under gaining conditions:

Gaining: $$\cos\bar{x}\, e^{\bar{y}} + |\bar{q}_{\mathbf{V}}|\bar{x} - \bar{q}_{\mathrm{U}}\bar{y} = \cos\bar{x}_0 + |\bar{q}_{\mathbf{V}}|\bar{x}_0 \tag{C8}$$

To reflect this last equation about the $\bar{y}$-axis we set $\bar{x}_{\mathrm{R}} = -\bar{x}$ and $\bar{x}_{\mathrm{R0}} = -\bar{x}_0$, and obtain:

Reflected & Gaining: $$\cos\bar{x}_{\mathrm{R}}\, e^{\bar{y}} - |\bar{q}_{\mathrm{V}}|\bar{x}_{\mathrm{R}} - \bar{q}_{\mathrm{U}}\bar{y} = \cos\bar{x}_{\mathrm{R0}} - |\bar{q}_{\mathrm{V}}|\bar{x}_{\mathrm{R0}} \tag{C9}$$

The corresponding streamline equation for a losing velocity field follows directly from equation (C7):

Losing: $$\cos\bar{x}\, e^{\bar{y}} - |\bar{q}_{\mathbf{V}}|\bar{x} - \bar{q}_{\mathrm{U}}\bar{y} = \cos\bar{x}_0 - |\bar{q}_{\mathbf{V}}|\bar{x}_0 \tag{C10}$$

Equations (C9) and (C10) are mathematically identical when $\bar{x}_{\mathrm{R}}$ and $\bar{x}_{\mathrm{R0}}$ are substituted for $\bar{x}$ and $\bar{x}_0$, or vice versa. In words, the streamlines for losing and gaining streams are identical after reflection about the $\bar{y}$-axis (vertical dashed line in **Figure C.4**).

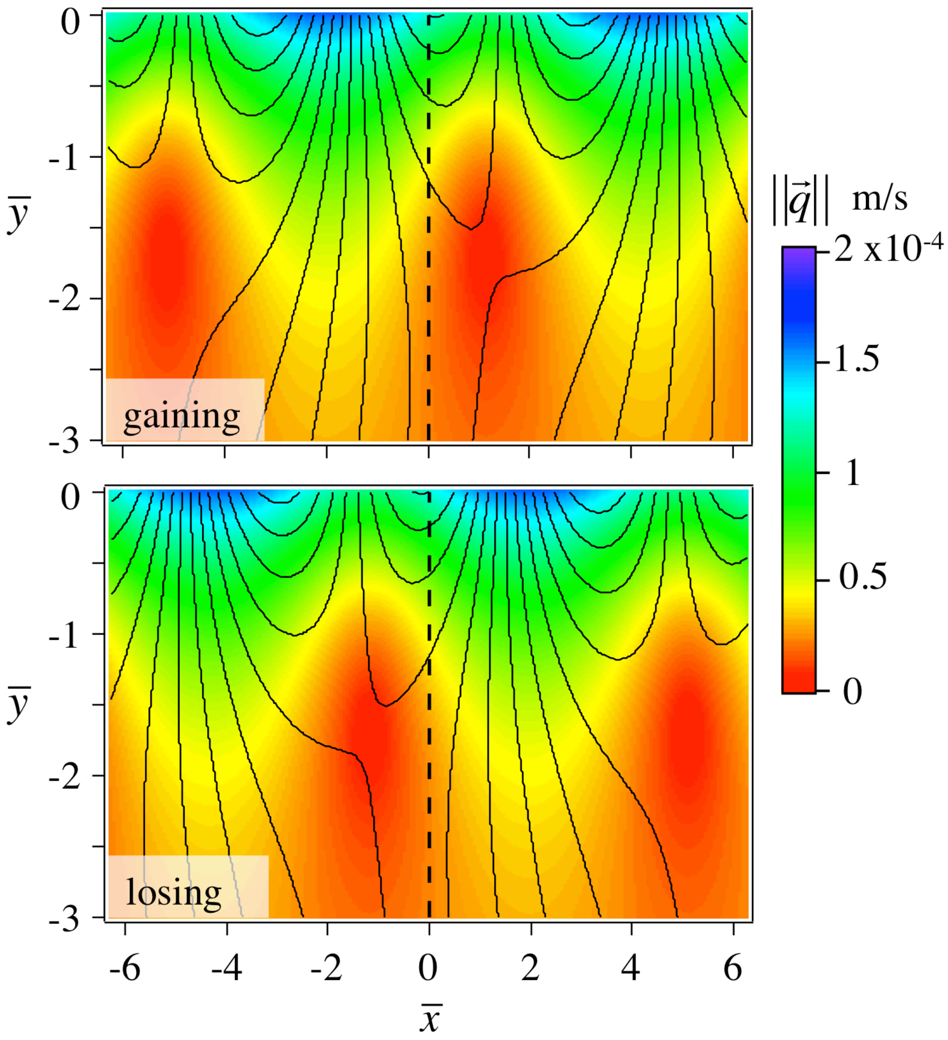

Figure C.4. Streamlines in the hyporheic zone of a gaining (upper panel) and losing (lower panel) stream. The color scale, vertical dashed line, and black curves represent modulus of the Darcy flux $\|\vec{q}\|$ (units m s^{-1}), $\bar{y}$ -axis (at $\bar{x} = 0$), and streamlines, respectively. Parameters used to generate these plots are the same as described in **Figure C.3** (see legend). Comparing the two panels we see that the streamlines are reflected about the vertical dashed line (corresponding to the $\bar{y}$ -axis).

C.3.3. Downwelling and Upwelling Zone Symmetry

In **Figure C.5** we show the same set of streamlines plotted in **Figure C.4**, but with the direction of the flow added (denoted by the small arrows). Here we see regions at the sediment-water interface that are upwelling in the gaining case, are reflected and downwelling in the losing case (e.g., compare regions of the sediment-water interface denoted by A in the gaining case and A_R in the losing case). This result follows from our earlier discussion of the reflected velocity field, where we showed that when the y-component of the gaining velocity field is reflected around the $\bar{y}$-axis it becomes equal to the <u>negative</u> of the y-component of the losing velocity field (equations (C5a) and (C6)).

C.3.4. Hyporheic Exchange Flux Symmetry

Hyporheic exchange flux refers to the flux of stream water circulating through the IEZ, passing from the stream to the sediment and returning to the stream; it excludes groundwater flux, which moves in only one direction, either from the stream to the sediment under losing conditions, or from the sediment to the stream under gaining conditions.

According to Boano et al., stream water circulating through the IEZ is called “small-scale exchange”, while water moving from the stream to groundwater (or vice versa) is “large-scale exchange”. Thus, our use of the term “hyporheic exchange flux” in **Chapter 4** is equivalent to Boano et al.’s “small-scale exchange flux”. To calculate the small-scale exchange flux, we begin by focusing on a single IEZ in a gaining stream (see area

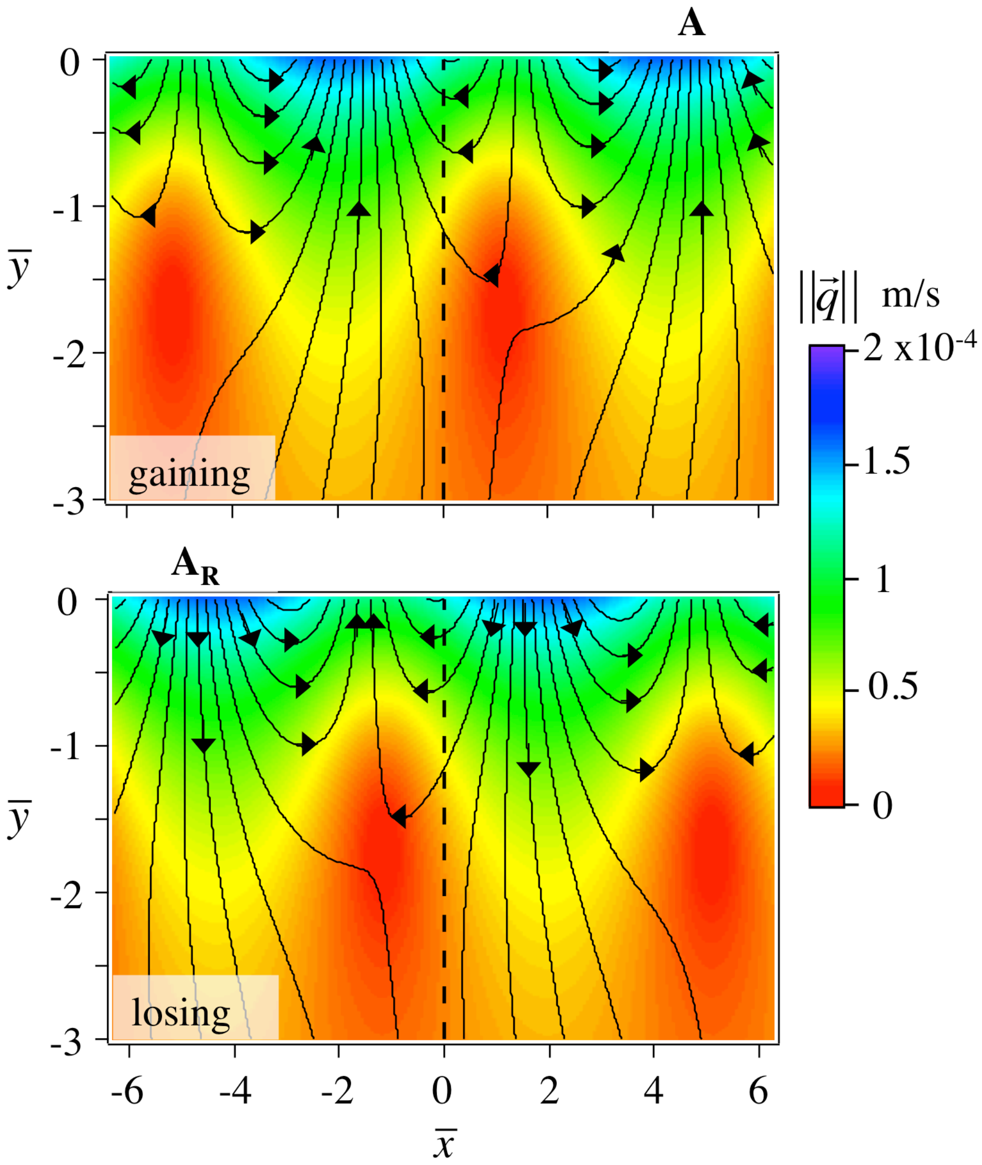

Figure C.5. Same flow fields as displayed in **Figure C.3** and **C.4**, but with the direction of flow indicated for each streamline.

enclosed by the thick solid curve in **Figure C.6**). Within each IEZ we can identify upstream and downstream flow cells separated by a streamline we refer to here as the "separation streamline" (thick dashed curve in **Figure C.6**). Let the variable $\bar{x}_{\text{sep}} = 2\pi x_{\text{sep}}/\lambda$ represent the normalized x-position where the separation streamline intersects the sediment-water interface. This intersection point is located between $\bar{x} = \bar{a}$ and $\bar{x} = \bar{b}$, where the latter represent the normalized boundaries between upwelling and downwelling zones in, respectively, the upstream and downstream flow cells (see **Figure C.6**): $\bar{a} < \bar{x}_{\text{sep}} < \bar{b}$. Expressions for calculating $\bar{a}$ and $\bar{b}$ are presented later (see equations (C15a) and (C15b)).

The value of $\bar{x}_{\text{sep}}$ can be found by identifying the streamline that includes both the separation point $\left(\bar{x}_{\text{sep}}, \bar{y} = 0\right)$ and the stagnation point $\left(\bar{x}_{\text{SP}}, \bar{y}_{\text{SP}}\right)$:

$$\cos \bar{x}_{\text{SP}}\, e^{\bar{y}_{\text{SP}}} + \bar{q}_{\text{V}} \bar{x}_{\text{SP}} - \bar{q}_{\text{U}} \bar{y}_{\text{SP}} = \cos \bar{x}_{\text{sep}} + \bar{q}_{\text{V}} \bar{x}_{\text{sep}} \tag{C11}$$

This last equation follows from equation (C7), where we have assigned the streamline starting position as $\bar{x}_0 = \bar{x}_{\text{sep}}$ and let $\left(\bar{x}, \bar{y}\right) = \left(\bar{x}_{\text{SP}}, \bar{y}_{\text{SP}}\right)$. The stagnation point $\left(\bar{x}_{\text{SP}}, \bar{y}_{\text{SP}}\right)$ is the point in the flow field where the modulus of the velocity field is zero (indicated by the red circle in **Figure C.6**); note that the stagnation point also coincides with the location where the separation streamline and the IEZ boundary intersect. The stagnation point can be calculated by setting the horizontal and vertical components of the velocity field (q_{x} and q_{y}, see equations (C1a) and (C1b)) equal to zero, and solving the resulting set of equations:

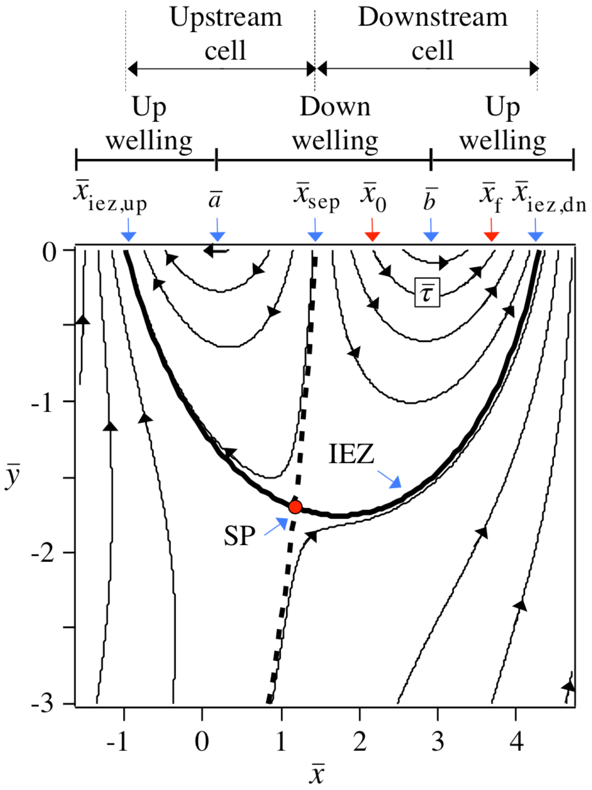

Figure C.6. Key features of the hyporheic zone velocity field predicted by Boano et al.'s model for a gaining stream. Model parameters are the same as in **Figure C.3** (see legend), and stream flow above the sediment-water interface is from left to right. Hyporheic exchange is confined to an Interfacial Exchange Zone (IEZ, bold black curve) within which two circulation flow cells are evident—an "upstream cell" located to the left of the thick dashed line and a "downstream cell" located to the right of the thick dashed line. The thick dashed line separating the two flow cells is referred to as a "separation streamline". The boundary of the IEZ and the separation streamline both pass through a stagnation point ($\bar{x}_{\text{SP}}$, $\bar{y}_{\text{SP}}$) where the modulus of the Darcy flux is zero. Streamlines within the upstream or downstream flow cells have a unique residence time ($\bar{\tau}$), starting position ($\bar{x}_0$), and ending position ($\bar{x}_{\text{f}}$) (as illustrated for one streamline in the downstream flow cell, red arrows). The point where the separation streamline intersects the sediment-water interface ($\bar{x} = \bar{x}_{\text{sep}}$,$\bar{y} = 0$) represents the starting position of the longest streamlines (with the largest residence times) in both upstream and downstream flow cells. The ending positions of the longest streamlines at the sediment-water interface are located at ($\bar{x} = \bar{x}_{\text{iez,up}}$, $\bar{y} = 0$) and ($\bar{x} = \bar{x}_{\text{iez,dn}}$, $\bar{y} = 0$) in the upstream and downstream flow cells, respectively. The locations $\bar{x} = \bar{a}$ and $\bar{x} = \bar{b}$ at the sediment-water interface ($\bar{y} = 0$) represent boundaries between upwelling and downwelling zones within the upstream and downstream flow cells, respectively.

$$\bar{x}_{\mathrm{SP}} = \tan^{-1}\left(\bar{q}_{\mathrm{V}}/\bar{q}_{\mathrm{U}}\right) \tag{C12a}$$

$$\bar{y}_{\mathrm{SP}} = \ln\left(\sqrt{\bar{q}_{\mathrm{U}}^{\,2} + \bar{q}_{\mathrm{V}}^{\,2}}\right) \tag{C12b}$$

In summary, to locate the boundary between the upstream and downstream cell (i.e., to find the value of $\bar{x}_{\mathrm{sep}}$) we first compute $\left(\bar{x}_{\mathrm{SP}}, \bar{y}_{\mathrm{SP}}\right)$ from equations (C12a) and (C12b), substitute their values into equation (C11), and numerically solve for $\bar{x}_{\mathrm{sep}}$, subject to the constraint $\bar{a} < \bar{x}_{\mathrm{sep}} < \bar{b}$.

Once the separation point $\bar{x}_{\mathrm{sep}}$ has been found, the small-scale exchange flux can be calculated by integrating the differential small-scale exchange flux ($-q_{\mathrm{y,g}}(x, y=0)dA$ where the differential area is $dA = Wdx$, W is the width of the stream, and the negative sign is included to ensure that the hyporheic exchange flux is always positive) over downwelling zones in the upstream flow cell (x ranging from a to x_{sep}) and in the downstream flow cell (x ranging from x_{sep} to b):

$$q_{\mathrm{H},g} = -\frac{1}{W\lambda}\int_{a}^{b} q_{\mathrm{y},g}(x, y=0)W\,dx = \frac{q_{\mathrm{H},0}}{2}\int_{\bar{a}}^{\bar{b}}\left(\sin\bar{x} - \left|\bar{q}_{\mathrm{V}}\right|\right)dx \tag{C13}$$

The hyporheic exchange flux (or small-scale exchange flux) is expressed per unit area of the periodic bedform, which is why the quotient $1/(W\lambda)$ is included on the right hand side of equation (C13). Again the subscript "*g*" refers to gaining conditions. The limits $\bar{a}$ and $\bar{b}$ appearing in equation (C13) can be calculated from the following previously published expressions [Boano et al., 2009]:

$$\bar{a} = \frac{2\pi a}{\lambda} = \sin^{-1}\bar{q}_{\mathrm{V}} + 2n\pi;\ \ n \in \text{Integers} \tag{C14a}$$

$$\bar{b} = \frac{2\pi b}{\lambda} = \pi - \sin^{-1}\bar{q}_{\mathrm{V}} + 2n\pi;\ \ n \in \text{Integers} \tag{C14b}$$

For the particular IEZ illustrated in **Figure C.6**, the values of $\bar{a}$ and $\bar{b}$ are:

$$\bar{a} = \sin^{-1}\left|\bar{q}_{\mathrm{V}}\right| \tag{C15a}$$

$$\bar{b} = \pi - \sin^{-1}\left|\bar{q}_{\mathrm{V}}\right| \tag{C15b}$$

Combining equations (C13), (C15a), and (C15b) we obtain Boano et al.'s solution for the hyporheic exchange flux, which appears as equation (7a) in **Chapter 4**.

Next we show that, all else being equal, precisely the same hyporheic exchange flux is derived if the stream is losing instead of gaining (see **Figure C.7**). For the losing case, the small-scale exchange flux can be calculated by integrating the differential small-scale exchange flux over the two upwelling zones within the IEZ, one in the upstream flow cell (x ranging from $-b$ to $-x_{\mathrm{sep}}$) and one for the downstream flow cell (x ranging from $-x_{\mathrm{sep}}$ to $-a$):

$$q_{\mathrm{H},l} = \frac{1}{W\lambda}\int_{-b}^{-a} q_{\mathrm{y},l}\left(x, y=0\right) W dx = \frac{q_{\mathrm{H},0}}{2}\int_{\bar{a}}^{\bar{b}} \left(\sin\bar{x} - \left|\bar{q}_{\mathrm{V}}\right|\right) d\bar{x} \tag{C16}$$

Note that in the last step we used the following identity: $q_{y,l}\left(-\bar{x}, \bar{y}=0\right) = -q_{y,g}\left(\bar{x}, \bar{y}=0\right)$. The integrals in equations (C13) and (C16) are mathematically identical, and therefore all else being equal, the small-scale exchange flux is equal for gaining and losing conditions:

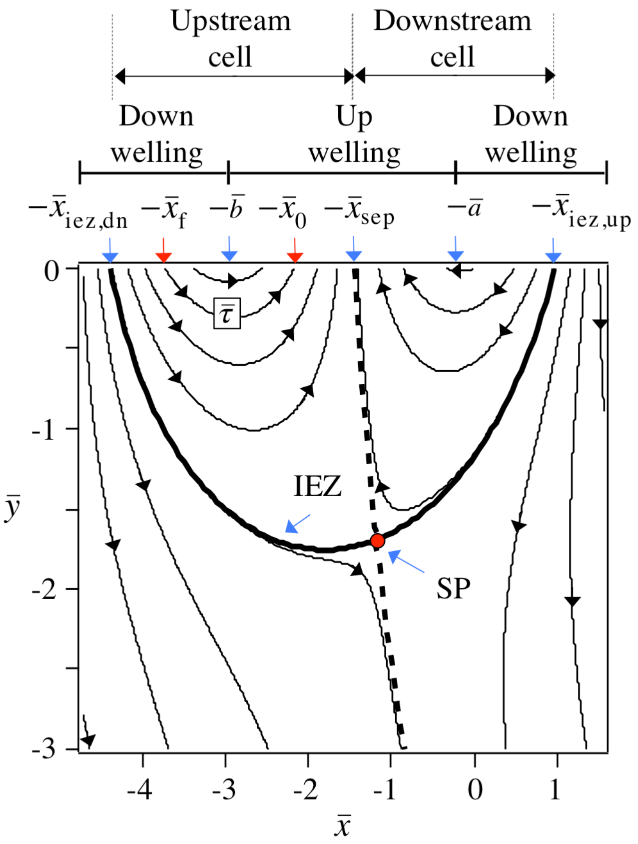

Figure C.7. Same as **Figure C.6** but the sign of the vertical ambient groundwater flux has been reversed, so that the stream is losing in this case. Note that the resulting velocity field is the same as depicted in **Figure C.6**, after reflection about the $\bar{y}$-axis, and taking the negative of the vertical component of the velocity field (so that upwelling zones become downwelling zones, and vice versa).

$$q_{\mathrm{H},l} = q_{\mathrm{H},g} .$$

Text C.4. Residence Time Distribution (RTD) Derivation

In this section we derive: (i) the RTD function for hyporheic exchange in a gaining stream (see equations (9a) through (9c) in **Chapter 4**); (ii) the RTD function for hyporheic exchange in a losing stream; and (iii) the coupled set of equations that relates the streamline starting position, ending position, and residence time (equations (10a) and (10c) in **Chapter 4**).

C.4.1. Derivation of RTD Function for a Gaining Stream

Here we derive from Boano et al.'s solution an analytical expression for the residence time distribution (RTD) of water undergoing hyporheic exchange, assuming that the stream is gaining (equation (9a) through (9c) in **Chapter 4**). We begin by adopting the standard chemical engineering definition of the cumulative distribution function (CDF) form of the RTD ($F_{\mathrm{RTD}}(\tau)$) as the fraction of water volume exiting a chemical reactor with a residence time τ or younger [Levenspiel, 1972; Hill, 1977; Rawlings and Ekerdt, 2013]. In our case, the "chemical reactor" is the IEZ.

As noted earlier, within the upstream or downstream flow cell of the IEZ, every treamline has a unique residence time (τ), starting position ($\overline{x}_0$), and ending position ($\overline{x}_{\mathrm{f}}$) (see **Figure C.6**). For the derivation that follows, it is convenient to express the RTD as a function of the streamline starting position $F_{\mathrm{RTD}}(\overline{x}_0(\tau))$; the functional relationship between $\overline{x}_0$ and τ is derived later.

Accounting for water exchanged through the upstream and downstream flow cells within a single IEZ, the RTD function for a gaining stream ($F_{\mathrm{RTD},g}$) can be calculated by integrating the differential hyporheic exchange flux over the downwelling zone in the upstream and downstream flow cells, normalized by the volume of water per time circulating through the IEZ (equal to $\lambda W q_{\mathrm{H}}$, see **Text C.3** (Section 4) and **Figure C.6**):

$$F_{\mathrm{RTD},g}\left(\tau\right)=\frac{-W\left[\int_{a}^{x_0^{\text{up-cell}}(\tau)} q_{y,g}\left(x,y=0\right)dx-\int_{b}^{x_0^{\text{down-cell}}(\tau)} q_{y,g}\left(x,y=0\right)dx\right]}{\lambda W q_{\mathrm{H}}} \tag{C17a}$$

$$a \le x_0^{\text{up-cell}}\left(\tau\right) \le x_{\mathrm{sep}} \tag{C17b}$$

$$x_{\mathrm{sep}} \le x_0^{\text{down-cell}}\left(\tau\right) \le b \tag{C17c}$$

In this equation $x_0^{\text{up-cell}}\left(\tau\right)$ and $x_0^{\text{down-cell}}\left(\tau\right)$ refer to starting position of streamlines in the upstream and downstream flow cells, respectively, with residence time τ. In the upstream flow cell, the streamline with the longest residence time ($\tau=\tau_{\max}^{\text{up-cell}}$) has a starting position of $x_0^{\text{up-cell}}=x_{\mathrm{sep}}$, while the streamline with the smallest residence time ($\tau=0$) has a starting position of $x_0^{\text{up-cell}}=a$ (see equation (C11) and discussion thereof for calculating x_{sep}). Thus, the streamline starting positions in the upstream flow cell are bounded between a and x_{sep} (see equation (C17b) and **Figure C.6**).

Likewise, in the downstream flow cell, the streamline with the longest residence time ($\tau=\tau_{\max}^{\text{down-cell}}$) has a starting position of $x_0^{\text{down-cell}}=x_{\mathrm{sep}}$, while the streamline with the smallest residence time ($\tau=0$) has a starting position of $x_0^{\text{down-cell}}=b$. Thus, the streamline starting positions in the downstream flow cell are bounded between x_{sep} and b (see equation (C17c)).

Normalizing all variables appearing in equation (C17a) through (C17c) in accordance with our previous convention, we obtain the following result:

$$F_{\mathrm{RTD},g}(\overline{\tau}) = \frac{-\int_{\overline{a}}^{\overline{x}_0^{\text{up-cell}}(\overline{\tau})} \overline{q}_{\mathrm{y},g}(\overline{x},\overline{y}=0)\,d\overline{x} + \int_{\overline{b}}^{\overline{x}_0^{\text{down-cell}}(\overline{\tau})} \overline{q}_{\mathrm{y},g}(\overline{x},\overline{y}=0)\,d\overline{x}}{2\pi\overline{q}_{\mathrm{H}}} \tag{C18a}$$

$$\overline{a} \le \overline{x}_0^{\text{up-cell}}(\overline{\tau}) \le \overline{x}_{\mathrm{sep}} \tag{C18b}$$

$$\overline{x}_{\mathrm{sep}} \le \overline{x}_0^{\text{down-cell}}(\overline{\tau}) \le \overline{b} \tag{C18c}$$

New variables appearing here are normalized forms of the hyporheic exchange flux q_{H} and the residence time τ :

$$\overline{q}_{\mathrm{H}} = \frac{q_{\mathrm{H}}}{\pi q_{\mathrm{H},0}} = \frac{1}{2\pi}\int_{\sin^{-1}|\overline{q}_{\mathrm{V}}|}^{\pi-\sin^{-1}|\overline{q}_{\mathrm{V}}|} \left(\sin\overline{x} - |\overline{q}_{\mathrm{V}}|\right)d\overline{x} = \frac{1}{2\pi}\left[-\pi|\overline{q}_{\mathrm{V}}| + 2\sqrt{1-|\overline{q}_{\mathrm{V}}|^2} + 2|\overline{q}_{\mathrm{V}}|\sin^{-1}|\overline{q}_{\mathrm{V}}|\right] \tag{C19a}$$

$$\overline{\tau} = \frac{2\pi^2 q_{\mathrm{H},0}\tau}{\lambda\theta} \tag{C19b}$$

The variable θ represents the porosity of the sediment bed.

The integrals appearing in equation (C18a) can be solved analytically (see first two rows of **Table C.1**), after substituting the y-component of the velocity field (see equation (C1b)) and the expressions presented earlier for $\overline{a}$ and $\overline{b}$ (equation (C15a) and (C15b)). Combining these results we obtain the following solution for the RTD of water parcels undergoing hyporheic exchange in a gaining stream (equation (9a) through (9c) in **Chapter 4**):

$$F_{\mathrm{RTD},g}(\overline{\tau}) = F_{1,g}(\overline{\tau}) + F_{2,g}(\overline{\tau}) \tag{C20a}$$

$$F_{1,g}(\overline{\tau})=\frac{|\overline{q}_{\mathrm{V}}|\left(\overline{x}_0^{\text{up-cell}}(\overline{\tau})-\sin^{-1}|\overline{q}_{\mathrm{V}}|\right)-\sqrt{1-|\overline{q}_{\mathrm{V}}|^2}+\cos\left[\overline{x}_0^{\text{up-cell}}(\overline{\tau})\right]}{2\left(|\overline{q}_{\mathrm{V}}|\left(\pi/2-\sin^{-1}|\overline{q}_{\mathrm{V}}|\right)-\sqrt{1-|\overline{q}_{\mathrm{V}}|^2}\right)} \tag{C20b}$$

$$F_{2,g}(\overline{\tau})=\frac{|\overline{q}_{\mathrm{V}}|\left(\pi-\overline{x}_0^{\text{down-cell}}(\overline{\tau})-\sin^{-1}|\overline{q}_{\mathrm{V}}|\right)-\sqrt{1-|\overline{q}_{\mathrm{V}}|^2}-\cos\left[\overline{x}_0^{\text{down-cell}}(\overline{\tau})\right]}{2\left(|\overline{q}_{\mathrm{V}}|\left(\pi/2-\sin^{-1}|\overline{q}_{\mathrm{V}}|\right)-\sqrt{1-|\overline{q}_{\mathrm{V}}|^2}\right)} \tag{C20c}$$

C.4.2. Derivation of RTD Function for Losing Stream

The RTD for a losing stream is derived using a similar approach (see last section), with one exception: for the losing case the hyporheic exchange flux is integrated over upwelling zones instead of downwelling zones. Referring to **Figure C.7** and using the same definition of the RTD described in the last section, we obtain the following result:

$$F_{\mathrm{RTD},l}(\tau)=\frac{W\left[\int_{-b}^{x_{\mathrm{f}}^{\text{up-cell}}(\tau)} q_{\mathrm{y},l}(x,y=0)\,dx-\int_{x_{\mathrm{f}}^{\text{down-cell}}(\tau)}^{-a} q_{\mathrm{y},l}(x,y=0)\,dx\right]}{\lambda W q_{\mathrm{H}}} \tag{C21a}$$

$$-b\le x_{\mathrm{f}}^{\text{up-cell}}\le -x_{\mathrm{sep}} \tag{C21b}$$

$$-x_{\mathrm{sep}}\le x_{\mathrm{f}}^{\text{down-cell}}\le -a \tag{C21c}$$

In this equation $x_{\mathrm{f}}^{\text{up-cell}}(\tau)$ and $x_{\mathrm{f}}^{\text{down-cell}}(\tau)$ refer to final (ending) positions of streamlines in the upstream and downstream flow cells, respectively, with residence time τ. In the upstream flow cell, the streamline with the longest residence time ($\tau=\tau_{\max}^{\text{up-cell}}$) has an ending position of $x_{\mathrm{f}}^{\text{up-cell}}(\tau)=x_{\mathrm{sep}}$, while the streamline with the smallest residence time (

$\tau = 0$) has an ending position of $x_{\mathrm{f}}^{\text{up-cell}}(\tau) = -b$. Thus, streamline ending positions in the upstream flow cell are bounded between $-b$ and $-x_{\text{sep}}$ (see equation (C21b)). Likewise, in the downstream flow cell, the streamline with the longest residence time ($\tau = \tau_{\max}^{\text{down-cell}}$) has an ending position of $x_{\mathrm{f}}^{\text{down-cell}}(\tau) = x_{\text{sep}}$, while the streamline with the smallest residence time ($\tau = 0$) has an ending position of $x_{\mathrm{f}}^{\text{down-cell}}(\tau) = -a$. Thus, streamline starting positions in the downstream flow cell are bounded between $-x_{\text{sep}}$ and $-a$ (see equation (C21c)). Normalizing all variables appearing in equation (C21a) in accordance with our previous conventions, the RTD function becomes:

$$F_{\mathrm{RTD},l}(\overline{\tau}) = \frac{\displaystyle\int_{-\overline{b}}^{\overline{x}_{\mathrm{f}}^{\text{up-cell}}(\overline{\tau})} \overline{q}_{\mathrm{y},l}(\overline{x}, \overline{y} = 0)\, d\overline{x} + \int_{\overline{x}_{\mathrm{f}}^{\text{down-cell}}(\overline{\tau})}^{-\overline{a}} \overline{q}_{\mathrm{y},l}(\overline{x}, \overline{y} = 0)\, d\overline{x}}{2\pi \overline{q}_{\mathrm{H}}} \tag{C22a}$$

$$-\overline{b} \le \overline{x}_{\mathrm{f}}^{\text{up-cell}}(\overline{\tau}) \le -\overline{x}_{\text{sep}} \tag{C22b}$$

$$-\overline{x}_{\text{sep}} \le \overline{x}_{\mathrm{f}}^{\text{down-cell}}(\overline{\tau}) \le -\overline{a} \tag{C22c}$$

Solving the integral terms appearing in equation (C22a) (see last two rows of **Table C.1**), we obtain the following solution for the RTD of a losing stream:

Table C.1. Analytical solutions for the integrals appearing in the RTD expressions (see equations (C19a)-(C19c) and (C22a)-(C22c) for gaining (*g*) and losing (*l*) streams, respectively. Variables defined in Notation section of **Chapter 4**).

GW condition / HZ cell	**RTD solution**
Gaining/up-cell	$\frac{-\int_{\bar{a}}^{\bar{x}_0^{\text{up-cell}}(\bar{\tau})} \bar{q}_{\text{y},g}(\bar{x},\bar{y}=0)\,d\bar{x}}{2\pi\bar{q}_{\text{H}}} = \frac{\lvert\bar{q}_{\text{V}}\rvert\left(\bar{x}_0^{\text{up-cell}}(\bar{\tau})-\sin^{-1}\lvert\bar{q}_{\text{V}}\rvert\right)-\sqrt{1-\lvert\bar{q}_{\text{V}}\rvert^2}+\cos\left[\bar{x}_0^{\text{up-cell}}(\bar{\tau})\right]}{2\left(\lvert\bar{q}_{\text{V}}\rvert\left(\pi/2-\sin^{-1}\lvert\bar{q}_{\text{V}}\rvert\right)-\sqrt{1-\lvert\bar{q}_{\text{V}}\rvert^2}\right)}$
Gaining/down-cell	$\frac{\int_{\bar{b}}^{\bar{x}_0^{\text{down-cell}}(\bar{\tau})} \bar{q}_{\text{y},g}(\bar{x},\bar{y}=0)\,d\bar{x}}{2\pi\bar{q}_{\text{H}}} = \frac{\lvert\bar{q}_{\text{V}}\rvert\left(\pi-\bar{x}_0^{\text{down-cell}}(\bar{\tau})-\sin^{-1}\lvert\bar{q}_{\text{V}}\rvert\right)-\sqrt{1-\lvert\bar{q}_{\text{V}}\rvert^2}-\cos\left[\bar{x}_0^{\text{down-cell}}(\bar{\tau})\right]}{2\left(\lvert\bar{q}_{\text{V}}\rvert\left(\pi/2-\sin^{-1}\lvert\bar{q}_{\text{V}}\rvert\right)-\sqrt{1-\lvert\bar{q}_{\text{V}}\rvert^2}\right)}$
Losing/up-cell	$\frac{\int_{-\bar{b}}^{\bar{x}_{\text{f}}^{\text{up-cell}}(\bar{\tau})} \bar{q}_{\text{y},l}(\bar{x},\bar{y}=0)\,d\bar{x}}{2\pi\bar{q}_{\text{H}}} = \frac{\lvert\bar{q}_{\text{V}}\rvert\left(\pi+\bar{x}_{\text{f}}^{\text{up-cell}}(\bar{\tau})-\sin^{-1}\lvert\bar{q}_{\text{V}}\rvert\right)-\sqrt{1-\lvert\bar{q}_{\text{V}}\rvert^2}-\cos\left[\bar{x}_{\text{f}}^{\text{up-cell}}(\bar{\tau})\right]}{2\left(\lvert\bar{q}_{\text{V}}\rvert\left(\pi/2-\sin^{-1}\lvert\bar{q}_{\text{V}}\rvert\right)-\sqrt{1-\lvert\bar{q}_{\text{V}}\rvert^2}\right)}$
Losing/down-cell	$\frac{\int_{\bar{x}_{\text{f}}^{\text{up-cell}}(\bar{\tau})}^{-\bar{a}} \bar{q}_{\text{y},l}(\bar{x},\bar{y}=0)\,d\bar{x}}{2\pi\bar{q}_{\text{H}}} = \frac{-\lvert\bar{q}_{\text{V}}\rvert\left(\bar{x}_{\text{f}}^{\text{down-cell}}(\bar{\tau})+\sin^{-1}\lvert\bar{q}_{\text{V}}\rvert\right)-\sqrt{1-\lvert\bar{q}_{\text{V}}\rvert^2}+\cos\left[\bar{x}_{\text{f}}^{\text{down-cell}}(\bar{\tau})\right]}{2\left(\lvert\bar{q}_{\text{V}}\rvert\left(\pi/2-\sin^{-1}\lvert\bar{q}_{\text{V}}\rvert\right)-\sqrt{1-\lvert\bar{q}_{\text{V}}\rvert^2}\right)}$

$$F_{\text{RTD},l}(\bar{\tau}) = F_{1,l}(\bar{\tau}) + F_{2,l}(\bar{\tau}) \tag{C23a}$$

$$F_{1,l}(\bar{\tau}) = \frac{\lvert\bar{q}_{\text{V}}\rvert\left(\pi+\bar{x}_{\text{f}}^{\text{up-cell}}(\bar{\tau})-\sin^{-1}\lvert\bar{q}_{\text{V}}\rvert\right)-\sqrt{1-\lvert\bar{q}_{\text{V}}\rvert^2}-\cos\left[\bar{x}_{\text{f}}^{\text{up-cell}}(\bar{\tau})\right]}{2\left(\lvert\bar{q}_{\text{V}}\rvert\left(\pi/2-\sin^{-1}\lvert\bar{q}_{\text{V}}\rvert\right)-\sqrt{1-\lvert\bar{q}_{\text{V}}\rvert^2}\right)} \tag{C23b}$$

$$F_{2,l}(\bar{\tau}) = \frac{-\lvert\bar{q}_{\text{V}}\rvert\left(\bar{x}_{\text{f}}^{\text{down-cell}}(\bar{\tau})+\sin^{-1}\lvert\bar{q}_{\text{V}}\rvert\right)-\sqrt{1-\lvert\bar{q}_{\text{V}}\rvert^2}+\cos\left[\bar{x}_{\text{f}}^{\text{down-cell}}(\bar{\tau})\right]}{2\left(\lvert\bar{q}_{\text{V}}\rvert\left(\pi/2-\sin^{-1}\lvert\bar{q}_{\text{V}}\rvert\right)-\sqrt{1-\lvert\bar{q}_{\text{V}}\rvert^2}\right)} \tag{C23c}$$

Comparing our RTD solutions for losing and gaining streams (equations (C23a)-(C23c) and (C20a)-(C20c)) we see that $F_{1,l}(\overline{\tau}) = F_{2,g}(\overline{\tau})$ and $F_{2,l}(\overline{\tau}) = F_{1,g}(\overline{\tau})$ when $\overline{x}_{\mathrm{f}}^{\text{down-cell}}$ and $\overline{x}_{\mathrm{f}}^{\text{up-cell}}$ are substituted for $-\overline{x}_0^{\text{up-cell}}$ and $-\overline{x}_0^{\text{down-cell}}$, respectively. These last replacement rules are consistent with the symmetry of gaining and losing streamlines described earlier (see **Text C.3** and **Figure C.5**). In words, the RTD is unchanged when the sign of the ambient vertical groundwater flux is changed, from gaining to losing or vice versa.

C.4.3. Streamline Starting and Ending Positions

The RTD functions derived in the last section were expressed in terms of either the starting ($\overline{x}_0(\overline{\tau})$) or ending ($\overline{x}_{\mathrm{f}}(\overline{\tau})$) position of a streamline with residence time $\overline{\tau}$. The mathematical relationship between $\overline{x}_0$ and $\overline{x}_{\mathrm{f}}$ can be easily obtained from equation (C8) by setting $\overline{y} = 0$ and $\overline{x} = \overline{x}_{\mathrm{f}}$:

$$\cos \overline{x}_{\mathrm{f}} + |\overline{q}_{\mathrm{V}}| \overline{x}_{\mathrm{f}} = \cos \overline{x}_0 + |\overline{q}_{\mathrm{V}}| \overline{x}_0 \qquad \text{(C24)}$$

This relationship was derived from the streamline equation for a gaining stream, but it also applies for a losing stream, as can be shown by reflecting the solution around the $\overline{y}$-axis (by letting $x_{\mathrm{f}} \to -x_0$ and $x_0 \to -x_{\mathrm{f}}$) and reversing the sign of the vertical component of the groundwater flux (i.e., replacing $|q_{\mathrm{V}}| \to -|q_{\mathrm{V}}|$).

C.4.4. Streamline Residence Time

As noted in the text, to find the value of τ corresponding to any starting position (x_0) in either the upstream or downstream flow cell we can solve the parametric equations for the position of the water parcel as it travels through the hyporheic zone:

$$\frac{dx}{d\tau}=q_{\mathrm{x}}(x,y)/\theta \tag{C25a}$$

$$\frac{dy}{d\tau}=q_{\mathrm{y}}(x,y)/\theta \tag{C25b}$$

$$x(0)=x_0\ ,\ y(0)=0 \tag{C25c}$$

The right hand side of equations (25a) and (25b) has been divided by sediment porosity (θ) to convert Darcy fluxes into pore-scale velocities. Substituting Boano et al.'s solutions for q_{x} and q_{x} into equations (25a) and (25b) and rearranging we obtain equations (10a)-(10c) in **Chapter 4**:

$$\bar{x}'(\bar{\tau})=-\cos\bar{x}(\bar{\tau})e^{\bar{y}(\bar{\tau})}+\bar{q}_{\mathrm{U}} \tag{C26a}$$

$$\bar{y}'(\bar{\tau})=-\sin\bar{x}(\bar{\tau})e^{\bar{y}(\bar{\tau})}+\bar{q}_{\mathrm{V}} \tag{C26b}$$

$$\bar{x}(0)=\bar{x}_0\ ,\ \bar{y}(0)=0 \tag{C25c}$$

Here the normalized variables are $\bar{x}=2\pi x/\lambda$, $\bar{y}=2\pi y/\lambda$, $\bar{\tau}=2\pi^2 q_{\mathrm{H},0}\tau/(\lambda\theta)$, $\bar{q}_{\mathrm{U}}=q_{\mathrm{U}}/(\pi q_{\mathrm{H},0})$, and $\bar{q}_{\mathrm{V}}=q_{\mathrm{V}}/(\pi q_{\mathrm{H},0})$. As noted in **Chapter 4**, the normalized residence time $\bar{\tau}$ corresponding to any choice of $\bar{x}_0$, $\bar{q}_{\mathrm{U}}$, and $\bar{q}_{\mathrm{V}}$ can be found by solving equations (C26a) and (C26b) numerically, and then recording the time the solution crosses the sediment-water interface at $\bar{y}=0$.

Text C.5. Numerical Implementation of the Analytical RTD Solution.

Given the above results, the hyporheic zone RTD can be calculated for arbitrary choice of ambient groundwater flow (i.e., values of $\bar{q}_{\mathrm{U}}$ and $\bar{q}_{\mathrm{V}}$) as follows.

Step 1: Calculate the location where the separation streamline intersects the sediment-water interface ($\bar{x}_{\mathrm{sep}}$, see **Figure C.6**). This can be accomplished by numerically solving the following equation, which was obtained by combining equations (C11) and (C12a,b):

$$\begin{aligned}&\cos\left[\tan^{-1}\left(\bar{q}_{\mathrm{V}}/\bar{q}_{\mathrm{U}}\right)\right]\sqrt{\bar{q}_{\mathrm{U}}{}^{2}+\bar{q}_{\mathrm{V}}{}^{2}}\\&+\bar{q}_{\mathrm{V}}\tan^{-1}\left(\bar{q}_{\mathrm{V}}/\bar{q}_{\mathrm{U}}\right)-\bar{q}_{\mathrm{U}}\ln\left(\sqrt{\bar{q}_{\mathrm{U}}{}^{2}+\bar{q}_{\mathrm{V}}{}^{2}}\right)=\cos\bar{x}_{\mathrm{sep}}+\bar{q}_{\mathrm{V}}\bar{x}_{\mathrm{sep}}\end{aligned} \tag{C26}$$

Given a choice of $\bar{q}_{\mathrm{U}}$ and $\bar{q}_{\mathrm{V}}$, equation (C26) can be solved numerically to yield $\bar{x}_{\mathrm{sep}}$. We did this by using the "FindRoot" function in Mathematica, given the starting point:

$$\bar{x}_{\mathrm{sep},0}=\frac{\bar{a}+\bar{b}}{2}=\frac{\pi}{2} \tag{C27}$$

The second equal sign in equation (C27) follows from substitution of equations (C15a) and (C15b) for $\bar{a}$ and $\bar{b}$, respectively.

Step 2. Compute the fraction of the hyporheic exchange flux that circulates through the upstream flow cell ($f_{\mathrm{RTD}}^{\mathrm{Up}}$) and downstream flow cell ($f_{\mathrm{RTD}}^{\mathrm{Dn}}$); note that $f_{\mathrm{RTD}}^{\mathrm{Up}}+f_{\mathrm{RTD}}^{\mathrm{Dn}}=1$.

Referring to **Figure C.6**, these can be calculated from (C28a) and (C28b) where F_1 and F_2 are our solutions for the RTD CDF presented in **Chapter 4** (equations (9b) and (9c)):

$$f_{\mathrm{RTD}}^{\mathrm{Up}} = F_1\left(\overline{x}_0^{\text{up-cell}} = \overline{x}_{\mathrm{sep}}\right) \tag{C28a}$$

$$f_{\mathrm{RTD}}^{\mathrm{Dn}} = F_2\left(\overline{x}_0^{\text{down-cell}} = \overline{x}_{\mathrm{sep}}\right) \tag{C28b}$$

<u>Step 3</u>. Prepare a probability distribution for the RTD of the upstream cell:

(a) Draw a random number between 0 and 1 ($\chi \in [0,1]$);

(b) Find a corresponding starting position in the upstream flow cell $\overline{x}_0^{\text{up-cell}} \in \left[\overline{a}, \overline{x}_{\mathrm{sep}}\right]$ by numerically solving the following equation: $\chi f_{\mathrm{RTD}}^{\mathrm{Up}} = F_1\left(\overline{x}_0^{\text{up-cell}}\right)$. For this step we used the "FindRoot" function in Mathematica with a starting value of $\overline{x}_0^{\text{up-cell}} = \left(\overline{a} + \overline{x}_{\mathrm{sep}}\right)/2$.

(c) Calculate the corresponding normalized residence time by solving equations (26a) and (26b) for $\overline{x}(0) = \overline{x}_0^{\text{up-cell}}$ and recording the dimensionless time $\overline{\tau}$ the solution crosses the sediment-water interface at $\overline{y} = 0$.

(d) Repeat steps (a) through (c) N=10,000 times, and prepare from these realizations an empirical CDF for residence times in the upstream cell, $F_{\mathrm{RTD}}^{\mathrm{Up}}(\overline{\tau})$. We constructed the empirical CDF using the Mathematica command "SmoothKernelDistribution". By defining the RTD as a probability distribution (and not just an interpolating function) we could rest assured that the RTD is appropriately bounded for all choices of the residence time $\overline{\tau}$; namely,

$0 \le F_{\mathrm{RTD}}^{\mathrm{Up}}(\bar{\tau}) \le 1$. This last point becomes critically important when solving for the nitrate uptake velocity using the integral expression in equation (1b) (see main text).

<u>Step 4</u>. Repeat Step 3 for the downstream cell:

(e) Draw a random number between 0 and 1 ($\chi \in [0,1]$);

(f) Find a corresponding starting position $\bar{x}_0^{\text{down-cell}} \in \left[\bar{x}_{\text{sep}}, \bar{b}\right]$ by numerically solving the following equation: $\chi f_{\mathrm{RTD}}^{\mathrm{Dn}} = F_2\left(\bar{x}_0^{\text{down-cell}}\right)$. Here we also used the "FindRoot" function in Mathematica with a starting value of $\bar{x}_0^{\text{down-cell}} = \left(\bar{b} + \bar{x}_{\text{sep}}\right)/2$.

(g) Calculate the corresponding residence time by solving equations (26a) and (26b) for $\bar{x}(0) = \bar{x}_0^{\text{down-cell}}$ and recording the dimensionless time $\bar{\tau}$ the solution crosses the sediment-water interface at $\bar{y} = 0$.

(h) Repeat steps (a) through (c) N=10,000 times, and prepare from these realizations an empirical CDF for residence times in the downstream cell using the Mathematica function "SmoothKernelDistribution" described above. The net result is a CDF for the downstream RTD, $F_{\mathrm{RTD}}^{\mathrm{Dn}}(\bar{\tau})$.

<u>Step 5</u>. Prepare a final CDF for hyporheic zone RTD that accounts for circulation in both the upstream and downstream cells:

$$F_{RTD}(\bar{\tau}) = f_{\mathrm{RTD}}^{\mathrm{Up}} F_{\mathrm{RTD}}^{\mathrm{Up}}(\bar{\tau}) + f_{\mathrm{RTD}}^{\mathrm{Dn}} F_{\mathrm{RTD}}^{\mathrm{Dn}}(\bar{\tau}) \tag{C28}$$

By differentiating equation (C28), the corresponding PDF can be substituted directly into the integral expression in equation (1b) to calculate the nitrate uptake velocity, or used to calculate $E(\log_{10} \tau)$ as outlined in **Chapter 4**.

The Mathematica script for carrying out these five steps is presented in **Code C.2**; the corresponding script for calculating all three forms of the nitrate uptake velocity is presented in **Code C.3**.

Text C.6. Comparing the Analytical RTD Solution to Numerical Solutions and Particle Tracking Experiments

As a test of the RTD solution described above, we compared it with RTDs generated by a numerical solution to the streamfunction equation (equation (C3a)) and also with previously published particle-tracking results [Boano et al., 2009]. For this comparison we adopted the conditions utilized in Boano et al.'s particle tracking study of $\overline{q}_{\mathrm{U}} = 0.1$ and $\overline{q}_{\mathrm{V}} = 0.3$.

Numerically solving the stream function involved the following steps:

<u>Step 1.</u> Divide the upwelling flow in the upstream and downstream flow cells into equal increments of flow, as represented by a fixed change in the streamline function, $\Delta \overline{\psi}$ where $\overline{\psi} = 2\psi / \lambda q_{\mathrm{H},0}$. Recall that the flow between any two streamlines (per unit width of stream) is equal to the difference in the value of the streamfunction corresponding to the two streamlines. The increment of flow $\Delta\bar{\psi}$ was determined by dividing the total hyporheic exchange flow $\left(\bar{\psi}_{\bar{a}} - \bar{\psi}_{\bar{b}}\right)$ into N equal fractions: $\Delta\bar{\psi} = \left(\bar{\psi}_a - \bar{\psi}_b\right)/N$.

Step 2. The dimensionless travel time $\bar{\tau}$ for each streamline was calculated by numerically integrating the travel time along the streamline between the point at which the streamline enters the IEZ ($\bar{y} = 0$) until it exits again at sediment-water interface. By initiating streamlines at uniform increments of $\Delta\bar{\psi}$ between $\bar{x}_{\mathrm{iez,up}}$ and $\bar{a}$ and between $\bar{x}_{\mathrm{iez,dn}}$ and $\bar{b}$, each streamline represents an equal fraction of the total flow through the IEZ, equal to $\Delta\bar{\psi}/\left(\bar{\psi}_{\bar{a}} - \bar{\psi}_{\bar{b}}\right)$. Note that we used the same value of $\Delta\bar{\psi}$ for both the upstream and downstream flow cells. The first streamline began at $\bar{\psi}_{\mathrm{SP}} \pm \Delta\bar{\psi}/2$ (where the sign is positive for upstream and negative for downstream).

In **Figure C.8A** we present RTD as plots of $E\left(\log_{10}\tau\right)$ versus $\log_{10}\tau$, as recommended in the text (see Section 5 in **Chapter 4**). The same set of results are plotted as $E(\tau)$ versus $\log_{10}\tau$ (a more conventional, but not recommended, presentation) in **Figure C.8B**. In these plots we compare results obtained from our analytical solution (solid green curve), the numerical solution of the streamfunction (dashed green curve), and Boano et al.'s particle tracking results (dashed red curve). We also show for the first two solutions the fraction of the PDF associated with circulation through the upstream cell (blue curves) and downstream cell (yellow curves).

The RTD estimated from our analytical solution agrees closely with the RTD estimated from the numerical solution of the streamfunction. Apparent differences between these two solution approaches are a sampling artifact associated with the preparation of the two empirical distributions (using Mathematica's "SmoothKernelDistribution" command) from which the respective PDFs were constructed. Indeed, CDFs generated from the two approaches align precisely (results not shown). Interestingly, for Boano et al.'s particle tracking results, it appears that the PDF is truncated prematurely at long residence times, perhaps due to the finite number of particles used in their simulation. Overall, these results affirm that both approaches trialed here—the analytical solution and integration of the streamfunction—are equally valid ways of estimating residence times associated with Boano et al.'s solution for hyporheic exchange in the presence of ambient groundwater.

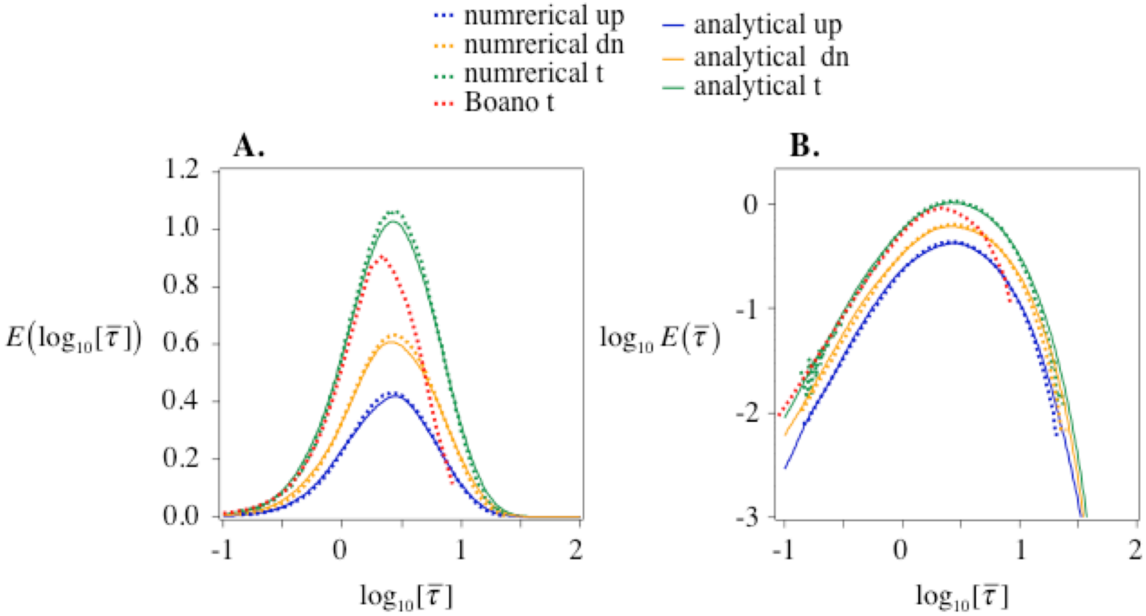

Figure C.8. Comparison of RTDs estimated from our analytical and numerical solutions, together with previously published particle tracking results [Boano et al., 2009]. Curves correspond to calculations for: (1) the upstream cell ("analytical up" and "numerical up", blue solid and dashed curves, respectively); (2) downstream cell ("analytical up" and "numerical up", orange solid and dashed curves, respectively); and (3) overall RTD ("analytical up" and "numerical up", green solid and dashed curves, respectively). Boano et al.'s particle tracking results are shown as a red dashed curve. The two panels correspond to different plotting formats (see Section 5 of **Chapter 4** for a detailed discussion of graphical representation of RTDs).

Table C.2. Uptake velocity of Ripples (variables defined in Notation section of **Chapter 4**).

	H-Q								
q_{V} (m/s)	+/- 23.1E-06			+/- 5.8E-06			0		
q_{H} (m/s)	6.03E-05			6.86E-05			7.14E-05		
τ_{T} (s)[1]	31.9			31.9			31.9		
	v_{f} (m/s)								
	up	down	total	up	down	total	up	down	total
KSL	1.65E-07	7.28E-08	9.24E-08	2.88E-07	1.21E-07	1.67E-07	4.30E-07	1.75E-07	2.55E-07
PRM	6.98E-06	3.05E-06	3.93E-06	1.10E-05	4.55E-06	6.50E-06	1.35E-05	5.23E-06	8.24E-06
NCC	8.91E-07	3.92E-07	4.99E-07	2.43E-06	1.01E-06	1.42E-06	5.79E-06	2.23E-06	3.56E-06
	$v_{f\,Dw}$ (m/s)								
	up	down	total	up	down	total	up	down	total
KSL	-1.56E-09	-6.34E-10	-9.24E-10	-2.71E-09	-8.89E-10	-1.82E-09	-4.05E-09	-8.82E-10	-3.17E-09
PRM	-2.47E-08	-9.96E-09	-1.47E-08	-5.27E-08	-1.57E-08	-3.69E-08	-1.96E-07	-1.58E-08	-1.80E-07
NCC	-1.75E-08	-7.11E-09	-1.04E-08	-3.08E-08	-1.01E-08	-2.08E-08	-4.82E-08	-9.98E-09	-3.82E-08
	$v_{f\,Dn}$ (m/s)								
	up	down	total	up	down	total	up	down	total
KSL	-5.43E-12	-2.01E-12	-3.42E-12	-1.86E-11	-4.75E-12	-1.64E-11	-6.28E-11	-4.73E-12	-6.98E-11
PRM	-3.92E-09	-1.42E-09	-2.50E-09	-2.01E-08	-4.86E-09	-1.81E-08	-1.63E-07	-5.10E-09	-1.88E-07
NCC	-3.89E-10	-1.35E-10	-2.53E-10	-2.68E-09	-7.49E-10	-2.31E-09	-1.98E-08	-7.69E-10	-2.27E-08
	L-Q								
q_{V} (m/s)	+/- 23.1E-06			+/- 5.8E-06			0		
q_{H} (m/s)	1.78E-05			2.56E-05			2.84E-05		
τ_{T} (s)	80.3			80.3			80.3		
	v_{f} (m/s)								
	up	down	total	up	down	total	up	down	total
KSL	8.08E-08	3.09E-08	5.00E-08	1.97E-07	6.86E-08	1.29E-07	3.42E-07	1.09E-07	2.33E-07
PRM	3.33E-06	1.26E-06	2.07E-06	7.17E-06	2.39E-06	4.77E-06	9.63E-06	2.85E-06	6.78E-06
NCC	4.97E-07	1.89E-07	3.08E-07	1.98E-06	6.71E-07	1.31E-06	5.41E-06	1.54E-06	3.87E-06
	$v_{f\,Dw}$ (m/s)								
	up	down	total	up	down	total	up	down	total
KSL	-7.62E-10	-2.74E-10	-4.88E-10	-1.86E-09	-4.93E-10	-1.36E-09	-3.22E-09	-5.27E-10	-2.70E-09
PRM	-1.28E-08	-4.91E-09	-7.86E-09	-3.92E-08	-9.63E-09	-2.96E-08	-1.87E-07	-1.07E-08	-1.76E-07
NCC	-9.01E-09	-3.51E-09	-5.50E-09	-2.18E-08	-6.17E-09	-1.57E-08	-3.96E-08	-6.57E-09	-3.30E-08
	$v_{f\,Dn}$ (m/s)								
	up	down	total	up	down	total	up	down	total
KSL	-4.08E-12	-1.87E-12	-2.21E-12	-1.94E-11	-4.43E-12	-1.50E-11	-7.41E-11	-5.00E-12	-6.91E-11
PRM	-3.12E-09	-1.53E-09	-1.59E-09	-2.10E-08	-4.19E-09	-1.68E-08	-1.97E-07	-5.08E-09	-1.92E-07
NCC	-3.56E-09	-3.39E-09	-1.67E-10	-6.93E-09	-4.73E-09	-2.19E-09	-2.86E-08	-4.94E-09	-2.36E-08

---

[1] The variable τ_{T} (units s) represents the characteristic transport timescale for hyporheic exchange. For fluvial ripples, we set τ_{T} equal to the characteristic transport timescale described earlier for Boano et al.'s advective pumping model (see equation (7d) in **Chapter 4**).

Table C.3. Uptake velocity of Riffle-Pools (variables defined in Notation section of **Chapter 4**).

	H-Q				
q_V (m/s)	- 23.1E-06	- 5.8E-06	0	+5.8E-06	+ 23.1E-06
q_H (m/s)	5.41E-06	1.03E-05	1.32E-05	1.15E-05	7.18E-06
τ_T (s)[1]	5505.6	6514.8	7919.6	7345.2	6357.7
	v_f (m/s)				
KSL	4.87E-07	1.14E-06	1.84E-06	1.43E-06	7.32E-07
PRM	5.19E-06	8.18E-06	7.52E-06	7.86E-06	6.18E-06
NCC	1.35E-05	3.29E-05	5.18E-05	4.24E-05	2.13E-05
	$v_{f\,Dw}$ (m/s)				
KSL	-4.58E-09	-1.08E-08	-1.76E-08	-1.35E-08	-6.89E-09
PRM	-7.34E-07	-2.18E-06	-4.06E-06	-3.00E-06	-1.30E-06
NCC	-5.99E-08	-1.84E-07	-4.82E-07	-2.25E-07	-9.12E-08
	$v_{f\,Dn}$ (m/s)				
KSL	-2.32E-10	-7.13E-10	-1.51E-09	-9.78E-10	-3.80E-10
PRM	-9.04E-07	-2.72E-06	-5.10E-06	-3.75E-06	-1.62E-06
NCC	-8.08E-08	-5.47E-07	-2.32E-06	-6.69E-07	-1.37E-07
	L-Q				
q_V (m/s)	- 23.1E-06	- 5.8E-06	0	+ 5.8E-06	+ 23.1E-06
q_H (m/s)	3.04E-06	6.72E-06	9.48E-06	7.29E-06	2.66E-06
τ_T (s)	5504.3	7202.8	10115.8	8578.3	7074.6
	v_f (m/s)				
KSL	2.72E-07	8.12E-07	1.60E-06	1.01E-06	2.94E-07
PRM	2.89E-06	4.68E-06	3.20E-06	3.98E-06	2.06E-06
NCC	7.56E-06	2.44E-05	4.65E-05	3.13E-05	8.81E-06
	$v_{f\,Dw}$ (m/s)				
KSL	-2.56E-09	-7.69E-09	-1.54E-08	-9.54E-09	-2.77E-09
PRM	-4.16E-07	-1.70E-06	-3.90E-06	-2.33E-06	-5.86E-07
NCC	-3.35E-08	-1.16E-07	-3.74E-07	-1.41E-07	-3.67E-08
	$v_{f\,Dn}$ (m/s)				
KSL	-1.30E-10	-5.27E-10	-1.50E-09	-7.16E-10	-1.57E-10
PRM	-5.13E-07	-2.13E-06	-4.91E-06	-2.93E-06	-7.31E-07
NCC	-4.53E-08	-2.82E-07	-1.75E-06	-3.48E-07	-5.58E-08

[1] The variable τ_T (units s) represents the characteristic transport timescale for hyporheic exchange. For riffle-pool sequences, we first fit Trauth et al.'s RTDs (obtained from particle tracking experiments) to a lognormal distribution, and equated τ_T to the geometric means thus obtained.

References

Bird, R. B., W. E. Stewart, and E. W. Lightfoot (2007), Transport Phenomena, John Wiley, New York.

Boano, F., R. Revelli, and L. Ridolfi (2009), Quantifying the impact of groundwater discharge on the surface-subsurface exchange, Hydrol. Processes, 23, 2108–2116.

Hill, C. G. (1977), An Introduction to Chemical Engineering Kinetics and Reactor Design, chap. 11, John Wiley, New York.

Levenspiel, O. (1972), Chemical Reaction Engineering, John Wiley, New York.

Peres-Neto, P. R., D. A. Jackson, K. M. Somers (2005), How many principal components? Stopping rules for determining the number of non- trivial axes revisited, Comput. Stat. Data Anal. 49, 974–997.

Rawlings, J. B., and J. G. Ekerdt (2013), Chemical Reactor Analysis and Design Fundamentals, chap. 8, Nob Hill Publ., Madison, Wis.

Computing Chemistry Solution

Calculation involves 4 steps.

Step 1: Assign parameter values (user must specify values for the following parameters)

(a) In-stream concentrations of oxygen (cO20), nitrate (cNO30) and ammonium (CNH40) (all units of mol m^-3).

(b) Saturation constant for the inhibition of denitrification by oxygen concentration: kO2Inh, units of mol m^-3

(c) Saturation constant for the dependence of aerobic respiration on oxygen concentration: kO2Sat, units of mol m^-3

(d) Saturation constant for the dependence of denitrification on nitrate concentration: kNO3Sat, units of mol m^-3

(e) Second-order nitrification rate constant: kNI, units of m^3 mol^-1 s^-1

(f) Carbon mineralization rate: rmin, units of mol m^-3 s^-1

(g) Stoichiometric relationship between aerobic respiration and denitrification (kappa, unitless).

(h) Ammonification rate expressed as a fraction of organic carbon mineralization (gcn, unitless).

Parameter values for KSL scenario:

```
Clear[cO20]; cO20 = 2.60 * 10^-1;
Clear[cNH40]; cNH40 = 1.71 * 10^-3;
Clear[cNO30];  cNO30 = 1.2 * 10^-2;
Clear[kO2Inh]; kO2Inh = 3 * 10^-3;
Clear[kNO3Sat]; kNO3Sat = 9 * 10^-2;
Clear[kO2Sat];  kO2Sat = 6 * 10^-3;
Clear[kNI];  kNI = 4 × 10^-4;
Clear[rmin]; rmin = 3.26 * 10^-6;
Clear[kappa];  kappa = 0.38;
Clear[gcn]; gcn = 14;
```

Step 2: Calculate parameters derived from the above parameter values

(a) Respiration time scale (taur, units s).

(b) Relative rates of nitrification and aerobic respiration (delta, unitless).
(c) Normalized denitrification saturation constant (kNO3SatHat, unitless).
(d) Normalized aerobic saturation constant (kO2SatHat, unitless).
(e) Normalized denitrification inhibition saturation constant (kO2InhHat, unitless).
(f) Relative in-stream concentrations of ammonium and oxygen (alpha, unitless).
(g) Relative in-stream concentrations of nitrate and oxygen (beta, unitless).

```
Clear[tr]; tr = kO2Sat / rmin
Clear[delta]; delta = tr kNI cO20
Clear[kO2SatHat]; kO2SatHat = kO2Sat / cO20
Clear[kNO3SatHat]; kNO3SatHat = kNO3Sat / cO20
Clear[kO2InhHat]; kO2InhHat = kO2Inh / cO20
Clear[alpha]; alpha = cNH40 / cO20
Clear[beta]; beta = cNO30 / cO20
```

```
1840.49

0.191411

0.0230769

0.346154

0.0115385

0.00657692

0.0461538
```

Step 3: Solve the mass balance equations

The following equations are expressions of mass balance for the concentrations of oxygen (cO2), stream ammonium (cNH4st), sediment ammonium (cNH4sed), stream nitrate (cNO3st), new nitrate from stream ammonium (cNO3stN), new nitrate from sediment ammonium (cNO3sedN), nitrogen gas denitrified from all stream nitrate (cN2st), nitrogen gas denitrified from new nitrate from stream ammonium (cN2stN), and nitrogen gas denitrified from new nitrate from sediment ammonium (cN2sedN); all normalized by in-stream oxygen concentration as a function of non-dimensional travel time (taur=tau/tr) through the hyporheic zone. Note that the starting time is assumed to be taur=10^-10, while the integral stops integrating when the nitrate concentration falls below 10^-5 of the in-stream nitrate concentration; the time at which this threshold is reached is called “end”, a parameter that is used later to set the upper limits for both plots and the integration of vf.

```
Clear[kO2Satvar, kNO3Satvar, kO2Inhvar, deltavar,
  alphavar, betavar, gcnvar, kappavar, cO2, cNH4st, cNH4sed,
  cNO3st, cNO3stN, cNO3sedN, cN2st, cN2stN, cN2sedN, soln, end];
soln[kO2Satvar_, kNO3Satvar_, kO2Inhvar_, deltavar_,
   alphavar_, betavar_, gcnvar_, kappavar_] :=
  NDSolve[{(1 / 2.303) cO2'[u] == (10^u) (-cO2[u] / (cO2[u] / kO2Satvar + 1) -
        2 deltavar cO2[u] (cNH4st[u] + cNH4sed[u])), cO2[-10] == 1,
    (1 / 2.303) cNH4sed'[u] == (10^u) (kO2Satvar / gcnvar - deltavar cO2[u] cNH4sed[u]),
    cNH4sed[-10] == 0, (1 / 2.303) cNH4st'[u] == (10^u) (-deltavar cO2[u] cNH4st[u]),
    cNH4st[-10] == alphavar,
    (1 / 2.303) cNO3st'[u] == (10^u) (-kappavar kO2Satvar kO2Inhvar cNO3st[u] /
         ((cO2[u] + kO2Inhvar) (cNO3st[u] + cNO3stN[u] + cNO3sedN[u] + kNO3Satvar))),
    cNO3st[-10] == betavar, (1 / 2.303) cNO3stN'[u] == (10^u)
      (deltavar cO2[u] cNH4st[u] - kappavar kO2Satvar kO2Inhvar cNO3stN[u] /
          ((cO2[u] + kO2Inhvar) (cNO3st[u] + cNO3stN[u] + cNO3sedN[u] + kNO3Satvar))),
    cNO3stN[-10] == 0, (1 / 2.303) cNO3sedN'[u] == (10^u)
      (deltavar cO2[u] cNH4sed[u] - kappavar kO2Satvar kO2Inhvar cNO3sedN[u] /
          ((cO2[u] + kO2Inhvar) (cNO3st[u] + cNO3stN[u] + cNO3sedN[u] + kNO3Satvar))),
    cNO3sedN[-10] == 0, (1 / 2.303) cN2sedN'[u] == (10^u)
      ((1 / 2) kappavar kO2Satvar kO2Inhvar cNO3sedN[u] /
         ((cO2[u] + kO2Inhvar) (cNO3st[u] + cNO3stN[u] + cNO3sedN[u] + kNO3Satvar))),
    cN2sedN[-10] == 0, (1 / 2.303) cN2stN'[u] == (10^u)
      ((1 / 2) kappavar kO2Satvar kO2Inhvar cNO3stN[u] / ((cO2[u] + kO2Inhvar)
           (cNO3st[u] + cNO3stN[u] + cNO3sedN[u] + kNO3Satvar))), cN2stN[-10] == 0,
    (1 / 2.303) cN2st'[u] == (10^u) ((1 / 2) kappavar kO2Satvar kO2Inhvar cNO3st[u] /
         ((cO2[u] + kO2Inhvar) (cNO3st[u] + cNO3stN[u] + cNO3sedN[u] + kNO3Satvar))),
    cN2st[-10] == 0, WhenEvent[cO2[u] < 10^-5, cO2[u] → 0],
    WhenEvent[(cNO3st[u] + cNO3stN[u] + cNO3sedN[u]) / beta < 10^-5,
     {end = u, "StopIntegration"}]},
   {cO2, cNH4sed, cNH4st, cNO3st, cNO3stN, cNO3sedN, cN2sedN, cN2stN, cN2st},
   {u, -10, 10}];
```

Step 4: Plot the concentrations versus non-dimensional (tau/tr) and real (tau, s) travel time through the hyporheic zone.

```
Clear[sn];
sn = soln[kO2SatHat, kNO3SatHat, kO2InhHat, delta, alpha, beta, gcn, kappa];
LogPlot[{cO2[u] /. sn, (cNH4st[u] + cNH4sed[u]) / alpha /. sn, (cNO3st[u] + cNO3stN[u] +
       cNO3sedN[u]) / beta /. sn}, {u, -3, First[end /. sn]}, PlotRange → {.00001, 10},
 AxesLabel → {"log10(tau/tr)", "C_HZ/C_Stream"}, PlotStyle → {Blue, Orange, Green},
 PlotLabels → Placed[{"oxygen", "ammonium", "nitrate"}, {Scaled[1], Before}]]
```

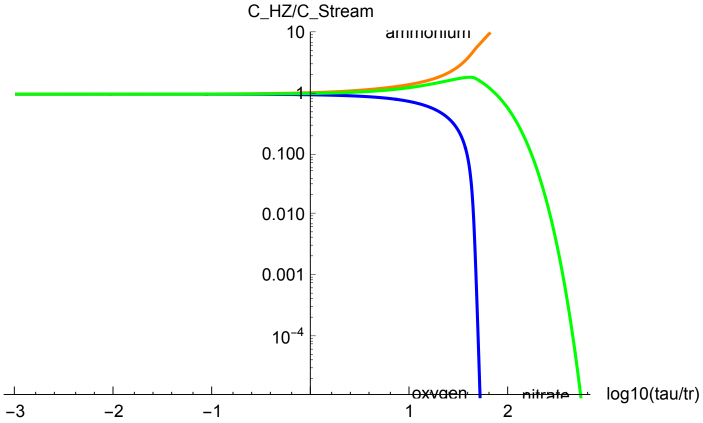

```
LogPlot[{cO2[x - Log10[tr]] /. sn,
   (cNH4st[x - Log10[tr]] + cNH4sed[x - Log10[tr]]) / alpha /. sn,
   (cNO3st[x - Log10[tr]] + cNO3stN[x - Log10[tr]] + cNO3sedN[x - Log10[tr]]) / beta /.
    sn}, {x, Log10[tr / 1000], Log10[ tr 10 ^ (First[(end /. sn)])]},
 PlotRange → {.01, 10}, AxesLabel → {"log10(tau,s)", "C_HZ/C_Stream"},
 PlotStyle → {Blue, Orange, Green},
 PlotLabels → Placed[{"oxygen", "ammonium", "nitrate"}, {Scaled[1], Before}]]
```

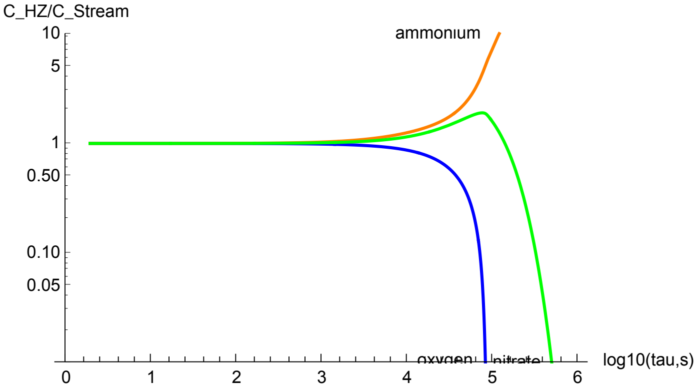

Computing RTDs from the Analytical Solution for Ripples

Calculation involves four steps.

Step 1: Parameter definition (user must specify values for the following three parameters)

qubar= the normalized horizontal groundwater Darcy flux (see description in Section 5.2.1 of the main text)

qvbar = the normalized vertical groundwater Darcy flux (see description in Section 5.2.1 of the main text)

tT= characteristic travel time in ripples (see description in Section 5.2.1 of the main text)

```
Clear[qubar]; qubar = 4.46 * 10^-2;
Clear[qvbar]; qvbar = 1.03 * 10^-1;
Clear[tT]; tT = 31.9;
```

Step 2: Define variables and functions

*F1 and F2 are the CDFs for the upstream and downstream flow cells.

*end (returned by the function “endtime”) is the normalized travel time along a streamline through the hyporheic zone with a particular starting position x0val along the sediment-water interface (see description in Section 5.2.1 of the main text).

*frtdupmax and frtddnmax are the maximum fractions of the hyporheic flux circulating through the upstream and downstream flow cells, respectively (note that these fractions should add to unity).

*xbarsep (returned by the function “xbarsepfunc”) is the normalized x - coordinate where the streamline separating the upstream and downstream flow cells intersects the sediment-water interface.

*abar is the normalized x - coordinate separating upwelling and downwelling regions in the upstream flow cell

*bbar is the normalized x - coordinate separating upwelling and downwelling

regions in the downstream flow cell
*f1func returns the fraction of the hyporheic exchange flux flowing through the upstream flow cell that has starting streamlines between x0bar and abar.
*f2func returns the fraction of the hyporheic exchange flux flowing through the downstream flow cell that has starting streamlines between x0bar and bbar.
*x0valup is the normalized x - coordinate at the sediment-water interface returned by x0valuesup, denoting the streamline starting position associated with a given value of F1
*x0valdn is the normalized x - coordinate at the sediment-water interface returned by x0valuesdn, denoting the streamline starting position associated with a given value of F2

```
(*compute the x-coordinate where the separation
  streamline intersects the sediment-water interface*)
Clear[xbarsepfunc];
xbarsepfunc := FindRoot[Cos[xbarsep] + qvbar xbarsep ==
    Cos[ArcTan[qvbar / qubar]] Sqrt[qubar ^ 2 + qvbar ^ 2] + qvbar ArcTan[qvbar / qubar] -
     qubar Log[Sqrt[qubar ^ 2 + qvbar ^ 2]], {xbarsep, Pi / 2}]
(*compute the x-coordinate separating upwelling and
  downwelling zones in the upstream flow cell*)
Clear[abar]; abar = ArcSin[qvbar];
(*compute the x-coordinate separating upwelling
  and downwelling zones in the downstream flow cell*)
Clear[bbar]; bbar = Pi - ArcSin[qvbar];
(*compute the fraction of flow circulating through the upstream flow
 cell downwelling between abar and x0bar; this is equal to F1(xobar)*)
Clear[f1func];
f1func[x0bar_] :=
 (Abs[qvbar] (x0bar - ArcSin[Abs[qvbar]]) - Sqrt[1 - Abs[qvbar] ^ 2] + Cos[x0bar]) /
  (2 (Abs[qvbar] (Pi / 2 - ArcSin[Abs[qvbar]]) - Sqrt[1 - Abs[qvbar] ^ 2]));
(*compute the fraction of flow circulating through the downstream flow
 cell downwelling between x0bar and bbar; this is equal to F2(xobar)*)
Clear[f2func];
f2func[x0bar_] :=
 (Abs[qvbar] (Pi - x0bar - ArcSin[Abs[qvbar]]) - Sqrt[1 - Abs[qvbar] ^ 2] - Cos[x0bar]) /
  (2 (Abs[qvbar] (Pi / 2 - ArcSin[Abs[qvbar]]) - Sqrt[1 - Abs[qvbar] ^ 2]));
(*compute the fraction of the hyporheic exchange flux
 associated with the upstream flow cell*)
Clear[frtdupmax]; frtdupmax = f1func[xbarsep /. xbarsepfunc];
(*compute the fraction of the hyporheic
 exchange flux associated with the downstream flow cell*)
```

```
Clear[frtddnmax]; frtddnmax = f2func[xbarsep /. xbarsepfunc];
(*compute the streamline starting position
 in the upstream flow cell for a given F1 value*)
Clear[x0valuesup, f1val];
x0valuesup[xbarsep_, f1val_] := FindRoot[Abs[qvbar] x0valup + Cos[x0valup] ⩵
   2 f1val (Abs[qvbar] (Pi / 2 - ArcSin[qvbar]) - Sqrt[1 - Abs[qvbar] ^ 2]) + Sqrt[1 -
      Abs[qvbar] ^ 2] + Abs[qvbar] ArcSin[Abs[qvbar]], {x0valup, (abar + xbarsep) / 2}];
(*compute the streamline starting position in the downstream
 flow cell for a given F2 value *)
Clear[x0valuesdn, f2val];
x0valuesdn[xbarsep_, f2val_] := FindRoot[Abs[qvbar] x0valdn + Cos[x0valdn] ⩵
   -2 f2val (Abs[qvbar] (Pi / 2 - ArcSin[qvbar]) - Sqrt[1 - Abs[qvbar] ^ 2]) -
    Sqrt[1 - Abs[qvbar] ^ 2] + Abs[qvbar] (Pi - ArcSin[Abs[qvbar]]),
  {x0valdn, (bbar + xbarsep) / 2}];
(*compute the travel time associated with the streamline in either
 the upstream or downstream flow cell that starts at x0bar;
the travel time is returned as "end"*)
Clear[endtime];
endtime[x0bar_] :=
 NDSolve[{(1 / 2.303) x'[u] == - (10^u) Cos[x[u]] Exp[y[u]] + (10^u) qubar,
   (1 / 2.303) y'[u] ⩵ - (10^u) Sin[x[u]] Exp[y[u]] + (10^u) qvbar, x[-5] ⩵ x0bar,
   y[-5] ⩵ 0, WhenEvent[y[u] > 0, {end = u, "StopIntegration"}]}, {x, y}, {u, -5, 5}];
```

Step 3: Prepare probability distributions for residence times in the upstream and downstream flow cells (note this step will take a few moments to complete)

*Dup and Ddn are the probability distributions constructed from 10,000 realizations of the FRTDs associated with the upstream and downstream flow cells, respectively.

```
Clear[𝒟up];
𝒟up = SmoothKernelDistribution[Table[Clear[a, b, x0valup, xbarsep];
   a = RandomReal[];
   b = x0valup /. x0valuesup[xbarsep /. xbarsepfunc, Evaluate[a frtdupmax]];
   end /. First[endtime[b]], {i, 1, 10 000}], 0.1];
Clear[𝒟dn];
𝒟dn = SmoothKernelDistribution[Table[Clear[a, b, x0valdn, xbarsep];
   a = RandomReal[];
   b = x0valdn /. x0valuesdn[xbarsep /. xbarsepfunc, Evaluate[a frtddnmax]];
   end /. First[endtime[b]], {i, 1, 10 000}], 0.1];
```

Step 4: Plot results and check output

```
(*check to make sure that the total probability associated with the
 upstream and downstream flow cells sum to unity*)frtdupmax + frtddnmax == 1
(*plot the upstream, downstream, and total RTD PDFs*)
Plot[{frtdupmax CDF[𝒟up, x], frtddnmax CDF[𝒟dn, x],
  frtdupmax CDF[𝒟up, x] + frtddnmax CDF[𝒟dn, x]}, {x, -1, 3},
 PlotLabels → {"upstream cell", "downstream cell", "total"},
 AxesLabel → {"log10(taubar)", "F1,F2, or FRTD"},
 PlotStyle → {Blue, Orange, Green}, PlotLabel → CDF]
Plot[{frtdupmax PDF[𝒟up, x], frtddnmax PDF[𝒟dn, x],
  frtdupmax PDF[𝒟up, x] + frtddnmax PDF[𝒟dn, x]},
 {x, -1, 3}, AxesLabel → {"log10(taubar)", "dFRTD/dlog10(tau)"},
 PlotStyle → {Blue, Orange, Green}, PlotLabel → PDF]
```

```
True
```

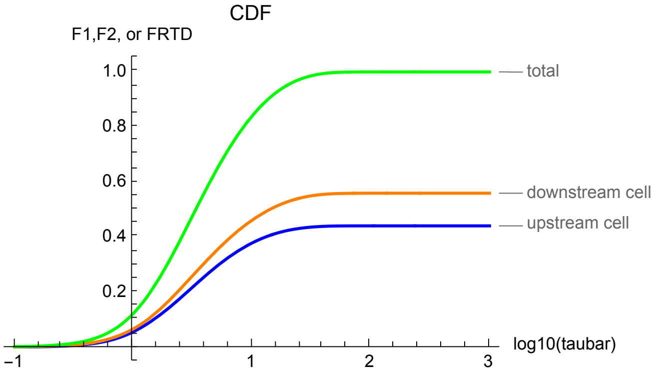

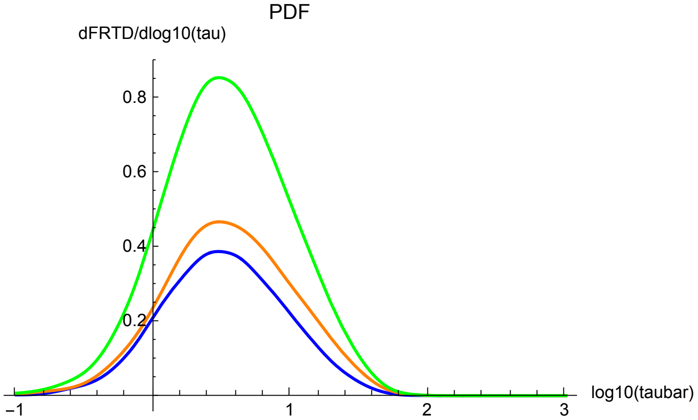

Computing RTDs Trauth et al. 2013 Analysis

Calculation involves 4 steps.

Step 1: Import the RTD data from Trauth et al. 2013

* Imported data is in the following order: {cdf, log10(tau,s)}, where cdf is cumulative distribution function of particle's residence times in the hyporheic zone, and tau is the residence time of particles in the hyporheic zone (units of seconds)

* Imported data is associated with 10 different surfacewater and groundwater scenarios including: High-Discharge (HQ), Low-Discharge(LQ) of streamflow, and groundwater discharge with magnitude of 23x10^6 (m/s), 5.8x10^6 (m/s) (both under gaining (gain) and losing (los) conditions), and 0x10^6 (m/s).

```
Clear[taucdf58HQlos];
taucdf58HQlos = {{0.03120892895514402`, 3.5363025007672872`}, {0.08506079109191823`,
    3.5763025007672873`}, {0.13893048696444985`, 3.6163025007672873`},
  {0.1961373953170287`, 3.6563025007672874`}, {0.25834120552179973`,
    3.6963025007672874`}, {0.33820645398592264`, 3.7363025007672874`},
  {0.418087915456812`, 3.7763025007672875`}, {0.4921746590814004`,
    3.8163025007672875`}, {0.5893170243687391`, 3.856302500767287`},
  {0.6804571213123665`, 3.896302500767287`}, {0.7425563358994368`,
    3.936302500767287`}, {0.8339364236461503`, 3.976302500767287`},
  {0.874275659340223`, 4.016302500767287`}, {0.9206520390648121`,
    4.056302500767287`}, {0.9523077118188857`, 4.096302500767287`},
  {0.9632225669476896`, 4.136302500767287`}, {0.982666121074215 8`,
    4.176302500767287`}, {0.9875965350206799`, 4.216302500767287`},
  {0.9923388455025676`, 4.256302500767287`}, {1.`, 4.296302500767287`}};
Clear[taucdf23HQlos];
taucdf23HQlos = {{0.016327458510520518`, 3.496302500767287`}, {0.03264791239373428`,
    3.5263025007672875`}, {0.06594887462214497`, 3.5563025007672873`},
  {0.13930007053867643`, 3.586302500767287`}, {0.18999396990644168`,
    3.6163025007672873`}, {0.26878504211587545`, 3.646302500767287`},
  {0.3356152272374727`, 3.6763025007672874`}, {0.43096160272951994`,
    3.706302500767287`}, {0.4812113445339057`, 3.7363025007672874`},
  {0.5706732764927755`, 3.7663025007672872`}, {0.6603379250556435`,
    3.796302500767287`}, {0.7160217765974567`, 3.8263025007672873`},
  {0.7888970918321025`, 3.8563025007672875`}, {0.8334535679456436`,
    3.8863025007672873`}, {0.9010735931697382`, 3.916302500767287`},
  {0.9227589383471768`, 3.9463025007672874`}, {0.9331137806853065`,
    3.9763025007672876`}, {0.9608677426109484`, 4.006302500767287`},
  {0.9890353708375084`, 4.036302500767287`}, {1.`, 4.0663025007672875`}};
Clear[taucdf58HQgain];
taucdf58HQgain = {{0.024544533304438215`, 3.6163025007672873`},
  {0.04909805045882064`, 3.6493025007672872`},
```

```
  {0.09122748208384279`, 3.682302500767287`},
  {0.1562622017873248`, 3.715302500767287`}, {0.2241286380770786`,
   3.7483025007672874`}, {0.28730195770704614`, 3.7813025007672874`},
  {0.3987867842698687`, 3.8143025007672873`}, {0.48895410881156276`,
   3.847302500767287`}, {0.5794440550172205`, 3.8803025007672876`},
  {0.6398354803523698`, 3.9133025007672875`}, {0.6930246915754754`,
   3.9463025007672874`}, {0.7537518032327444`, 3.9793025007672873`},
  {0.7909659557605963`, 4.012302500767287`}, {0.8335209172670788`,
   4.045302500767288`}, {0.8757728616866794`, 4.078302500767288`},
  {0.9286990770907905`, 4.111302500767287`}, {0.9534085959785605`,
   4.144302500767288`}, {0.9806378254558777`, 4.177302500767287`},
  {0.9852941890362752`, 4.210302500767288`}, {1.`, 4.243302500767288`}};
Clear[taucdf23HQgain];
taucdf23HQgain = {{0.026667731017709823`, 3.5913025007672874`},
  {0.04904727088532383`, 3.6163025007672873`},
  {0.09507806211346416`, 3.6413025007672872`},
  {0.13600571642152687`, 3.666302500767287`}, {0.1820277576000396`,
   3.6913025007672875`}, {0.2610804481804992`, 3.7163025007672874`},
  {0.31647235281328123`, 3.7413025007672873`}, {0.3955159091006888`,
   3.7663025007672872`}, {0.44641012285430093`, 3.791302500767287`},
  {0.525240594275569`, 3.8163025007672875`}, {0.6040639109869971`,
   3.8413025007672874`}, {0.6969527500807484`, 3.8663025007672873`},
  {0.7427287198247091`, 3.8913025007672872`}, {0.8166436915768909`,
   3.916302500767287`}, {0.8905523014252855`, 3.9413025007672875`},
  {0.9216298706838143`, 3.9663025007672874`}, {0.9628986066929245`,
   3.9913025007672873`}, {0.9800974912046911`, 4.016302500767288`},
  {0.9923963790535877`, 4.041302500767287`}, {1.`, 4.0663025007672875`}};
Clear[taucdf58LQlos];
taucdf58LQlos = {{0.036394511190044186`, 3.5763025007672873`},
  {0.07259439998686038`, 3.613302500767287`},
  {0.08466102887513009`, 3.650302500767287`},
  {0.15745005125521847`, 3.687302500767287`}, {0.22284339710855838`,
   3.7243025007672874`}, {0.31275924552489376`, 3.7613025007672873`},
  {0.3612203877352147`, 3.7983025007672873`}, {0.43849515715862303`,
   3.835302500767287`}, {0.5278271341312604`, 3.872302500767287`},
  {0.6087903268750232`, 3.9093025007672875`}, {0.698316934768916 7`,
   3.9463025007672874`}, {0.7637102806222565`, 3.9833025007672873`},
  {0.8366939211315588`, 4.020302500767287`}, {0.8970270677049145`,
   4.057302500767287`}, {0.9338108236814147`, 4.094302500767287`},
  {0.945682829750055`, 4.131302500767287`}, {0.9898622622533036`,
   4.168302500767287`}, {0.9933654772706471`, 4.205302500767287`},
  {0.9966740690419597`, 4.242302500767288`}, {1.`, 4.279302500767288`}};
Clear[taucdf23LQlos];
taucdf23LQlos = {{0.007510383207496022`, 3.481302500767287`}, {0.03765223265509525`,
```

```
    3.5113025007672873`}, {0.0754053179269017`, 3.541302500767287`},
   {0.1710183923327015`, 3.5713025007672874`}, {0.22235990697978256`,
    3.601302500767287`}, {0.2594746121672557 6`, 3.6313025007672874`},
   {0.3115752136001925`, 3.6613025007672872`}, {0.4078765639291494`,
    3.6913025007672875`}, {0.45145448998557625`, 3.7213025007672873`},
   {0.473428797003828`, 3.751302500767287`}, {0.5988591693495493`,
    3.7813025007672874`}, {0.6357936225383967`, 3.811302500767287`},
   {0.7319512041964711`, 3.8413025007672874`}, {0.8198763337134827`,
    3.871302500767287`}, {0.8411500309311661`, 3.9013025007672875`},
   {0.9145388133537837`, 3.9313025007672873`}, {0.9433915599080024`,
    3.9613025007672875`}, {0.9582884051014461`, 3.9913025007672873`},
   {0.970695558086502`, 4.021302500767288`}, {1.`, 4.051302500767288`}};
Clear[taucdf58LQgain];
taucdf58LQgain = {{0.02006892384401403`, 3.6763025007672874`},
   {0.035069937807800045`, 3.7013025007672873`},
   {0.06101763838373665`, 3.726302500767287`},
   {0.09770930851355834`, 3.751302500767287`}, {0.1210216942388807`,
    3.7763025007672875`}, {0.1800121661840647`, 3.8013025007672874`},
   {0.22156902637311396`, 3.8263025007672873`}, {0.277113320760091 6`,
    3.851302500767287`}, {0.33306304650086527`, 3.876302500767287`},
   {0.37725522154052876`, 3.9013025007672875`}, {0.44921954377368106`,
    3.9263025007672874`}, {0.5217920130375274`, 3.9513025007672873`},
   {0.5884857083321862`, 3.976302500767287`}, {0.6766673454973501`,
    4.001302500767287`}, {0.7484289492908693`, 4.0263025007672875`},
   {0.8418812106317918`, 4.051302500767288`}, {0.922359618922011`,
    4.076302500767287`}, {0.9750658827814763`, 4.101302500767288`},
   {0.9931076426733991`, 4.126302500767287`}, {1.`, 4.1513025007672875`}};
Clear[taucdf23LQgain];
taucdf23LQgain = {{0.003762346685173018`, 3.630302500767287`},
   {0.00790551135454834`, 3.6473025007672875`},
   {0.012042610063947148`, 3.6643025007672874`},
   {0.01346477972478985`, 3.6813025007672873`}, {0.04544540120036268`,
    3.698302500767287`}, {0.05381665607568957`, 3.7153025007672875`},
   {0.06334317153036029`, 3.7323025007672874`}, {0.08446946872708185`,
    3.7493025007672873`}, {0.11544343397180351`, 3.7663025007672872`},
   {0.14700279605615202`, 3.783302500767287`}, {0.21724450133192297`,
    3.8003025007672875`}, {0.27084277893055647`, 3.8173025007672874`},
   {0.3414572145933785`, 3.8343025007672873`}, {0.4341179744670428`,
    3.8513025007672876`}, {0.587899680803063`, 3.8683025007672875`},
   {0.7911958207942456`, 3.8853025007672874`}, {0.883836362088894 7`,
    3.9023025007672874`}, {0.9265627902489897`, 3.9193025007672873`},
   {0.974310625562706`, 3.9363025007672876`}, {1.`, 3.9533025007672875`}};
Clear[taucdf0HQ];
taucdf0HQ = {{0.027261626`, 3.63`}, {0.064555214`, 3.67`}, {0.122623653`, 3.71`},
```

```
  {0.199599585`, 3.75`}, {0.273995895`, 3.79`}, {0.362862156`, 3.83`},
  {0.444245993`, 3.87`}, {0.521417281`, 3.91`}, {0.633374844`, 3.95`},
  {0.701419106`, 3.99`}, {0.754741471`, 4.03`}, {0.805486459`, 4.07`},
  {0.851784022`, 4.11`}, {0.888966235`, 4.15`}, {0.925671504`, 4.19`},
  {0.95559359`, 4.23`}, {0.978267226`, 4.27`}, {0.988787807`, 4.31`}, {1.`, 4.35`}};
Clear[taucdf0LQ];
taucdf0LQ =
 {{0.026557328`, 3.6963025007672874`}, {0.055220669`, 3.726302500767287`},
  {0.085778126`, 3.7563025007672874`}, {0.122256572`, 3.7863025007672872`},
  {0.171224838`, 3.8163025007672875`}, {0.211915311`, 3.8463025007672873`},
  {0.258525149`, 3.876302500767287`}, {0.317627235`, 3.9063025007672874`},
  {0.374809278`, 3.9363025007672876`}, {0.417356589`, 3.9663025007672874`},
  {0.465824078`, 3.996302500767287`}, {0.512585849`, 4.0263025007672875`},
  {0.561453633`, 4.056302500767288`}, {0.61645268`, 4.086302500767287`},
  {0.671650663`, 4.116302500767287`}, {0.773877005`, 4.146302500767288`},
  {0.873758697`, 4.176302500767288`}, {0.928917782`, 4.206302500767288`},
  {0.96351386`, 4.236302500767287`}, {1.`, 4.266302500767288`}};
```

Step 2: Create interpolation functions for the RTD data (log10(tau,s) vs. FRTD)

All the interpolation functions are labeled with “Interp” suffix

```
Clear[taucdf58HQlosInterp, taucdf23HQlosInterp, taucdf58HQgainInterp,
 taucdf23HQgainInterp, taucdf58LQlosInterp, taucdf23LQlosInterp,
 taucdf58LQgainInterp, taucdf23LQgainInterp, taucdf0HQInterp, taucdf0LQInterp];
taucdf58HQlosInterp = Interpolation[taucdf58HQlos];
taucdf23HQlosInterp = Interpolation[taucdf23HQlos];
taucdf58HQgainInterp = Interpolation[taucdf58HQgain];
taucdf23HQgainInterp = Interpolation[taucdf23HQgain];
taucdf58LQlosInterp = Interpolation[taucdf58LQlos];
taucdf23LQlosInterp = Interpolation[taucdf23LQlos];
taucdf58LQgainInterp = Interpolation[taucdf58LQgain];
taucdf23LQgainInterp = Interpolation[taucdf23LQgain];
taucdf0HQInterp = Interpolation[taucdf0HQ];
taucdf0LQInterp = Interpolation[taucdf0LQ];
```

Step 3: Prepare probability distributions for residence times

```
𝒟58HQlos = SmoothKernelDistribution[Table[Clear[a];
    a = RandomReal[{First[taucdf58HQlos[[{1}, 1]]], 1}];
    taucdf58HQlosInterp[a], {i, 1, 10 000}]];
𝒟23HQlos = SmoothKernelDistribution[Table[Clear[a];
    a = RandomReal[{First[taucdf23HQlos[[{1}, 1]]], 1}];
    taucdf23HQlosInterp[a], {i, 1, 10 000}]];
𝒟58HQgain = SmoothKernelDistribution[Table[Clear[a];
    a = RandomReal[{First[taucdf58HQgain[[{1}, 1]]], 1}];
    taucdf58HQgainInterp[a], {i, 1, 10 000}]];
𝒟23HQgain = SmoothKernelDistribution[Table[Clear[a];
    a = RandomReal[{First[taucdf23HQgain[[{1}, 1]]], 1}];
    taucdf23HQgainInterp[a], {i, 1, 10 000}]];
𝒟58LQlos = SmoothKernelDistribution[Table[Clear[a];
    a = RandomReal[{First[taucdf58LQlos[[{1}, 1]]], 1}];
    taucdf58LQlosInterp[a], {i, 1, 10 000}]];
𝒟58LQgain = SmoothKernelDistribution[Table[Clear[a];
    a = RandomReal[{First[taucdf58LQgain[[{1}, 1]]], 1}];
    taucdf58LQgainInterp[a], {i, 1, 10 000}]];
𝒟23LQlos = SmoothKernelDistribution[Table[Clear[a];
    a = RandomReal[{First[taucdf23LQlos[[{1}, 1]]], 1}];
    taucdf23LQlosInterp[a], {i, 1, 10 000}]];
𝒟23LQgain = SmoothKernelDistribution[Table[Clear[a];
    a = RandomReal[{First[taucdf23LQgain[[{1}, 1]]], 1}];
    taucdf23LQgainInterp[a], {i, 1, 10 000}]];
𝒟0HQ = SmoothKernelDistribution[Table[Clear[a];
    a = RandomReal[{First[taucdf0HQ[[{1}, 1]]], 1}];
    taucdf0HQInterp[a], {i, 1, 10 000}]];
𝒟0LQ = SmoothKernelDistribution[Table[Clear[a];
    a = RandomReal[{First[taucdf0LQ[[{1}, 1]]], 1}];
    taucdf0LQInterp[a], {i, 1, 10 000}]];
```

Step 4: Plot Trauth’s RTDs

```
Plot[{CDF[𝒟58HQlos, x], CDF[𝒟23HQlos, x], CDF[𝒟58HQgain, x],
  CDF[𝒟23HQgain, x], CDF[𝒟58LQlos, x], CDF[𝒟58LQgain, x], CDF[𝒟23LQlos, x],
  CDF[𝒟23LQgain, x], CDF[𝒟0HQ, x], CDF[𝒟0LQ, x]}, {x, 3, 4.5},
 AxesLabel → {"log10(tau,s)", "FRTD[log10(tau,s)]"}, PlotLabel → CDF]
```

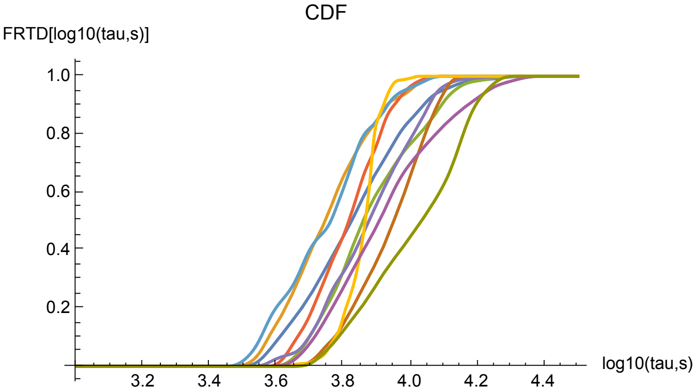

```
Plot[{PDF[𝒟58HQlos, x], PDF[𝒟23HQlos, x], PDF[𝒟58HQgain, x],
  PDF[𝒟23HQgain, x], PDF[𝒟58LQlos, x], PDF[𝒟58LQgain, x],
  PDF[𝒟23LQlos, x], PDF[𝒟23LQgain, x], PDF[𝒟0HQ, x], PDF[𝒟0LQ, x]},
 {x, 3, 4.5}, AxesLabel → {"log10(tau,s)", "dFRTD/dlog10(tau,s)"},
 PlotLabel → PDF, PlotRange → {0, 14}]
```

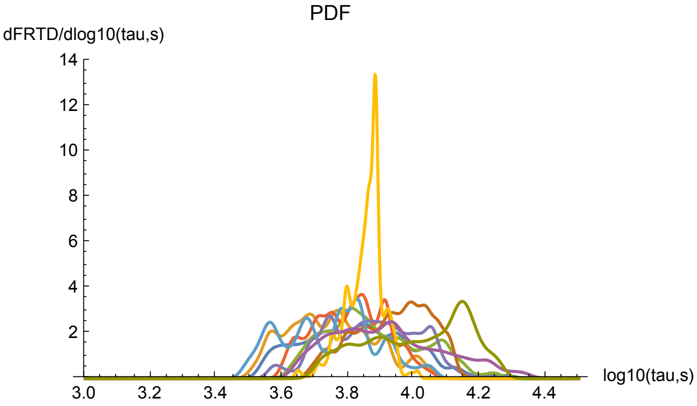

Note: Before running this analysis: (1) run “RTD.nb” code and (2) run “chemistry.nb” code.

Compute the nitrate uptake and denitrification velocity for ripples

(a) Calculate the flow-weighted concentration of nitrate breaking through the hyporheic zone (note that this value is normalized by the in-stream concentration of nitrate).

```
Clear[cNO3bar];
cNO3bar = NIntegrate[((cNO3st[u + Log10[tT / tr]] + cNO3stN[u + Log10[tT / tr]] +
        cNO3sedN[u + Log10[tT / tr]]) /. sn)
    (1 / beta) (frtdupmax PDF[𝒟up, u] + frtddnmax PDF[𝒟dn, u]),
   {u, -10 - Log10[tT / tr], First[end /. sn] - Log10[tT / tr]}, WorkingPrecision → 10]
Clear[cNO3barup];
cNO3barup = NIntegrate[((cNO3st[u + Log10[tT / tr]] + cNO3stN[u + Log10[tT / tr]] +
        cNO3sedN[u + Log10[tT / tr]]) /. sn) (1 / beta) (frtdupmax PDF[𝒟up, u]),
   {u, -10 - Log10[tT / tr], First[end /. sn] - Log10[tT / tr]}, WorkingPrecision → 10]
Clear[cNO3bardn];
cNO3bardn =
 NIntegrate[((cNO3st[u + Log10[tT / tr]] + cNO3stN[u + Log10[tT / tr]] + cNO3sedN[
         u + Log10[tT / tr]]) /. sn) (1 / beta) (frtddnmax PDF[𝒟dn, u]),
   {u, -10 - Log10[tT / tr], First[end /. sn] - Log10[tT / tr]}, WorkingPrecision → 10]
```

```
{1.339187838}
```

```
{0.3965637639}
```

```
{0.9426230748}
```

(b) Calculate the flow-weighted concentration of nitrogen gas “generated from stream nitrate” and breaking through the hyporheic zone (note that this value is normalized by the in-stream concentration of nitrate).

```
Clear[cN2barst]; cN2barst = NIntegrate[(cN2st[u + Log10[tT / tr]] /. sn)
    (1 / beta) (frtdupmax PDF[𝒟up, u] + frtddnmax PDF[𝒟dn, u]),
   {u, -10 - Log10[tT / tr], First[end /. sn] - Log10[tT / tr]}, WorkingPrecision → 10]
Clear[cN2barupst];
cN2barupst =
 NIntegrate[(cN2st[u + Log10[tT / tr]] /. sn) (1 / beta) (frtdupmax PDF[𝒟up, u]),
  {u, -10 - Log10[tT / tr], First[end /. sn] - Log10[tT / tr]}, WorkingPrecision → 10]
Clear[cN2bardnst];
cN2bardnst =
 NIntegrate[(cN2st[u + Log10[tT / tr]] /. sn) (1 / beta) (frtddnmax PDF[𝒟dn, u]),
  {u, -10 - Log10[tT / tr], First[end /. sn] - Log10[tT / tr]}, WorkingPrecision → 10]
```

```
{0.0006973134584}

{0.0001157206618}

{0.0005815999727}
```

(c) Calculate the flow-weighted concentration of nitrogen gas “generated from coupled nitrification-denitrification of sediment and stream ammonium” and breaking through the hyporheic zone (note that this value is normalized by the in-stream concentration of nitrate).

```
Clear[cN2barNH4];
cN2barNH4 = NIntegrate[((cN2stN[u + Log10[tT / tr]] + cN2sedN[u + Log10[tT / tr]]) /. sn)
    (1 / beta) (frtdupmax PDF[𝒟up, u] + frtddnmax PDF[𝒟dn, u]),
   {u, -10 - Log10[tT / tr], First[end /. sn] - Log10[tT / tr]}, WorkingPrecision → 10]
Clear[cN2barupNH4];
cN2barupNH4 = NIntegrate[((cN2stN[u + Log10[tT / tr]] + cN2sedN[u + Log10[tT / tr]]) /.
      sn) (1 / beta) (frtdupmax PDF[𝒟up, u]),
   {u, -10 - Log10[tT / tr], First[end /. sn] - Log10[tT / tr]}, WorkingPrecision → 10]
Clear[cN2bardnNH4];
cN2bardnNH4 =
 NIntegrate[((cN2stN[u + Log10[tT / tr]] + cN2sedN[u + Log10[tT / tr]]) /. sn)
    (1 / beta) (frtddnmax PDF[𝒟dn, u]),
   {u, -10 - Log10[tT / tr], First[end /. sn] - Log10[tT / tr]}, WorkingPrecision → 10]
```

```
{0.0005027710722}

{0.00008700723375}

{0.0004157767615}
```

Note: Before running this section, modify the corresponding riffle-pool RTD name in the breakthrough concentration commands below.

Compute the nitrate uptake and denitrification velocity

for riffle-pools

(a) Calculate the flow-weighted concentration of nitrate breaking through the hyporheic zone (note that this value is normalized by the in-stream concentration of nitrate).

(b) Calculate the flow-weighted concentration of nitrogen gas “generated from stream nitrate” and breaking through the hyporheic zone (note that this value is normalized by the in-stream concentration of nitrate).

(c) Calculate the flow-weighted concentration of nitrogen gas “generated from coupled nitrification and denitrification of sediment and stream ammonium” and breaking through the hyporheic zone (note that this value is normalized by the in-stream concentration of nitrate).

```
Clear[cNO3barRP]; cNO3barRP = NIntegrate[
  ((cNO3st[u - Log10[tr]] + cNO3stN[u - Log10[tr]] + cNO3sedN[u - Log10[tr]]) /. sn)
   (1 / beta) (PDF[𝒟23HQlos, u]),
  {u, -10 + Log10[tr], First[end /. sn] + Log10[tr]}, WorkingPrecision → 10]
Clear[cN2barRPst]; cN2barRPst = NIntegrate[
  (cN2st[u - Log10[tr]] /. sn) (1 / beta) (PDF[𝒟23HQlos, u]),
  {u, -10 + Log10[tr], First[end /. sn] + Log10[tr]}, WorkingPrecision → 10]
Clear[cN2barRPNH4]; cN2barRPNH4 = NIntegrate[
  ((cN2stN[u - Log10[tr]] + cN2sedN[u - Log10[tr]]) /. sn) (1 / beta) (PDF[𝒟23HQlos, u]),
  {u, -10 + Log10[tr], First[end /. sn] + Log10[tr]}, WorkingPrecision → 10]
```

```
{3.501544669}

{0.005527064584}

{0.007457780693}
```

Appendix D

Factoring Physics into Local and Global Assessments of Nitrogen Pollution

Text D.1. Derivation of Equation (1) in Chapter 5

From a steady-state mass balance over the mass transfer circuit presented in **Figure 5.1A** (**Chapter 5**) we deduce that the flux of nitrate toward the sediment bed (J_{bed} , units mol m^{-2} s^{-1}) is the sum of per area rates of nitrate uptake by assimilation or denitrification in the benthic algal layer (R''_{algae} , units mol m^{-2} s^{-1}) and in the hyporheic zone (R''_{HZ} , units mol m^{-2} s^{-1}).

$$J_{\text{bed}} = R''_{\text{algae}} + R''_{\text{HZ}} \tag{D1}$$

Next we define nitrate uptake velocities in the benthic algal layer and hyporheic zone as the ratio of the per area uptake rates in these two layers divided by the nitrate concentration at the sediment-water interface $\left[\text{NO}_3^-\right]_{\text{SWI}}$:

$$v_{\text{algae}} = \frac{R''_{\text{algae}}}{\left[\text{NO}_3^-\right]_{\text{SWI}}} \tag{D2}$$

$$v_{\text{HZ}} = \frac{R''_{\text{HZ}}}{\left[\text{NO}_3^-\right]_{\text{SWI}}} \tag{D3}$$

In the main text we hypothesize that flux of nitrate into the sediment bed may be rate-limited by turbulent transport across a concentration boundary layer, which we model using a mass transfer coefficient (k_{m} , units m s^{-1}):

$$J_{\mathrm{bed}} = k_{\mathrm{m}}\left(\left[\mathrm{NO}_3^-\right]_{\mathrm{stream}} - \left[\mathrm{NO}_3^-\right]_{\mathrm{SWI}}\right) \qquad \text{(D4)}$$

Combining the last three equations and solving for the nitrate concentration at the sediment-water interface we obtain:

$$\left[\mathrm{NO}_3^-\right]_{\mathrm{SWI}} = \frac{k_{\mathrm{m}}\left[\mathrm{NO}_3^-\right]_{\mathrm{stream}}}{\left(v_{\mathrm{algae}} + v_{\mathrm{HZ}} + k_{\mathrm{m}}\right)} \qquad \text{(D5)}$$

Substituting equation (D5) into equation (D4) we obtain a solution for the flux of nitrate into the sediment bed from the stream:

$$J_{\mathrm{bed}} = k_{\mathrm{m}}\left[\mathrm{NO}_3^-\right]_{\mathrm{stream}}\left(1 - \frac{k_{\mathrm{m}}}{\left(v_{\mathrm{algae}} + v_{\mathrm{HZ}} + k_{\mathrm{m}}\right)}\right) \qquad \text{(D6)}$$

From the definition of the removal efficiency, equation (D6) can be rearranged into the form appearing in the main text where

$$\alpha = \frac{v_{\mathrm{f}}}{k_{\mathrm{m}}} = \frac{J_{\mathrm{bed}}}{k_{\mathrm{m}}\left[\mathrm{NO}_3^-\right]_{\mathrm{stream}}} = 1 - \frac{1}{\psi + 1} \qquad \text{(D7a)}$$

$$\psi = \frac{v_{\mathrm{algae}} + v_{\mathrm{HZ}}}{k_{\mathrm{m}}} = \frac{\text{uptake velocities in algal layer and HZ}}{\text{maximum turbulent flux across boundary layer}} \qquad \text{(D7b)}$$

Text D.2. Derivation of Equation (3) in Chapter 5

We derived equation (3) in Chapter 5, by performing mass balance over a stream reach assuming steady uniform flow: $f = 1 - \exp\left(-v_{\mathrm{f}}/H_{\mathrm{L}}\right)$ where $H_{\mathrm{L}} = Uh/L$ is the hydraulic loading rate of the stream. Equation (3) follows by substituting equations (1a) and (2a).

Text D.3. Simplification of the Relationship between ψ and α

A first-order Taylor series expansion of equation (1b) around $\psi = 0$ yields $\alpha = \psi + O(\psi^2)$, $0 < \psi \ll 1$ and thus $\psi \approx \alpha = v_\mathrm{f}/k_\mathrm{m}$ when $0 < \psi \ll 1$. When combined with equation (1b) the resulting formula for the efficiency ($\alpha = 1-(1+v_\mathrm{f}/k_\mathrm{m})^{-1}$) is likely valid even when the restriction $\psi \ll 1$ does not apply, because the efficiency is insensitive to ψ as the latter becomes large (i.e., $\alpha \to 1$ as $\psi \to \infty$, see equation (1b)).

Text D.4. Back Calculating the Fraction of Nitrate Removed at LINX II Sites

LINX II researchers calculated their uptake velocities from measurements of the fraction of ^{15}N-labeled nitrate removed (or ^{15}N-labeled N_2 generated) over an experimental reach (see Mulholland et al. [2008]). Using nutrient spiraling theory [Ensign and Doyle, 2006], we back-calculated these fractions from reported values of the denitrification and assimilation uptake velocities ($v_\mathrm{f,den}$ and $v_\mathrm{f,asm}$, units m s^{-1}), reach length L (units m), stream discharge Q (units m^3 s^{-1}), and width of the stream w (units m):

$$f_\mathrm{den} = 1 - \frac{[\mathrm{NO_3^-}]}{[\mathrm{NO_3^-}]_0} = 1 - \exp\left[-\frac{v_\mathrm{f,den} L}{(Q/w)}\right] \tag{D8a}$$

$$f_\mathrm{asm} = 1 - \frac{[\mathrm{NO_3^-}]}{[\mathrm{NO_3^-}]_0} = 1 - \exp\left[-\frac{v_\mathrm{f,asm} L}{(Q/w)}\right] \tag{D8b}$$

Values of the assimilation velocity ($v_\mathrm{f,asm}$) were calculated from site-specific values reported for the total ($v_\mathrm{f,tot}$) and denitrification ($v_\mathrm{f,den}$) uptake velocities: $v_\mathrm{f,asm} = v_\mathrm{f,tot} - v_\mathrm{f,den}$.

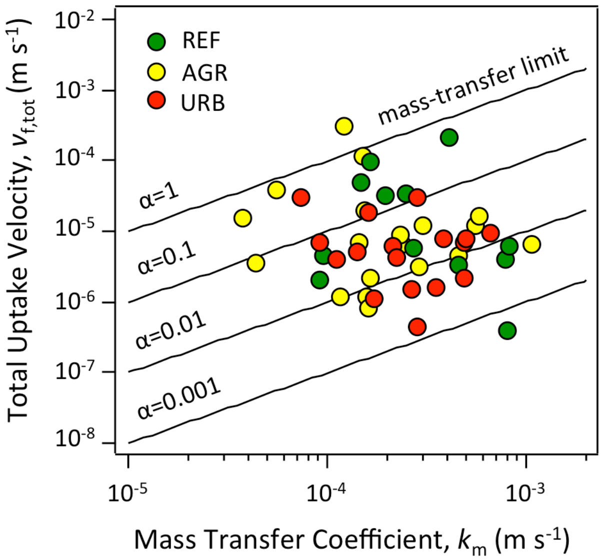

Figure D.1. Cross plot of the total uptake velocity (defined as the sum of uptake velocities for denitrification and assimilation) against the mass transfer coefficients calculated from equation (2a). Color denotes LINX II sites with different land-use types, including reference (REF), agriculture (AGR), and urban (URB).

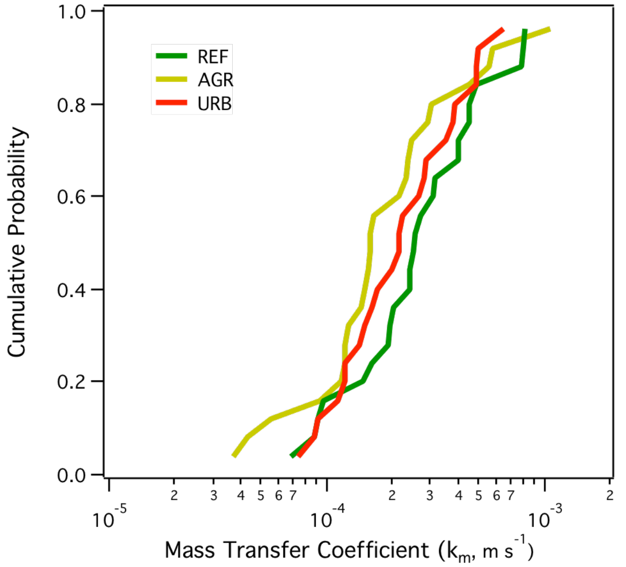

Figure D.2. Cumulative distribution functions (CDFs) for mass transfer coefficients calculated from equation (2a) at LINX II sites with different land-use types, including reference (REF), agriculture (AGR), and urban (URB).

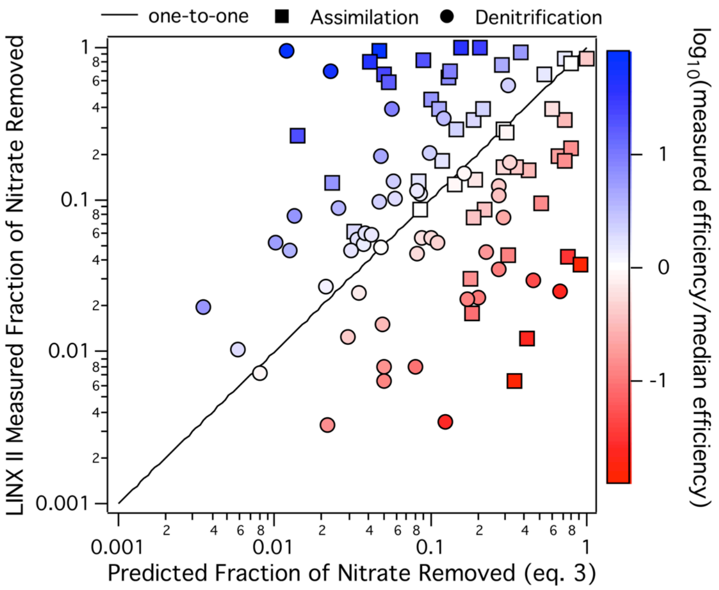

Figure D.3. Cross plot of measured and predicted values of the fraction of nitrate removed over the LINX II experimental reaches. Predicted removal fractions are calculated from equation (3) assuming median values for denitrification ($\alpha_{\mathrm{den}} = 0.0045$) and assimilation ($\alpha_{\mathrm{asm}} = 0.0183$) efficiencies. Color denotes the log-transformed ration of site-specific estimates of the denitrification or assimilation efficiency normalized by the corresponding median value. Sites where the measured efficiency is close to the median values (denoted by white symbols) fall close to the one-to-one line.

References

Ensign, S.H., M.W. Doyle (2006) Nutrient spiraling in streams and river networks. J. Geophys. Res. 111, G04009.

Mulholland, P.J. et al. (2008) Stream denitrification across biomes and its response to anthropogenic nitrate loading. Nature 452, 202-206.